Year: 2024

# THE ROLE OF PROGLACIAL FOREFIELDS IN FILTERING THE SIGNAL OF SUBGLACIAL SEDIMENT EXPORT

## Mancini Davide

FACULTÉ DES GÉOSCIENCES ET DE L'ENVIRONNEMENT

INSTITUT DES DYNAMIQUES DE LA SURFACE DE LA TERRE


**THE ROLE OF PROGLACIAL FOREFIELDS IN FILTERING THE SIGNAL OF SUBGLACIAL SEDIMENT EXPORT**


THÈSE DE DOCTORAT

présentée à la

Faculté des Géosciences et de l'environnement
de l'Université de Lausanne

pour l'obtention du grade de

Docteur en Géographie

par

**Davide Mancini**
B.Sc., M.Sc., Université de Lausanne, Suisse


Directeur de thèse
Prof. Dr. Stuart Nicholas Lane


Co-directeur de thèse
Prof. Dr. Andrew Paul Nicholas


Jury

Prof. Dr. Céline Rozenblat
Prof. Dr. Gregoire Mariethoz
Prof. Dr. Richard Williams
Prof. Dr. Simone Bizzi


LAUSANNE
(Octobre 2024)

# IMPRIMATUR

La Faculté des géosciences et de l'environnement de l'Université de Lausanne, vu le rapport du jury d'examen, autorise l'impression de la thèse de doctorat rédigée par

## Davide MANCINI

intitulée

### *The role of proglacial forefields in filtering the signal of subglacial sediment export.*

sans se prononcer sur les opinions exprimées dans cette thèse.

Directeur          Monsieur le Professeur Stuart Lane

Co-directeur       Monsieur le Professeur Andrew Nicholas

Lausanne, le 04.10.2024

Professeur Torsten Vennemann, Doyen

"Imagine a flat-bottomed cup full of tea. At the bottom there are some tea leaves, which stay there because they are rather heavier than the liquid they have replaced. If the liquid is made to rotate by a spoon, the leaves will soon collect in the center of the bottom of the cup. The rotation of the liquid causes a centrifugal force to act on it. This in itself would give rise to no change in the flow of the liquid if the latter rotated like a solid body. But in the neighborhood of the walls of the cup the liquid is restrained by friction, so that the angular velocity with which it rotates is less there than in other places nearer the center. In particular, the angular velocity of rotation, and therefore the centrifugal force, will be smaller near the bottom than higher up. The result of this will be a circular movement [helical flow] of the liquid which goes on increasing until, under the influence of ground friction, it becomes stationary. The tea leaves are swept into the center by the circular movement and act as proof of its existence. The same sort of things happens with a curving stream […] revealing the causes of the formation of meanders".

Albert Einstein (1954). *The cause of formation of meanders in the courses of rivers and of the so-called Bear's Law.*

## Acknowledgements

very big thank goes to my former flat mates Giacomo, Giovanni and Matteo for all the unforgettable moments spent together.

Cycling and my bike, which taught me to never give up, especially when the road becomes steeper and the legs are filled of fatigue. This lesson has been fundamental for the completion of this long and hilly PhD journey. Many thanks to my cycling buddies for the fun, for the beautiful rides and for providing me with moments of freedom during stressful periods. Great rides and new adventures are now waiting for us!

My girlfriend Rita, for her love, patience, support and wonderful memories during these years spent together. I feel blessed to have met you, and I am very proud to share my life with yours. Many thanks also to our cat Whisky for keeping me company during the writing of this thesis. You are now a *giovane geomorfologo*.

My family, who always believed in me. Thank you for your sacrifices to give me the opportunity to pursue my interests, for your motivation and support throughout my academic journey, and for teaching me the curiosity about the world around us.

*Lausanne, July 2024*

Davide Mancini

# Summary

The rapid recession of glaciers due to climate warming is increasing the total surface of proglacial margins, landscapes relatively poor at first in terms of organic matter but shaped by high geomorphic activity, including hillslope processes and river morphodynamics. Under suitable conditions, proglacial forefields may develop and contain morphologically active braid plains. These are zones of accumulation, transport and erosion of glacially-outwashed sediment characterized by a network of shallow, unstable channels which continually shift their position in response to discharge and sediment load variation associated with glacial meltwater and sediment supply.

Field measurements, numerical simulations and scaled laboratory experiments have all been used to study the formation, maintenance and evolution of these fluvial systems. However, knowledge on how forefield morphodynamics interact with upstream boundary conditions (i.e. subglacial sediment export and meltwater runoff variation), and the effects of these interactions on downstream sediment transport, is still lacking. This gap arises from practical limitations related to the inability to collect continuous (subglacial) sediment transport rates, notably for bedload sized sediment, concurrent with spatially extensive, high resolution and high precision information on river morphodynamics.

Given the above, the core aim of the thesis is to undertake the first, coupled study of the relationship between continuous records of subglacial sediment export, proglacial forefield morphodynamics and downstream sediment fluxes for a retreating Alpine glacier. The focus is on the Glacier d'Otemma proglacial floodplain (south-western Swiss Alps), a region particularly suitable for this study as characterized by a high disconnectivity between the valley-sidewalls and the valley-bottom minimizing hillslope influences on the river. A set of methodological approaches for continuously quantifying sediment transport for both suspended sediment and bedload particles through the proglacial forefield were deployed. The comparison of sediment transport data collected at the glacier terminus with that at the forefield outlet using established signal post-processing techniques revealed that morphodynamic processes rapidly filter (i.e. dampen and delay) the subglacial sediment export signal related to bedload, while that of suspended sediment passes almost unimpeded through the proglacial margin.

To understand the operation of this filter, an intensive survey of fluvial morphodynamics and surface sedimentology was undertaken. Daily drone surveys of the floodplain were used to quantify spatial patterns of erosion and deposition. Central to the latter was the development of a heuristic model for predicting water depth distribution in highly-turbid braided rivers to generate elevation models for both dry and inundated areas. These were then combined with the subglacial sediment export rates to quantify the influence of proglacial morphodynamics for downstream sediment transport. Changes in the balance between glacial sediment supply and transport capacity resulted in rapid changes in river morphodynamics. During periods when subglacial bedload supply exceeded transport capacity there was aggradation in the forefield, accompanied by more intense bar construction, increased channel instability and rising braiding intensity and surficial coarsening of floodplain deposits. The forefield acted as a sink for both bedload and suspended load sediment. In contrast, when the subglacial bedload export rates were lower than transport capacity, the forefield continued to act as a sediment sink for fine sediment, but the system was net degradational for bedload sediment.

To generalize these findings to situations with different topographical, sedimentological and hydrological settings, it was used an hydromorphological calibrated with field-collected data. Results confirmed the central role of the supply to transport capacity ratio in determining both proglacial stream geomorphic response and downstream sediment delivery rates; with lower ratios leading to more hydraulically efficient scenarios and more ready transfer of the

subglacial sediment export signal to downstream. However, this effect was also influenced by larger-scale forcing of valley topography including accommodation space, suggesting that the filtering effect varies between geomorphological settings.

The results of this thesis demonstrate that proglacial forefields play a significant role for the sediment connectivity between glacier *termini* and downstream regions. These findings have important implications for natural hazards mitigation, ecosystem development, hydropower plants management and glaciological studies in the actual context of rapid glacier recession.

## Résumé

La rapide récession des glaciers due au réchauffement climatique accroît la surface totale des marges proglaciaires, paysages relativement pauvres en matière organique mais façonnés par une activité géomorphologique intense, comprenant les processus de versant et la morphodynamique fluviale. Dans des conditions géomorphologiques appropriées, des marges proglaciaires peuvent se former et contenir des cours d'eau tressés morphologiquement actifs. Ces derniers sont des zones d'accumulation, de transport et d'érosion des sédiments glaciaires caractérisées par un réseau de chenaux peu profonds et instables qui changent continuellement leur position en réponse aux variations de débit et de charge sédimentaire associées à la fonte glaciaire et à l'approvisionnement en sédiments.

Les mesures sur le terrain, les simulations numériques et les expériences de laboratoire à l'échelle réduite sont des outlis qui ont été utilisés pour étudier la formation, la maintenance et l'évolution de ces systèmes fluviaux. Cependant, les connaissances dont la morphodynamique des avant-pays interagit avec les conditions limites en amont (c'est-à-dire l'exportation de sédiments sous-glaciaires et la variation du ruissellement de fonte), et les effets de ces interactions sur le transport sédimentaire en aval, font encore défaut. Cette lacune découle de limitations pratiques liées à l'incapacité à collecter en continu des taux de transport de sédiments (sous-)glaciaires, notamment pour les sédiments transportés en contact avec le lit du cours d'eau, simultanément avec des informations spatialement étendues, à haute résolution et précision sur la morphodynamique fluviale.

L'objectif principal de la thèse est d'entreprendre la première étude couplée de la relation entre les enregistrements continus de l'exportation de sédiments subglaciaires, la morphodynamique des marges proglaciaires actives et les flux sédimentaires aval pour un glacier alpin en retrait. L'accent est mis sur la plaine d'inondation proglaciaire du Glacier d'Otemma (Alpes suisses du sud-ouest), une région particulièrement propice à cette étude car caractérisée par une forte déconnexion sédimentaire entre les versants et le fond de la vallée. Un ensemble d'approches méthodologiques pour quantifier en continu le transport de sédiments en suspension et du charriage de fond à travers la marge proglaciaire ont été déployé. La comparaison des données de transport de sédiments collectées au terminus du glacier avec celles à la sortie du système proglaciaire à l'aide de techniques de post-traitement du signal ont révélé que les processus morphodynamiques filtrent rapidement (atténuent et retardent) le signal d'exportation de sédiments sous-glaciaires lié au charriage, tandis que celui des sédiments en suspension passe presque sans entrave à travers la marge proglaciaire.

Pour comprendre le fonctionnement de ce filtre, une enquête intensive sur la morphodynamique fluviale et la sédimentologie de surface a été menée. Des relevés quotidiens par drone de la plaine d'inondation ont été utilisés pour quantifier la distribution spatiale d'érosion et de dépôt. Au cœur de cette analyse, il y avait le développement d'un modèle heuristique pour prédire la distribution de la profondeur de l'eau dans les rivières tressées très turbides afin de générer des modèles numériques de terrain pour les zones sèches et inondées. Ces derniers ont ensuite été combinés avec les taux d'exportation de sédiments sous-glaciaires pour quantifier l'influence de la morphodynamique proglaciaire sur le transport sédimentaire aval. Les changements dans l'équilibre entre l'approvisionnement en sédiments glaciaires et la capacité de transport ont entraîné des changements rapides dans la morphodynamique fluviale. Pendant les périodes où l'exportation en charriage sous-glaciaires dépassait la capacité de transport, il y avait une aggradation de la plaine alluviale, accompagnée d'une construction de barres plus intense, d'une instabilité accrue des chenaux et d'un grossissement des dépôts superficiels. La marge proglaciaire a agi comme un puits pour les sédiments fins et grossiers. En revanche, lorsque les taux d'exportation de sédiments de charriage sous-glaciaires étaient inférieurs à la capacité de transport, la plaine alluviale a

continué à agir comme un puits pour les particules fines, mais le système était en nette dégradation pour les sédiments grossiers.

Pour généraliser ces résultats à des situations avec des configurations topographiques, sédimentologiques et hydrologiques différentes, un modèle hydromorphologique a été calibré avec les données collectées directement sur le terrain. Les résultats ont confirmé le rôle central du rapport entre l'approvisionnement et la capacité de transport pour la détermination de la réponse géomorphologique des rivières proglaciaires et des débits sédimentaires vers l'aval; avec des ratios plus faibles conduisant à des scénarios plus hydrauliquement efficaces et un transfert plus facile du signal d'exportation de sédiments sous-glaciaires à travers la marge proglaciaire. Cependant, cet effet était également influencé par les forçages à plus grande échelle de la topographie de la vallée, notamment l'espace d'accommodation et la pente, suggérant que l'effet de filtrage varie beaucoup en fonction des configurations géomorphologiques.

Les résultats de cette thèse démontrent que les cours d'eau proglaciaires tréssés jouent un rôle significatif pour la connectivité sédimentaire entre les terminus glaciaires et les régions aval. Ces résultats ont d'importantes implications pour l'atténuation des risques naturels, le développement des écosystèmes, la gestion des centrales hydroélectriques et les études glaciologiques dans le contexte actuel de rapide récession des glaciers.

**Riassunto**

Il riscaldamento climatico sta modificando profondamente il paesaggio alpino, causando una rapida recessione dei ghiacciai e aumentando la superficie totale dei loro margini, detti margini proglaciali. I margini proglaciali sono zone relativamente povere in materia organica ma modellate da un'attività geomorfologica intensa, compresi i processi di versante e la morfodinamica fluviale. In condizioni geomorgologiche adeguate, possono formarsi margini proglaciali ospitanti corsi d'acqua intrecciati e morfologicamente attivi. Questi corsi d'acqua sono zone di accumulo, trasporto ed erosione dei sedimenti glaciali e sono caratterizzati da una fitta rete di canali poco profondi e instabili che cambiano continuamente la loro posizione in risposta alle variazioni di portata e di carico sedimentario che, a loro volta, sono associati alla fusione glaciale e all'approvvigionamento in sedimenti.

Gli strumenti utilizzati in passato per studiare la formazione, il mantenimento e l'evoluzione di questi sistemi fluviali sono le misure sul campo, le simulazioni numeriche e gli esperimenti di laboratorio in scala ridotta. Tuttavia, si conosce ancora poco di come l'esportazione di sedimenti subglaciali e la variazione del deflusso di fusione a monte interagisca con la morfodinamica dei margini proglaciali attivi, e gli effetti di queste interazioni sul trasporto sedimentario a valle. Questa lacuna deriva da limiti pratici legati all'incapacità di raccogliere in modo continuo e simultaneo sia i tassi di trasporto di sedimenti (sotto-)glaciali (in particolare per i sedimenti trasportati in contatto con il letto fluviale), sia le informazioni sulla morfodinamica fluviale su ampie superfici, ad alta risoluzione e di alta precisione.

Considerando quanto sopra, l'obiettivo principale della tesi è di intraprendere il primo studio congiunto della relazione tra registrazioni continue dell'esportazione di sedimenti subglaciali, morfodinamica dei corsi d'acqua proglaciali intrecciati e flussi sedimentari a valle per un ghiacciaio alpino in ritirata. La zona di studi scelta per questa tesi è la pianura alluvionale proglaciale del Ghiacciaio di Otemma (Alpi svizzere sud-occidentali), una regione particolarmente adatta per questo progetto poiché caratterizzata da una forte disconnessione sedimentaria tra i versanti e il fondo valle attenuante l'apporto di sediment verso il fiume. Il margine proglaciale è stato analizzato usando molteplici approcci metodologici per quantificare in modo continuo e simultaneo sia il trasporto di sedimenti in sospensione, sia il trasporto di sedimenti di fondo. I dati di trasporto dei sedimenti raccolti al portale glaciale sono stati confrontati con quelli all'uscita del margine proglaciale utilizzando tecniche di post-elaborazione del segnale; tali dati hanno rivelato che i processi morfodinamici filtrano rapidamente, ovvero attenuano e ritardano, il segnale di esportazione di sedimenti subglaciali legato al trasporto di fondo, mentre quello dei sedimenti in sospensione passa quasi senza ostacoli attraverso il margine proglaciale.

Per comprendere il funzionamento di questo filtro, è stata condotta un'indagine intensiva sulla morfodinamica fluviale e sulla sedimentologia superficiale. Sopralluoghi giornalieri con drone della pianura alluvionale sono stati utilizzati per quantificare la spazialità dell'erosione e della deposizione. Al centro di quest'ultimo vi era lo sviluppo di un modello euristico per predire la distribuzione della profondità dell'acqua nei fiumi intrecciati torbidi al fine di generare modelli numerici del terreno sia per le aree asciutte che per le aree inondate. Questi ultimi sono stati poi combinati con i tassi di esportazione di sedimenti subglaciali per quantificare l'influenza della morfodinamica proglaciale sul trasporto sedimentario a valle. I cambiamenti nell'equilibrio tra l'approvvigionamento di sedimenti sotto-glaciali e la capacità di trasporto hanno comportato cambiamenti rapidi nella morfodinamica fluviale. Durante i periodi in cui l'approvvigionamento sotto-glaciale di ghiaia superava la capacità di trasporto, c'era una aggradazione della pianura alluvionale, accompagnata da una costruzione di isole più intensa, una maggiore instabilità dei canali, un'intensificazione dell''intreccio, e un ingrossamento dei depositi superficiali. Il margine proglaciale ha agito come un pozzo sia per i sedimenti grossieri

che per quelli fini. Al contrario, quando i tassi di esportazione sotto-glaciale di ghiaia erano inferiori alla capacità di trasporto, la pianura alluvionale ha continuato ad agire come un pozzo per i sedimenti fini, ma il sistema era netto degradativo per i sedimenti grossieri.

Per generalizzare questi risultati a situazioni con diverse configurazioni topografiche, sedimentologiche e idrologiche, è stato utilizzato un modello idromorfologico calibrato e validato utilizzando dati raccolti direttamente sul campo. I risultati hanno confermato il ruolo centrale del rapporto tra approvvigionamento sedimentario e capacità di trasporto nella determinazione sia della risposta geomorfologica dei corsi d'acqua proglaciali sia dei tassi d'esportazione sedimentaria a valle; con rapporti più bassi che portano a scenari più idraulicamente efficienti e un trasferimento più facile del segnale di esportazione di sedimenti subglaciali attraverso il fiume proglaciale. Tuttavia, questo effetto è anche influenzato da fattori a più grande scala come la topografia della valle, in particolare lo spazio di alloggiamento laterale e la pendenza, suggerendo che l'effetto di filtraggio varia tra le configurazioni geomorfologiche.

I risultati di questa tesi dimostrano che i margini proglaciali attivi svolgono un ruolo significativo per la connettività sedimentaria tra i termini glaciali e le regioni a valle. Questi risultati hanno importanti implicazioni per la mitigazione dei rischi naturali, lo sviluppo degli ecosistemi, la gestione delle centrali idroelettriche e gli studi glaciologici nel contesto attuale di rapida recessione dei ghiacciai.

## Zusammenfassung

Die rasche Gletscherschmelze infolge der Klimaerwärmung vergrößert die Gesamtfläche der proglazialen Ränder, Landschaften, die anfangs relativ arm an organischem Material sind, aber durch hohe geomorphologische Aktivität, einschließlich Hangprozesse und Flussmorphodynamik, geformt werden. Unter geeigneten Bedingungen können sich proglaziale Vorfelder entwickeln und morphologisch aktive verzweigte Flussebenen enthalten. Diese Zonen der Akkumulation, des Transports und der Erosion von glazial abgelagerten Sedimenten sind durch ein Netzwerk von flachen, instabilen Kanälen gekennzeichnet, die ihre Position kontinuierlich in Reaktion auf Abfluss- und Sedimentlaständerungen ändern, die mit Gletscherschmelzwasser und Sedimentzufuhr verbunden sind.

Feldmessungen, numerische Simulationen und maßstabsgetreue Laborexperimente wurden verwendet, um die Entstehung, Aufrechterhaltung und Entwicklung dieser Flusssysteme zu untersuchen. Es mangelt jedoch noch an Wissen darüber, wie die Morphodynamik der Vorfelder mit den Bedingungen am Oberlauf (d. h. dem subglazialen Sedimentexport und der Variation des Schmelzwasserabflusses) interagiert und welche Auswirkungen diese Interaktionen auf den Sedimenttransport flussabwärts haben. Diese Lücke entsteht aus praktischen Einschränkungen, die es unmöglich machen, kontinuierliche (subglaziale) Sedimenttransportraten zu erfassen, insbesondere für Sediment in Geschiebekornfraktion, zusammen mit räumlich ausgedehnten, hochauflösenden und präzisen Informationen über die Flussmorphodynamik.

Vor diesem Hintergrund ist das Hauptziel der Dissertation, die erste gekoppelte Studie zur Beziehung zwischen kontinuierlichen Aufzeichnungen des subglazialen Sedimentexports, der Morphodynamik proglazialer Vorfelder und den Sedimentflüssen flussabwärts für einen sich zurückziehenden alpinen Gletscher durchzuführen. Der Fokus liegt auf der proglazialen Überflutungsebene des Glacier d'Otemma (südwestliche Schweizer Alpen), einer Region, die sich besonders gut für diese Studie eignet, da sie durch eine hohe Dissoziation zwischen den Talwänden und dem Talboden gekennzeichnet ist, was den Einfluss von Hangprozessen auf den Fluss minimiert. Eine Reihe methodischer Ansätze zur kontinuierlichen Quantifizierung des Sedimenttransports für sowohl Schwebstoffe als auch Geschiebesedimente durch das proglaziale Vorfeld wurden eingesetzt. Der Vergleich der am Gletschertor gesammelten Sedimenttransportdaten mit denen am Ausgang des Vorfelds unter Verwendung etablierter Signalverarbeitungstechniken zeigte, dass morphodynamische Prozesse das Signal des subglazialen Sedimentexports, das mit Geschiebe verbunden ist, schnell filtern (d. h. dämpfen und verzögern), während das der Schwebstoffe fast ungehindert durch das proglaziale Vorfeld gelangt.

Um das Funktionieren dieses Filters zu verstehen, wurde eine intensive Untersuchung der Flussmorphodynamik und der Oberflächensedimentologie durchgeführt. Tägliche Drohnenvermessungen der Überflutungsebene wurden verwendet, um räumliche Muster von Erosion und Ablagerung zu quantifizieren. Im Mittelpunkt dieser Analyse stand die Entwicklung eines heuristischen Modells zur Vorhersage der Wassertiefenverteilung in stark trüben, verzweigten Flüssen, um Höhenmodelle für sowohl trockene als auch überflutete Bereiche zu erstellen. Diese wurden dann mit den subglazialen Sedimentexport-Raten kombiniert, um den Einfluss der proglazialen Morphodynamik auf den Sedimenttransport flussabwärts zu quantifizieren. Veränderungen im Gleichgewicht zwischen der glazialen Sedimentzufuhr und der Transportkapazität führten zu schnellen Veränderungen in der Flussmorphodynamik. Während Perioden, in denen die subglaziale Geschiebezufuhr die Transportkapazität überstieg, kam es zu einer Aufhöhung im Vorfeld, begleitet von intensiverer Barrenbildung, erhöhter Kanalinstabilität, gesteigerter Verzweigungsintensität und Oberflächenvergröberung der Überflutungsebenenablagerungen. Das Vorfeld fungierte als Senke sowohl für Geschiebe

als auch für Schwebstoffe. Im Gegensatz dazu, wenn die subglazialen Geschiebe-Export-Raten unter der Transportkapazität lagen, fungierte das Vorfeld weiterhin als Senke für feine Sedimente, aber das System war netto degradiert für Geschiebesedimente.

Um diese Erkenntnisse auf Situationen mit unterschiedlichen topographischen, sedimentologischen und hydrologischen Gegebenheiten zu verallgemeinern, wurde ein hydromorphologisches Modell verwendet, das mit Felddaten kalibriert wurde. Die Ergebnisse bestätigten die zentrale Rolle des Verhältnisses von Zuführung zu Transportkapazität bei der Bestimmung der geomorphologischen Reaktion proglazialer Flüsse und der Sedimentlieferungsraten flussabwärts. Niedrigere Verhältnisse führten zu hydraulisch effizienteren Szenarien und einem leichteren Transfer des subglazialen Sedimentexport-Signals nach flussabwärts. Dieser Effekt wurde jedoch auch durch großmaßstäbliche Einflüsse der Taltopographie wie den Akkommodationsraum beeinflusst, was darauf hindeutet, dass der Filtereffekt zwischen geomorphologischen Einstellungen variiert.

Die Ergebnisse dieser Dissertation zeigen, dass proglaziale Vorfelder eine bedeutende Rolle für die Sedimentkonnektivität zwischen Gletschertoren und flussabwärts gelegenen Regionen spielen. Diese Erkenntnisse haben wichtige Implikationen für die Minderung von Naturgefahren, die Entwicklung von Ökosystemen, das Management von Wasserkraftwerken und glaziologische Studien im aktuellen Kontext der raschen Gletscherschmelze.

## Table of contents

## List of Figures

## List of Tables

# Nomenclature

## Acronyms

| | |
|---|---|
| 2D | Two-dimensional |
| 3D | Three-dimensional |
| AlpWISE | Alpine Water, Ice, Sediment and Ecology |
| AS1 | Active Survey 1 |
| AS2 | Active Survey 2 |
| ASL | Above Sea Level |
| CH1903 | Old Swiss geographic coordinate system |
| CH1903+ | New Swiss geographic coordinate system |
| CPU | Central Processing Unit |
| DEM | Digital Elevation Model |
| DFT | Discrete Fourier Transform |
| DAS | Distributed Acoustic Sensing |
| dGPS | differential GPS |
| DoD | DEMs of Difference |
| DOY | Day of the year from $1^{st}$ of January |
| FFM | Force Motrice de Mauvoisin |
| FMI | Fluvial Model Inversion |
| *eRiDynaS* | Electronic River Dynamic Simulation |
| eseis | Environmental Seismology toolbox |
| GCP | Ground Control Point |
| GLUE | Generalized Likelihood Uncertainty Estimation |
| GPS | Global Positioning System |
| GS1 | Gauging Station 1 |
| GS2 | Gauging Station 2 |
| GSG | Gauging Station Glacier |
| GUI | Graphical User Interface |
| HLL | Harten-Lax-Van Leer solver |
| HPC | High Performance Computer |
| HSTAR | Hydrodynamics and Sediment Transport in Alluvial Rivers |
| IDYST | Institut des Dynamiques de la Surface de la Terre |
| IN | Inlet |
| IRLS | Iteratively-Reweighted Least Squares |
| JD or jd | Julian Day |
| LiDAR | Light Detection And Ranging |
| LHS | Latin Hypercube Sampling |
| LoD | Limit of Detection |
| MAAT | Mean Atmospheric Air Temperature |
| MLR | Multiple Linear Regression |
| MPI | Message Passing Interface |
| MVS | Multi-View Stereo |
| NTU | Nephelometric Turbidity Unit |
| PpenMP | open MultiProcessing |
| PhD | Doctor of Philosophy |
| PIT | Passive Integrated Transponder |
| RFID | Radio Frequency Identification |
| RGB | Red-Green-Blue |

| RMSE | Root-Mean-Square error |
| SNSF | Swiss National Science Foundation |
| SDE | Standard Deviation of Error |
| SE | Shannon Entropy |
| SSC | Suspended Sediment Concentration |
| SfM | Structure-from-Motion |
| TB | Terabyte |
| UAV | Unmanned Aerial Vehicle |
| UNIL | Université de Lausanne |
| UoE | University of Exeter |
| USDH-48 | United States Depth Integrated sampler 1948 |
| VIF | Variance Inflector Function |

**Roman symbols**

| $°C$ | Celsius degree |
| $A$ | constant rating curve coefficient |
| $Ah$ | Ampere |
| $a_w$ | channel slope |
| $b$ | average channel width |
| $B_1, B_2$ | affinity and orthogonally parameters |
| $BA$ | mean bar area |
| $Bc$ | braiding index |
| $BI$ | mean braiding index |
| $B_r$ | rate of sediment erosion from the bank |
| $BN$ | mean number of bars |
| $Bv$ | vegetation blockage rate |
| $C$ | transport capacity or Chezy roughness coefficient |
| $cos$ | cosine function |
| $C_d$ | bulk drag |
| $C_y, C_x$ | Principal point offsets |
| $D_{50}$ | $50^{th}$ percentile, or median, diameter |
| $D_{84}$ | $84^{th}$ percentile diameter |
| $d$ | cell size (resolution) |
| $dB$ | decibels |
| $Dc$ | domain configuration |
| $D_h$ | horizontal diffusivity |
| $D_k$ | mean sediment diameter in class k |
| $D_m$ | geometric mean sediment diameter in the active layer |
| $D_r$ | rate of sediment deposition |
| $d_s$ | median bedload diameter |
| $D_s$ | stem diameter |
| $e_0$ | $q_0$ increase with frequency |
| $e$ | elevation uncertainty |
| $E$ | porosity |
| $E_x$ | daily sine wave |
| $e_f$ | transport efficiency factor |
| $E_r$ | rate of sediment erosion from the bed |
| $f_0$ | reference frequency |
| $f$ | model frequency range |
| $F$ | impact force |

| | |
|---|---|
| $f_b$ | unvegetated fraction of the grid cell |
| $f_v$ | vegetated fraction of the grid cell |
| $f_k$ | fraction of size class k in the active bed layer |
| $f_{fines}$ | fraction of the active bed layer composed of silt and clay |
| $f_{Spert}$ | fractional variability in the sediment supply generated using random numbers |
| $g$ | gravitational force |
| $G$ | Green's function |
| $h$ or $h_w$ | water depth |
| $H$ | bank height |
| $Hz$ | Hertz |
| $i$ | cell in longitudinal dimension |
| $j$ | cell in latitudinal dimension |
| $K_1, K_2, K_3$ | radial distortions |
| $k$ | angular wavenumber, von Karman constant (ca. 0.4) or $k^{th}$ sediment size class |
| $kg$ | kilogram |
| $km$ | kilometer |
| $k_s$ | roughness length scale |
| $L$ | adaptation length scale |
| $Lb$ | cumulative bedload |
| $L_B$ | horizontal length of the bank zone |
| $log$ | logarithm |
| $Ls$ | cumulative suspended sediment load |
| $m$ | meter |
| $M$ | daily mass of transported sediment |
| $mm$ | millimeter |
| $m$ | mobility factor |
| $n_c$ | total number of channels |
| $n_s$ | total number of cross-sections |
| $q_0$ or $K$ | material quality factor |
| $Q_b$ or $q_b$ | bedload discharge |
| $Q$, $Q_w$ or $q$ | water discharge |
| $Q_c$ | critical discharge |
| $Q_{initial}$ | initial water discharge |
| $Q_n$ | discharge rate at model intlet |
| $Q_{Peak}$ | peak discharge |
| $Q_s$ or $q_s$ | suspended sediment discharge |
| $Q_t$ | discharge rate at time t |
| $p_0$ | variation coefficient for $v_0$ |
| $P_1, P_2$ | decentering distortions |
| $P$ | seismic magnitude |
| phi | unit of sediment grain-size scale for sediments (i.e. $-\log_2 S$, where S is the size in mm) |
| $r$ or $R$ | correlation |
| $R\#$ | region number # |
| $r_0$ | distance river center to geophone |
| $R_c$ | local streamline radius of curvature |
| $R_C*$ | stream radius curvature |
| $R_g$ | submerged specific gravity of sediment |
| $r_h$ | hydraulic radius |

| | |
|---|---|
| $r_s$ or R | sediment density |
| $r_w$ | fluid density |
| S# | simulation number |
| S* | excess in bed slope |
| s | mean river slope |
| S | subglacial sediment supply or bed slope |
| sin | sinuous function |
| $S_{Long}$ | effect of bedslope on sediment transport in longitudinal direction |
| $S_R$ | scour rate constant |
| $s_s$ | grain diameter standard deviation |
| $S_{Tran}$ | effect of bedslope on sediment transport in transverse direction |
| t | tons or time [days] |
| $T_e$ | trapping efficiency of the surface riverbed |
| $T_{Flood}$ | flood duration |
| $T_{Lead}$ | flood duration with constant discharge |
| $t_i$ | instantaneous time |
| U* | shear velocity |
| u | depth-averaged velocity in x direction |
| $v_0$ | Rayleigh wave phase velocity at $f_0$ |
| v | depth-averaged velocity in y direction |
| V | Volume |
| $v_b$ | virtual velocity for bedload wave |
| $V_D cr$ | Critical velocity for deposition |
| $V_E cr$ | Critical velocity for erosion |
| $V_{fines}$ | reference excess velocity of fine particles |
| $v_g$ | seismic wave group velocity |
| $V_{ij}$ | depth-mean water velocity |
| $v_p$ | seismic wave phase velocity at $f_0$ |
| $V_s$ | virtual velocity for suspended sediment wave |
| $V_v$ | virtual velocity |
| VOL | Threshld erosion vlume |
| W* | dimensionless transport rate over the entire stream section |
| W, $w_w$ or b | average channel width |
| $w_s$ | particle fall velocity |
| $\bar{x}$ | mean value |
| x | longitudinal dimension |
| y | latitudinal dimension |
| z | vertical dimension |
| Z | amplification factor |

**Greek symbols**

| | |
|---|---|
| σ | Standard deviation |
| βr | local radius of curvature |
| Δ | difference |
| $\varepsilon$ or $e_A$ | magnitude of the curvature effect on sediment transport |
| Φ | spiral motion intensity |
| $\rho_s$ | relative sediment density |
| $\rho_w$ | relative water density |
| φ | exponent for the frequency-dependency decay |

| | |
|---|---|
| Ω | constant having a value of 0.001, 0.0059 or 32.2 depending on sediment transport equation |
| $\theta_U$, $\theta_M$ and $\theta_D$ | diffusive flow coefficients |
| $\Theta_y$ | bank erodibility |
| π | Pi |
| $\psi$ | fine sediment concentration supply |
| $\gamma$ | effect of sediment transport cohesive sediment in the bed layer |
| т | turbulent stress |
| $\tau^*$ or $\tau_b$ | dimensionless bed shear stress |
| $\tau_r^*$ | dimensionless reference bed shear stress |
| $\chi$ | hiding factor |

# Chapter 1: Introduction

## 1.1 Thesis overview and structure

This PhD thesis focuses on the geomorphic response of proglacial forefields to subglacially-exported sediments. It attempts to understand how the morphdynamic processes occurring in active braided proglacial streams alter the longitudinal sediment connectivity for both suspended sediment and bedload. This PhD thesis is part of the "Glacier recession, glacial sediment export and the morphodynamics of proglacial forefields" project, a Swiss National Science Foundation (SNSF) funded scientific project (N°188734 awarded to S.N. Lane) divided into two connected PhD thesis. The second one, led by PhD candidate Matthews Jenkin, is based on studying the subglacial sediment export mechanisms at the glacier margin. These are important as they represent the boundary conditions driving proglacial forefield morphodynamics.

The thesis is built around four chapters, each representing the main scientific papers produced from the project. These are based on a case study, the Glacier d'Otemma proglacial forefield, then generalized to broader boundary conditions using a numerical model. The aim of this Chapter is to outline the current state of knowledge on the subject and to highlight the scientific gaps justifying the research questions of the thesis. It also provides a set of complementary contributions arising from various collaborations realized within the frame of this PhD, but which are not examined in this thesis. Chapter 2 is a fundamental study, on which the entire thesis is based upon, proving that proglacial forefields are effectively able to filter the subglacial sediment export signal. Chapter 3 presents a methodological contribution necessary to quantify river erosion and deposition patterns (and hence forefield morphodynamics) in high turbid, shallow, braided streams. Chapter 4 uses results issued from the previous two chapters, to investigate the geomorphic response of a proglacial forefield to variations in subglacial sediment export to reveal the physical mechanisms that control the filtering. Chapter 5 aims to generalize the obtained findings to forefields having different boundary conditions by deploying a hydromorphodynamic numerical model. Chapter 6 provides a general discussion of the findings to highlight the main contributions of the thesis to the actual scientific knowledge on the subject, the weaknesses and the perspectives for future studies on proglacial forefields. Finally, Chapter 7 concludes the thesis.

## 1.2 Scientific state-of-the-art on proglacial forefields

The aim of this sub-section is to define what proglacial forefields are, and to determine both general geomorphic and fluvial conditions necessary for their development (Section 1.2.1). Then, considering the thesis's objectives, proglacial forefields are discussed in the context of rapid glacier retreat (Section 1.2.2). The relationship between subglacial sediment export mechanisms and proglacial forefields geomorphic response is presented in Sections 1.2.3 and 1.2.4 while their role in the longitudinal sediment connectivity with downstream regions is contextualized in Section 1.2.5. Given current knowledge on this topic, the importance of the thesis and the research questions upon which it is base are justified in Section 1.3. The rest of the Chapter is dedicated to explaining the linkage between the research questions and the structure of the thesis (Section 1.4), to presenting the study area (Section 1.5) and to providing a general overview of both methodology and methods (Section 1.6). A set of complementary contributions resulting from collaboration within the frame of this PhD, but not part of the main body of the thesis, are presented in Section 1.7.

### 1.2.1 Proglacial forefields: geomorphic definition and associated fluvial processes

Proglacial forefields are defined as zones of glacial outwash that form in front of glacier margins (i.e. proglacial margins) characterized by a network of shallow, unstable braided channels separated by temporary bars which continually shift their position in response to sediment load and discharge variations associated to glacial meltwater (Smith, 1985; Maizels, 2002). In general, their formation and morphology are dictated by the co-existence of five factors: (i) the deglaciated valley bottom in front of shrinking glacier has to have a gentle slope preventing river incision and consequent sediment evacuation from the system; (ii) sufficient availability of sediment sources delivering material to the valley bottom; (iii) sufficient lateral accommodation space for lateral river migration; (iv) no natural lakes or over-deepening to affect the flowing water in the proglacial margin; and (v) absence, or sparse, in-channel and riparian vegetation colonization (Maizels, 2002; Ashmore, 2013).

Braided rivers can be characterized by sand- or gravel- dominated riverbeds depending on the size fraction of the sediment supplied or reworked (Schuum, 1977; 1985). Consequently, these streams transport fine sediments, coarser particles, or even a mixture of the two. Fine sediment transport, also referred as suspended sediment transport, concerns the downstream motion of fine material in suspension in the water column due to turbulence, without direct contact with the riverbed over long distances (Van Rijn, 1984). The transport of coarser fractions is known as bedload and it may occur by sliding, rolling and saltation near the riverbed (Einstein, 1950; Bagnold, 1973). Given this classification, it is, however, always the combination of stream power and turbulence rate (i.e. drag and lift forces) that ultimately determines whether a given particle size is transported in suspension or as bedload at any given time because of the resisting forces to bed mobilization (Abbott and Francis, 1977; Turowski et al., 2010; Church and Ferguson, 2015).

In the past, the geomorphic evolution of both systems has been extensively studied in relatively small-scale field settings (e.g. Ashworth and Ferguson, 1989; Brasington et al., 2000; Wheaton et al., 2013), scaled laboratory experiments (e.g. Ashmore, 1991a,b; Ferguson and Ashworth, 1992; Ferguson, 1993; Ashworth et al., 1996) and numerical simulations (e.g. Nicholas, 2013a,b; Nicholas et al., 2013; Schuurman and Kleinhans, 2015; Williams et al., 2016a,b). These studies showed that braiding is associated with one or more of four principal mechanisms. Central bar deposition occurs when deposition of material immediately downstream of a flow converge region gradually promotes the emergence of a bar in the middle of the channel due to the continuous lateral and headward accretion of portions of upstream-coming bedload sheets (Ashmore, 1991a). Transverse bar conversion involves the generation of lobate and migratory features initiated from a symmetrical transverse unit bar formed downstream a confluence scour, progressively developing a fairly gently lateral sloping face along which sediment tends to be transported (Ashmore, 1991a). Chute cutoff of point bars, or avulsion, manifest when the arrival of a pulse of sediment from upstream produce a rapid point bar accretion leading to the diversion of water flow into adjacent areas of the streambed. Water flowing on the aggradated region (lobes) has a steeper path compared to the outer thalweg, thus promoting headward erosion generating a new channel (or chutes) progressively capturing larger volumes of water (Ashmore, 1991a). Avulsion is a particular time of chute cutoff process consisting in a large-scale sudden switching of the river course from one channel to another (Ferguson, 1993). Finally, multiple dissection of lobes involves the dissection of individual lobes into multiple smaller-scale channels (chutes) that branch of from the main flow, generating new bars (Ferguson, 1993). These segmented lobes may subsequently merge back together or be further dissected depending on both river discharge and sediment transport dynamics. Other minor mechanisms include bank erosion, bar edge trimming, channel incision, confluence pool scour, overbank deposition and lateral bar

development (Ashmore and Parker, 1983; Ferguson and Werritty, 1983; Wheaton et al, 2013). Braiding is then maintained over time by repetition of these processes in individual channels composing the braided network because of their high instability, controlled by the temporal variations in transport rare and the frequent redistribution of the river discharge among the individual channels (Ashmore, 2013).

## 1.2.2 Subglacial sediment export and proglacial forefield morphodynamics

The global mean atmospheric air temperature (MAAT) has increased by 0.74±0.18°C in the last 100 years, at a greater rate in mountain regions, resulting in the rapid retreat of glaciers and ice sheets all over the world (Auer et al., 2007; IPCC, 2007; Moon, 2007). In the European Alps, between 1850 and early 2000, glaciers lost about 50% of their surface with major implications for proglacial margins which have increased in size (Zemp et al., 2014). A recent study quantified that in the Swiss and Austrian Alps alone almost 930 km$^2$ of newly deglaciated terrain have been exposed since the end of the Little Ice Age (LIA, ca. 1850) (Carrivick et al., 2018).

Recently deglaciated terrains were traditionally thought of as "inorganic" landscapes characterized by lack of a vegetation and massive amounts of detrital material deposited following from glacier erosion (Church and Ryder, 1972; Ballantyne 2002; Benn and Evans, 2010). These are known to be characterized by unstable over-steepened slopes and unconsolidated sediment sources that, due to glacial debuttressing, can be highly dynamic (Cossart et al., 2008; Carrivick et al., 2013; Mancini and Lane, 2020). Glacier recession leads to (i) rockfalls related to stress-release in bedrock outcrops (Heckmann et al., 2016; Vehling et al., 2017) and (ii) gullying of moraine deposits (Curry et al., 2006; Schiefer and Gilbert, 2007; Lane et al., 2017; Mancini and Lane, 2020) leading to debris cone formation; (iii) dead ice melt-out (Bosson et al., 2015); (iv) rock glacier formation (Micheletti et al., 2015a); and (v) paraglacial landsliding (Hugenholtz et al., 2008). The period of time during which there is significant landscape reworking following deglaciation is called the "paraglacial", as first termed by Church and Ryder (1972). This model states that there is normally increased geomorphic activity immediately after deglaciation then a slightly decline over time as a result of sediment exhaustion and negative feedbacks on the sediment cascade (i.e. stabilization due to vegetation colonization, reduction in sediment connectivity). At the same time, it is now largely known that deglaciation leads to increasing amount of sediment export, both suspended- and bedload fractions, from subglacial channels due to enhanced subglacial erosion (Lane et al., 2017; Delaney and Adhikari, 2020).

An important geomorphological feature that may develop in proglacial margins following deglaciation is the proglacial forefield (Section 1.2.1). If the above-mentioned geomorphic features are connected to the forefield, meaning that there is lateral transfer of sediment within the proglacial margin, they can influence its morphodynamics as long as they remain accessible for fluvial erosion (Fryris, 2013; Church and Ryder, 1972). This happens especially during very high flow conditions triggered by meteorological events or glacial lake outburst floods that can enhance the sediment transport rates of both suspended sediment and bedload and the reworking of grain sizes up to several meters in diameter (Carrivick and Rushmer, 2009; Beawert and Morche, 2014). However, especially if paraglacial landforms are stable and dis-connected from the proglacial stream (Section 1.5; Fryirs and Brierely, 1999; Lane et al., 2017; Mancini and Lane, 2020), subglacial sediment export and meltwater dynamics are recognized to be the primary sources determining sediment transport flux and morphodynamic evolution in proglacial rivers (Goff and Ashmore, 1994; Lane et al., 1996; Maizels, 2002).

### 1.2.3 Subglacial hydrology and sediment export mechanisms

Glacial erosion involves removal and transport of sediment by four main processes, namely, quarrying, plucking, abrasion and melt water erosion (Hamberey and Glasser, 2005). However, controls on subglacial sediment export rates to proglacial floodplains are poorly known and not yet quantified (Koppes and Montgomery, 2009; Hiliger and Beylich, 2019). In a general way, sediment export is strongly dependent on the ability of the glacier to erode and to transport sediment, by the ice itself or by water, to the glacier terminus (Hallet et al., 1996).

Subglacial hydrographs are not only important for determining subglacial sediment evacuation rates, but also for the sediment transport potential in the proglacial margin (Mao et al., 2014, 2019; Comiti et al., 2019). Together, these two variables determine the boundary conditions for proglacial forefield morphodynamics (Smith, 1985; Maizels, 2002). The hydrograph of Alpine subglacial and glacier-fed streams is usually characterized by strong diurnal amplitudes reflecting daily cycles of atmospheric temperature variation. The timing of daily peak flow along the melt season depends on the transit time for water to flow through the glacier system from different part of the ablation zone (Raymond et al., 1995; Fountain and Walder, 1998; Nienow et al., 1998; Sharp et al., 1998). According to Sharp et al. (1998), four different runoff periods exist: (i) spring meltwater flows maintained by break-up of river ice, where the majority of produced meltwater is retained and stored as superimposed ice, in snow and in ice capillaries and channels; (ii) by early to mid-summer, the rapid rise of atmospheric temperature promotes snow- followed by ice-melt promoting the progressive development of the englacial drainage network; (iii) by late summer, the establishment of a well-developed subglacial network allows minimum delay in runoff which becomes strictly related to glacier ablation rates and rainfall events but, as soon as the temperatures decline towards the end of the melt season, discharge rates decline consequently; until (iv) there is a return to minimal flows and undetectable diurnal cycle at the end of autumn because of low melt rates and the onset of freezing conditions. This temporal evolution in flow efficiency and spatial extent of subglacial conduits not only affects the hydraulic potential for subglacial sediment export (Gimbert et al., 2016), but also causes seasonal variation in glacier velocity and hence basal erosion (Harper et al., 2002; Mair et al., 2002).

In recent years, several attempts have been made to quantify glacial erosion rates and sediment export but, as they are not directly measurable in the field, their determination is quite challenging (e.g. Hallet et al., 1996; Herman et al., 2015; Herman and King, 2018). As proposed by Herman et al. (2015), a method to quantify subglacial erosion rates is to infer them from characteristics of the evacuated sediment (quantity, calibre, provence). Even if data collected at the glacier snout avoid the confounding effects of periglacial and paraglacial sediment supply, this approach assumes that erosion at the glacier bed translates directly into transfer of eroded sediment to the glacier outlet, without considering the existence of a temporal delay between these two processes (Church, 1972; Riihimaki et al., 2005). That said, Alley et al. (1997) showed that subglacial streams are efficient in evacuating sediment from their beds but, at the same time, they are pinned by glacier's hydraulic potential (Shreve, 1972; Gimbert et al., 2016). As a consequence, till may accumulate in zones away from channels with strong implications for bedrock erosion and sediment production as glaciers can only erode their bed if they are capable of evacuating eroded sediment (Copland et al., 1997; Elgholm et al., 2012). Long-term models of glaciers growth and decay suggest that most of the eroded sediments remain subglacial and that they are released only during deglaciation (de Winter, 2012). Thus, maintaining high sediment export rates depends on the capacity of the subglacial channels to erode subglacial till (Alley et al., 1997).

Given the above, recent studies pointed out that glacier sediment export is variable over several timescales. Riihimaki et al. (2005) and Gimbert et al. (2016) showed that

subglacial sediment export declines though the melt season because of the progressive evacuation and exhaustion of winter-eroded sediment coinciding with the shift from a poorly developed subglacial drainage network buffered by snow cover to a more efficient and connected system. On the other hand, Perolo et al. (2019) suggested that the reason for this decline was not a supply effect, but rather a transport capacity effect related to the form of subglacial hydrographs such that they were no longer capable of maintaining continuous sediment transport (i.e. overnight discharge lows fell below the critical threshold required for sediment transport). This leads to discontinued subglacial transport characterized by two distinct phases: (i) overnight clogging causing subglacial channel size reduction and a temporarily pressurized flow promoting glacier uplift and lateral transfer of water out of the defied subglacial channels, followed by (ii) late morning flushing during the rising limb of the hydrograph. The actual knowledge on subglacial sediment export mechanisms was essentially based on direct monitoring of subglacial sediment evacuation rates at the glacier terminus or in close proximity to it (e.g. Richards, 1984; Swift et al., 2005; Dell'Agnese et al., 2014; Delaney et al., 2018; Comiti et al., 2019; Perolo et al., 2019; Carillo and Mao, 2020).

### 1.2.4 Proglacial forefield geomorphic response to deglaciation

Following glacier retreat, forefield response is a function of the ratio of sediment supply, either by paraglacial landforms or subglacial channels, to sediment transport capacity (Collins, 2008).

The dividend of increased runoff during glacier retreat may increase sediment transport drastically, but morphodynamic response depends on whether or not there is concomitant increase in sediment supply (Kaser et al., 2010; Lane et al., 2017; Lane and Nienow, 2019). There is evidence that supply does not keep up with capacity and this is reflected in proglacial margins by spatial patterns of incision-aggradation: incision occurs in from of retreating glaciers where capacity exceeds supply, which then provides material necessary for downstream aggradation also promoted by the progressive reduction in downstream valley bottom slope (Marren, 2002; Beylich et al., 2009; Roussel et al., 2018). As highlighted by Marren and Thoomath (2013), this phenomenon may by associated with terrace formation within the proglacial margin. In their conceptual model, incision in proximity to the glacier terminus may be related to different factors: (i) sediment disconnection (e.g. alluvial fans, proglacial moraine ridges; Fryris, 2013; Lane et al., 2017; Mancini and Lane, 2020); (ii) exhaustion of proglacial or subglacial sediment stocks (Beylich et al., 2009; Roussel et al., 2018); (iii) changes in channel networks controlled by the large amount of meltwater during the spring melt in conjunction with a lowered equilibrium profile associated with glacier retreat (Marren, 2002); or (iv) stream capture events (Roussel et al., 2018). Cycles of incision and deposition can also be related to the formation of proglacial lakes or temporary kettle holes buffering downstream sediment supply (Marren, 2005; Hasholt et al., 2008; Bogen et al., 2015). However, situations have been observed where supply can keep up with capacity. In this case, aggradation patterns are measured throughout the entire forefield (Curran et al., 2017) having repercussions for channel patterns. Germanoski and Schumm (1993) used flume experiments to show that channel patterns associated with incision-aggradation are mostly braided in aggradational zones, while they can be either braided or straight in incision zones depending on incision rates. In contrast, aggrading forefields are basically associated with braided systems (Curran et al., 2017).

Nevertheless, to better understand forefield morphodynamics, it is also necessary to take into account topographical constraints. As reported in Maizels (2002), even if proglacial margins are commonly associated with braided channel networks, channel patterns close to

the glacier terminus can be confined between bedrock walls and moraines. Consequently, proximal channels may be deep, straight and having high transport capacity.

## 1.2.5 Proglacial forefield morphodynamics and implication for sediment connectivity

Several studies based on field measurements and mathematical simulations have studied the formation, maintenance and evolution of both sand- and gravel- riverbed braided fluvial systems in relation to sediment supply (Ashmore, 2013). Results have given a good understanding of their morphodynamics (Section 1.2.1) and geomorphological responses (Section 1.2.2). As, by definition, forefields are characterized by braided rivers where sediment transport is known to be discontinuous, these latter attenuate (or buffer) downstream sediment fluxes (Kasprak et al., 2015; Antoniazza et al., 2019; Misset et al., 2020). This discontinuity may be both exogenically-forced (i.e. by diurnal discharge variation related to glacier runoff, and hence sediment transport capacity; Guillon et al., 2018; Perolo et al., 2019) and autogenically-affected (i.e. deposition at one time-period determines both topographic influence on, and sediment available for, erosion at the next time period; Marren and Toomath, 2014; Bakker et al., 2019; Antoniazza et al., 2019). This latter case has been particularly studied in Lane et al. (1996) where authors showed that forefield dynamics depends on the relationship between discharge and upstream sediment supply, determining patterns of erosion and deposition within channels. In general, in the absence of sediment supply, scour was observed during the rising limb of the hydrograph and deposition on the falling limb. As upstream areas supplied sediment as discharge increase, morphological changes became dominated by the relative timing of discharge and sediment waves ("sediment pulses" or "sediment slugs"; Nicholas et al., 1995), local channel morphology and local erosion and deposition patterns. These latter factors are relevant as they determine hydraulic conditions such as bed texture, critical shear stress and hence transport capacity (Kasprak et al., 2015). Both external and autogenic factors result in limitation of particle advection lengths, which are function of particle size, settling height and ambient flow velocity, with important implication for downstream sediment fluxes (Jerolmack and Paola, 2010; Ganti et al., 2014; Pelosi and Parker, 2014) and the downstream sorting of transported sediment (Boothroyd and Ashley, 1975; Bluck, 1982; Powell, 1998).

Given the above, there is a common assumption that forefields influence downstream sediment supply over two different timescales: in the form of long-term permanent sinks and short-term temporary sinks. Long-term sinks are related to the fact that most glacially-exported and paraglacially-derived sediment accumulates in outwash plain (Maizels, 2002). In contrast, short-term deposits are generated by the hydraulics of the fluvial environment (Lane et al., 1996; Antoniazza et al., 2019).

## 1.3 Justification of the PhD thesis and research questions

Whilst the impacts of climate warming upon glacier recession and consequent proglacial margin evolution are well-established over timescale of years to decades (Sections 1.2.1 and 1.2.2), the geomorphic response of proglacial forefields has been largely overlooked, especially the relationship between subglacial sediment export, stream morphodynamics and downstream sediment flux (Sections 1.2.3 and 1.2.4; Carrivick and Heckmann, 2017). Forefields are actually recognized as having a role in controlling the spatial distribution and depth of sediment sinks (Warburton, 1990: Fryris, 2013; Guillon et al., 2018), but without explicitly understanding the physical and fluvial mechanisms associated with this process. This arises from a series of limitations.

First, unlike suspended sediment transport which has well-established monitoring techniques (i.e. turbidity-suspended sediment-discharge relationships; Gurnell, 1982; Clifford et al., 1995; Stott and Mount, 2007), measurement of bedload flux is challenging task for both theoretical and practical reasons. Theoretically, the high variability of bedload transport means that measurements need to be continuous to identify when it happens and with which intensity as it is impossible to know its variance *a priori* (Meyer-Peter and Müller, 1948; Fernandez Luque and van Beek, 1976; Rickenmann, 2001; Turowski et al., 2010). Practically, except for a few studies (i.e. Dell'Agnese et al., 2014; Comiti et al., 2019; Perolo et al., 2019; Carillo and Mao, 2020), there is no monitoring infrastructure located close enough to glacier termini to capture the subglacial export signal (Herman et al., 2015; Lane et al., 2017; Delaney and Adhikari, 2020). Direct bedload samplers (i.e. Helley-Smith sampler; Helley and Smith, 1971) have been used in the past (e.g. Lane et al., 1996) but they only allow point-in-time measurements. The installation of indirect methods (i.e. hydrophones and plate geophones) for continuous monitoring can be difficult, expensive, and subject to a careful calibration against manual samplings (Vericat et al., 2006; Bunte et al., 2008; Perolo et al., 2019).

Second, the morphological effects of subglacial sediment evacuation on proglacial stream must be surveyed and quantified. The morphological evolution of dry regions is nowadays easily monitored over large spatial scales using remote sensing techniques involving, for example, terrestrial and aerial LiDAR (i.e. Baewert and Morche, 2014; Bakker et al., 2019; Lague, 2020) and SfM-MVS photogrammetry (i.e. Staines et al., 2014; Bakker and Lane 2017; Lane et al., 2017; James et al., 2017a,b; 2020); while in inundated regions the use of these methods largely depends on water conditions. If the water body is sufficiently clear and the riverbed visible on imagery, optical (i.e. Gilvear et al., 1995, 1998; Legleiter et al., 2004), two-media photogrammetry (i.e. Dietrich, 2017) and green wavelength LiDAR (i.e. Mandlburger et al., 2015; Kasvi et al., 2019) approaches can be implemented to predict the elevation of inundated areas. However, in proglacial forefields having high turbidity these approaches are not suitable and topographical surveys are commonly undertaken using manual techniques, such as differential GPS (dGPS) and total station (Lane et al., 1994; Brasington et al., 2000; Chandler et al., 2002). Manual survey can be subject to a trade-off between spatial extent and spatial resolution in the first case, and also be limited in the frequency of resurvey (Lane, 1998; Roy et al., 2021).

The recent development of innovative and cheap bedload monitoring using seismic methods, UAV surveys and SfM-MVS techniques, as well as water depth prediction algorithms, means it is now possible to undertake spatially-extensive and temporally-intensive studies of the linkage between glaciers and their downstream proglacial forefields (Section 1.6; e.g. Burtin et al., 2008, 2011; Fonstad et al., 2013; Javernick et al., 2014; Larose et al., 2015; Dietrich, 2017; James et al., 2020).

In the actual context of rapid deglaciation, understanding the changing sediment connectivity between glacierized catchments and downstream regions is important. According to "peak water" theory, during a long recessional phase a glaciated catchment may experience increasing glacier-melt runoff rates for a period lasting several decades, as does the intensity of daily discharge variation (Lane and Nienow, 2019), before decreasing as either ice stocks run out or increases of debris layer cover slowing down melt rates (Huss et al., 2017; Zhang et al., 2022, 2023). At the same time, shifts in hydrological conditions also impact sediment supply to proglacial rivers in two main ways: (i) as glacier erosion depends on basal sliding, that in turn is a function of ice thickness, in the long term a constant negative mass balance leads to ice volume loss limiting the ability of the glacier to produce glaciogenic material (Hallet et al., 1996); and (ii) deglaciation leads to exposure of unstable sediment sources adjusting to non-glacial conditions that, through several geomorphic processes, supply proglacial

floodplain until their exhaustion (Church and Ryder, 1972). This progressive decrease in sediment availability following glacier retreat has been hypothesized as a cause of "peak sediment" (Zhang et al., 2022). The ability of proglacial forefields to act as sediment sinks thus depends on the relative timings of sediment supply and transport capacity peaks (Li et al., 2021; Zhang et al., 2022, 2023). Given the above, both the Swiss government and Alpine hydropower companies argue that glacierized catchments have an extremely high potential for the Energy Strategy 2050 program, which aims to enhance energy production from renewable sources (Gaudard et al., 2014; Martinez-Jaramillo et al., 2023). Thus, it is necessary to properly understand the mechanisms driving forefield evolution following glacier retreat to realize the issues and the benefits that can affect Alpine hydropower plans in future decades, but also for better planning both management and eventual expansion of hydropower plants.

Given the above, the core aim of this PhD thesis is to undertake the first, coupled study of the relationship between subglacial sediment export, proglacial forefield morphodynamics and downstream sediment flux for retreating Alpine glaciers. This is done through the intensive study of a single geomorphic system (Section 1.5; Chapters 2 and 4), the Glacier d'Otemma proglacial forefield, while the generalization of the obtained results is conducted using a hydromorphodynamic model (Chapter 5). The PhD thesis addresses four inter-related research questions:

I. Do forefields filter the signal related to subglacial sediment export? If yes, over which timescales this filtering occurs?
II. Is it possible to predict water depth distribution in high turbid, shallow, mountain braided stream using basic planimetric information?
III. How do forefields geomorphologically respond to subglacial sediment export? And which are the implications for the longitudinal sediment connectivity?
IV. How does the proglacial morphodynamic filter react to changing boundary (topographical, sedimentological and hydrological) conditions?

Each research question listed above is carefully addressed in a scientific contribution (Chapters 2 to 5).

## 1.4 Thesis structure and research questions

Given the research questions reported above, each one is addressed within a specific Chapter (Chapter 2 to 5) representing a scientific article (submitted or published) in international scientific journals. Each of them details the research context and aims based on the actual knowledge on the topic, the used methodology, and the presentation and discussion of the obtained results. Supporting Information associated to these contributions also provide more scientific details on both methodology and results.

Chapter 2 addresses research question I providing the first fundamental study investigating the filtering of subglacial sediment export signals by a proglacial forefield in terms of both suspended sediment and bedload transport, and using field-collected data. Indirectly, this also provides the only existing dataset having continuous quantification of sediment export from a retreating Alpine glacier for two entire melt seasons. The findings and the conclusions issued from this Chapter were then taken as the foundations for the other research questions.

Chapter 3 (research question II) is not intended to offer scientific understanding of the relationship between glacier recession and proglacial forefield response. However, it provides a methodological development necessary to address research question III (Chapter 4) and based upon a heuristic-statistical approach for predicting the spatial distribution of riverbed elevations. Riverbed maps can be then included into digital elevation models (DEMs) of dry

regions to produce DEMs of the entire proglacial forefield system with the final aim to compute temporal volumetric changes estimates at the entire forefield scale.

Chapter 4, addressing research question III, investigates how an Alpine proglacial forefield geomorphologically reacts to subglacially-exported sediment to highlights the hidden physical and fluvial mechanisms driving the filtering, and the effects on downstream sediment supply. This involves temporal comparison between sediment budget data (Chapter 2), proglacial stream configuration and topographic changes. For this latter aspect, thanks to the riverbed elevation data derived to application of the method developed in Chapter 3, topographic changes for the entire proglacial floodplain scale can be linked to changing sediment supply conditions.

Finally, Chapter 5 (research question IV) seeks to go deeper into this investigation generalizing the results for proglacial forefields affected by different hydrological, sedimentological and topographical boundary conditions compared to the investigated one. This uses a numerical simulation model and gives further insights on the evolution of sediment budgets in glacierized catchments experiencing rapid deglaciation.

## 1.5 Study site

The study site of the thesis is the Glacier d'Otemma proglacial forefield, located in the south-western Swiss Alps (Val de Bagnes, Canton Valais) at an elevation of ca. 2'450 m above sea level (Figure 1.1; 45.93510 N, 7.41372 E). It has formed since the early 2000s following a rapid retreat of the glacier (up to -50 m/year) driven by the combination of increased mean atmospheric air temperatures (MAAT, +1.4°C) and decreasing winter snow accumulation (-50%) since 1960 (Micheletti et al., 2015b; Mancini and Lane, 2020). The forefield is situated just below the lower limit of the discontinuous permafrost belt (Lambiel and Reynard, 2001; Deluigi et al., 2017). This suggests that large reworking events of non-cohesive Quaternary deposits (e.g. lateral moraine, till-mantled valley sidewalls) and cliffs can potentially still affect the geomorphic system, leading to its re-equilibration to present climatic and non-glacial conditions. However, Mancini and Lane (2020) found high dis-connectivity between the valley sidewalls and the outwash floodplain due to the presence of large alluvial fans buffering the transfer of sediment between these two regions. This allows consideration of a unique and coupled glacier-proglacial margin system with relatively little sidewall influence, a perfect condition for studying the direct relationship between subglacial sediment export and proglacial forefield morphodynamics. Geologically, the region is dominated by granitic bedrock outcrops, primarily gneiss, containing highly-foliated minerals like quartzite and mica (Burri et al., 1998). The physical and chemical weathering of these features, as well as mechanical glacial erosion, provides the sediment necessary to form both the Quaternary deposits and geomorphic landforms.
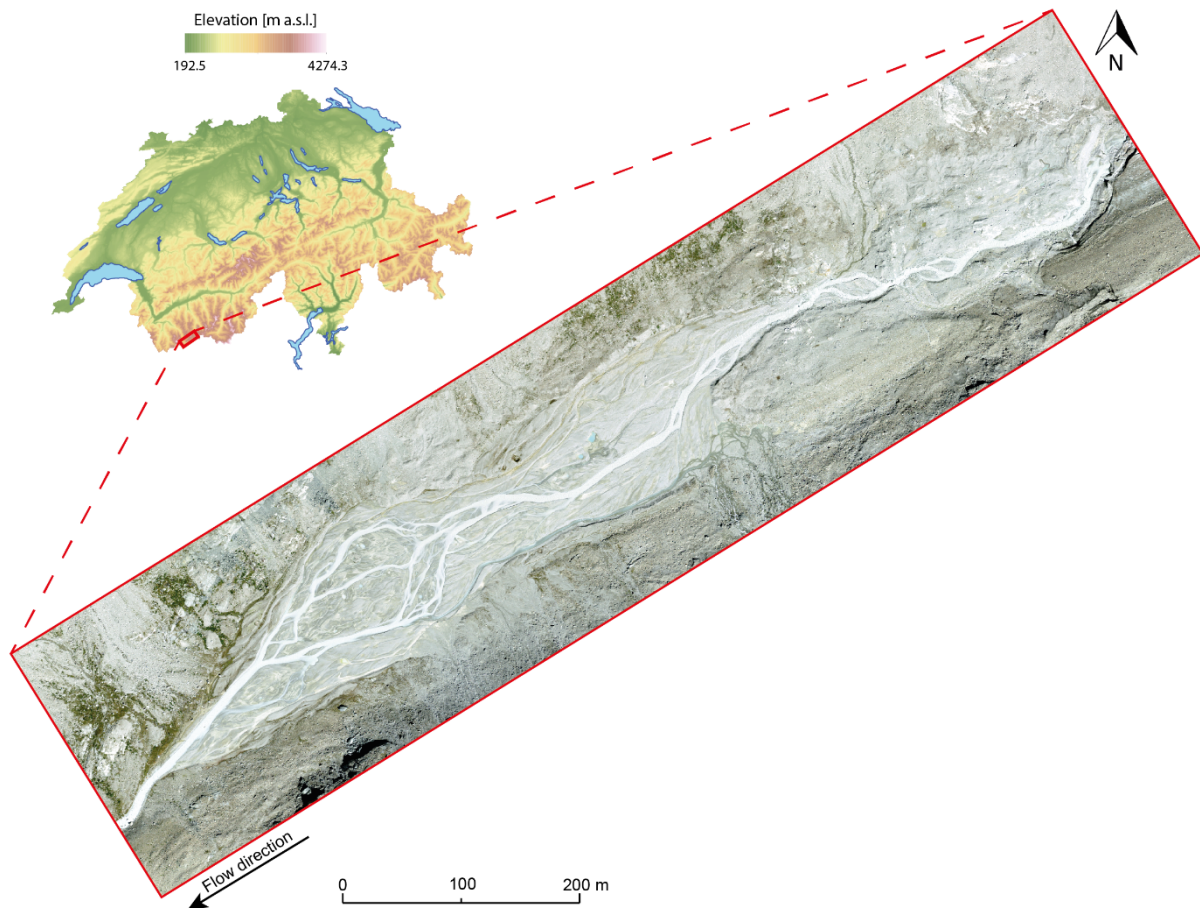
Figure 1.1: Location in relation to Switzerland and spatial configuration of the Glacier d'Otemma proglacial forefield (45.93510 N, 7.41372 E), the study area upon which the thesis is focused on.

During the two summers of data collection, the proglacial forefield was ca. 1000 m long and ca. 200 m wide, characterized by a well-developed gravel-bed braided stream network. Closer to the glacier terminus and at the forefield outlet flow is confined into a single channel, with only occasional braiding where lateral accommodation space permits. Within the forefield the longitudinal mean slope is ca. 2.5% in its upstream, and ca. 1.25% in its downstream part. According to manual grain size measurements using the Wolman pebble count procedure (Wolman, 1954), the in-stream grain size ($D_{50}$) fines from 78 mm at the glacier terminus down to 37 mm at the forefield end.

The Glacier d'Otemma proglacial forefield is remote, located upstream of a water intake of the Force Motrice de Mauvoisin (FMM) and untouched by human intervention. This remoteness gives other reasons for its choice for the study: first, water discharge and sediment flux rates are natural reflecting the actual influence of climate warming on glaciers; and second, it prevents interference from large numbers of people visiting the area during ongoing experiments.

Since 2017, the ALpWISE (ALpine, Water, Ice, Sediment and Ecology) group led by Prof. Dr. Stuart N. Lane, other groups of the Institute of the Earth Surface Dynamics (IDYST) of the Université de Lausanne (UNIL) and research groups based outside of Switzerland used this natural laboratory for studying different aspects of the ongoing deglaciation, such as biofilm development (Roncoroni et al., 2022, 2023a, 2024), subglacial channels (Egli et al., 2021a,b) and groundwater dynamic (Müller et al., 2022, 2024), subglacial sediment export mechanisms (Jenkin et al., 2023, submitted), vegetation colonization (Siegfried et al., 2023) and landscape evolution to deglaciation (Mancini and Lane, 2020; Wetterauer et al., 2022). This allows the

thesis to be inserted into a wider research project, including accessing additional data collection and analysis support, but also allowing the derived data to be of use to others.

## 1.6 Overview of the methodological approach to address the research questions

The three research questions were addressed using a wide range of methodological approaches.

The first research question aims to determine the filtering effect operated by the morphodynamics of the proglacial forefield on the subglacial sediment export signal for both suspended sediment and bedload (Chapter 2). This is addressed in two steps. First, continuous quantification of suspended sediment (i.e. conventional turbidity-suspended sediment-discharge relationship; Gurnell, 1982; Clifford et al., 1995; Stott and Mount, 2007) and bedload (i.e. seismic inversion; Larose et al., 2015; Burtin et al., 2008, 2011; Dietze, 2018; Dietze et al., 2019a) transport were monitored at the glacier terminus and at the forefield outlet for two entire melt seasons. Second, the magnitude and the timescales of the filtering were investigated using signal post-processing techniques, of which principles are described in Jerolmack and Paola (2010).

The second research question investigates the use of basic planimetric information for predicting the water depth distribution in high turbid, shallow braided streams (Chapter 3). Structure-from-Motion (SfM) Multi-View Stereo (MVS) photogrammetric derived orthomosaics and DEMs of the proglacial forefields are used to extract five morphological variables (i.e. distance from the nearest river bank; total inundated width along a line tangential to the local flow direction; local curvature magnitude and direction; and distance from the nearest flow divergence and convergence regions). Datasets were pooled together, and the most significant ones extracted using a multiple stepwise regression approach calibrated against field-collected water depth measurements. The obtained multiple linear regression is then applied to all cells composing the inundated area to predict water depth distribution maps. Following best practices given in Westaway et al. (2003), these can then be included into DEMs or dry regions to conduct temporal geomorphic and volumetric change estimates for entire floodplains (Lane et al., 2003; Westaway et al., 2003).

The third research question relates the subglacial sediment export signals to the geomorphic response of the proglacial forefield (Chapter 4). Our initial hypotheses were that (i) the subglacial bedload export drives both the geomorphic and morphodynamic response of the proglacial stream, (ii) controlling in turn the downstream sediment supply. These were tested under two boundary conditions: periods when subglacial sediment supply (S) exceeded transport capacity (C) and, in contrast, periods when capacity kept up with supply. Theoretical transport capacity was calculated along the melt seasons using a shear-stress based sediment transport equation (Schneider et al., 2015; Rickenmann, 2020; Antoniazza et al. 2022). The continuous subglacial sediment export quantifications issued from Chapter 2 were combined with high-frequency (i.e. daily) surficial geomorphic and grain-size changes of the floodplain (Roncoroni et al., 2023a) obtained from drone imagery of the forefield. Drone imagery was post-processed through SfM-MVS photogrammetry (e.g. Westoby et al., 2012; Fonstad et al., 2013) according to best practices described in James et al. (2017a,b, 2020) to obtain DEMs and orthomosaics.  Geomorphic changes were quantified using DEMs of difference (DoD; Brasington et al., 2003; Lane et al., 2003). Orthomosaics were first used to extract temporal morphological information on the proglacial stream (inundated area, total number of bars, braiding index and bar area), and to generate surficial grain-size maps using statistical models described in Lane et al. (2020) and in Carbonneau et al. (2004, 2005).

Given the findings issued from research questions I (Chapter 2) and III (Chapter 4), which used field-collected data from a specific proglacial forefield, Chapter 5 aimed to generalize scientific findings to proglacial margins bounded by different boundary conditions. This was achieved through numerical modelling, particularly using the 2D hydromorphodynamic physical-based model *eRiDynaS* developed by Prof. Dr. Andrew P. Nicholas of the University of Exeter (UoE). The model is largely based on the HSTAR (Hydrodynamics and Sediment Transport in Alluvial Rivers) model developed in Nicholas (2013a,b) and further tested in Nicholas et al. (2013). In practice, the model was first calibrated and validated for the Glacier d'Otemma proglacial forefield against field-collected data (i.e. sediment budget and morphological statistics of proglacial forefield configuration). Then, its boundary conditions were modified to study the effects of proglacial stream morphodynamics on subglacial sediment transport signals under different conditions. Four scenarios were investigated: (i) proglacial forefields characterized by a steeper valley bottom slope and a larger accommodation space, (ii) by transport capacity (C) conditions higher and (iii) lower than the subglacial sediment supply (S) rates, and (iv) by a time-varying condition of the C-S ratio.

## 1.7 Scientific collaborations in the frame of the PhD

In addition to the four main contributions composing the core of the thesis, during my PhD, I had the opportunity to collaborate with and assist some fellow PhD students with their projects. Some of these were subsequently published. The aim of this Section is to summarize them, highlighting my personal contributions to the overall projects. Most of these collaborations arose during the summers 2020 to 2023, when the ALpWISE group organized intensive fieldwork campaigns at the Glacier d'Otemma in an interdisciplinary investigation (ice, water, sediment, ecosystems) of the response of both the glacier and proglacial systems to deglaciation. Two collaborations were set in this context.

As already mentioned, PhD student Matthew Jenkin led the glaciological part focused on the subglacial sediment export mechanisms of this SNSF project (Section 1.1). In this collaboration, I actively participated for the realization of two scientific projects:

Jenkin, M., Hofmann, M., Hubbard, B., **Mancini, D.**, Miesen, F.M., Herman, F. & Lane, S.N. (2023). Tracking coarse sediment in Alpine subglacial channel using radio-tagged particles. *Journal of Glaciology*, 1-15. https://doi.org/10.1017/jog.2023.77.

This is a methodological contribution focused on developing a new method for tracking radio-tagged pebbles and cobbles though subglacial meltwater channels under shallow temperate glaciers using an array of antennas located at the glacier surface. RFID-tagged particles were injected directly in the main subglacial channel though boreholes created using a hot water ice drill. My contribution to this study was the help in the field for (i) the realization of the boreholes and (ii) the installation of the sensors at the glacier surface.

Jenkin, M., **Mancini, D.**, Miesen, F.M., Müller, T., Fischer, M., Dietze, M. & Lane, S.N. (submitted to Journal of Geophysical Research: Earth Surface). Subglacial sediment Export from an Alpine Glacier.

This study investigated the relationship between snowline retreat and subglacial export rates for both suspended sediment load and bedload. Results showed a strong correlation between these two variables, especially for bedload. This confirms that the increasing efficiency of the subglacial drainage system drives the bedload export rates, but it also highlights that the magnitude of evacuation is limited by the ability of the subglacial channels

to extent further upstream, a condition controlled by the altitude of the snow line. My personal contribution to this work was to provide the subglacial suspended- and bed-load quantifications for the three melt seasons (2020 to 2023) under investigation.

Former PhD student Matteo Roncoroni worked on the stream ecology of glacier-fed braided proglacial rivers, with a specific focus on the role of biofilm development for the geomorphic stability in these environments. I took part in three projects, primarily contributing to data acquisition in the field and to their post-processing:

Roncoroni, M., **Mancini, D.**, Kohler, T.J., Miesen, F.M., Gianini, M., Battin, T.J. & Lane, S.N. (2022). Centimeter-scale mapping of phototrophic biofilms in glacial forefields using visible band ratios and UAV imagery. *International Journal of Remote Sensing*, 43(13), 4723-4775. https://doi.org/10.1080/01431161.2022.2079963.

This work demonstrated that low-cost and consumer grade UAVs can produce sufficiently high-quality RGB images for benthic biofilm mapping at high temporal and spatial resolution. Biofilm distribution from RGB bands was also determined developing a new index based on a logistical regression approach. Since the study shares the same study area (i.e. proglacial forefield), method (i.e. high-frequency UAV surveys) and post-processing technique (i.e. SfM-MVS photogrammetry) and the study period (i.e. 2020 melt season) with Chapter 3 and 4 of this thesis, I was actively involved in the collection and in the post-processing phase for the generation of both DEMs and orthomosaics.

Roncoroni, M., **Mancini, D.**, Miesen, F.M., Müller, T., Gianini, M., Ouvry, B., Clémençon, M., Lardet, F., Battin, T.J. & Lane, S.N. (2023). Decrypting the stream periphyton physical habitat of recently deglaciated floodplains. *Science of The Total Environment*, 867, 191374. https://doi.org/10.1016/j.scitotenv.2022.161374.

The aim of this study was to investigate the physical proprieties of the habitats defining the spatial and temporal assemblage of periphyton during a melt season of an Alpine temperate glacier in the context of rapid climate warming. The authors showed that periphyton development is constrained by two conditions: geomorphic stability and water accessibility. These conditions are difficult to meet in highly-active braided streams, resulting in very short windows of opportunity for biofilm growth. As for the previous contribution, I provided assistance for the acquisition and the SfM-MVS post-processing of UAV imagery.

Roncoroni, M., Ballu, A., Selitaj, A., **Mancini, D.**, Miesen, F.M., Aguet, M., Battin, T.J. & Lane, S.N. (2024). Ecosystem engineering by periphyton in Alpine proglacial streams. *Earth Surface Processes and Landforms*, 49(1), 417-431. https://doi.org/10.1002/esp.5712.

This study aimed to better understand the role of periphyton in engineering the ecosystem of hillslope-fed tributaries in the terrace zones of a proglacial margin alluvial plain. To do that, two flume experiments were run directly on a terrace system to reproduce as closely as possible the environmental conditions (i.e. light condition, water proprieties) found in these environments. The main outcomes indicated that periphyton development on the riverbed effectively modifies the near-bed hydraulics, notably turbulence magnitude and direction, affecting at the same time the infiltration of water. I participated in the collection of imagery for small-scale SfM-MVS photogrammetry needed to detect morphological changes of the riverbed, as well as in the acquisition of repeated near-bed 3D flow velocity measurements to assess modification of hydraulic proprieties due to biofilm development.

Former PhD student Tom Müller also conducted research in the Glacier d'Otemma proglacial forefields to investigate the dynamics of groundwater storage during deglaciation. I was involved in the realization of one project:

Müller, T., Roncoroni, M., **Mancini, D.**, Lane, S.N. and Schaefli, B. (2024). Current and future role of meltwater-groundwater dynamics in a proglacial Alpine outwash plain. *Hydrology and Earth System Science*, 28(4), 735-759. https://doi.org/10.5194/hess-28-735-2024.

The study is meant to understand the hydrological functioning of outwash plains during deglaciation. As more terrain become ice-free, the interaction between surface and subsurface waters become more significant impacting the potential changes in groundwater storage and release. By calibrating a hydrological groundwater flow model using field observations, the results showed (i) a strong interaction between the upstream river and the aquifer, with infiltration from the proglacial stream as the dominant process of recharge compared to hillslope, rain and snowmelt contributions; and (ii) the ability of the groundwater to maintain water at the surface even during long dry periods. For this project, I provided the DEMs for both wet and dry regions (Chapter 3), which were used in the physical model to simulate groundwater flow magnitude and direction.

In addition to the above collaborations having in common the same study area, three other collaborations were established with other members of the ALpWISE, ICE (Interactions between Climate and Earth surface processes led by Prof. Dr. Georgina King) and GLACE (Glacier-Landscape interactions in Alpine and Arctic Catchments and Environments led by Dr. Ian Delaney) groups of the IDYST due to my expertise with specific methods.

Antoniazza, G., Dietze, M., **Mancini, D.**, Turowski, J.M., Rickenmann, D., Nicollier, T., Boss, S. & Lane, S.N. (2023). Anatomy of an Alpine Bedload Transport Event: A Watershed-Scale Seismic-Network Perspective. *Journal of Geophysical research: Earth Surface*, 128, e2022JF007000. https://doi.org/10.1029/2022JF007000.

This study monitors the transfer of coarser sediment at an entire Alpine catchment scale (Vallon de Nant, 13.4 km$^2$ located in the South-Western Swiss Alps) to better understand erosion and deposition of material during a relatively high-magnitude bedload transport event. This was achieved deploying a network of 24 seismic sensors spread across the entire watershed. Results suggest the relative inefficiency of Alpine catchments in evacuating coarse material. This inefficiency arises because upstream inputs from tributaries were rapidly attenuated in regions where the main channel was characterized by braided patterns, hence less hydraulic efficient reaches. Given my previous experience with environmental seismology methods, I assisted in the calibration of the geophysical inversion model of Dietze et al. (2019a) used to convert seismic records into continuous bedload sediment flux (Chapter 2). In particular, I provided the Rcode for the determination of seismic ground parameter values (i.e. seismic wave propagation and attenuation) from active seismic surveys.

Yuskar, Y., **Mancini, D.**, Bartz, M., Schmidt, C., Choanji, T., Nicholas, A.P., Lane, S.N. & King, G.E. (in prep.). Fluvial dynamics and climate change in a tropical river throughout the Late Quaternary (Kampar River, Sumatra, Indonesia).

This study investigates Quaternary landscape evolution in tropical river environments in response to changing climate, focusing on the Kampar river (Indonesia). Chrono-stratigraphy records obtained with luminescence dating suggest that fluvial morphodynamics

were primarily a consequence of climate-controlled sedimentation process rather than tectonic processes. To determine long-term sedimentation events and consequent landscape evolution, the 2D hydro-morphodynamic numerical model *eRiDynaS* (Nicholas, 2013a,b; Nicholas et al., 2015) was mobilized. I was involved in this project by providing technical support and assistance with the calibration of the numerical model, drawing on my previous experience with it (Chapter 5).

Gevers, M., Lane, S.N., Miesen, F.M., **Mancini, D.**, Jenkin, M., Bouscary, C., Perchanok, F. and Delaney, I. (in prep.). Seasonal variations in sediment transport from ice sheet terminus though a proglacial forefield. A case study from Leverett glacier, Western Kalaallit Nunaat (Greenland).

This work focuses on the geomorphic role of proglacial areas on the downstream sediment supply in land-terminating glacier-fed rivers in the Greenland Ice Sheets. This is achieved for both suspended sediment and bedload over a complete summer season using conventional discharge-turbidity relationship and seismic techniques, respectively. My contribution to this project was to train the field operators in the installation of geophones and to provide technical support for calibrating the geophysical inversion model of Dietze et al. (2019a) to convert the seismic records into continuous bedload flux quantifications (Chapter 2).

# Chapter 2: Filtering of the signal of sediment export from a glacier by its proglacial forefield

## 2.1 Chapter overview

This Chapter aims to define the effects of proglacial forefields morphodynamics on the subglacial export signal for both suspended sediment and bedload addressing the first research question of the thesis: "Do forefields filter the signal related to subglacial sediment export? If yes, over which timescales this filtering occurs?". This investigation is conducted by applying signal post-processing techniques to sediment transport timeseries recorded using conventional turbidity-discharge relation and environmental seismology techniques, collected directly in the field at both the glacier terminus and the forefield outlet. The objective was to determine the nature of the proglacial morphodynamic filtering (i.e. delaying, dampening or shredding), the timescales over which it operates and the potential driving mechanisms.

The chapter was published as a peer-review paper: Mancini, D., Dietze, M., Müller, T., Jenkin, M., Miesen, F., Roncoroni, M., Nicholas, A. & Lane, S.N. (2023). Filtering of the signal of sediment export from a glacier by its proglacial forefield. *Geophysical Research Letters*, 50(21), e2023GL106082. https://doi.org/10.1029/2023GL106082.

## 2.2 Filtering of the signal of sediment export from a glacier by its proglacial forefield

### 2.2.1 Introduction

Mountain glaciers and ice sheets are retreating globally (Moon, 2017). In the European Alps glaciers lost about 50% of their surface between 1850 and 2000 (Zemp et al., 2006). This rapid retreat results in rapidly growing proglacial margins which, in the Swiss and Austrian Alps alone, consist of ca. 930 $km^2$ of deglaciated terrain exposed since the end of the Little Ice Age (Carrivick et al., 2018). Concurrently increasing subglacial sediment evacuation rates (Lane et al., 2017) impact the morphodynamics of the forefields that form downstream of glaciers given the observed influence of sediment supply (Ashmore, 1988, 1991a; Lane et al., 1996).

Sediment flux in geomorphic systems including alluvial rivers (e.g. Ashmore, 1991a), hillslope- catchment systems (e.g. Hasbargen and Paola, 2000; Lancaster and Casebeer, 2007) and river deltas (e.g. Kim et al, 2006; van Dijk et al., 2009) is characterized by significant temporal variability (Phillips, 2003; Coulthard et al., 2005). Variability is not only a function of external forcing, such as precipitation events or daily discharge variations, but are also induced by autogenic processes resulting in self-organizing behavior (Coulthard and Van de Wiel, 2007; Carling et al., 2016) and the strong filtering of exogenic forcing over a wide range of timescales (Jerolmack and Paola, 2010). Such filtering has been attributed to two related scales of behavior: (1) progressive reworking of fluvial landforms (Beerbower, 1964), meaning that sediment cannot always pass easily through a river reach without encountering a depositional environment; and (2) limits on the advection length for sediment, which are a function of ambient flow velocity, particle settling height and particle size (Ganti et al., 2014). The former are well known for proglacial margins (e.g. bank failure following lateral erosion, in-channel and alluvial channel storage, channel bifurcation, avulsion and channel abandonment,...) (Ashmore, 1991b, 2013; Cudden and Hoey, 2003; Van De Viel and Coulthard, 2010; Hundey and Ashmore, 2009; Kasprak et al., 2015). Advection limits are related to this morphological forcing. For instance, Kasprak et al. (2015) found that the particle displacement lengths in a laboratory flume vary with the mean distance between confluences and diffluences. This is because diffluences set maximum advection lengths by promoting flow deceleration and a local reduction in settling height (Ashworth, 1996) and so deposition.

The above statements suggest that proglacial forefields have the potential to filter the signal of sediment exported from glaciers, but the extent to which this might be the case has never been demonstrated. Our current knowledge of subglacial sediment export by glacier-fed streams is dominated by suspended sediment monitoring (e.g. Richards, 1984; Swift et al., 2005; Delaney et al., 2018), only one part of the sediment export signal. Difficulties in measuring bedload transport have resulted in major uncertainties in absolute bedload amounts, the relative importance and temporal variation of bedload and suspended load transport rates in both glacial and proglacial environments, and how rates vary from the event scale to the diurnal, seasonal and eventually multi-year scales. As yet, we have no continuous records of bedload transport in proglacial marginal settings.

Morphodynamic filtering of downstream sediment transport signals can occur to different degrees, including (1) dampening when the signal amplitude is scaled down but the amplitude-frequency dependence remains; (2) delaying which may or may not accompany dampening but where there is a shift in phase; and (3) shredding where the amplitude-frequency dependence is partially or completely destroyed (Straub et al., 2020). Understanding the extent to which there is filtering and the distance over which it occurs is important for several disciplines. Glaciologists commonly estimate glacial erosion rates from subglacial sediment export measurements (Humphrey and Raymond, 1994; Riihimaki et al., 2005; Swift et al., 2005; Herman et al., 2015) and relate these to contemporaneous measurements of ice sliding velocity (i.e. sliding erosion law; Amundson and Iverson, 2006). The non-linear relationship between glacier sliding velocity and measured erosion rates remains highly uncertain (Cook et al., 2020) due to difficulties in correctly inferring the erosion rate itself. Sediment transport rates are commonly determined from fixed installations located several kilometers away from glacier termini (e.g. Dell'Agnese et al., 2014; Delaney et al., 2018; Comiti et al., 2019; Carillo and Mao, 2020), potentially obscuring recorded sediment transport rates in the presence of signal filtering. A dampened signal may translate into errors in the magnitude of estimated transport rates. A delayed signal may cause temporal uncertainty in which ice velocity variation should be related to erosion rate variation. A partially-shredded signal may contain only a partial signals of glacial erosion. A completely shredded signal may still provide a reliable long-term mean erosion rate but no signal of variation in glacial erosion.

Here, we present the first high-frequency, continuous, seasonal-scale data for bedload, accompanied by suspended load, for a proglacial margin. The data allow us to quantify how proglacial morphodynamics filter the signal of the sediment exported from the snout margin of an Alpine glacier for both suspended load and bedload in a context of rapid deglaciation, and the timescale over which the filtering occurs. This is achieved by combining passive seismic monitoring and more classical discharge and suspended sediment load measurements.

**2.2.2 Methods**

The study is focused on the Glacier d'Otemma proglacial margin (Figure 2.1) located in the southern-western Swiss Alps (Bagnes Valley, Valais) at an altitude of about 2450 m a.s.l.. The proglacial forefield is ca. 1 km long and ca. 200 m wide with a mean valley bottom slope of about 1.2 %. The configuration of the proglacial stream follows the available accommodation space, limited by steep valley sidewalls, and the valley bottom slope. Where the lateral accommodation space is at a maximum, and slope is lower (mean of 0.18%), the channel pattern is dominated by an active braided network. Towards the upstream glacier terminus and at the downstream forefield end, flow is confined into a single bedrock-dominated channel due to the combination of a narrower and steeper (3.18%) valley section. According to field grain size measurements using the Wolman pebble count procedure (Wolman, 1954),

the proglacial stream flows on a bed mostly composed of quaternary morainic deposits with a mixed sand, gravel and cobble particle size range: close to the glacier terminus the texture of the riverbed is dominated by gravels and cobbles ($D_{50}$ of ca. 78 mm and $D_{84}$ of ca. 92 mm, n = 345), while towards the forefield end more sandy deposits are also present ($D_{50}$ of ca. 37 mm and $D_{84}$ of ca. 48 mm, n = 348).
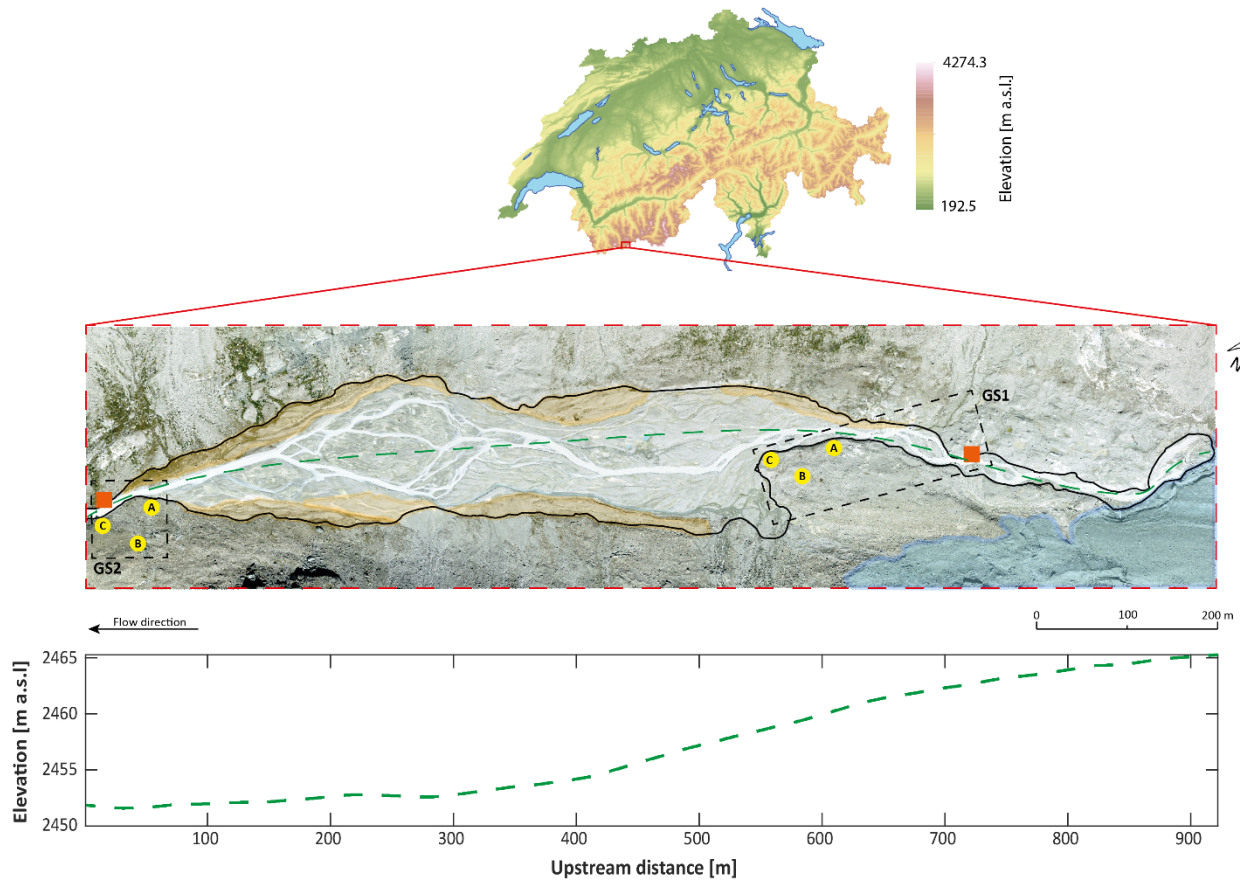


Figure 2.1: Location of GS1 and GS2 in the Glacier d'Otemma proglacial forefield. Yellow circles refer to geophones, orange squares to turbidity probes and water pressure sensors, the light blue region highlights bare and debris-covered glacier, while orange regions the terraces and the black line the proglacial forefield limits. The green dashed line is the elevation profile.

This proglacial forefield was chosen for two reasons. First, Mancini and Lane (2020) showed that the forefield and the valley sidewalls were largely disconnected from each other due to the development of alluvial fans that buffer hillslope to forefield sediment flux. Second, the active forefield is located within stable terrace systems reflecting a long-term state of sediment supply being lower than potential transport capacity (Collins, 2008; Marren and Toomath, 2013; Roussel et al., 2018). Thus, the glacier is the primary source of both suspended load and bedload. We studied two melt seasons experiencing different climatic conditions (Supplementary Information 2.3.1): summer 2020 from June 25th (Julian Day [JD] 177) to August 29th (JD 242), which was warmer and drier; and summer 2021 from June 11th (JD 162) to August 21st (JD 233), which was colder and wetter especially in the first part of the season.

Continuous suspended load and bedload transport rates were indirectly monitored at two gauging stations located ca. 350 m from the glacier terminus (GS1) and at the forefield outlet (GS2) with a distance of ca. 850 m between them (Figure 2.1). They were equipped with turbidity probes, water pressure sensors and geophones. Suspended loads were derived using a conventional turbidity-sediment concentration relationship (Supplementary Information 2.4.2 and 2.4.3), whilst bedload transport was monitored seismically (Supplementary Information

2.4.4, 2.4.5, 2.4.6 and 2.4.7). The post-processing of collected seismic data to quantify bedload transport rates used the geophysical inversion model of Dietze et al. (2019a) in the open source R package *eseis* (version 0.5.0) (Dietze, 2018; Supplementary Information 2.4.4). Model calibrations for both GS1 and GS2 are explained in Supplementary Information 2.4.4 through 2.4.7. Given the extreme difficulty of direct measurement of bedload (e.g. with a portable sampler) in this kind of river, we used the fact that water stage is an output of the seismic inversion which if successful should reproduce water stages measured at GS1 and GS2 (Supplementary Information 2.4.5 through 2.4.7). Second, in 2021, we installed an additional station at the glacier terminus (GSG) 300 m upstream of GS1. With a relatively straight steep, semi-alluvial reach between GS1 and GSG we expected them to have similar signals and so used GSG as a control on the repeatability of the method (Figure 2.1; Supplementary Information 2.4.6). Finally, recognizing that the inversion model contains parameters (e.g. ground proprieties) that are unlikely to be stationary, we applied Latin Hypercube Sampling to plausible parameter ranges to estimate uncertainty in each seismically-estimated bedload transport rate (Supplementary Information 2.4.4).

We combined analysis of sediment transport time-series with power spectra to detect the kind and nature of filtering of the signals travelling through the floodplain (Supplementary Information 2.3.8). We compared correlations of water discharge and sediment transport signals, both suspended sediment load and bedload, at GS1 and GS2 to determine spatial differences in transport dynamics. Results were combined with cross-correlation of signals monitored at GS1 and GS2 to define the nature of the proglacial forefield filtering on them. This latter aspect was then further investigated using power spectra analysis following Jeromlack and Paola (2010) (Supporting Information S8). This approach applies a Discrete Fourier Transform to both instantaneous suspended sediment load and bedload signals at GS1 and GS2 to convert them from the time into the frequency domain. Frequencies were then converted into timescales (days) by relating them to their sampling interval (i.e. 2 minutes; 0.00014 JD), while amplitudes were squared to convert them from complex number into powers ($10\log_{10}(kg/s)^2$, hence dB). We expected fluctuations in power to increase as a power-law function of time within timescales having significant variability in sediment flux (i.e. sub-daily to daily), followed by a situation marked by only slight increases at longer timescales (i.e. seasonal). If the forefield acts as a non-linear filter, the power-period relations for GS1 and GS2 should have non-zero slopes, with the local gradient of the spectrum proportional to the filtering magnitude. The spatial comparison of spectra allows determining how the forefield has filtered the signal. At the same time, we also assessed if the diurnal suspended sediment load and bedload export signals are still recorded at the forefield outlet by comparing the daily export periodicity to the characteristic timescale of the system.

Once both filter strength and timescales were determined, we investigated the responsible morphodynamic filtering mechanisms (Supplementary Information 2.4.8). We calculated the difference between GS1 and GS2 in the timing of discharge, suspended load and bedload signal peaks, assuming a straight-line travel distance, to derive a measure of the virtual velocities ($V_v$) of water and sediment waves following Hassan et al. (1991). It is important to note here that the braided nature of the reach should increase the effective travel distance calculations giving maximum possible velocities. Then, by knowing for each transport cycle the duration for which discharge exceeded the transport capacity threshold $Q_c$, calculated according to Rickenmann (1991), we were able to retrieve daily advection lengths. The latter were defined as the distance travelled by a particle before it settles to the bed (Ganti et al. 2014). We derived them by multiplying the virtual propagation velocities of the suspended sediment load and the bedload waves by the daily duration for which discharge was higher than $Q_c$. As shown in Métivier (1999), for a sediment transport signal to be modified between

two points in space the length-scales of transporting events (i.e. their advection lengths) must be shorter than the distance between those points, in this case GS1 and GS2 (Figure 2.1). This is related to the different propagation velocities of discharge and sediment waves, and it reflects the observation of Ganti et al. (2014) that the bounds on advection lengths are constrained by sediment settling velocities. Finally, we used the daily Shannon Entropy index (SE) (Lane and Nienow, 2019) to study the relationship between the changing variability of transport signals at GS1 and GS2 and discharge variation during the melt season (SE index is proportional to signal variability: higher values means a more spread-out distribution). Assuming sediment export from the glacier tracks discharge, we would expect signal filtering to manifest as a reduction in the intensity of daily transport variation and hence a reduction in Shannon Entropy.

### 2.2.3 Suspended sediment load and bedload transport dynamics

Daily hydrographs have an asymmetrical shape characterized by: rapid increase during the rising limb, starting around 10 am, to maxima of ca. 13.5 $m^3/s$ in 2020 and of ca. 11 $m^3/s$ in 2021; followed by a gentler decrease in the falling limb, usually starting around 6 pm ($Q_w$, Figure 2.2a). Suspended sediment load reflects this variation at GS1 and GS2 for both melt seasons with discharge versus suspended sediment load ($Q_s$) correlations of 0.632 (2020, $p<0.05$) and 0.681 (2021, $p<0.05$) for GS1 and 0. 574 (2020, $p<0.05$) and 0.557 (2021, $p<0.05$) for GS2. As discharge increases, (i) suspended load increases at both sites with only small differences in magnitude between sites; (ii) maximum loads coincide with maximum discharges at both sites; but (iii), during daily hydrograph recession, loads diverge with GS1 values higher than GS2 values. Given the absence of river-connected kettle holes and lakes that have been shown to buffer proglacial suspended sediment flux (Geilhausen et al., 2013; Bogen et al., 2015), these differences are likely due to local temporary trapping of fine sediment due to bed roughness (Parsons et al., 2018), the incorporation of fine sediment during falling limb bar formation (Richards, 1984; Orwin and Smart, 2004) and overbank fine sediment deposition. Bedload transport rates ($Q_b$; Figure 2.2a) also show some association with discharge but correlations are only significant upstream at GS1 (0.437 and 0.611 for 2020 and 2021 respectively, $p<0.05$ in both cases) and not downstream at GS2 (0.309 and 0.162 for 2020 and 2021 respectively, $p>0.05$ in both cases), suggesting the breakdown of capacity-driven bedload transport due to the presence of the proglacial forefield. While there can be a significant suspended load at all discharges, bedload seems to be delayed compared to discharge closer to the glacier at GS1 (Beaud et al., 2016; 2018a,b) and strongly threshold-limited at GS2 (Perolo et al., 2019). In 2021, the correlation between $Q_b$ and $Q_w$ is similar (0.611) to $Q_s$ and Q (0.681) at GS1. However, the $Q_b$ and $Q_w$ correlation at GS1 is lower in 2020 (0.437) than for $Q_s$ (0.632) because subglacial sediment export rates, and hence the transport rates measured at GS1, reduced significantly from early August onwards. The correlation between $Q_b$ and $Q_w$ at GS1 was 0.522 until August 5th when this reduction occurred.

### 2.2.4 Filtering of subglacial sediment export signals by forefield morphodynamics

The lower correlations between $Q_w$ and, respectively, $Q_s$ and more notably $Q_b$ at GS2 suggest a direct impact of proglacial morphodynamic processes on downstream transport signals. Cross-correlations of instantaneous sediment flux time series between GS1 and GS2 (Figure 2.2b) suggest little delay in $Q_s$; maximum correlations are significant with values of ca. 0.75 and ca. 0.85 at a lag of ca. 0 days for both melt seasons, while the cross-correlations are symmetrical. $Q_b$ show lower maxima values of ca. 0.4 and ca. 0.3 at 0 lag days, but signals are asymmetrical tending towards negative lags, hence a situation where the signal at GS2 peaks usually later then at GS1. The more marked asymmetry for 2020 is due to the decreasing $Q_b$ flux during the melt seasons (Figure 2.2a). This means that the $Q_b$ signal

recorded in GS1, unlike the $Q_s$ signal, was both dampened (Figure 2.2a) and delayed (Figure 2.2b) as it passed through the forefield.

Viewing the $Q_s$ signals in the frequency domain, Figure 2.2c suggests high power (ca. $10^5$ dB) at the shortest time-scales (ca. $10^{-3}$ days), followed by a significant decrease in magnitude (ca. $10^{-1}$ dB at $2 \times 10^{-3}$ days) before a gradual and linear increase up to $10^5$ dB at the seasonal scale. The latter has a slope of about 0.23. The evolution of the signals for GS1 and GS2 are similar in both melt seasons, especially in 2021. This suggests limited filtering of the signal for suspended load. For bedload transport, as for suspended transport, both spectra show a decrease to a timescale of ca. $2 \times 10^{-3}$ days, followed by a weak and unsteady increase until ca. $10^2$ dB at $10^{-1}$ days; the increase is more marked for the GS1 signal than the GS2 one (slopes of ca. 0.6), suggesting a stronger non-linear filtering compared to suspended sediment load for subdaily scales. From timescales of $10^{-1}$ to $10^0$ days, the power continues to increase albeit at a lower rate in both 2020 and 2021, suggesting a cross-over timescale after which the intensity of the non-linear filtering decreases. At GS2 in 2021, power becomes almost constant for bedload transport until time-scales longer than $10^{-1}$.

Figure 2.2: Timeseries and analyses on transport signals revealing the proglacial filtering. Field collected discharge, suspended sediment load and bedload time series (a; dashed and solid black lines refer to Q$_c$ in GS1 and GS2, respectively). Cross-correlation of suspended sediment load and bedload signals at GS1 and GS2: a one-day running mean is applied to raw correlations to remove diurnal variations and long-term structures. Lag (lead) means that peak at GS1 occurs earlier (later) than at GS2 (b). Power spectra of instantaneous transport rates (c).

Figure 2.2c also shows that diurnal transport cycles are maintained along the forefield, as spectra are all characterized by a peak in power at ca. $10^0$ days even if, especially for bedload, damped at GS2 (Figure 2.2a). However, signal cross-correlations (Figure 2.2b) suggests that it is unlikely that bedload transport peaks at GS2 are related to the same wave of sediment because of proglacial delay. Indeed, the significant removal of scales of variability at GS2 at time-scales longer than those associated with the diurnal variation suggests little transmission of the signal measured at GS1 through the proglacial forefield to GS2.

**2.2.5 Insight into the mechanisms driving forefield morphodynamic filtering**

Given the above, Figure 2.3 shows the daily timing difference in peak arrivals within GS1 and GS2 for discharge, suspended sediment load and bedload waves. Discharge shows a good correlation in peak times at GS1 and GS2 for both 2020 (r = 0.91) and 2021 (r = 0.97), even if in 2021 there is a slight tendency for peaks to occur progressively earlier in the day during the melt seasons. The relationship between GS1 and GS2 for sediment transport is significant for suspended load (r = 0.93 in 2020; r = 0.94 in 2021), but less significant for bedload (r = 0.69 in 2020; r = 0.53 in 2021). There are a few days when the daily transport peak at GS2 occurs before the one at GS1 especially for bedload, which is likely to be related to a peak caused by within-reach erosion. In turn, this suggests the presence of multiple sources of sediments (Ashmore, 1988, 1991a; Mao et al., 2014; Comiti et al., 2019). Thus, the sediment signals at GS2 contains both the subglacial export signal recorded at GS1, and the signal of erosion and deposition events due to reworking events taking place in the forefield.

If we select only the events in which clear peaks in $Q_w$, $Q_s$ and $Q_b$ were identified at GS2 after a peak at GS1, we can calculate the time taken for waves to transit the reach (t(travel), Figure 2.3). To date, there is no *a priori* knowledge of virtual velocities in braided stream systems for bedload particles because of their relative long residence time in depositional areas and the difficulty of determining step lengths from field data (Church, 2006; Kasprak et al., 2015; Vázquez-Tarrío et al., 2019). Suspended sediment waves move on average at velocities that are 76.5% and 82.1% of the discharge wave in 2020 and 2021, respectively. Bedload moves at 25% and 14.1% of the discharge wave.
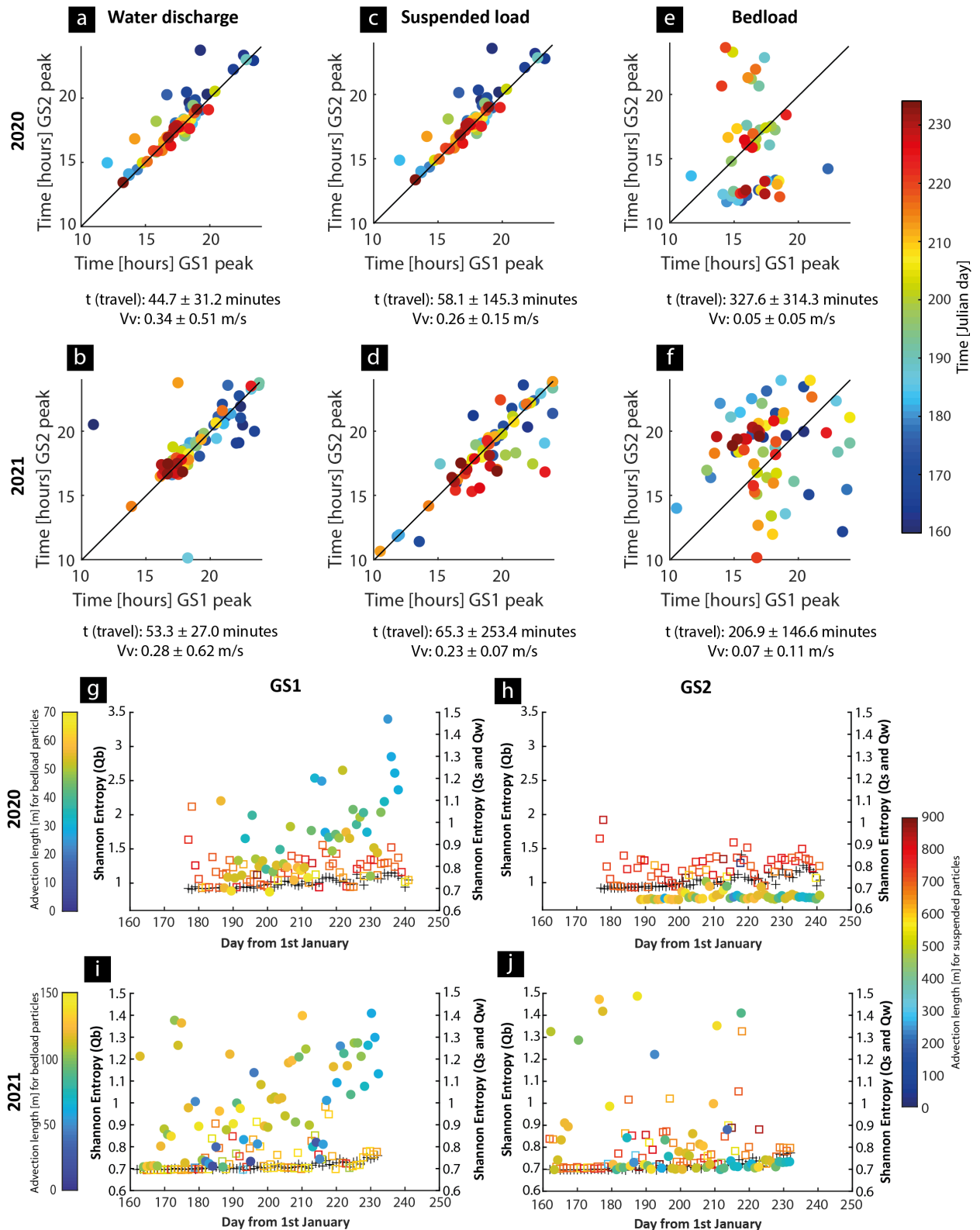
Figure 2.3: Proglacial filtering mechanisms. Timing difference in peak arrivals between GS1 and GS2 (a to f) and daily Shannon entropy indexes and particle advection lengths for discharge (crosses), suspended sediment (squares) and bedload (circles) during melt seasons 2020 and 2021 (g to j). Colors in g to j refer to daily particle advection length for suspended (jet colormap, right color ramp) and bedload (parula colormap, left color ramp).

The intense diurnal discharge variation in glacier fed Alpine streams means that if wave velocities are insufficient, sediment exported from the glacier will not reach GS2 before discharge falls below that required for transport, and deposition occurs, delaying the

59

downstream transmission of the bedload export signal (Figure 2.2b). We can compare the time-scales for bedload transport in Figure 2.3 with the time-scales of likely sediment transport competence. Daily $Q_w$-$Q_b$ rating curve established that the critical discharge $Q_c$ required for bedload transport to occur is 3.8 ± 1.25 m$^3$/s at GS1 and 3.2 ± 1.54 m$^3$/s at GS2 based on pooling data for 2020 and 2021 (Supplementary Information 2.4.8). The standard deviations here reflect seasonal changes in characteristics of available sediments and on the degree of armoring of the riverbed (Ashmore, 1988; Hoey and Sutherland, 1991; Vázquez-Tarrío et al., 2019). Figure 2.3 (a to f) shows the duration of possible transport ($t \mid t_{Q>Qc}$) for $Q_s$ and $Q_b$, and the likely advection lengths estimated from wave speeds. For $Q_s$, advection lengths up to 900 m are generally comparable with the reach length (Figure 2.1) such that morphodynamic forcing is insufficient to modify the signal of glacial suspended sediment export at GS2 as advection lengths keep up with discharge (Ganti et al., 2014). However, advection lengths are always less than the reach length for $Q_b$ (up to 70 m in 2020 and up to 150 m in 2021) implying morphodynamic forcing of transport, whether due to microscale sediment entrainment-deposition processes or macroscale divergence between flow and sediment transport paths forced by river braiding (e.g. Bridge and Gabel, 1992; Ashworth, 1996). These distances imply transport delays of up to 7-11 days (Figure 2.2b). This confirms that transport peaks considered in computing virtual velocities (Figure 2.3) are unlikely to be associated with the same grains because of their longer travel time in the proglacial channel. The preservation of the diurnal evacuation cycles (Figure 2.2c) is likely related to hydraulically-driven transition of former-evacuated bedload waves, progressively moved downstream towards the forefield end by successive discharge waves ("pulses"). This phenomenon also comes with a dampening of the signal (Figure 2.2a and Figure 2.2b) suggesting that part of the subglacially-exported bedload wave are deposited moving downstream, and highlighted in the field by the sorting of particles going from GS1 to GS2 (Figure 2.1).

Figure 2.3 (g to j) further supports the proglacial filtering of the signal related to subglacial bedload evacuation as the signal entropy (i.e. daily variability) declines due to the forefield. Given the above, the modification of the bedload export signal seems to be driven by particle advection lengths, which in turn depend on grain size and on discharge conditions. It is well established that the intensity of diurnal discharge variation increases during the melt season in glacier-fed streams (Nienow et al., 1998; Lane and Nienow, 2019) because of a progressive reduction in the buffering of glacial melt by snow as the snow-ice interface retreats up glacier and related, a progressive upstream extension of the sub-glacial drainage system (Nienow et al., 1998). Discharge variability constantly increases over time (Figure 2.3g to Figure 2.3j; Mann-Kendall test $p<0.05$ confirming monotonic trends in both 2020 and 2021) suggesting (i) a progressive increase in daily peak discharge, or even a decrease in daily minimum discharge, and (ii) the increasing likelihood of discharge falling below the critical value $Q_c$ later in the season (Figure 2.2a).

Given this discharge evolution we would expect bedload advection lengths to become progressively longer over time, before dropping toward the end of the season, making transport largely transport-limited (Perolo et al., 2019). This is exactly the case for GS1, where the transport entropy is higher for bedload than either suspended load or discharge, and it increases systematically through the melt season. In both cases this is combined with a general reduction in advection lengths (Figure 2.3g and 2.3i; Mann-Kendall test $p<0.05$ for both Shannon entropy and advection length). However, at GS2, even if there are also seasonally monotonic trends for both entropy and advection lengths (Mann-Kendall test $p<0.05$), they are less strong, suggesting less dependence of bedload transport on discharge variation (Figure 2.3h and 2.3j). Thus, the seasonal evolution of subglacial bedload export is strongly damped and delayed between GS1 and GS2 (Figure 2.2b and Figure 2.2c).

Studies on (pro-)glacial suspended sediment transport involving similar experimental setup shown high variability at daily to seasonal scales (Hodson and Ferguson, 1999; Leggat et al., 2015; Mao and Carillo, 2017). This because the changing upstream conditions, in terms of subglacial discharge (i.e. Hodgkins et al., 2003) and sediment export (i.e. Stott and Mount, 2007) rates, activate the proglacial morphodynamic response buffering, delaying and changing the transport dynamics of subglacially-exported particles (e.g. Ashmore, 1988; Hodson et al., 1998; Orwin and Smart, 2004; Antoniazza et al., 2019; Misset et al., 2020). The signal of subglacial suspended sediment export is effectively transmitted downstream, even if some degree of non-linear filtering is detected due to short-lived deposition events at low transport capacity (Guillon et al., 2018; Figure 2.2a and Figure 2.2c). In contrast, the short advection lengths for bedload explain why the subglacial bedload export signal at diurnal time-scales is substantially reduced in both melt seasons (Figure 2.3); it is generally not possible for coarse particles to move fast enough to travel through the proglacial forefield in a single diurnal discharge cycle, a mechanism that is itself conditioned by evolution in seasonal sub-glacial discharge conditions (Figure 2.3g to Figure 2.3j). However, morphodynamic filtering mechanisms for bedload need to be further investigated.

Given current research in glacial erosion is based upon deployment of monitoring stations located 100s of meters to kilometers downstream of glacier termini (e.g. Herman et al., 2015), it is not clear if they provide reliable erosion rate estimates over relatively short-time scales. The extent to which this is the case will depend on the relative importance of bedload and suspended load export from a glacier, something that remains poorly quantified. In principle, the miscalculation might come from wrongly assuming that subglacial channels always evacuate all eroded sediment (Alley et al., 1997), leading to an overestimation of suspended load as a glacial erosion product. The filtering is likely to be scale limited as in larger glaciers, and notably for ice sheet outlets, the larger spatial melt extent leads to attenuation of diurnal discharge variation (e.g. Cowton et al., 2013) such that subglacial discharge is always greater than the critical value required to maintain transport.

## 2.2.6 Conclusion

The first field-based glacial forefield quantification of continuous suspended load and bedload transport rates provides evidence of an autogenic influence of river morphodynamics on coarse sediment flux, and less on finer sediment flux. The result is a significant dampening and delaying of the signal related to subglacial bedload export, and hence a difference in the erosion rates that would be inferred from sediment transport signals as measurement sizes move donwstream. The modification of coarse sediment flux results from advection lengths that are constrained by both diurnal and seasonal variations in discharge. This is due to (i) proprieties of the subglacial hydrological system which evolve to having baseflows lower and peak flows higher than the the critical discharge required for bedload transport, and (ii) spatially changing proglacial hydraulic and morphological conditions. These findings are important for the understanding of the sediment connectivity in proglacial margins, especially in terms of natural hazard mitigation and sediment management for hydropower infrastructures, but also for potential geomorphic influences on ecological succession in recently deglaciated terrains. From a glaciological perspective, they suggest that inferences of the relative importance of suspended sediment load and bedload and the timescales of their variation cannot be reliably estimated except where measurements are collected close to glacier termini.

## 2.3 Chapter summary

The Chapter has shown that proglacial forefield morphodynamics is effectively able to filter the subglacial sediment export signal. This filtering is more significant for bedload than for suspended sediment particles, whose signal pass almost unimpeded though the proglacial forefield. The subglacial bedload export signal is rapidly delayed and dampened by the autogenic reorganization processes of the proglacial stream already at sub-daily timescales, while that related to suspended sediment export is only slightly dampened.

Spatial cross-correlation between water discharge and sediment signals reveals that the main reason for the filtering is due to the way particles move in the proglacial forefields. Fine sediments are transported downstream synchrony with the daily water discharge wave, meaning that they can travel the entire floodplain length within a single hydrograph. However, coarser particles, moving in contact with the riverbed and dependent on a critical discharge for their entrainment, have smaller advection lengths meaning that they need multiple reworking events before to be evacuated out of the proglacial margin system.

These findings open new perspectives on the role of proglacial forefields in influencing the downstream transport of subglacially-exported sediments (Section 1.4). First, there is the need to establish the relationship between forefield geomorphic response and longitudinal sediment connectivity under specific boundary conditions (Chapters 3 and 4), and then to generalize it to scenarios involving varying topographical, sedimentological and hydrological settings (Chapter 5).

## 2.4 Supplementary information

### 2.4.1 Climatic conditions in the Glacier d'Otemma proglacial forefield in the 2020 and 2021 melt seasons

The summers 2020 and 2021 were characterized by similar climatic conditions in terms of atmospheric air temperatures, but not in terms of precipitation (Figure S2.1).

In 2020 the time period under investigation had a mean temperature of ca. 7.7 °C characterized by a warming phase comprised between the beginning and the of July (mean of ca. 7.8 °C) followed by a short cold period (mean of ca. 4.3 °C) in the beginning of August, and again a warm and more stable phase lasting until end of August (mean of ca. 8.2 °C). In 2021 the studied period had a mean atmospheric temperature of about 7.4 °C. The mid-June period was characterized by rapid warming (mean of c. 8.2 °C), followed by a general cooling trend (mean of ca. 6.9 °C) until mid-July, but with short very warm days for the altitude (2450 m a.s.l.) with temperatures up to ca. 15°C. The rest of the melt season had very similar conditions to those of 2020 with a warming period until the end of July (mean of ca. 7.5 °C), a slightly longer cold period at the beginning of August (mean of ca. 5.3 °C) and a warmer phase in mid-August (mean of ca. 8.4 °C) with atmospheric temperatures reaching ca. 18°C.
Concerning precipitation, Figure S2.1 shows that the 2021 melt season was affected by higher rainfall rates compared to 2020. During 2021 there was 263 mm of precipitation with a particularly intense phase in the first half of July. In 2020 only a total of 76 mm was recorded mainly distributed in multiple short-lived events.
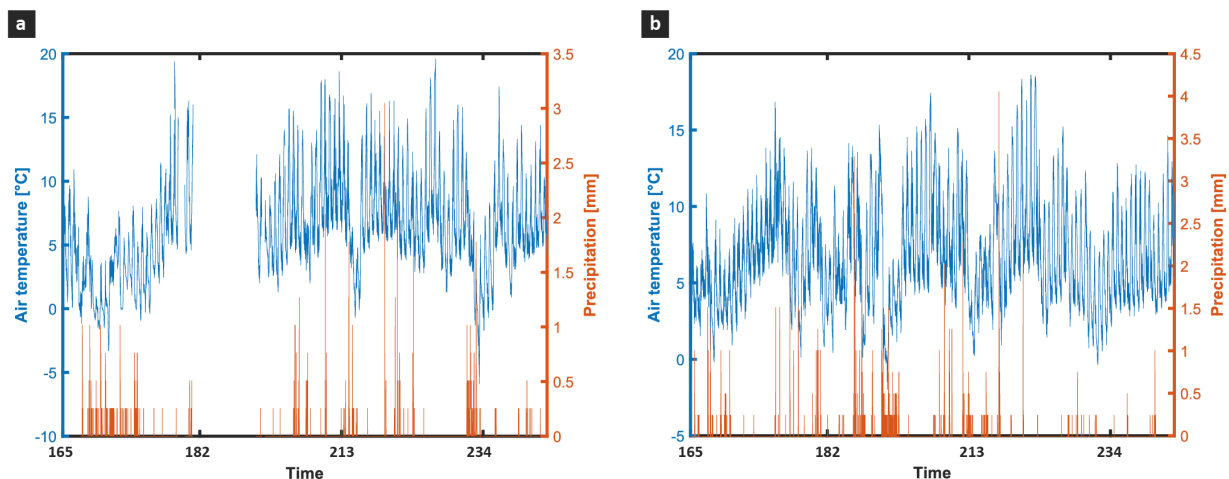


Figure S2.1: Atmospheric temperature (average over 5 minutes) and rainfall (average over 10 minutes) records measured in the Glacier d'Otemma proglacial forefield in melt seasons 2020 (a) and 2021 (b).

### 2.4.2 Continuous water discharge measurements

Water heights records were automatically collected at both GS1 and GS2 at a sampling rate of 2 minutes using a CS451 water pressure sensors from Cambell Scientific. These were combined with point discharge measurements using dye tracing techniques to obtain continuous discharge records. Table S2.1 shows the total number of samples used to calibrate the discharge-water stage relationship and the calibrated equation for both GS1 and GS2 over the two melt seasons under investigation. The monitoring station were designed to avoid burial (see Supplementary Material 2.4.3). However, the time series (Figure 2.2) were truncated at the end of August in both melt seasons, due to the increasing periods in which the sensors were out of the water, hence the reliability the data. The data, the methodology and the methods used for the post-processing of the field collected data are available in Müller and Miesen (2022).

Table S2.1: Site-specific discharge-water stage calibration relation for 2020 and 2021.

| Date | Site | | | | | |
|---|---|---|---|---|---|---|
| | GS1 | | | GS2 | | |
| | Running period | # obs | Q-Hw | Running period | # obs | Q-Hw |
| 2020 | 25th June 14th September | 25 | Q = 0.05 + 18.50h$^{2.53}$ | 26th June 14th September | 19 | Q = 0.17 + 18.86h$^{2.46}$ |
| 2021 | 10th June 8th September | 27 | Q = 0.02 + 11.28h$^{1.95}$ | 10th June 8th September | 25 | Q = 0.13 + 14.75h$^{2.83}$ |

## 2.4.3 Determination of suspended sediment loads

Table S2.2: Summary of suspended sediment calibration and analysis results.

| Date | 2020 | | 2021 | |
|---|---|---|---|---|
| Site | GS1 | GS2 | GS1 | GS2 Period 1; Period 2 |
| Start date | 25th June | 26th June | 10th June | 10th June |
| End date | 14th September | 14th September | 8th September | 8th September |
| Analysis period after cleaning | 26th June 31st August | 26th June 31st August | 10th June 21st August | 10th June 21st August |
| Percentage of record common to both stations after cleaning | 89.6% | | 90.0% | |
| Manual suspended sediment samples | 66 | 67 | 45 | 28 ; 30 |
| a | 0.0040 | 0.0032 | 0.0038 | 0.0072 ; 0.0043 |
| b | 0.467 | -0.007 | 0.180 | -0.107 ; 0.026 |
| R$^2$ | 85.3 % | 91.7 % | 93.5% | 85.8 % ; 77.1% |

Suspended sediment loads were derived indirectly using conventional turbidity-sediment concentration-discharge relationship (e.g. Gurnell, 1982; Fenn et al., 1985; Clifford et al., 1995; Swift et al., 2005; Stott and Mount, 2007; Stott et al., 2008; Leggat et al., 2015).

Turbidity records were automatically collected at a sampling rate of 2 minutes using an OBS300+ turbidity probe from Cambell Scientific. For each gauging station and for each year we developed a calibration curve describing the relation between manually collected suspended sediment concentration using a USDH-48 sampler and recorded turbidity (Table S2.2).

In 2020, we had single probes at both stations. As these were set to reduce the risk of burial, at low flows, they were occasionally out of the water. This was very rarely the case at GS1 affecting only 5.5% of data points and primarily in the last third of the measurement season. A higher proportion of points at GS2 (10.4%) were prone to this problem and the frequency of this occurrence increased markedly at the beginning of September. For both GS1 and GS2, data points where the probe was out of the water were manually identified. At times of very low flow, they often included the lowest diurnal turbidity. This made interpolation of values difficult and so we left them as missing. In both cases, all manual samples were

unaffected by this problem and could be used to develop a calibration curve specific to each station. We decided to truncate the analysis at the 31st August given the increase in the low flow problem at GS2 after this date.

In 2021, as we had installed two probes one above the other to deal with this problem, we made composite records. At GS1, the record from both probes was highly correlated (r = 0.995) up until the last 20 or so days of the record. After 20 days, the lower probe became very slightly prone to burying. Thus, for GS1, we focused all analyses on the higher probe noting that at no point in 2021 was it too high to be out of the water. This required a single calibration curve which used all 45 manual suspended sediment sampled obtained at GS1. The situation at GS2 was slightly more complicated. The lower probe was occasionally buried up until about the 14th August 2021. After this date, this was no longer the case. The higher probe gave very high quality data until the 6th August 2021 when there was an electronics failure in the probe. To the 6th August and with manual removal of errors in the lower probe, there was a correlation of R = 0.994. Thus, we used the higher probe until the 6th August and the lower probe from the 6th August, but for the latter, the data between the 11th and the 14th August needed some editing, before the occasional burial largely ended. This solution required two calibration curves, one for each probe. Of the 56 manual samples, 28 were coincident with reliable measurements of turbidity for the upper probe and 30 for the lower probe.

Calibration curves were fitted using robust regression using the iteratively-reweighted least squares (IRLS) method after Beaton and Tukey (1974) (also known as the bi-square method). The only difference to the Beaton and Tukey method is that we standardize the residuals for their leverage. For both stations in 2020 and 2021 we observed the relationship between turbidity and concentration to be linear as expected for the range of concentrations sampled given the probe specification, thus we fitted first order polynomials (y = ax+b, where y is the concentration [g/l] and x is the turbidity [NTU]). We determined confidence intervals for each fit. The results are shown in Table S2.2. The $R^2$ values are generally very high. The calibration also produces sensitivities of concentration to turbidity that reflect the probes used, noting that a probe with a higher sensitivity was used for the upper station at GS2 in 2020. The calibration curves were then combined with the cleaned turbidity data to estimate time-series of concentration ($C_i$, where $i$ is the time stamp). The confidence intervals were used to determine the uncertainty in concentration for each estimation ($\sigma_{C,i}$).

The instantaneous load was calculated for each time period as $Q_iC_i$, where $Q_i$ is measured following Supplementary Information 2.4.2. For each melt season under investigation, instantaneous load time series were truncated to fit that of bedload records to allow comparison between different data (see Supplementary Information 2.4.4). We applied a product rule (Taylor, 1997) to estimate the associated uncertainty ($\sigma_{QC,i}$) under the assumption that the errors are Gaussian and independent:

$$\sigma_{QC,i} = \pm Q_i C_i \left[ \left( \frac{\sigma_{Q,i}}{Q_i} \right)^2 + \left( \frac{\sigma_{C,i}}{C_i} \right)^2 \right]^{0.5} \qquad \text{Eq. S2.1}$$

Data concerning suspended sediment concentration and suspended loads in both melt seasons, as well as associated protocols are available in Mancini et al. (2023b).

### 2.4.4 Seismic data collection, basics of the Fluvial Model Inversion (FMI) and calibration approaches

To infer bedload transport rates we installed two passive seismic stations, one in close proximity to GS1 at about 330 m from the glacier terminus and another one close to GS2 at

the forefield outlet (Figure 2.1). Each station was equipped a DiGOS DATA-CUBE type 2 logger and three 3-components PE-6/B geophones deployed in a triangular array with two geophones located at a safe distance from the proglacial stream (3 to 5 m) and another one more spaced out of ca. 70 m towards the valley sidewall (Dietze et al., 2019b). Loggers were set to collect data at a sampling frequency of 400 Hz and to have an amplifier gain of 32. Geophones were buried between ca. 0.3 m and 0.5 m in the ground to reduce noise associated with wind and rainfall events. The precise synchronization of the seismic records was achieved via a BY-GPS-07 GPS antenna connected directly to loggers. For both stations, the system was powered by two 9V/200 Ah super-alkaline batteries stored into thermically-isolated plastic boxes.

Seismic data were post-processed to quantify bedload transport rates using the geophysical inversion model of Dietze et al. (2019a), available in the open source R package *eseis* v. 0.5.0 (Dietze, 2018). The principle consists of comparing the measured seismic spectra to a set of pre-calculated simulations of physical models predicting the spectra of fluvial turbulence and bed sediment transport. Both models are essentially based on the general equation describing a seismic signal given in Eq. S2.2 (Aki and Richards, 2002; Burtin et al., 2016; Bakker et al., 2020):

$$u(f,x) = 2\pi f F(f,x_0)G(f,x,x_0)$$   Eq. S2.2

Where:

$u(f,x)$ = seismic signal ground velocity at frequency f and at a distance x from the source
$F(f, x_0)$ = Fourier transform of the magnitude at a given temporal period t
$G(f,x,x_0)$ = Green's function converting force to ground velocity and describing the frequency-dependent wave attenuation related to proprieties of the medium through which the seismic waves have passed. Under the assumption that seismic forces impact orthogonal against the seismic device and that Rayleigh surface waves are the main excited waves, G can be expressed as (e.g. Sanchez-Sesma et al., 2011):

$$G(f,x,x_0) = \frac{k}{8p_s v_p v_g}\sqrt{\frac{2}{\pi k r}}e^{-\pi f r}/(v_g Q)$$   Eq. S2.3

Where:

$p_s$ = volumetric mass density of the medium [kg/m$^3$]
$v_p$ = seismic wave phase velocity at $f_0$ [m/s]
$v_g$ = seismic wave group velocity [m/s]
$k$ = angular wavenumber ($k = 2\pi f/v_c$)
$r$ = distance seismic source-receiver ($|x-x_0|$) [m]
$Q$ = quality factor [-]

The FMI takes into account the two physical models to describe the seismic signals generated by water turbulence (Gimbert et al., 2014) and the motion of bedload particles on the riverbed (Tsai et al., 2012). These rely on a set of 15 constant site-specific parameters describing the sedimentological proprieties of bedload particles and of the fluid, the topography of the studied reach, the computational needs for the inversion and the seismic ground proprieties of the surveyed area (Table S2.3). However, these two physical models differ in terms of used seismic ground parameters: the turbulence model involves the use of only three parameters ($v_0$, $p_0$ and $p_0$), while the bedload one also includes that accounting for the quality factor increase with frequency ($e_0$).

Table S2.3: Input parameters describing the FMI and calibrated values for both seismic stations.

| | Parameter | Symbol | GS1 | GS2 |
|---|---|---|---|---|
| Sedimentological and fluid proprieties | $D_{50}$ bedload grain diameter [m] | $d_s$ | 0.08 | 0.04 |
| | Grain diameter standard deviation [log m] | $s_s$ | 1.1 | 1.4 |
| | Sediment density [kg/m³] | $r_s$ | 2650 | 2650 |
| | Fluid density [kg/m³] | $r_w$ | 1040 | 1040 |
| Topography | Average channel width [m] | $w_w$ | 10 | 8 |
| | Channel slope [rad] | $a_w$ | 0.03 | 0.02 |
| | Distance river center to sensor [m] | $r_0$ | 10 | 11 |
| Computational | Reference frequency [Hz] | $f_0$ | 1 | 1 |
| | Model frequency range [Hz] | $f$ | 20-70 | 20-90 |
| Seismic ground proprieties | Material quality factor at $f_0$ [-] | $q_0$ | 32.84 | 32.14 |
| | Rayleigh wave phase velocity at $f_0$ [m/s] | $v_0$ | 197 | 4550.9 |
| | Variation coefficient for $v_0$ [-] | $p_0$ | 0.43 | 0.95 |
| | Q increase with frequency [-] | $e_0$ | 0.02 | 0.004 |
| Variables | Bedload flux [kg/ms] | $q_s$ | 0.001 - 10 | 0.001 - 10 |
| | Water depth [m] | $h_w$ | 0.3 - 1 | 0.3 - 1 |

These parameter values were quantified directly in the field, or extracted from previous studies, as was the case for both sediment ($r_s$) and fluid ($r_w$) densities which were retrieved from Dietze et al. (2019a). The three parameters describing the topography of the seismically monitored stream reaches ($w_w$, $a_w$ and $r_0$) were quantified using dGPS measurements, while the computational ones are set according to conventional seismic rules ($f_0$) and quality of the collected data ($f$). This latter parameter was determined looking at the shape of the empiric spectra recorded in periods having different hydraulic conditions in terms of water stage and bedload transport rates. The median diameter of moving bedload particles ($d_s$) and their standard deviation ($s_s$) were quantified using a log-"raised cosine" distribution function following Tsai et al. (2012) to take into account the disproportionately large effect of larger grain sizes that have on the signal compared to smaller ones because of the higher vertical impact velocity when they are moving (hopping) in contact with the riverbed. To deal with this, a log-"raised cosine" function is fitted to in-situ measured grains to derive a probabilistic grain size distribution. This is defined as:

$$\hat{p}(x; d_s, s_s) = \frac{1}{2s_s}\left[1 + \cos\pi\left(\frac{x-d_s}{s_s}\right)\right] \qquad \text{Eq. S2.4}$$

Where:

$\hat{p}$ = probabilistic log-"raised cosine" distribution

$d_s$ = measured mean grain size

$s_s = \sigma_g / \sqrt{\frac{1}{3} - \frac{2}{\pi^2}}$ (where $\sigma_g$ is the measured grain size standard deviation)

In practice, this procedure involves the sorting of the collected grain size data (in our case obtained through the Wolman count technique on the riverbed in proximity to the seismic station) into several volumetric classes according to their b-axis which is then compared to a series of probabilistic log-"raised cosine" distributions were built using an iterative model (n = 10,000) applied to Eq. S2.4 involving different possible μ and s values. The log-"raised cosine" distribution having the lowest RMS error with the empirical data is kept and the associated μ and $\sigma_g$ values are used into the FMI (Table S2.3).

The seismic ground properties are used in the Green's function (Eq. S2.3) and they describe the way in which seismic waves propagate through the ground ($v_0$ and $p_0$), and the attenuation imposed by the medium on the carried seismic magnitude ($q_0$ and $e_0$). Following Tsai et al. (2012) and Bakker et al. (2020) these two sets of parameters are defined, respectively, by Eq. S2.5 and Eq. S2.6.

$$v_g = v_0 f^{-p_0}/(1 + p_0)$$

Eq. S2.5

Where:

$$v_g = v_p/(1 + \varphi)$$
$$v_p = v_{p0}(f/f_0)^{-\varphi}$$

$v_g$ = wave group velocity [m/s]
$v_p$ = wave phase velocity [m/s]
$\varphi$ = exponent used to quantify the frequency-dependency decay [-]
$f$ = frequency of ground motion fluctuation [Hz]
$f_0$ = reference frequency of 1 Hz

$$K = q_0(f/f_0)^{e_0}$$

Eq. S2.6

$K$ = quality factor at frequency f [-]
$q_0$ = quality factor at 1 Hz [-]
$f$ = frequency [Hz]
$f_0$ = reference frequency [Hz]
$e_0$ = exponent defining the frequency dependency of K with distance [-]

Seismic ground parameters values are commonly determined by an active survey performed in the area under investigation (Bakker et al., 2020; Lagarde et al. 2021; Antoniazza et al., 2023). In this study, we developed an alternative way largely based on a Generalized Likelihood Uncertainty Estimation (GLUE) approach allowing to calibrate these unknown parameter values statistically. We test the method for seismic station GS1 and we validated model outputs by comparing them to those issued from an active survey in order to justify its application to GS2, where the topographical constrains do not permit the collection of active seismic data.

The GLUE model is a statistical method for quantifying the uncertainty of model predictions (Beven and Binley, 1992, 2014). Given an un-calibrated model having large potential parameter ranges and at least one observation relative to the object for which the model was built for, GLUE allows to find a set of plausible values minimizing the difference between the prediction and the observation. In practice, we defined plausible parameter ranges using the *gui_model* function, a graphical user interface allowing to investigate FMI sensitivity to changing parameter values available in the *eseis* package. Following Dietze et al. (2019a), once all constant parameters representing the sedimentological and morphological characteristics of the study area are determined (Table S2.3), the *gui_model* allows exploration the meaningful seismic ground parameter space by interactively changing their values to define synthetic spectra until they match the overall shape of an empirical one observed at a specific temporal period $t_i$ of which at least one observation between bedload flux or water stage rate is known a priori (we used independent measurements issued from the closest water pressure sensors; Figure 2.1). To constrain parameter ranges we exploited the fact that the two physical models (i.e. water turbulence and bedload flux) differ by just one parameter: the quality factor increase with frequency ($e_0$). At first, the turbulence model was run in a Monte

Carlo simulation (n = 10,000) for several $t_i$ having no bedload transport letting randomly vary the three seismic ground parameters ($v_0$, $p_0$ and $p_0$) within previously determined ranges. The obtained synthetic seismic spectra are compared to the empirical ones recorded at $t_i$ and their affinity is determined through RMS errors. For each comparison the best 100 simulations were retained and final parameter values are quantified averaging them. The issued values were used in the bedload model. The same approach described above was applied but this time considering as reference spectra those recorded during period having bedload transport (i.e. spectra coinciding with the highest water stages) and letting vary exclusively the seismic ground parameter $e_0$ into the Monte Carlo simulation.

The active seismic survey consists of producing artificial seismic sources to study how the geological proprieties of the area under investigation influence seismic waves propagation velocities and how they attenuate the carried energy. To do that, we followed best practices described in Bakker et al. (2020), dividing the active tests into two parts. The used procedure for the collection of active seismic data is detailed in Supplementary Information 2.4.5. In both cases, artificial seismic sources were generated by hitting a metal plate (ca. 30 cm x 30 cm x 1 cm having a mass of about 20 kg) with a sledgehammer. The first part (AS1) is dedicated to the determination of seismic ground propagation velocities per frequency band, an information described by parameters $v_0$ and $p_0$ (Eq. S2.5). The vertical component of the collected raw seismic signal was deconvolved, detrended, bandpass filtered for 50% overlapping intervals of 6 Hz (i.e. 1 to 120 Hz) and, finally, bounded using a Hilbert transform envelope. Sledgehammer impact arrivals were detected for each frequency band and, by knowing the source-to-geophone distances and the manually obtained time delays of seismic peak arrivals between the seismic source and the sensors, they were used to generate a wave group velocity dispersion curve of which best fitting line follows Eq. S2.5. In the second part of the active survey (AS2), the influence of the ground in attenuating seismic magnitude was determined through quantification of parameters $q_0$ and $e_0$ (Eq. S2.6). It was necessary to evaluate how seismic spectra evolve with an increasing distance r from an artificial seismic source. Collected raw data were post-processed using the same approach mentioned above to decompose the seismic spectra into several frequency bands. Following Bakker et al. (2020), resultant frequency-based spectra were normalized (Eq. S2.7) in order that quality factor values associated to each frequency band can be extrapolated from the Green's equation.

$$\frac{Pr}{(Pr)_{min}} = \frac{a(f)}{(Pr)_{min}} e^{-2\pi f r/(v_g K)}$$ 

<div align="right">Eq. S2.7</div>

Where:

$$a(f) = \left[\frac{\pi f F k Z}{4 \rho_s v_p v_g}\right]^2 \frac{2}{\pi k}$$

P = seismic magnitude [$m^2$ $s^{-2}$ $Hz^{-1}$]
r = source-to-geophone distance [m]
f = frequency [Hz]
a = constant and frequency-dependent variables included in the Green's equation
K = quality factor at 1 Hz [-]
F = impact force (kgm/s)
Z = amplification factor [-]
k = angular wavenumber [rad/m]
$\rho_s$ = rock density [$kg/m^3$]
$v_p$ = wave phase velocity [m/s]
$v_g$ = wave group velocity [m/s]

We then fitted the seismic power decay with distance following Eq. S2.6 to retrieve seismic ground parameters $q_0$ and $e_0$.

FMI calibration for both GS1 and GS2 was based on 2020 data. As the seismometers remained in the same exact location for the two melt seasons, parameters values shown in Table S2.3 are then also be applied to invert seismic records collected in 2021.

Once the FMI was calibrated, the inversion process to convert seismic date into bedload flux and water stage was applied, as schematically shown in Figure S2.2 (Dietze, 2018). First, the raw vertical component of the seismic records for the entire period of investigation measured at geophones A (Figure 2.1) was deconvoluted, detrended and finally clipped according to a pre-defined time step $t_i$ (3 minutes in our case) in order to be converted into the frequency domain to produce a series of observed seismic spectra (step 1 in Figure S2.2). Second, the two physical models describing the seismic activity related to flow turbulence (Gimbert et al., 2014) and bedload transport (Tsai et al., 2012) were used into a Monte Carlo simulation to produce a series of synthetic spectra describing different potential seismic conditions occurring in the monitored river reach that serve as a lookup table during the inversion process (Step 2 in Figure S2.2). This was achieved keeping all parameters values constant, but allowing for random variation of the two unknown parameters of interest (i.e. bedload flux and water depth) within pre-defined possible ranges (Table S2.3). As bedload transport is an unsteady variable over time, to enhance the representation of all possible seismic conditions that may have occurred, the FMI allows production of synthetic spectra with and without bedload transport. The inversion is then computed by comparing the observed and the synthetic spectra: for each spectrum measured at time $t_i$, the synthetic one having the lowest RMS error is kept and the associated instantaneous bedload flux and water depth values are retrieved from the lookup table (steps 3 and 4 in Figure S2.2).
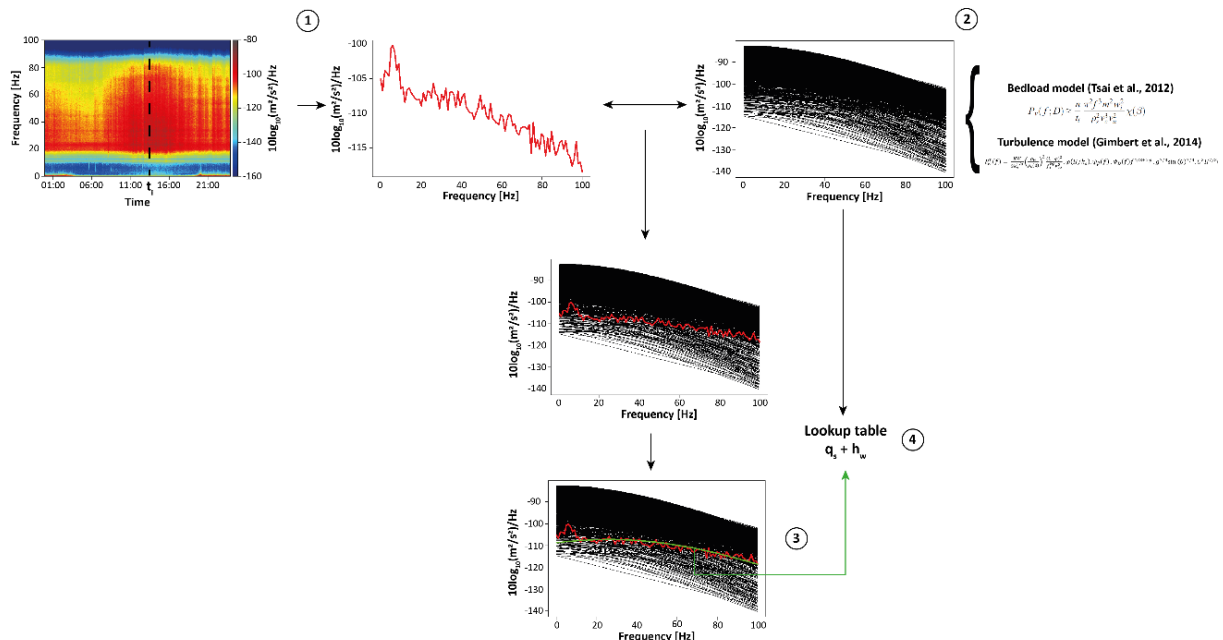


Figure S2.2: Schematic view of the inversion method implemented into the FMI: (1) extraction of empiric spectra according to time step $t_i$; (2) generation of synthetic seismic spectra using the turbulence (Gimbert et al., 2014) and the bedload (Tsai et al., 2012) model using parameter values found in Table S2.3; (3) identification of best fit synthetic spectra; and (4) extraction of bedload flux and water stage quantifications associated to retained best fit synthetic spectra for every $t_i$.

Inferred bedload transport rates were cleaned from potential interferences with unwanted seismic sources such as anthropogenic noise (e.g. hikers and operator footsteps, as well as seismic noise generated by other scientific activities taking place in the forefield) and other geomorphic processes (e.g. mass movements) occurring on adjacent hillslopes. We investigated the source of every single transport peak to be sure that they were effectively related to riverine processes. We extracted the temporal occurrence of these events and we localized the seismic source by applying the *signal_migrate* function (also available in the *eseis* R-package; Dietze, 2018) thanks to our triangular array of geophones used at each monitoring station (Figure 2.1). This allowed us to sort the signal into two origins: if the estimated source was located into or close to the nearest channel we kept the inversion result, in the opposite case we discarded it. Then, we also discarded results matching with the occurrence of strong seismic activates exciting the entire range of considered frequencies in power spectral density plots as due to activities occurring in close proximity to geophones (e.g. wild animals) re-interpolating bedload flux timeseries using a moving mean operator (window size of 20 elements). Finally, bedload flux estimations in kg/ms are converted into kg/s multiplying them by the average channel width (Table S2.3).

To improve the comparison between data, inverted bedload fluxes were resampled to the same sampling frequency of discharge and suspended sediment flux records (i.e. 2 minutes) and clipped in a way that they covered the same temporal length ($8^{th}$ of July (Julian day [jd] 191) to the $21^{st}$ of August (jd 234) for 2020; $14^{th}$ of June (jd 165) to the $22^{nd}$ of August (jd 234) for 2021).

As the main parameters controlling FMI performance are those describing seismic ground proprieties, bedload flux uncertainty was assessed using Latin Hypercube Sampling (LHS; McKay, 1992) applied to $q_0$, $v_0$, $p_0$, $e_0$ and $s_s$ parameters. This method consists of randomly sampling within a hypercube (i.e. a cube with dimension greater than 3) having the same dimensions of the investigated variables, in our case four, in a way that every combination of parameter value can be sampled only once. Ground seismic parameter ranges are based on both mean and standard deviation of the best 100 simulations used to define final parameter values, while that for $s_s$ is defined as the standard deviation obtained from the probabilistic log-raised cosine function. We generated a total of 1000 possible combinations and we classified ground seismic parameter sets according to a normal distribution in 5 different classes of standardized lengths for each parameter space. A total of 20 possible combinations (5 per parameter, one per each class associated to a specific $s_s$ value) are selected and implemented into the FMI to produce several time series of bedload flux. Each set of inversion took about two weeks for a whole melt season on a high performance computer, and this justifies our choice to limit the total number of inversions. To assess whether or not this was sufficient, we looked at the ranges of predictions for these 20 inversions. In all cases the inversion with the optimized parameter set fell with the range of the 20 uncertainty inversions. However, these included some parameter sets with poor fit to the reference spectrogram. Thus, we used the RMSE fit to the reference spectrogram to identify the best 5 inversions and then we took for each time period the highest and lowest inverted bedload transport rate. These optimized transport rate fell within the range defined by the maxima and minima for GS1 in 2020 and 2021 and GS2 in 2020, and thus they were deemed as behavioral and providing a basic uncertainty estimation. For GS2 in 2021 the optimized transport rate was higher than the maximum and so for that time series we considered the best 6 inversions.

Continuous bedload flux data at GS1 and GS2 with associated uncertainties are available in Mancini et al. (2023b).

## 2.4.5 Parametrization of sedimentological and seismic ground proprieties for the upstream (GS1) seismic station

The upstream station (GS1; Figure 2.1) is located at ca. 330 m from the glacier terminus on a bedrock outcrop covered by a thick layer (> 0.5 m) of morainic deposits composed of sediment ranging from fines to boulders. The monitored proglacial river reach was characterized by similar sedimentological proprieties and it appears stable as the riverbed was shaped by a highly armored surficial layer.

The probabilistic grain size distribution is applied to 345 *in situ* collected grain b-axis data. These are sorted into 12 granulometric classes (< 0.5 mm, 0.5-8 mm, 8-38 mm, 38-88 mm, 88-136 mm, 136-192mm, 192-280 mm, 280-400 mm, 400-550 mm, 550-700 mm, 700-900 mm and > 900 mm) and the best-fit raised-log cosine function (Eq. S2.4) was fitted to the empirical samples as shown in Figure S2.3. In this case we found that the best-fit raised cosine function was characterized by a D50 of 0.08 m and a σ of 1.1 (Table S2.3).
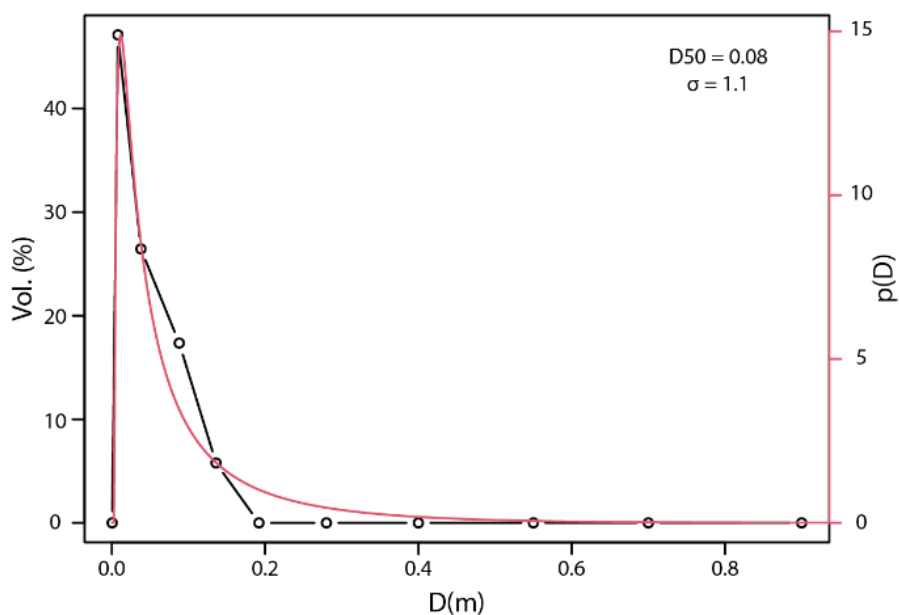


Figure S2.3: Best fit log-raised cosine function for grain size collected near to seismic station GS1.

FMI calibration started with the determination of the model frequency range (f, Table S2.3). Looking at empiric spectra collected at different water stage conditions, and consequently different bedload flux rates, it is evident that their shapes are divergent especially in the 25-90 Hz range (Figure S2.4). The spectrum recorded at low flow condition is characterized by an abrupt decrease in seismic power from about 25 Hz, while that for high flow condition shows a slight and more gradual decline with frequency. These differences are in line with findings of Schmandt et al. (2017) stating that frequency ranges between 20-100 Hz are typically linked to bedload transport at those distances, whereas < 20 Hz are rather correlated to water turbulence. Given this, we decided to focus our analysis on the frequency range comprised between 20 and 70 Hz.

Figure S2.4: Seismic spectra recorded during low (0.35 m on the 1$^{st}$ September 2020 at 11 am, red solid line) and high (0.80 m on the 23$^{rd}$ July 2020 at 6 pm, green solid line) water stage conditions in GS1.

Seismic ground proprieties ($q_0$, $v_0$, $p_0$ and $e_0$) were calibrated using the GLUE approach and then combined with results issued from the application of an active seismic survey (see Supplementary Information 2.4.4).

In the GLUE model, once all possible parameter ranges were identified in the *gui_model* environment, we ran the turbulence and the bedload models independently in a Monte Carlo simulation (n = 10,000) letting varying the involved seismic ground parameters within previously determined limits (Table S2.3) following the methods described in Supplementary Information 2.4.4. The turbulence model was applied to seismic data recorded in four periods $t_i$ during the lowest water stage conditions (0.38 m, 0.37 m, 0.36 m, and 0.35 m measured at, respectively, 01:40 am, 04:40 am, 07:40 am and 11:00 am on the 1$^{st}$ of September 2020), in which field observations confirmed the absence of bedload transport. In contrast, for the bedload model we used empiric seismic spectra issued from five temporal periods $t_i$ occurring at the highest water stage conditions (0.74 m, 0.75 m, 0.76 m, 0.79 m and 0.80 m at, respectively, 02:00 pm, 03:00 pm, 04:00 pm, 05:00 pm and 06:00 pm on the 23$^{rd}$ July 2020). Figure S2.5 shows the dot plots of possible seismic ground parameter ranges and associated RMSE for both turbulence (Figure S2.5a to Figure S2.5c) and bedload model (Figure S2.5d).
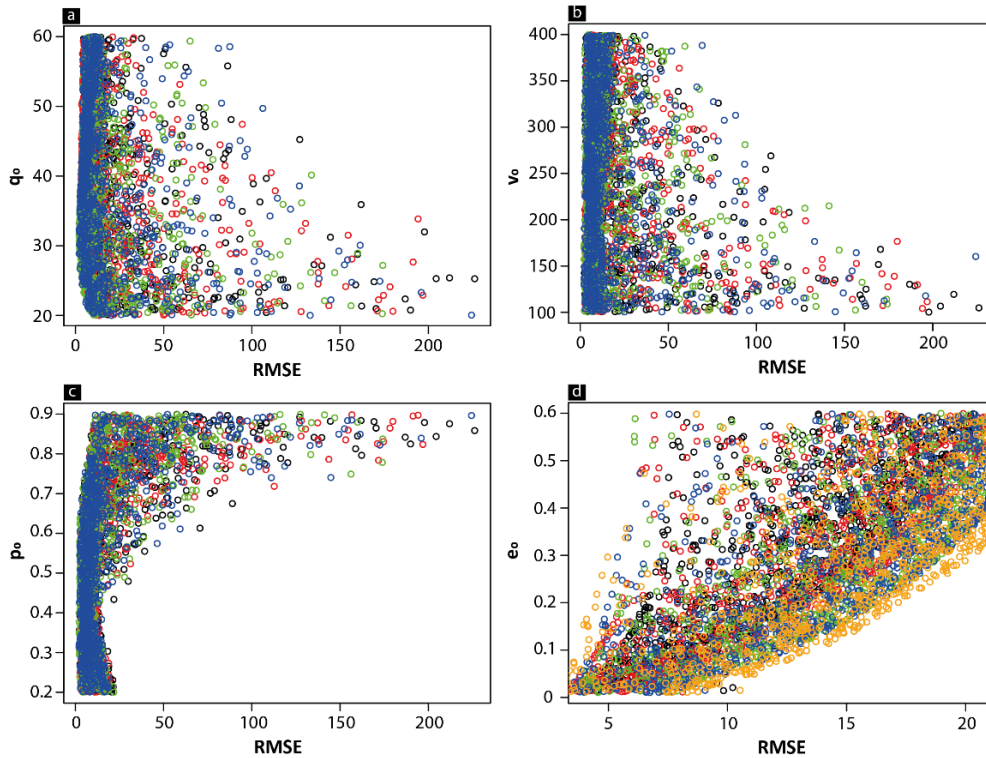
Figure S2.5: Dot plots showing the GLUE model results for each seismic ground parameter (Table S2.3) – a to c refers to the GLUE model apply to the turbulence model (Gimbert et al., 2014) and d to the bedload model (Tsai et al., 2012). Colors refers to the water stages considered for the analysis. In a to c 0.38 m (01:40 am, black), 0.37 m (04:40 am, red), 0.36 m (07:40 am, blue), and 0.35 m (11:00 am; green) measured on the 1st of September 2020. In d 0.74 m (02:00 pm, black), 0.75 m (03:00 pm, red), 0.76 m (04:00 pm, blue), 0.79 m (05:00 pm, green) and 0.80 m (05:00 pm, orange) on the 23rd July 2020 in GS1 (Figure 2.1).

As shown in Table S2.4, the GLUE model allowed to quantify $q_0$ as 33.04, $v_0$ as 212.16, $p_0$ as 0.43 and finally $e_0$ as 0.03.

Table S2.4: Possible seismic parameter ranges used into the GLUE model and best values for GS1. In brackets the respective standard deviation.

| | gui_model | GLUE model | |
|---|---|---|---|
| Parameter | | Turbulence model | Bedload model |
| $q_0$ | 20 - 60 | 33.04 (± 2.27) | - |
| $v_0$ | 100 - 400 | 212.16 (± 78.92) | - |
| $p_0$ | 0.2 - 0.9 | 0.43 (± 0.11) | - |
| $e_0$ | 0.01 - 0.60 | - | 0.03 (± 0.11) |

We then compared the obtained quantifications with independent results issued from the application of an active seismic survey performed on the 1st of July 2020 to validate those coming from the statistical approach. In AS1, we assessed the propagation velocity of seismic waves into the ground ($v_0$ and $p_0$) deploying two seismic stations (SC1 and SC2) composed of one DATA-CUBE type 2 and one 3-component PE-6/B geophone following a linear array in the middle of the forefield: seismic station SC1 was installed 1 m from the proglacial stream, while SC2 was located 75 m away and perpendicular to the local centerline of the main channel (Figure S2.6). The choice to undertake the survey far from the location of GS1 is due to the presence of similar sedimentological proprieties combined with less rough topography making

the test easier to undertake. We generated 10 artificial hammer blows at both ends of the seismic array measuring the position of each station with a differential GPS.
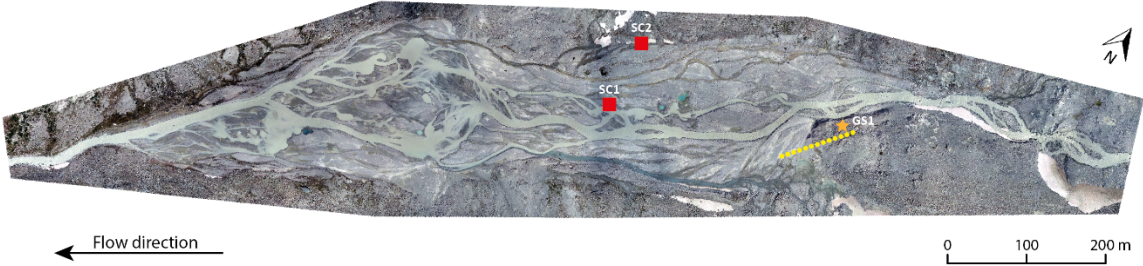


Figure S2.6: Location of the active seismic surveys to define seismic ground parameter values for seismic station GS1. SC1 and SC2 refers to the location of geophones used for AS1 ($v_0$ and $p_0$). Orange star refers to the permanent location of seismic station GS1, while yellow dots to the location of the artificial seismic sources used to define parameters $q_0$ and $e_0$ in AS2.

By knowing the seismic peak arrival times for each frequency band and the distance between the two stations, we generated a wave group velocity dispersion curve in which the best fit line follows Eq. S2.6 (Figure S2.7). Due to the high attenuation associated with braidplain deposits, and with the 75 m separation, we were only able to retrieve the magnitude peaks for frequency bands between 1 and 28 Hz. In our specific case we quantified $v_0$ as 201 and $p_0$ as 0.51, while Tsai et al. (2012) and Bakker et al. (2020) found higher values of, respectively, 680 and 1295 for $v_0$ and 0.31 and 0.374 for $p_0$ (Figure S2.7).
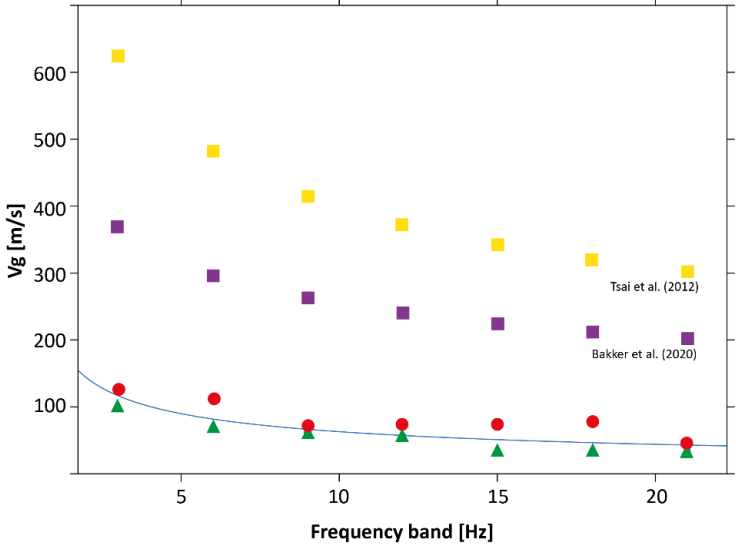


Figure S2.7: Relationship between wave group velocity and frequency band used to define seismic ground parameter $v_0$ and $p_0$. Green triangles are results issued from the active survey having the origin of artificial seismic sources close to SC1, while red dots close to SC2. Blue solid line is the best fit line which equation (Eq. S2.5) defines $v_0$ and $p_0$. Yellow and purple squares show results found in, respectively, Tsai et al. (2012) and Bakker et al. (2020).

In AS2 we determined the seismic magnitude attenuation with distance producing 14 artificial seismic sources spaced from each other by 5 m (Figure S2.6) in the region surveyed by GS1. As for AS1, also for this test we used a differential GPS to measure the position of sledgehammer impacts to retrieve precise source-to-sensor distances. For each frequency band of interest, the Green's function (Eq. S2.3) is solved in function of K and averaged for all 14 sledgehammer impacts. The best fit line having the equation expressed in the form of Eq. S2.6 allowed to quantify both seismic ground parameters $q_0$ and $e_0$. However, it is important to

mention that in contrast to Bakker et al. (2020) in which the active survey was performed using a large rock in which the generated force is always constant, in our case it is logical to expect large differences in emitted seismic source magnitudes. This can strongly affect the calculation of the frequency dependency of K. To solve this issued we decided to proceed with the computation of $q_0$ and $e_0$ for different frequency ranges of interest (Figure S2.8). As expected, both $q_0$ and $e_0$ values are highly variable and consistently dependent on the frequency range of interest: $q_0$ may vary from 11 at the shortest considered frequency range (20-60 Hz) up to 23 for the largest one (0-100 Hz), while inversely $e_0$ may oscillate between 0.05 and 0.51.
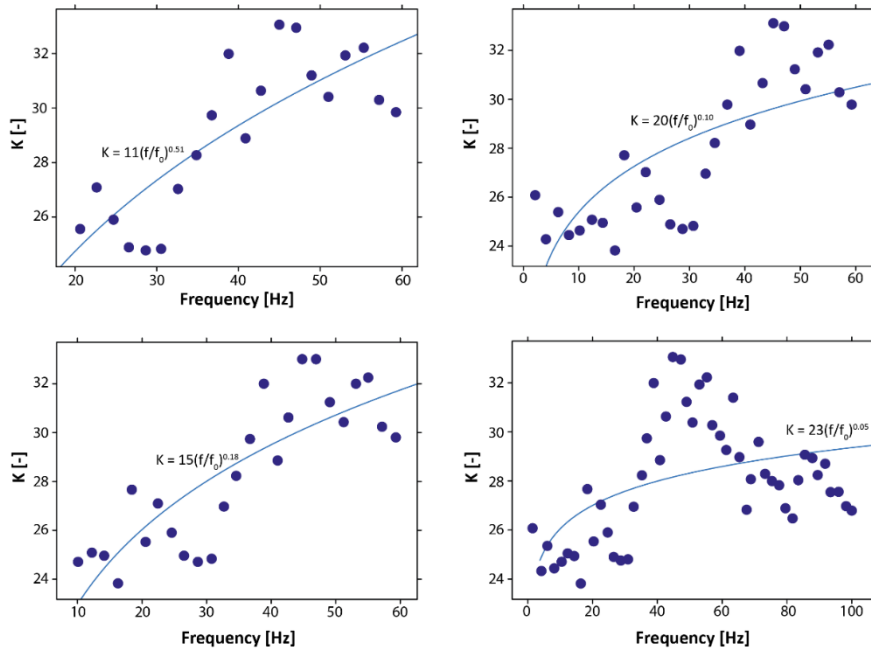


Figure S2.8: Relationship between quality factor and different frequency range of interest using data collected in AS2. Blue solid line is the best fit regression line defining $q_0$ and $e_0$ (Eq. S2.6).

Given the above, we decided to combine seismic ground quantifications issued from the GLUE model (Table S2.4) with those obtained from the active survey to further constrain possible parameter ranges into a second GLUE model. For seismic parameters $v_0$ and $p_0$ intervals were defined as ±20 and ±0.18 (i.e. double net difference between GLUE and active survey results) the value obtained from the active survey, while intervals for $q_0$ and $e_0$ were more arbitrary but largely based on the analysis of different frequency ranges of interest showed in Figure S2.8.

Table S2.5: Possible seismic parameter ranges used into the constrained GLUE model and final best values for GS1. In brackets the respective standard deviation used to compute the uncertainty using the LHS method (see Supplementary Information 2.4.4).

| Parameter | Active survey constrained GLUE model | |
| :---: | :---: | :---: |
| | Range (based on active survey) | Final value |
| $q_0$ | 10 - 36 | 33.02 (±1.23) |
| $v_0$ | 181 - 221 | 197.65 (±20.36) |
| $p_0$ | 0.42 - 0.60 | 0.43 (±0.02) |
| $e_0$ | 0.01 - 0.5 | 0.02 (±0.005) |

Table S2.5 shows seismic ground parameter quantifications issued from the active survey constrained GLUE model. Compared to *gui_model* based GLUE model (Table S2.4),

the constriction of possible ranges following the application of the active seismic survey largely impact $v_0$, with a final value dropping from 212 to 197, without having large effects on the other parameters. It is important to mention that the obtained low $v_0$ value may be related to a thick layer of loose sediment covering the underlying bedrock in the area surveyed in GS1.

We validated our final results in two ways: i) by comparing the inverted water stages with those issued from the water pressure sensor installed at the upstream station; and ii) by looking at the root-mean-squares error between the observed and the retained synthetic spectra during the inversion process.
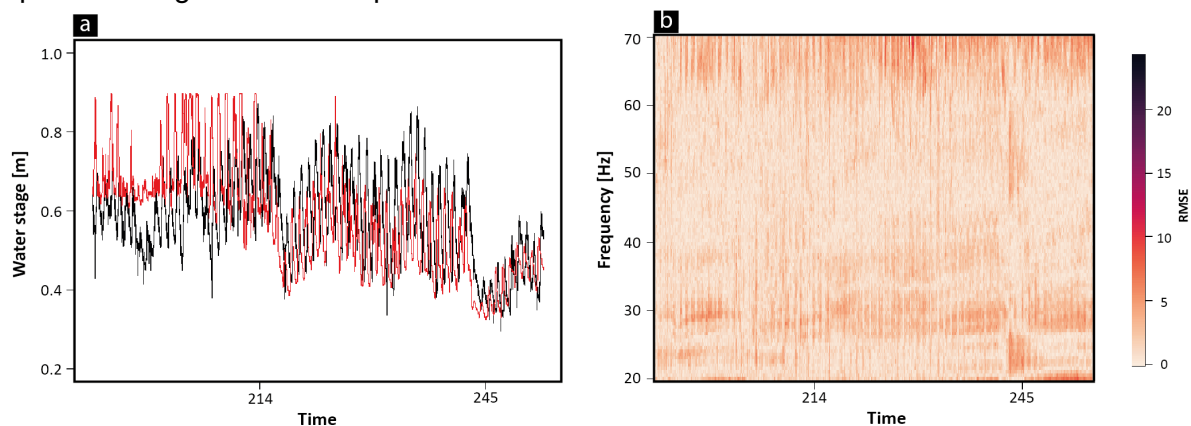


Figure S2.9: Evaluation of calibrated model for the inversion of seismic data collected in GS1. a) Comparison of measured (black) and seismically-inferred (red) water stage data, and b) root-mean-square errors of the difference between observed and retained synthetic spectra at each time t.

Figure S2.9a shows that the measured (GS1, Figure 2.1) and the seismically inferred water stage data are consistent especially from the end of July 2020, while previous estimations are divergent. A possible explanation of this difference may be attributed to a more intense phase of sediment transport involving the motion of coarse grains. Following Burtin et al. (2016), large grains excite low wavelength signals (i.e. low frequencies) which may have interfered with the frequency range related to flowing water influencing turbulence model outputs. Given this, the mean inversion error is ca. 1.5 dBs with only isolated peaks having values up to ca. 24.5 dBs (Figure S2.9b).

## 2.4.6 Parametrization of sedimentological and seismic ground proprieties for a control seismic station, GSG, in 2021

The above approach was further assessed by applying the same methodology to data collected by another non-permanent seismic station located at ca. 300 m upstream GS1 in direction of the glacier terminus (GSG; Figure S2.10) to see if the results were reproducible.
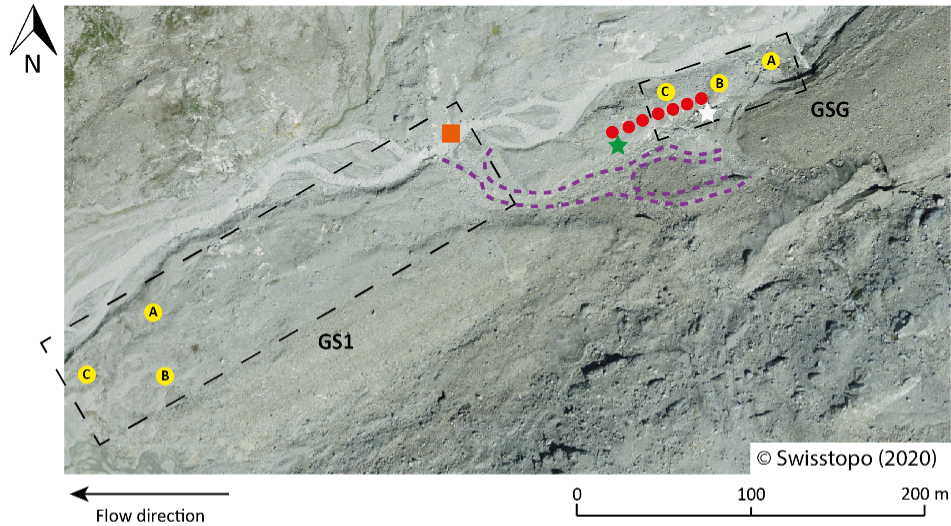
Figure S2.10: Location of GSG seismic station and seismic array used to perform the active survey. Stars are the locations of the temporary geophones used to quantify seismic parameters $V_0$ and $P_0$ (distance between geophones is 35 m; artificial seismic sources were generated close to the geophone marked in white); while red dots are artificial seismic sources allowing to quantify seismic parameters $Q_0$ and $E_0$ (every 5 m from the geophone highlighted in white). Purple dashed line is the secondary proglacial channel reach which was active in summer 2021.

Compared to the calibration for GS1 station, in this case we reversed the order of the approaches used to define seismic ground parameter values. This was because due to the complex topography where GSG was installed it was impossible to perform the active test installing the seismic array perpendicular to the stream as done for GS1. Consequently, additional potential seismic sources related to the flowing water may have influenced the test resulting in propagation of noises and high uncertainties into parameter value estimations. Thus, we constrained the GLUE model (n = 10'000) using possible values issued from the active survey letting vary their plausible ranges within intervals defined as ±x1.5 the value found using the active test (Table S2.6).

Table S2.6: FMI parameter values used to invert the seismic data into bedload flux and the different seismic ground parameters found using the active survey and the GLUE model approach.

| | Parameter | GSG | |
|---|---|---|---|
| | | Active survey | GLUE model |
| Sedimentological and fluid proprieties | $D_{50}$ bedload grain diameter [m] | 0.08 | |
| | Grain diameter standard deviation [log m] | 1.1 | |
| | Sediment density [kg/m³] | 2650 | |
| | Fluid density [kg/m³] | 1040 | |
| Topography | Average channel width [m] | 10 | |
| | Channel slope [rad] | 0.03 | |
| | Distance river center to sensor [m] | 20 | |
| Computational | Reference frequency [Hz] | 1 | |
| | Model frequency range [Hz] | 20-70 | |
| Variables | Bedload flux [kg/ms] | 0.001 - 3 | |
| | Water depth [m] | 0.25 - 1.3 | |
| Seismic ground proprieties | Material quality factor at $f_0$ [-] | 25.84 | 45.57 (±7.58) |
| | Rayleigh wave phase velocity at $f_0$ [m/s] | 2073.53 | 1850.66 (±54.79) |
| | Variation coefficient for $v_0$ [-] | 0.31 | 0.43 (±0.01) |
| | Q increase with frequency [-] | 0.18 | 0.02 (±0.02) |

Figure S2.11 shows the inverted seismic data issued in GSG (geophone A; Figure S2.10) compared to those issued in GS1 together with the associated spectra (see Supplementary Material 2.4.7). The two quantifications show very similar transport magnitudes for the entire period under investigation, especially from mid-July, with those collected at GS1 slightly higher than those in GSG (Figure S2.11a). The main reason may be related to the temporarily activation of an additional channel exporting a substantial amount of subglacial sediments, which was detected by GS1 but not by GSG (Figure S2.10). Despite this, the power spectra analysis plot for the two stations are identical highlighting that along the 300 m long straight reach the subglacial sediment export signal is conserved (Figure S2.11b and 2.11c). This makes sense as the channel between the two stations is confined by two bedrock outcrops where morphodynamic effects (i.e. erosion and deposition events) are occasional and limited to specific areas.
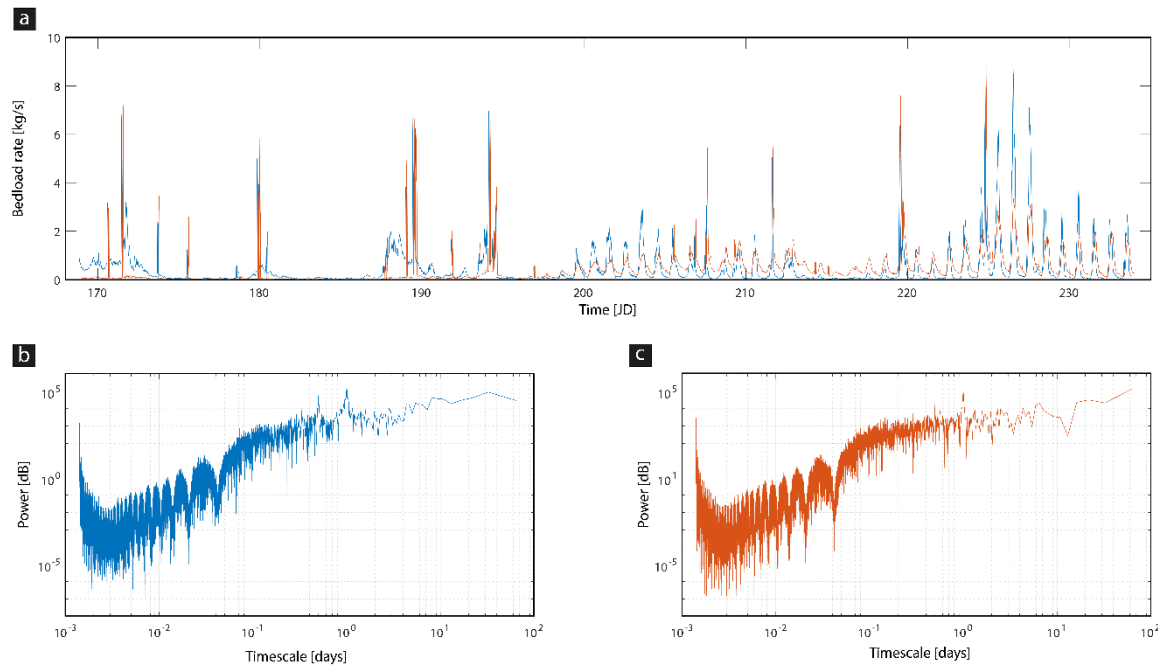


Figure S2.11: Bedload fluxes measured in GS1 and in GSG for the 2021 melt season (a) and associated power spectra (b and c). Blue solid line refers to GS1 data, while the orange line to GSG data.

### 2.4.7 Parametrization of sedimentological and seismic ground proprieties for the downstream (GS2) seismic stations

The downstream station was installed at the end of the proglacial forefield in a region characterized by a mixture of bedrock outcrops overlayed by a very thin layer of morainic deposits (< 0.2 m) and vegetated patches (GS1, Figure 2.1). Due to the fining of sediment along the proglacial margin, field observations suggest that the riverbed in the proximal river reach is less armored and mainly composed of sand and small gravel particles compared to the riverbed at the upstream station.

The probabilistic grain size distribution of grains composing the riverbed confirmed the above observations. We sorted all the 348 b-axis measurements into 12 classes (< 0.5 mm, 0.5-2 mm, 2-8 mm, 8-20 mm, 20-38 mm, 38-55 mm, 55-88 mm, 88-136 mm, 136-192 mm, 192-250 mm, 250-310 mm and > 310 mm) and applied Eq. S2.4 to retrieve both theoretic $D_{50}$ and σ that best fits the log-"raised cosine" function to the empiric grain sizes that we quantified as, respectively, 0.04 m and 1.4 (Figure S2.12).
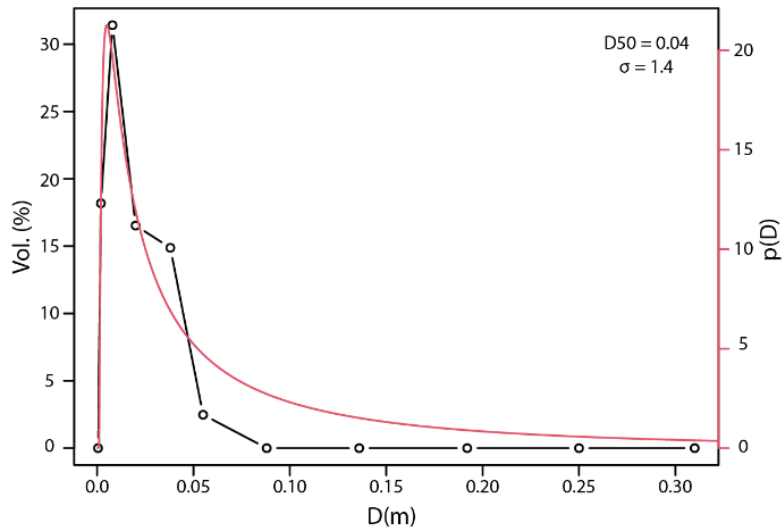
Figure S2.12: Best fit log-raised cosine function for grain size collected near to seismic station GS2.

Given the observations above, two major remarks can be made on FMI calibrations and on the computational needs to invert seismic data. First, as the surveyed area is geologically different from that in which the active survey has been performed, it is likely not possible to apply the same calibration results issued for the upstream station. Second, the characteristics of the riverbed suggest that for the same water discharge sediment transport at the end of the forefield tends to be continuous. This latter aspect is confirmed by direct field observations and also by spectra analysis issued during different flow conditions which, in contrast to the upstream site, are very similar in terms of shapes and magnitudes for different discharge rates (Figure S2.4 and Figure S2.13). Thus, following Burtin et al. (2016), to improve bedload transport quantification we decided to focus our analysis in the range comprised between 20 and 90 Hz to capture signals excited by the motion of sediment having a wide range of sizes.
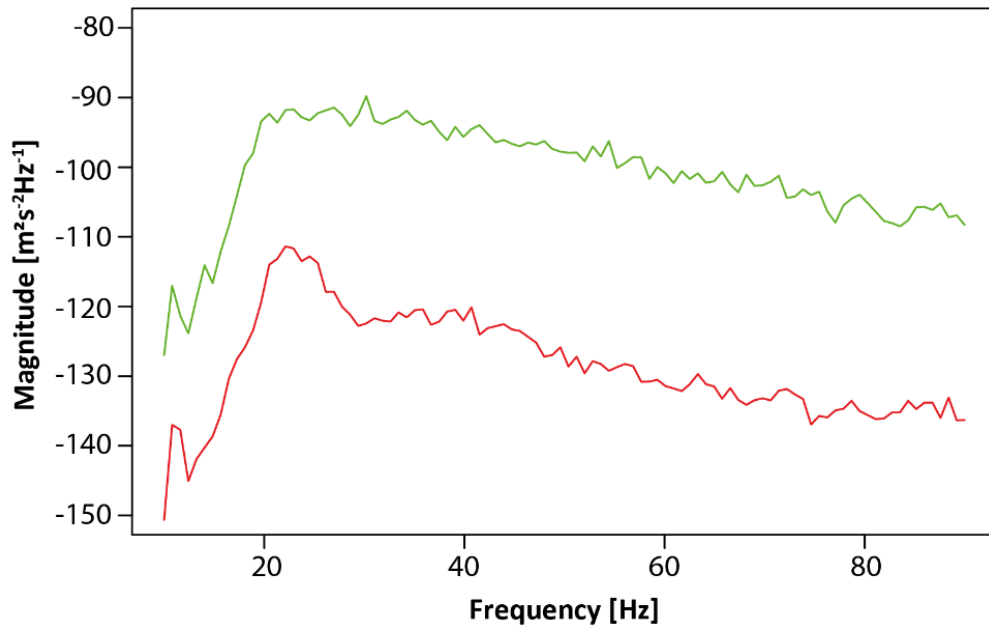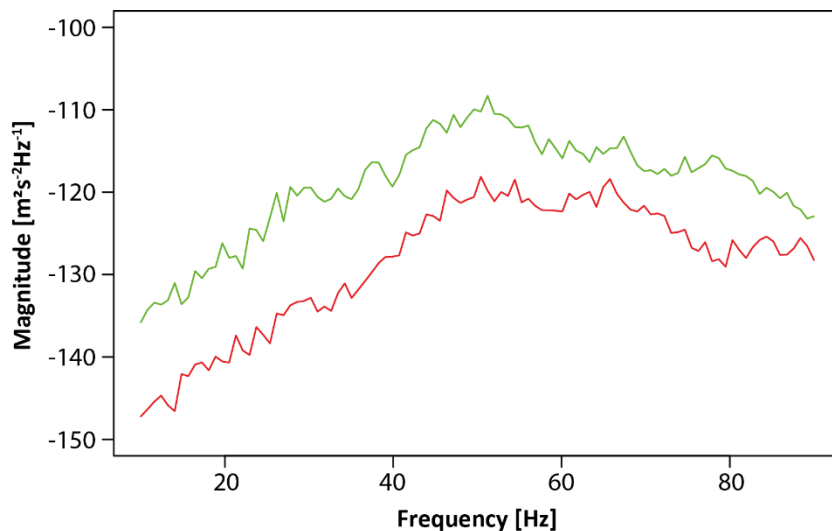


Figure S2.13: Seismic spectra recorded during low (0.35 m on the 3$^{rd}$ September 2020 at 6 am, red solid line) and high (0.75 m on the 27$^{th}$ July 2020 at 6 pm, green solid line) water stage conditions in GS2.

As sediment transport at the end of the forefield seems to be affected by different dynamics as compared to GS1, parametrization of seismic ground parameters cannot follow the same methodological approach (see Supplementary Information 2.4.5) because it is much more difficult to establish when transport is absent. To deal with it, we developed an alternative

way to calibrate the FMI still based on the GLUE model, but this time considering exclusively the bedload physical model (Tsai et al., 2012). In practice, given the water height of 0.35 m recorded on the 3$^{rd}$ of September 2020 at 06:00 am at GS2, we produced several synthetic seismic spectra to representing a variety of potential hydraulic conditions in a Monte Carlo simulation (n = 10'000) by setting possible seismic ground parameters values within large possible ranges identified in the *gui_model* environment (Table S2.7). At the same time, we also let iterate the bedload flux rate within 0 and 1 kg/ms to better represent potential noises coming from moving sediments in the synthetic spectra.

Table S2.7: Possible seismic parameter ranges used into the GLUE model (applied exclusively to the bedload model; Tsai et al., 2012) and best values for GS2 found constraining possible parameter ranges. In brackets the respective standard deviation used to compute the uncertainty using the LHS method (see Supplementary Information 2.4.4).

| Parameter | GLUE bedload model | | GLUE constrained model | |
|---|---|---|---|---|
| | Range (based on gui_model) | Final value | Range (based on bedload model) | Final value |
| $q_0$ | 1 - 50 | 30.43 (± 2.81) | 25 - 35 | 32.14 (±1.43) |
| $v_0$ | 100 - 5000 | 4421.74 (± 29.68) | 4300 - 4800 | 4550.94 (±31.62) |
| $p_0$ | 0.8 - 1.9 | 0.85 (± 0.96) | 0.8 - 1.1 | 0.96 (±0.022) |
| $e_0$ | 0 - 1.5 | 0.14 (± 0.003) | 0 - 0.15 | 0.004 (±0.002) |

The empirical spectrum was then compared to the synesthetic ones and the one having lower RMS error was retrieved from the pool with the aim to constrain possible ground parameter ranges. The best fit synthetic spectrum had a RMS error of 3.06 given by $q_0$ as 30.43, $v_0$ as 4421.74, $p_0$ as 0.85 and $e_0$ as 0.14 (Table S2.7 and Figure S2.14).
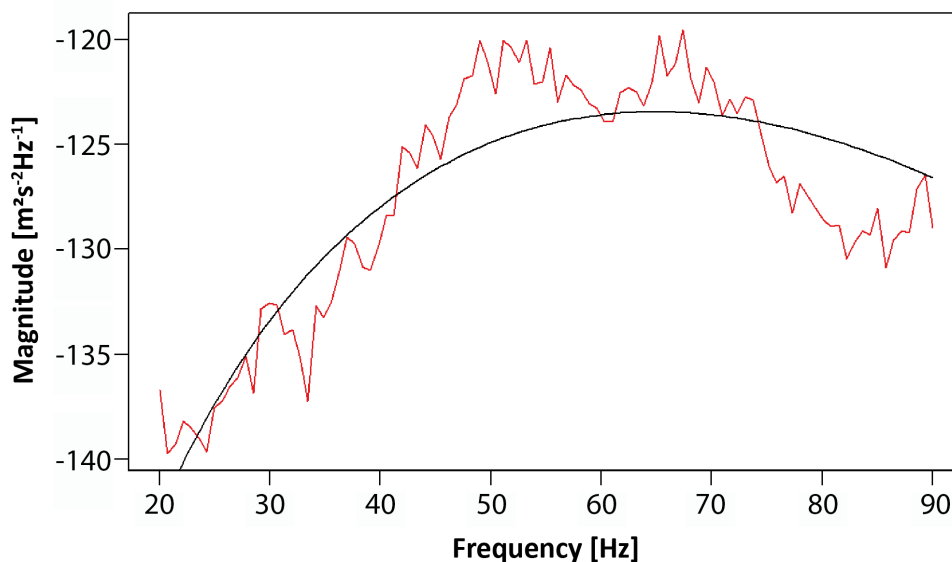


Figure S2.14: Empirical spectrum measured on the 3$^{rd}$ of September 2020 at 6 am at GS2 (red solid line) and best fit synthetic spectra issued from the constrained GLUE model (black solid line).

To increase the robustness of our results, we applied the same methodology described above to different measured water stages on the 27$^{th}$ July 2020 (0.35 m, 0.34 m, 0.33 m and 0.30 m recorded at 01:00 am, 02:00 am, 04:00 am and 08:00 am, respectively) iterating ground parameter values within constrained limits (Table S2.7). Figure S2.15 shows the obtained dot plot associated to each ground seismic parameter.
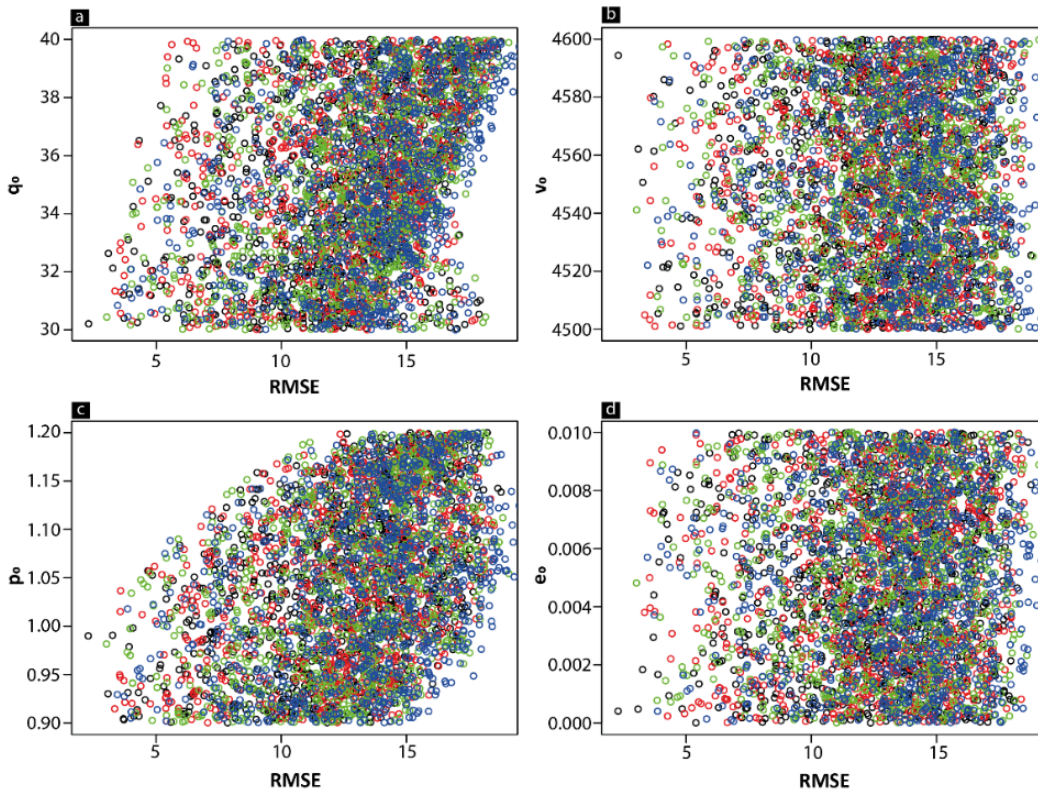
Figure S2.15: Dot plots showing the constrained GLUE model results applied to the bedload model (Tsai et al., 2020) for each seismic ground parameter. Colors refers to the water stages considered for the analysis: 0.35 m (01:00 am, black), 0.34 m (02:00 am, red), 0.33 m (04:00 am, blue) and 0.30 m (08:00 am, green) recorded on the 27th September 2020 in GS2 (Figure 2.1).

For each parameter, the first 100 simulations having the lowest RMS error were retrieved and final quantifications were performed averaging their values (Table S2.7): we quantified $q_0$ as 32.14, $v_0$ as 4550.94, $p_0$ as 0.96 and $e_0$ as 0.004. The obtained $v_0$ value for this location is much higher compared to that determined for GS1 (Table S2.3 and Table S2.5) and this can be explained by the thinner layer of loose gravel covering the underlying bedrock (Figure 2.1).

As for the upstream site, we validated our final results by comparing the inverted water stages with those issued from the water pressure sensor installed at GS2 (Figure 2.1), and by looking at the root-mean-squares error between the observed and the retained synthetic spectra during the inversion process.
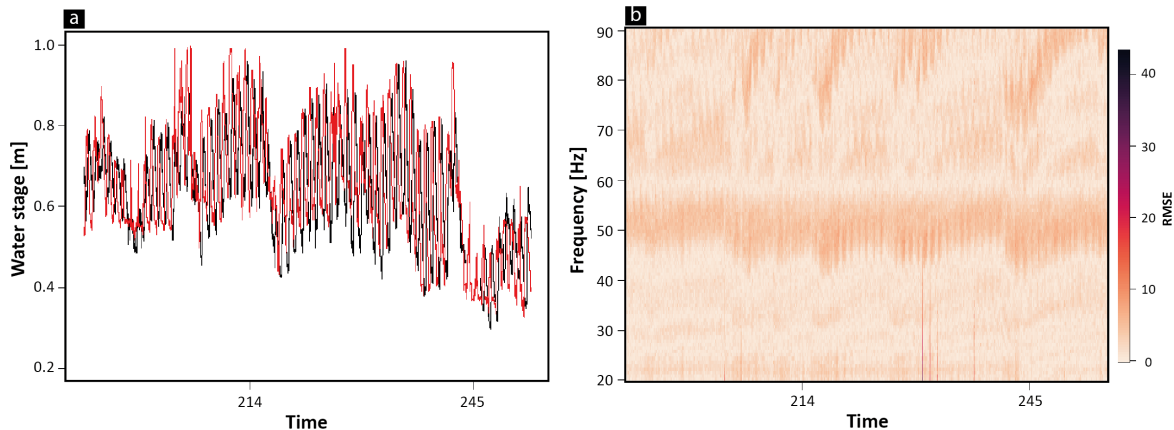


Figure S2.16: Evaluation of calibrated model for the inversion of seismic data collected in GS2. a) Comparison of measured (black) and seismically-inferred (red) water stage data, and b) root-mean-square errors of the difference between observed and retained synthetic spectra at each time t.

In this case, and in contrast to results issued from GS1, the inverted and the measured water stage data are much more similar and show the same temporal evolution for the entire period under investigation (Figure S2.16a). This is due to the finer size of sediment transported in this region consequently having less contribution to the observed spectra and on the general inversion. The mean inversion error is ca. 1.89 dBs with numerous spikes reaching values up to 43 dBs, a magnitude of error consistently higher compared to GS1 (Figure S2.16b). The filtering and the cleaning of the inverted data (see Supplementary Information 2.4.4) suggested that they are likely to be related to anthropic activities as this seismic station were located much closer to the main hiking path and to the base camp.

### 2.4.8 Modification of subglacially-exported suspended sediment and bedload signals by the proglacial forefield

The methodology used to detect the magnitude and the timescales of filtering operated by proglacial processes on subglacially-exported sediment transport signals, as well as the proglacial fluvial mechanisms responsible for it, is shown in Figure S2.17.
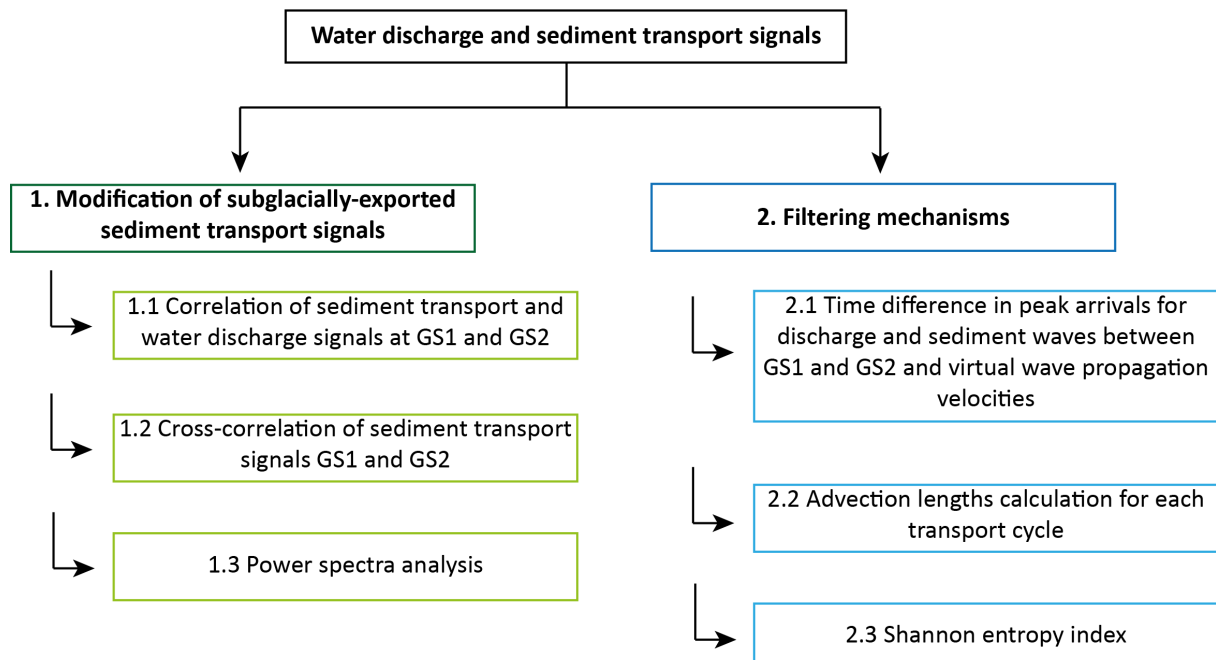
Figure S2.17: Methodology applied to the field collected data to quantify the morphodynamic effects, in terms of nature of the filtering (1.1 to 1.3) and fluvial mechanisms (2.1 to 2.3), on sediment transport signals.

All the analyses showed in Figure S2.17 were performed using instantaneous water discharge and sediment transport time series (Figure 2.2).

### 2.4.8.1 Magnitude, nature and timescales of the proglacial filtering

The modification of transport signals travelling though the proglacial forefield (point 1 in Figure S2.17) was investigated by combining three approaches:

1.1 Correlation of sediment transport signals with water discharge signals in GS1 and GS2 to define spatial differences in transport dynamics;

1.2 Cross-correlation of suspended sediment and bedload signals in GS1 and G2 to determine if the nature of the proglacial filtering operating on downstream sediment transport signals;

1.3 Power spectra analysis following modalities described in Jerolmack and Paola (2010) to the magnitude and timescales over which the filtering operates.

Analysis 1.1 allowed to establish if transport signals in GS1 and GS2 are affected by different behaviors or not, a first sign potentially reflecting the influence of morphodynamic effects on transport dynamics.

Analysis 1.2 define the nature of the filtering, and more in particular in which way it modifies the transport signals moving downstream the proglacial area (i.e. dampening, delaying or shredding). Results are shown in Figure 2.2b.

Finally, in analysis 1.3 we followed Jerolmack and Paola (2010) to investigate temporalities and magnitudes of the proglacial filtering on sediment transport signals. Time series of both instantaneous suspended sediment and bedload fluxes were converted from the time into their frequency domain by applying a Discrete Fourier Transform to produce spectral density plots at GS1 and GS2 (Figure 2.2c). Frequencies were then converted into timescale (days) by relating them to their sampling interval (i.e. 2 minutes; 0.00014 JD), while amplitudes were squared to convert them from complex number into powers ($10\log_{10}(kg/s)^2$, hence dB). We quantified the strength and the timescale over which the filtering operates by looking at the difference in shape between the upstream and the downstream spectra. If the proglacial forefield is acting as a non-linear filtering the spectrum have to be characterized by a slope higher than zero, with its steepness addressing the strength of the filtering on the signal itself (i.e. steeper slope means a more intense filtering effect). By looking at the evolution of the spectrum, in terms of its slope, over time it is thus possible to retrieve the timescales over which the filtering operates and the associated magnitudes.

However, given the above, to define the periodicities affected by the filtering, it is also important to take into account the relation between the characteristic period of the system $T_x$ (here intended as the time needed to morphodynamic processes to completely modify the export signals, which in turn depends on both system size and input rates) and the period T of the environmental signal (i.e. daily cycle of sediment evacuation) (Jerolmack and Paola, 2010). Two scenarios may be observed:

1. if $T > T_x$ the sediment evacuation signal is recorded at the outlet of the system as the sediment transport is quasi-steady and it responds directly to the boundary-conditions, but it can be attenuated or damped;
2. if $T < T_x$ the input signal is completely shredded unless if the magnitude of the perturbation is very large.

## 2.4.8.2 Filtering mechanisms responsible for the filtering

To investigate modalities by which proglacial morphodynamics interferes with the transmission of the subglacial sediment export signal (point 2 in Figure S2.17), we further investigated transport signals at GS1 and GS2 (Figure 2.2) by adopting three analyses:

2.1 Time difference in peak arrivals for discharge and sediment transport (suspended sediment and bedload) waves between GS1 and GS2 to confirm;
2.2 Computation of advection lengths for each daily transport cycle (i.e. t having $Q > Qc$) to infer potential downstream transport distances;
2.3 Shannon entropy index for investigating the spatial variability of sediment transport signals at the seasonal scale at GS1 and GS2.

In analysis 2.1, we extracted the timing of every single daily water discharge and sediment transport (i.e. suspended sediment and bedload) peak measured at GS1 and GS2. Daily measurements are compared, so that it was possible to retrieve the average time needed for both water and sediment waves to travel across the proglacial forefield. Then, knowing that, we were able to compute their virtual propagation velocities by dividing the distance between GS1 and GS2 (ca. 1 km, Figure 2.1) by the associated virtual velocities (velocity = space/time) following Hassan et al. (1991). For this computation we assumed a straight-line travel distance from GS1 to GS2. It is important to note here that the braided nature of the reach would increase the effective travel distance calculations giving maximum possible velocities. Results are shown in Figure 2.3.

The above information was used in analysis 2.2 to retrieve daily advection lengths for both suspended sediment and bedload particles. We first defined the critical discharge ($Q_c$), defined as the discharge, or shear stress, threshold needed to initiate sediment transport (Ferguson, 1994). However, this was only possible for bedload particles because being supply-limited suspended sediment transport cover the entire range of measured discharge. For bedload particles, we calculated Qc on the basis of the daily Q-$Q_b$ thresholds pooling together 2020 and 2021 data (Figure S2.18).
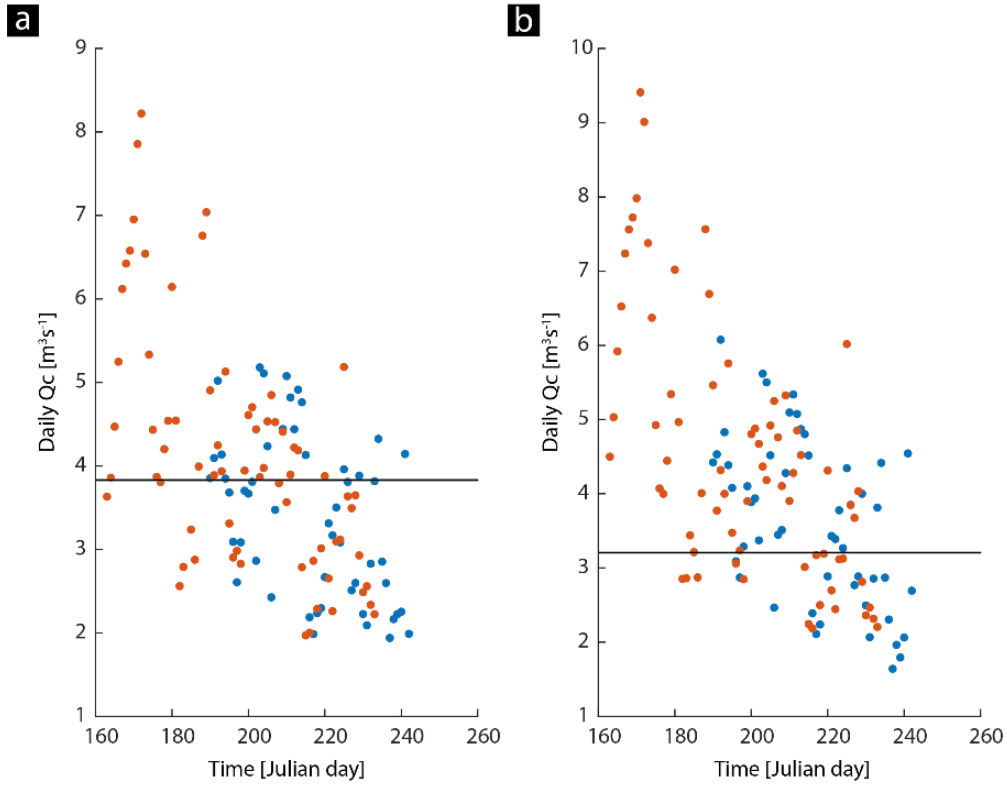


Figure S2.18: Daily discharge needed to initiate bedload transport in GS1 (a) and GS2 (b) for both 2020 (blue dots) and 2021 (orange dots) melt season. The horizontal black line refers to the mean seasonal $Q_c$.

Figure S2.18 shows that $Q_c$ in GS1 and GS2 is highly variable trough the melt seasons for various reasons given in the main text. Given this, we defined $Q_c$ as the mean seasonal discharge rate needed to initiate sediment motion. The validity of this approach was then verified applying the theoretical formula given in Rickenmann (1991) defined as:

$$Qc = [0.065 \left(\frac{\rho_s - \rho_w}{1000}\right)^{1.67} g^{0.5} D_{50}^{1.5} S^{-1.12}] \, w \qquad \text{Eq. S2.8}$$

85

Where:

ρs = particle density [kg/m$^3$]
ρw =water density [kg/m$^3$]
g = gravitational force [m/s$^2$]
D$_{50}$ = median grain diameter [m]
S = riverbed slope [tan(α)]
w = river width [m]

Table S2.8 compare the Q$_c$ values issued from the two above-mentioned methods. Even if results are very similar and comparable, we chose to use values derived from the rating curve as more empirical.

Table S2.8: Q$_c$ results obtained using the theoretical formula of Rickenmann (1991) and on the basis of daily discharge thresholds for sediment motion

| | Q$_c$ [m$^3$/s] | |
|---|---|---|
| Station | Method | |
| | Rickenmann (1999) | Rating curve |
| GS1 | 3.9 | 3.8 ±1.25 |
| GS2 | 3.4 | 3.2 ±1.54 |

Once Q$_c$ was established for both GS1 and GS2, we determined for each transport cycle the total amount of time where the water discharge rate was higher than Q$_c$. These were then used to calculate daily advection lengths (2.2 in Figure S2.18), defined as the average downstream distance a sediment particle travel before it settles to the bed (Ganti et al., 2014) for both suspended sediment and bedload particles. These are computed multiplying, for each daily transport cycle, the total amount of time having Q higher than Q$_c$ by the virtual velocity associated to the suspended (V$_s$) and the bedload (V$_b$) wave (Table S2.1), respectively.

We combined the above results with analysis 2.3, focused on the relation between seasonal variation in advection lengths and the variability of sediment transport signals, both variables driven by water discharge. At this purpose, we used the Shannon Entropy (SE) index (Lane and Nienow, 2019), also known as diversity index, to define the variability (also defined as entropy in the main text) of sediment transport signals over time. In practice, this index measures the amplitude of transport signals on a daily basis, so that the comparison of results issued at GS1 and GS2 give further insights on the relation between sediment transport and discharge dynamics, in terms of transport magnitudes and advection lengths. Results are shown in Figure 2.3.

The SE was computed daily for Q, Q$_s$ and Q$_b$ for the entire periods under investigation. It is calculated according to the duration of each transport cycle, defined as the time comprised between two daily transport peaks. This is defined as:

$$SE_j = \frac{1}{n}\sum_{i=1}^{n}\frac{Q_i}{\bar{Q_i}}log\frac{Q_i}{\bar{Q_i}}$$

Eq. S2.9

Where:

SE$_j$ = Shannon Entropy index for each transport cycle j
n = time steps within diurnal cycle j
Q$_i$ = water discharge or sediment transport rate for time step i

SE index highlights the variation within each transport cycle j from the mean discharge or transport rate measured for that specific cycle. Higher SE values may be pointing out either an

increase in the peak magnitude within two different cycle, or even a decrease in the minimum rate.

The changing discharge conditions matter for sediment transport, notably bedload, as discharge variation in subglacial drainage systems makes bedload export largely transport-limited (Perolo et al., 2019), with direct impact on both transport rates and advection lengths. Typically, the seasonal hydrograph of glacier-fed streams is characterized by an increasing diurnal discharge variation because of a progressive reduction in the buffering of glacial melt by snow as the snow-ice interference retreats up glacier, also promoted by a progressive upstream extension of the sub-glacial drainage system (Nienow et al., 1998; Lane and Nienow, 2019). Given this, we would expect advection lengths to become progressively longer over time before dropping toward the end of the season because of the increasing daily discharge amplitude increases, at the same time, the total amount of time of discharge being lower than the critical value $Q_c$.

# Chapter 3: Heuristic estimation of river bathymetry in braided streams using digital image processing

## 3.1 Chapter overview

This Chapter address the second research question: "Is it possible to predict water depth distribution in high turbid, shallow, mountain braided streams using basic planimetric information?". This is done using a heuristic approach based on a stepwise multiple linear regression model calibrated by correlating field-measured water depths to topographic variables of stream spatial configuration derived from SfM-MVS photogrammetric data. These variables include distance from the nearest river bank, total inundated width along a line tangential to the local flow direction, local curvature magnitude and direction, and distance from the nearest flow divergence and convergence regions). The Chapter presents the methodology used to quantify the variables, describes the basic principles of the statistical model, and discusses the quality of the obtained results for computing estimates of morphological volumetric changes over time.

This contribution was published after peer-review as: Mancini, D., Antoniazza, G., Roncoroni, M., Mettra, F. & Lane, S.N. (2024). Heuristic estimation of river bathymetry in braided streams using digital image processing. *Earth Surface Processes and Landforms*. https://doi.org/10.1002/esp.5944.

## 3.2 Heuristic measurement of river bathymetry in proglacial braided streams using SfM-MVS photogrammetry and statistical approaches

### 3.2.1 Introduction

River bathymetry is an important parameter in fluvial geomorphology for both geomorphological and ecosystem processes (Ward et al., 2002; Lane et al., 2010; Woodget et al., 2015). Its accurate measurement allows for quantitative detection of river channel changes through time (Lane et al., 2003; Westaway et al. 2003); better understanding of fluvial systems though hydraulic modelling (Lane et al., 2020); physical habitat assessment and river restoration (Maddock, 1999); and sediment budgeting studies (Hicks, 2012; Marcus et al., 2012).

The 1990s saw the first attempts (Lane et al., 1994) to represent river bathymetry as a continuous surface (i.e. Digital Elevation Models or DEMs) rather than a series of cross-sections. They relied upon interpolation of point data acquired using differential GPS (e.g. Brasington et al., 2000) or total stations, sometimes aided by terrestrial analytical photogrammetry for exposed areas (e.g. Lane et al., 1994; Chandler et al., 2002). Such field surveys are extremely time consuming and lead to a trade-off between spatial resolution, spatial extent and the frequency of resurvey that directly impacts the quality of the results that are acquired (Lane, 1998). They also require physical contact with the riverbed (e.g. walking in the river) potentially modifying it; and are limited to wadeable areas at high flows (Marcus and Fonstad, 2008; Bangen et al., 2014; Kasvi et al., 2019). The ease with which bathymetric mapping can be undertaken is thus much more limited compared to measurement of dry areas (Brasington et al., 2000; Westaway et al., 2003).

Developments in remote sensing, initially based upon the depth signature in airborne optical imagery (Gilvear et al., 1995, 1998), and eventually using multispectral (e.g. Winterbottom and Gilvear, 1997; Legleiter et al., 2004; Legleiter and Roberts, 2005) and hyperspectral (e.g. Marcus et al., 2003) imagery, addressed this limitation. The development

of digital photogrammetric analysis for airborne imagery increased the feasibility of photogrammetric-based approaches allowing for much larger spatial extents. Westaway et al. (2000, 2001) provided a fully photogrammetric solution based upon two media refraction correction for inundated zones where riverbed texture could be identified on the stream bed. Using airborne imagery, Westaway et al. (2003) showed that it was possible to combine water depths derived from optical imagery for inundated zones with photogrammetric data from exposed areas to provide very high resolution (< 0.5m), good precision (ca. ±0.2 to ±0.3 m) data over a large extent of braided river (3 km x 1.5 km). This required field calibration of the relationship between depth and spectral signature but Lane et al. (2010) showed that this method could be adapted for archival data where no calibration data were available.

Up until the 2010s, these approaches were limited by the cost of airborne imagery. This was revolutionized by the growing availability of low-cost Uncrewed Airborne Vehicles (UAVs) coupled with Structure-from-Motion Multi-View-Stereo (SfM-MVS) photogrammetry (Niethammer et al., 2010; Hugenholtz et al., 2013; Ouedraogo et al., 2014; Eltner et al., 2015; James et al., 2020). High vertical precision (ca. ±0.05 - ±0.2 m) and high resolution (ca. 0.01 to 0.1 m) data can now be acquired for rivers at a frequency dictated by the rate of morphological change rather than limited by the costs of data acquisition producing accurate DEMs of dry areas. The extension of two media refraction correction to UAV-derived data allows reconstruction of water depths and so production of models for both inundated and dry zones (Dietrich, 2017). The possibility of combining these two techniques represents a significant development in fluvial geomorphology, although subsequent research has identified limitations. Notably, the low-grade cameras in many UAVs makes camera calibration challenging for reliable change detection (Carbonneau and Dietrich, 2017; James et al., 2017a, b, 2020).

One major challenge remains: where rivers have high turbidity, water depths may exceed the maximum depths that can be seen in aerial imagery (i.e. the extinction depth). This may make the riverbed insufficiently visible for application of texture-based two-media photogrammetry approaches for water depth modelling (e.g. Flener, 2013; Flener et al., 2013; Tamminga et al., 2015; Dietrich, 2017; Kasvi et al., 2019). Light extinction depth measured using Secchi depths may be of the order of only a few centimetres in certain fluvial settings (Carrivick and Heckmann, 2017) eliminating the depth signature for image-based approaches. Green-band lidar typically only penetrates to 1.5 to 3 times the Secchi depth (Pratomo et al., 2019; Szafarczyk and Tos, 2023), limiting the suitability of airborne lidar for bathymetric measurement in high-turbidity rivers. Other active remote sensing techniques exist, including echo-sounding and acoustic Doppler current profiling. These perform better in high turbidity environments, but they cannot be used in water depths lower than 0.3 m to 0.5 m, limiting their application to large rivers (Kasvi et al., 2019).

Large-scale measurements suggest basic relationships between planform morphological proprieties (notably channel width) and water depth (Mersel et al., 2013; Almeida et al., 2018; Shaperow, 2019). Such relations are implicit in the long-established notion of hydraulic geometry (Leopold and Maddock, 1953) that allows stream widths, mean depths and mean velocities to be predicted from discharge. Such relationships were developed primarily for morphologically stable, single-channel streams. Bures et al. (2019) used linear multiple regression to predict cross-section bathymetry using morphometric data (i.e. overall curvature, planar curvature, profile curvature, overall slope and slope in the x- and y-direction). Interpolation between cross-sections were then applied to obtain a complete bathymetry of a meandering river.

In this paper, we estimate water depth distribution in a high turbid, braided, glacier outwash stream from basic planimetric information and assess its potential for creating DEMs

for volume change estimation. The approach is based on a heuristic argument, that is a set of qualitative statements of how we expect water depth to vary in a braided river. We then transform these into quantitative, statistical models for generating spatially continuous water depths in inundated zones. We then (1) integrate these depths into high resolution SfM-MVS derived topographic data from dry areas to create DEMs; and (2) assess whether they can be used for geomorphic change detection and volume estimation at the proglacial floodplain scale.

## 3.2.2 Methodology

### 3.2.2.1 Study area

The investigation is based in the proglacial margin of the Glacier d'Otemma, located at an altitude of 2450 m a.s.l. in the Val de Bagnes, south-western Swiss Alps (Figure 3.1). This includes a glacial outwash plain that has formed between the early 1980s and present following rapid glacier retreat (Mancini and Lane, 2020). The outwash plain varies between ca. 150 and 200 m wide and is just over ca. 1 km in length. There is no vegetation cover except on lateral terraces that are outside of the active braiding zone. The river has a median grain-size ($D_{50}$) of ca. 0.06 m and with surface particle sizes ranging from the sand through gravel to cobble size fractions. The mean valley slope is 1.2%. The river is typical of braided rivers found in outwash plains in front of both glaciers and ice sheet outlets. Field-measured maximum water depths varied from ca. 0.20 m in secondary channels to more than 0.60 m in main channels.

Applying empirical estimations for the attenuation coefficient based on water column turbidity, the lowest measured turbidity of ca. 250 NTU produce maximum extinction depths of around 0.30 to 0.50 m (Rose et al., 2014). At these depths, there is very little texture available on the bed and the form of the exponential absorption of light with depth means very poor precision in depth estimates. This is why both two-media photogrammetric correction and image-based approaches are not suitable for this kind of stream.

In this study, we used field-data collected on the 18th of August 2020 and on the 8th and 10th of September 2020. These have different measured water depth ranges because of the different melt rates and discharge rates (Qw) experienced by the glacier during the melt season (Figure 3.1): mean Qw during the data acquisition was of 5.29 m³/s on the 18th of August, 2.98 m³/s on the 8th and 3.11 m³/s on the 10th of September. We describe data collection below.
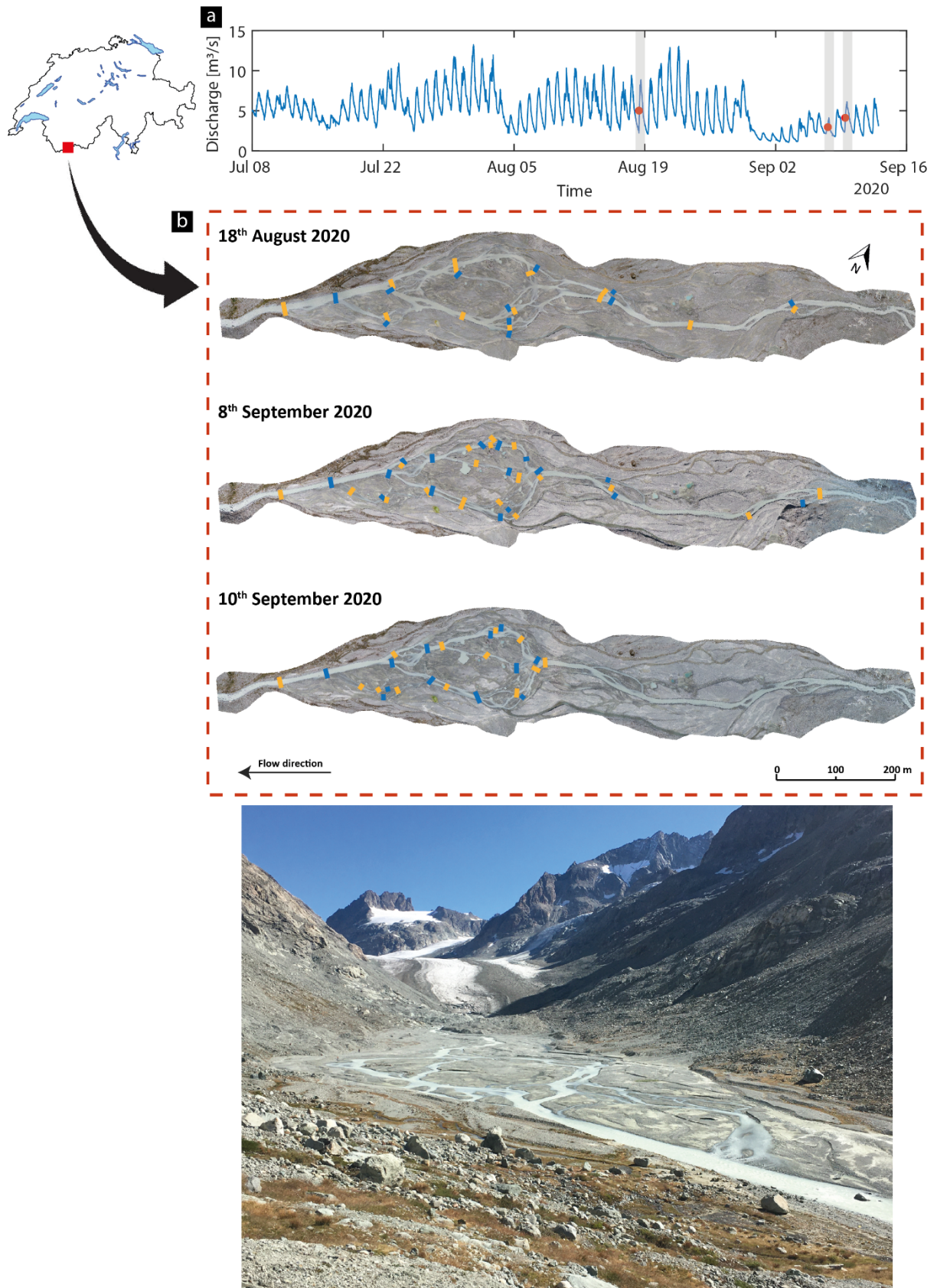
Figure 3.1: Location of the study area, streamflow hydrograph and spatial configuration of the Glacier d'Otemma proglacial forefield (45°.56'03.544''N, 7°24'42.197''E) from both aerial and ground-level perspective. Red dots on the flow hydrograph (a) show the three days of survey (Supplementary Information S3.4.1). Colored dots in the forefield maps (b) refers to measured cross-section water depths used for the calibration (orange) and for the validation (blue) process. Water stage data for the 2020 melt season are available in Müller and Miesen (2022).

### 3.2.2.2 Methodology

Figure 3.2 gives an overview of the methodology developed to estimate spatially-continuous water depths using morphometric parameters using: (1) orthomosaics of the alluvial plain; and (2) the related Digital Elevation Models (DEMs). These parameters are combined with geo-referenced point measurements of water depth from within the inundated zones obtained using differential GPS (dGPS) survey to develop statistical models for channel bathymetry. In this study, we focus on analyses conducted around at daily low discharge conditions (Figure 3.1) with the ultimate aim of producing daily DEMs for morphological change detection.

The bathymetric model is written in MATLAB (version 2019a) and freely available in Mancini et al. (2024b). The SfM-MVS derived orthomosaic is used to classify the study area into wet and dry regions. Following Westaway et al. (2003), the resulting classification is used with the associated DEM to extract elevations along the wet-dry interface. These are interpolated to create a flat water surface map which can be combined with texture-estimated water depths to obtain topographic data in inundated zones (Westaway et al., 2003). The field-collected water depth measurements are used to develop both single date-specific and pooled statistical models. These models are constructed from a series of heuristic statements that define which morphometric parameters we derive to model measured water depths. We justify the choice of these statements and explain their quantification below (Section 2.3.4).

For each field-collected dataset, a subset of depths is used in a stepwise linear regression to identify which of these parameters make a statistically significant contribution to water depth variation in space, and so to define the form of the final multiple regression model. The models are then applied to data points not used in calibration to validate them. The final models are applied to the full braidplain to provide spatially-continuous water depth maps at the proglacial-margin scale. The number of depths that can be measured is limited by the constraint that stage should not change significantly during data collection leading to relatively small sample sizes. Thus, we also tested the effect of merging the three 2020 datasets to increase sample size. Resulting water depth distributions for inundated zones are combined with SfM-MVS photogrammetric data for dry zones to create DEMs of the entire floodplain. Following Lane et al. (2003) we produce spatially-varying estimates of uncertainty and levels of detection, and then volumetric changes estimates in both dry and inundated regions. We would expect the quality of elevations in inundated zones to be degraded as compared with the dry zones and this last step allows us to assess whether or not this method is fit for the purpose of morphological change detection and volume estimation in an actively braiding glacier-fed stream.
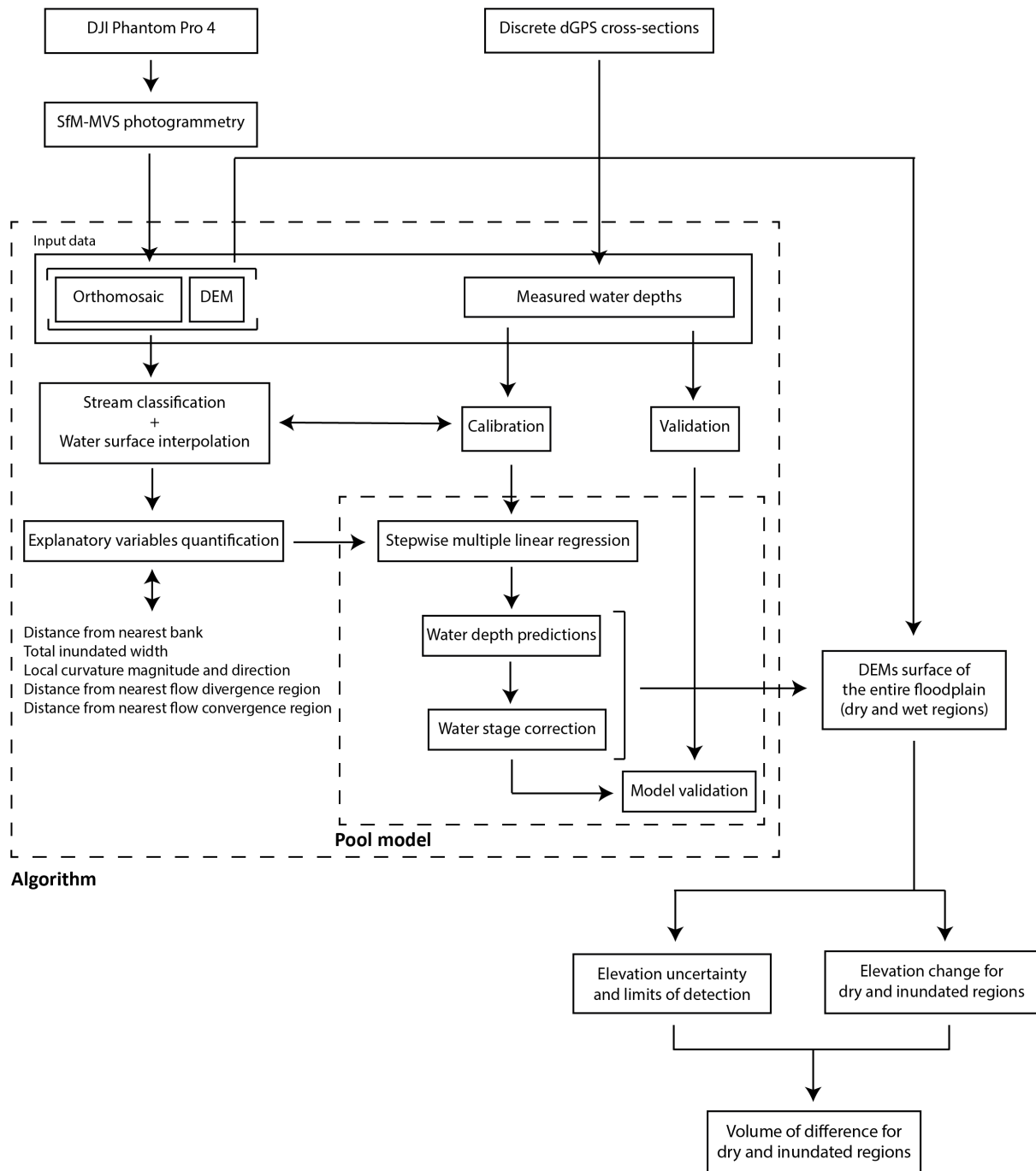
Figure 3.2. Schematic overview of the used methodology.

### 3.2.2.3 Methods

### 3.2.2.3.1 UAV data acquisition and SfM-MVS photogrammetric processing

Drone imagery was acquired using a DJI Phantom 4 Pro UAV in the early morning on each of the three survey dates when the floodplain experienced low flow and relatively stable conditions (Supplementary Information 3.4.1; Roncoroni et al., 2022). The drone was mounted with a FC6310 camera containing a 1-inch CMOS sensor having a focal length of 8.8 mm and a pixel pitch of 0.24 mm, so producing 5'472 x 3'648 pixel images. Flight plans were designed in Pix4DCapture (version 4.8), with an overlap of 80%. The survey strategy followed James et al. (2020) in order to optimize the photogrammetric process and to reduce the magnitude of systematic error in derived DEMs. The study area was divided into four zones, each one surveyed with two orthogonal grid missions having a camera angle at nadir (90° at 80 m height)

and with two additional circular missions at 60 m height where the camera was self-oriented towards the centre of the scene (Roncoroni et al., 2022). The theoretical ground sampling distance per flight varied between 0.6 and 0.8 cm/pixel depending on camera height and obliquity. Each survey started at 8 am and took ca. 3.5 hours to cover the entire proglacial outwash plain extent showed in Figure 3.1. This was undertaken daily throughout the melt season.

We installed 77 ground control points and collected 170 independent checkpoints to evaluate model quality. These were measured using rapid static GNSS-RTK surveys set at 2 minutes per point using a dGPS Trimble R10, with a known base station (corrected using the fixed monitoring Swiss Federal Office for Topography provided system via SwiPos©; Mancini and Lane, 2020). Data points were corrected to the the Swiss CH1903+/LV95 coordinate system. Point precisions were comprised between ±0.02 m and ±0.04 m in the horizontal and vertical, respectively.

For each day of survey, the post-processing of the imagery was performed using the SfM-MVS photogrammetric software Agisoft Metashape (version 1.5.5), following steps detailed in James et al. (2017a,b, 2020). First, images that were blurred and/or too contrasted, that had few (~500) and/or an uneven distribution of tie points, and/or that presented large tie point residuals (> 1 pixel), were discarded (James et al., 2020). Second, images were aligned and tie points were automatically extracted from matching images. At this stage, tie points that were observed in only a few images (< 3) were discarded (James et al., 2020). Third, we used a statistical method (James et al., 2017a, 2020), implemented in Agisoft Metashape as an external plugin to improve the SfM-MVS bundle adjustment. It uses Monte Carlo simulation: (a) to identify the camera model that minimizes systematic error; and (b) to investigate the impact of individual GCPs on overall model quality. This process is fully described in Roncoroni et al. (2022) for the datasets used here. The procedure resulted in a camera model composed of 5 parameters and 52 GCPs (Supplementary Information 3.4.1). Table 3.1 summarizes the results.

Fourth, aided by the semi-automatic marker identification available in Metashape, GCPs (Supplementary Information 3.4.1) were introduced to help to constrain the bundle adjustment. The RMS errors for both GCPs and 170 independent checkpoints are shown in Table 3.1. Finally, point clouds were densified and used to produce orthomosaics and DEMs for each survey at a resolution of 0.05 m and 0.20 m, respectively (Table 3.1). For the morphometric analysis described below, the orthoimages were resampled to 0.20 m for computational reasons. More details on the methodology are given in Roncoroni et al. (2022). Orthomosaics produced by and used in this study are freely available in Roncoroni et al. (2023b) and the final DEM products are available in Mancini et al. (2024c).

Table 3.1: Evaluation of bundle adjustment performance in terms of GCP error, point cloud quality and DEM vertical difference by comparison with 170 independent checkpoints.

|  | GCP RMS error [m] | Total number of points in dense cloud | Checkpoints Z mean and standard deviation of error (SDE, in brackets) [m] |
|---|---|---|---|
| 18th August 2020 | ±0.049 | 101'154'741 | 0.009 (±0.029) |
| 8th September 2020 | ±0.014 | 92'300'262 | 0.009 (±0.031) |
| 10th September 2020 | ±0.013 | 93'812'486 | 0.011 (±0.028) |

### 3.2.2.3.2 Sampled point data for model calibration and validation

The Trimble R10 dGPS was also used in rapid-static GNSS-RTK mode to obtain discrete geo-referenced points of the riverbed at the same time as UAV image acquisition. Due to the difficulties in maintaining the rover in a stable position for long periods because of water

currents, the sampling time per point was set to 30 seconds. As with the GCPs, data were precise to ±0.02 m in the horizontal and ±0.04 m in the vertical component.

For the bathymetric modelling, topographic measurements were collected in the form of cross-sections extending away from selected locations on channel banks. The use of cross-sections was deemed preferable as it made sure that we obtained a good depth range extending from the shallowest (near bank) to deepest water. Cross-sections were chosen such that we captured a range of different morphological features (e.g. ones with both fewer secondary channels and more secondary channels; some with convergence zones and some with divergence zones; and a range of channel widths). Within cross-sections we maintained an average point spacing of ca. 0.4 m. Due to safety considerations, data collection in the deepest regions was challenging meaning fewer data could be acquired. The collected cross-sections were then randomly split into two halves for calibration and validation purposes.

Table 3.2: Characteristics of the dGPS surveys in terms of total number of points and stream cross-sections for both calibration and validation sub-samples associated to each dataset (Figure 3.1). In square brackets the percentage of the number of points compared to the total number of points composing the dataset.

| Date | Total | | Calibration | | Validation | |
|---|---|---|---|---|---|---|
| | Number of points | Cross-sections | Number of points | Cross-sections | Number of points | Cross-sections |
| 18th August 2020 | 206 | 23 | 112 [54.4%] | 12 | 94 [46.4%] | 11 |
| 8th September 2020 | 259 | 37 | 136 [52.5%] | 21 | 123 [47.5%] | 20 |
| 10th September 2020 | 157 | 25 | 82 [52.2%] | 18 | 75 [47.8%] | 17 |

### 3.2.2.3.3 Image processing to obtain a water surface DEM

The SfM-MVS derived orthomosaics were classified into wet and dry zones. First, we converted the orthomosaic from RGB to grayscale to reduce unwanted noise related to changing light intensity (Gao et al., 2008; Liu et al., 2018). Random pixels falling within inundated regions were manually sampled to define the spectral range of turbid water. These were used to train a simple signature-based classification model in MATLAB to generate a binary raster of wet and dry regions: pixels having a value falling within the spectral range of turbid water were classified as 1, otherwise as 0. Second, the resulting inundation map was manually corrected by comparing it visually with the respective orthomosaic (Figure 3.3; Roncoroni et al. 2023a). Points in the dry-wet boundaries were identified and used to extract coordinate triplets from the DEMs obtained using the SfM-MVS photogrammetry. These were then interpolated using Delaunay triangulation in order to produce a flat water surface within each DEM for representing sub-critical flow conditions (Westaway et al., 2003).
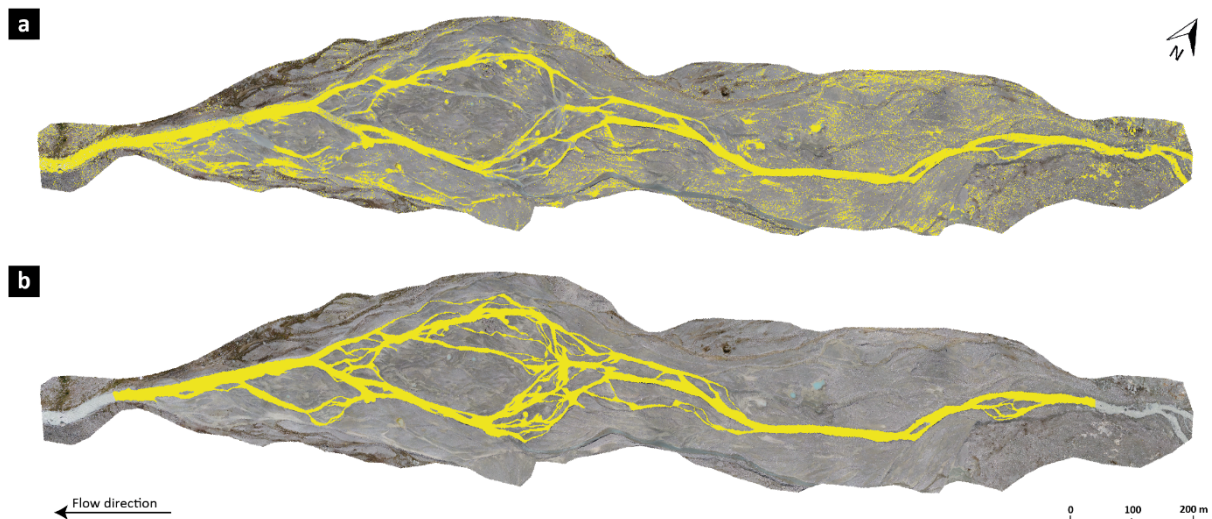
Figure 3.3: turbid water detection for the 18th of August dataset using (a) the automated spectral signature method and (b) final result after manual correction.

### 3.2.2.3.4 Morphometric parameters

Given that the focus is a braided river, we developed five heuristic statements that were then quantified to drive the statistical model for estimating water depth: (1) the depth of a river increases with distance from the nearest bank (this follows from within cross-section application of the principle of maximum entropy; Farina et al., 2015); (2) where the total inundated width of all channels in a braidplain cross-section is higher, flow velocities and hence erosion depths should be lower, assuming steady discharge (Mosley, 1983); (3) channel curvature redistributes momentum laterally and so causes the deepest zone to migrate towards the outer bank of the channel (Begin, 1981; Ashmore, 1982); (4) flow divergence leads to deposition and hence lower flow depths, while (5) flow convergence leads to scour and hence higher flow depths (Lisle et al., 1991; Ashworth, 1996). Their computation is described below and their spatial distribution is shown in Supplementary Information 3.4.2.

*Distance from the nearest bank*

In rivers, channel width, depth and velocity respond to water discharge via modification of topographic (e.g. via scour or via bank erosion) or hydraulic (roughness, bed slope) parameters (Mackin, 1948; Leopold and Maddock, 1953; Mosley, 1983). If discharge increases, within a cross-section, the river may become wider, deeper or faster (Leopold and Maddock, 1953). The increase in depth may result from either rising water level or (vertical) riverbed erosion; the increase in width is achieved through (lateral) bank erosion. Vertical and lateral erosion are not independent as where vertical erosion occurs close to a river bank there is a greater probability that the river bank will be over-steepened and, especially where the river bank is not cohesive, it will fail. It might then be stated that water depths are likely to be greater farther from a river bank. Thus we estimated the distance from the nearest bank by applying a Euclidean distance operator to the wet-dry image; this measures the shortest distance for each wet pixel to the river bank.

*Total inundated width*

The relation between discharge and morphologic modification is complex in a braided river as in addition to the river becoming wider and deeper as discharge rises there is also an increase in the number of channels. This reduces hydraulic efficiency and hence vertical erosion as compared to a single thread channel. Thus, we would expect river channel

97

bathymetry also to reflect total inundated width, with lower total widths likely to be faster and deeper.

Estimating total inundated width is not evident in a river with continuously converging and diverging channels across a number of different scales. The solution adopted here involves a two-step approach (Figure 3.4). First, we estimate the width of the local channel, here expressed as twice the Euclidean distance between the nearest dry point on the river bank (*b*) and the channel centerline (*c*) at each cell (*i*) in the inundated zone ($2d_{bc}^i$). The channel centerline is mapped using a skeletonization algorithm. This does not give the true "hydraulic" centre-line as the analysis is done on a surface map of inundated area rather than distributions of flow velocity and water depth; but comparisons with a manually digitized centre-line suggested an excellent level of agreement. Second, we add other non-local channel widths ($2d_{bc}^k$) falling on an imaginary orthogonal line to the considered cell *i* to get the total inundated width.

To obtain the total inundated width for each local channel *i*, we use a morphological structuring element (STREL) to identify which non-local channel widths *k* apply to each *i* (Figure 3.4). The STREL is a square matrix oriented so the diagonal is perpendicular to the local channel cell *i* with an angle given be the direction of local curvature (see below). The diagonal is set to be twice as long as the braidplain width, in our case 1400 cells. Any other intersection of the STREL diagonal with a centre-line (excluding the local centerline) indicates a non-local channel (*k*) of width $2d_{bc}^k$ contributing to the total inundation width for *i*. The total inundation width (Tiw) is then computed as:

$$Tiw = \sum_{k=1}^{n} 2d_{bc}^j + 2d_{bc}^k \qquad \text{Eq. 3.1}$$

Where:

$Tw$ = total inundation width;

$2d_{bc}^j$ = width of the local channel;

$2d_{bc}^k$ = non-local channel widths;

n = number of diagonal intersections.
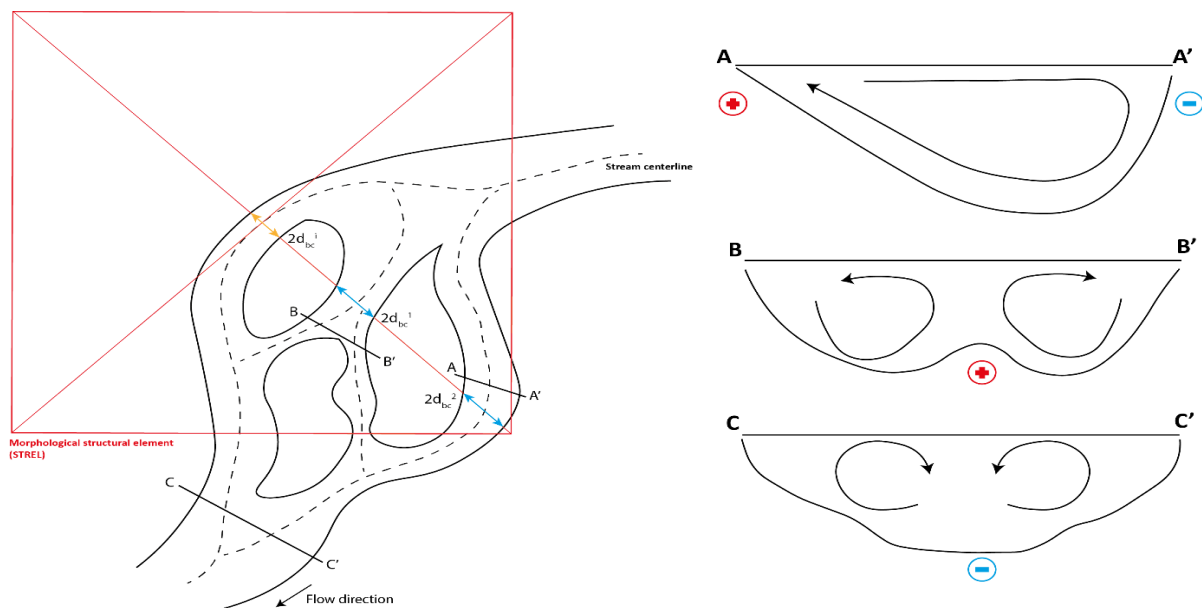


Figure 3.4: Illustration of the approach to total inundation width estimation using a morphological structuring elements (STREL, red square). In this example, the local channel width ($2d_{bc}^i$, orange arrow) is combined with two non-local channels widths ($2d_{bc}^k$, blue arrows) to give the total width for that specific cell. Transects illustrate the topographic effects of secondary circulations in curved channels (A) and in flow divergence (B) and convergence regions (C). Plus and minus refers to deposition and erosion, respectively.

*Local curvature magnitude and direction*

The local curvature magnitude and direction is based upon determining streamlines (or centerlines in terms of the digitized inundated area). As shown in studies of river meandering (e.g. Brice, 1975) and braiding (e.g. Richardson and Thorne, 1998; Ashworth, 1996), curvature is a key driver of fluvial morphodynamics because it leads to secondary circulation; it has been measured in proglacial rivers (Ashmore, 1982; Ashmore et al., 1992). Rivers flowing on flat and poorly-vegetated floodplains are likely to be shaped by this secondary flow, which has the effect of shifting erosion towards the outer bank and deposition towards the inner bank (Figure 3.4). This results in a transverse displacement of regions having higher and lower water depths within the channel cross-section (Ashmore, 1982; Powell, 1998). Thus, local curvature magnitude and direction can be used as a proxy to determine the spatial distribution of secondary flow (e.g. Parker et al., 2011; Frascati and Lanzoni, 2009, 2013) and its effects on water depths.

The local curvature magnitude and direction calculation (Figure 3.5) starts with the centerlines used in the estimation of total inundation width. First, a manual reworking of the centre-line is needed to remove unwanted segments coming from abrupt and sudden changes in the shape of the digitized polygon. Second, segmentation is used to create individual centre-line segments in individual reaches limited in their upstream and downstream direction by flow divergence and convergence units, respectively). These segments are subsequently smoothed using a loess filter to reduce noise in the data (Tate et al., 2005). Third, curvature is calculated following Mjaavatten (2020). This latter returns, for each cell composing a centerline segment the local curvature values and the coordinates ($k_{xi}$, $k_{yi}$) describing the direction of orthogonal vectors for each point composing the segment. These outputs were used in the fourth step to differentiate the stream into regions of positive curvature, which would displace momentum and hence depth away from the centre-line and regions of negative curvature with the opposite tendency (Figure 3.4). This is done for every point composing each segment by assigning them a diagonal matrix of specific length and angle. The length simply corresponds to the local channel width, while the angle is given by the difference between the direction of orthogonal vector in a local streamline cell ($k_{xi}$, $k_{yi}$) and the x-axis of an imaginary Cartesian plan calculated in a counter-clockwise direction; cells located on the half having the same orientation of the normal and hence in the direction of positive curvature were assigned a value of +1; those in the opposite orientation have -1. Finally, the magnitude of the curvature is calculated by attributing at the outermost diagonal cells the curvature magnitude found by applying Pythagoras' theorem to the previously determined normal vector components:

$$|K_{ji}| = \sqrt{k_{xi}^2 + k_{yi}^2} \qquad \text{Eq. 3.2}$$

Where:

$|K_{ji}|$ = magnitude, or length, of the normal vector *j* at point *i* of the centreline;
$k_{xi}$ = coordinate X of the normal vector having origin in *i*;
$k_{yi}$ = coordinate Y of the normal vector having origin in *i*.

As the total number of cells composing the normal vectors is known, we then fill cells in the rest of the diagonal by calculating a decreasing interval from the maximum magnitude value (+*K*) or an increasing interval from the minimum magnitude value (-*K*). This procedure is defined by:

$$n_{ji} = |K_i| - \sum_{n=1}^{n-1} 2|K_i|/(n-1) \qquad \text{Eq. 3.3}$$

Where:

$N_{ji}$ = curvature magnitude value at the cell $i$ of the normal vector $j$;

$|K_i|$ = magnitude/length of the normal vector at point $i$ of the centreline;

$n$ = total number of cell composing the vector $j$.

An interpolation (Delaunay triangulation) is then applied to fill points not falling in one of the diagonals in order to have a continuous matrix of curvature values.
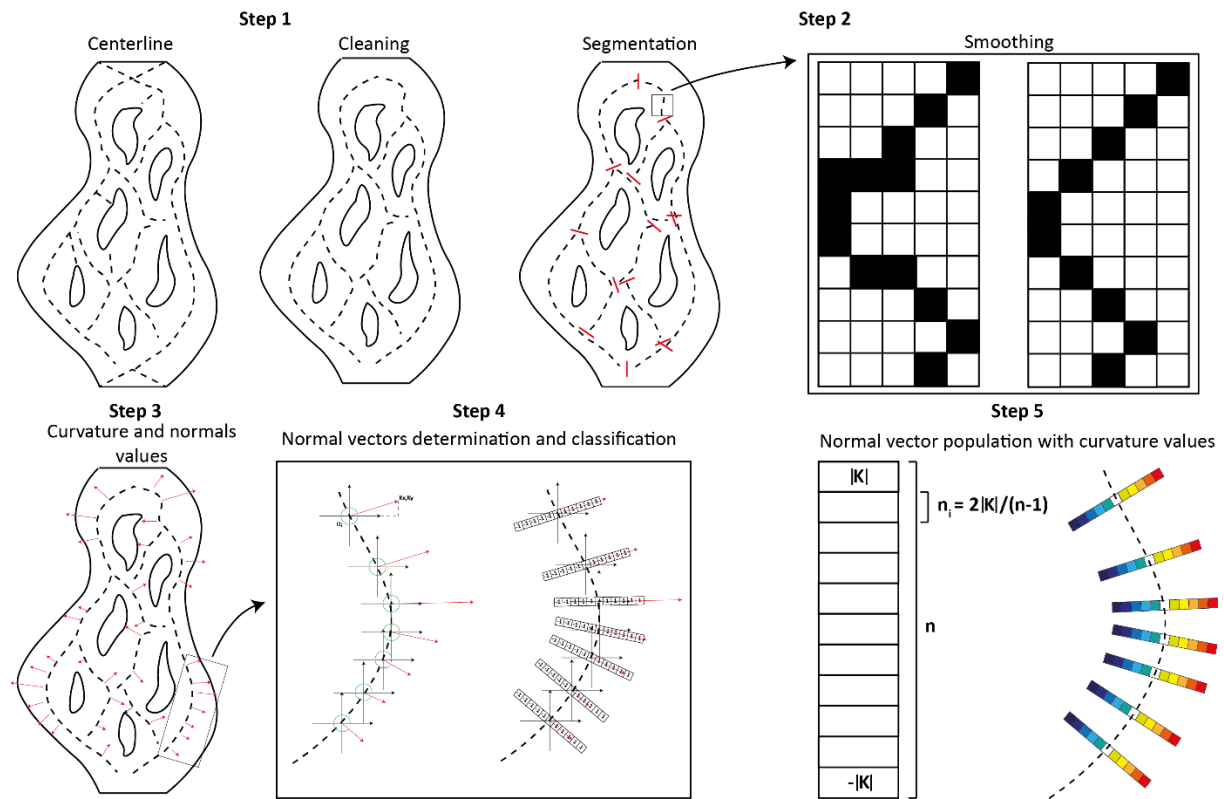


Figure 3.5: Methodological approach used to quantify the local curvature magnitude and direction variable. Step 1: centreline cleaning from noisy segments; step 2: segmentation of the cleaned centreline in multiple transects to apply a smoothing function needed to avoid abrupt direction changes having potential effect on real curvature values; step 3: determination of normal vectors coordinates and magnitudes; step 4: determination of normal vector angle in reference to the first quadrant; step 5: classification of pixels of regions of negative (blue gradient) and positive (red gradient) curvature regarding to the local magnitude and normal vector direction.

*Planform streamline convergence and divergence*

Streamline convergence and divergence locations related to bars in braided rivers can also influence erosion and deposition and hence water depth distributions. This is reflected in studies of deposition at bifurcations and on bar-heads (Figure 3.4; Best and Reid, 1984; Best, 1988; Ashworth, 1996), and erosion at confluences (Figure 3.4; Bristow and Best, 1993; Ashworth, 1996).

Flow convergence and divergence regions were visually identified based on the inundation map. The distance from each inundated cell to the nearest flow convergence and divergence region is then automatically computed in a procedure involving three steps. First, for each convergence and divergence region a null matrix having the same dimensions of the entire study area is generated, and the value 1 is attributed to their exact spatial location. Second, radial distances are computed. Third, for each cell composing the inundated area, the closest divergence and convergence regions were found by using the distance matrices as a lookup table.

*Measured water depth*

The surveyed water depth is the response variable of the model. The dGPS points give elevations which need to be combined with the water surface to give water depths. This is done by calculating the Euclidean distance between the 2D coordinates of each sampled dGPS topographic point and all the cells composing the triangulated water surface. The minimum calculated distance is kept, as the orthogonal and shorter distance between the riverbed and the water surface.

## 3.2.2.3.5 Water depth prediction: model calibration, application and validation

Before modelling water depths, we checked the basic assumptions required in multivariate regression analysis, notably regarding multi-collinearity between independent variables (Olsen et al., 2020). The degree of collinearity between variable pairs was computed using the variance inflection factor (VIF) (e.g. Neter et al., 1983; Thompson et al., 2017). A VIF value > 10 indicates that two variables were highly correlated between each other and could lead to multicollinearity if they were both included within a model.

Model calibration was based upon a step-by-step multiple linear regression (Maxwell, 1975; Breaux, 1967; James et al., 2013; Olsen et al., 2020) aimed at explaining the measured water depth from the set of morphometric variables):

$$y = b_0 + b_1 x_1 + \cdots + b_i x_i + e \qquad \text{Eq. 3.4}$$

Where:

$y$ = response variable (i.e. measured water depth);
$x_i$ = observations associated to the independent variable $i$;
$b_0$ = y-intercept;
$b_i$ = partial regression coefficients (weights) associated to $x_i$;
$e$ = residuals (i.e. variance not explained by the model).

Variables were added iteratively starting with the most important, in terms of percentage of explained variance, until no further variables resulted in a statistically significant ($p < 0.05$) increase in explanation (Draper and Smith, 1998).

Stepwise regression was applied to the three datasets individually (Figure 3.1 and Table 3.2). The resultant models were then applied to the entire study area to determine predicted water depths in all flooded cells for each calibration date. To account for difference in discharge rates over the 3.5 hours of UAV survey (2.55 m³/s to 8.04 m³/s [+315.33%] on the 18th of August, 1.81 m³/s to 4.16 m³/s [+231.33%] on the 8th and 2.24 m³/s to 3.99 m³/s [+177.89%] on the 9th of September; Figure 3.1), the results were corrected for the effects of changing water stage conditions. The associated methodology is fully presented in Supplementary Information 3.4.3.

The model was evaluated quantitatively in two ways. First, the residual errors of the fitted model and their spatial distribution were considered. Second, local predicted water depths were compared to independent measurements (validation dataset, Table 3.2) and differences between measured and predicted depths were quantified ($R^2$ and standard deviation of error).

## 3.2.2.3.6 Pooling of calibration data

As the number of datapoints available for each dataset was limited, a model calibrated with all available water depth measurements was developed (Figure 3.1 and Table 3.2). The aim was to obtain more statistically significant result that could be applied to dates where no

calibration data were available. The resulting relation was then applied individually to the three field-collected datasets to produce water depth prediction maps, and validated using the three sets of independent measurements (validation datasets, Figure 3.1 and Table 3.2).

## 3.2.2.3.7 Elevation estimation, elevation uncertainties, limits of detections and volumetric change estimates

Water depths were converted into wet-bed elevations following Westaway et al. (2003) by subtracting the predicted water depths from the interpolated water surface in the DEM. Elevation uncertainties for each cell *(i, j)* composing the inundated area were determined as the sum in quadrature of the uncertainties related to both water depth prediction and water surface in each single DEM as (Lane et al., 2003):

$$EU_{ij} = \pm\sqrt{\sigma d_{ij}^2 + \sigma e_{ij}^2} \qquad \text{Eq. 3.5}$$

Where:

$EU_{ij}$ = elevation uncertainty in cell *(i,j)*;

$\sigma d_{ij}$ = standard deviation of water prediction error in cell *(i,j)* derived from the confidence interval (95%) of the relationship between measured and predicted water depth;

$\sigma e_{ij}$ = standard deviation of water surface error in cell *(i,j)*, taken as the dry DEM uncertainty, determined by comparing the 170 field-measured and photogrammetrically reconstructed elevations of stable areas

For dry cells Eq. 3.5 is modified as $EU_{ij} = \sigma e_{ij}$. Given that $\sigma e_{ij}$ is constant and $\sigma d_{ij}$ is varying depending on model's prediction efficiency Eq. 3.5 gives a spatially explicit estimation of DEM uncertainty for both dry and wet cells.

DEMs of difference (DoD) were determined by subtracting the oldest DEM from the most recent one (i.e. DEM$_{t2}$-DEM$_{t1}$) and filtered according to the spatial distribution of the limits of detection (LoD) set at 68% (Brasington et al., 2003; Lane et al., 2003) using:

$$LoD_{ij} = \pm t\sqrt{(EU_{ij}^1)^2 + (EU_{ij}^2)^2} \qquad \text{Eq. 3.6}$$

Where:

$LoD_{ij}$ = limit of detection in cell *(i,j)* [m];

$t$ = Student's confidence interval threshold (1 at 68%)

$EU_{ij}^t$ = Elevation uncertainties in cell *(i,j)* at times t.

DEMs of difference were filtered according to LoD maps to highlight only statistically significant geomorphic changes. These were then classified into regions as inundated, dry and transient (i.e. inundated to dry or dry to inundated) between surveys. Finally, volumetric change maps were produced from spatially filtered DoD maps and total volumetric change estimates were computed following Lane et al. (2003) as:

$$V = d^2\sqrt{n \sum DoD} \qquad \text{Eq. 3.7}$$

Where:

V = Volume [m³];

d = cell size (i.e. 0.20) [m];

n = number of raster cells in DoD;

DoD = DEM$_{t2}$-DEM$_{t1}$ spatially filtered by LoDs (Eq. 3.6).

The associated uncertainties in volume estimates ($\sigma v_{ij}$) were derived as (Lane et al. 2003):

$$\sigma v_{ij} = \pm\left(\sum_{i=1}^{I}\sum_{j=1}^{J}\left[d_{ij}^{2}\left(EU_{1ij}^{2} + EU_{2ij}^{2}\right)^{0.5}\right]^{2}\right)^{0.5} \qquad \text{Eq. 3.8}$$

### 3.2.3 Results

### 3.2.3.1 Individual predictive models

No pairs of variables were associated with significant collinearity and so none needed to be excluded from the stepwise regression model (Supplementary Information 3.4.4). Table 3.3 shows for each dataset the most significant variables retained, their partial regression coefficient values (or weights) from the multiple linear regressions and the statistics comparing the observed and the predicted water depth values.

Table 3.3: Stepwise regression outputs. Variable considered into multiple linear regression and predictor relative weights obtained at each step. P-values show that the selected variables composing the multiple linear regressions are statistically significant, while both R-squared and standard deviation of error (SDE) behaviour highlight the effect of a new variable on the overall model prediction capacity.

| Date | Step | Variable | Coefficient b | | | | Statistics | | |
|---|---|---|---|---|---|---|---|---|---|
| | | | $b_0$ | $b_1$ | $b_2$ | $b_3$ | $R^2$ | SDE | p-value |
| 18th August | 1 | Dist. nearest bank | 0.190 | 0.093 | | | 0.375 | 0.138 | $2.2\times10^{-9}$ |
| | 2 | + Divergence | 0.144 | 0.069 | 0.004 | | 0.545 | 0.118 | $4.7\times10^{-9}$ |
| 8th September | 1 | Total Width | 0.371 | -0.012 | | | 0.367 | 0.081 | $7.3\times10^{-7}$ |
| | 2 | + Dist. nearest bank | 0.305 | -0.010 | 0.033 | | 0.450 | 0.075 | $7.2\times10^{-4}$ |
| | 3 | + Convergence | 0.261 | -0.008 | 0.026 | $8.8\times10^{-4}$ | 0.489 | 0.072 | 0.002 |
| 10th September | 1 | Dist. nearest bank | 0.148 | 0.076 | | | 0.434 | 0.088 | $1.3\times10^{-11}$ |
| | 2 | + Divergence | 0.134 | 0.064 | 0.001 | | 0.537 | 0.079 | $2.3\times10^{-6}$ |
| | 3 | + Convergence | 0.138 | 0.069 | 0.003 | -0.003 | 0.610 | 0.073 | $2.6\times10^{-4}$ |

Differences in the retained variables and their coefficients were found between dates although all of them include distance from the nearest stream bank. The model describing water depth distribution for the 18th of August 2020 has only two predictors (i.e. distance from nearest bank and distance from nearest divergence region), while the 8th of August and the 10th September 2020 datasets identified three. Levels of explained variance ($R^2$) for the final models are relatively high but differ between dates; and the standard deviations of error are between ±0.07 and ±0.12 m. These are degraded as compared with the precision of the dGPS instrument when used in this setting (between ±0.02 m and ±0.04 m).

The results of application of the prediction model for each date (Table 3.3) are shown in Figure 3.6 after correction for changing stage between the start and the end time of UAV surveys (Supplementary Information 3.4.3).
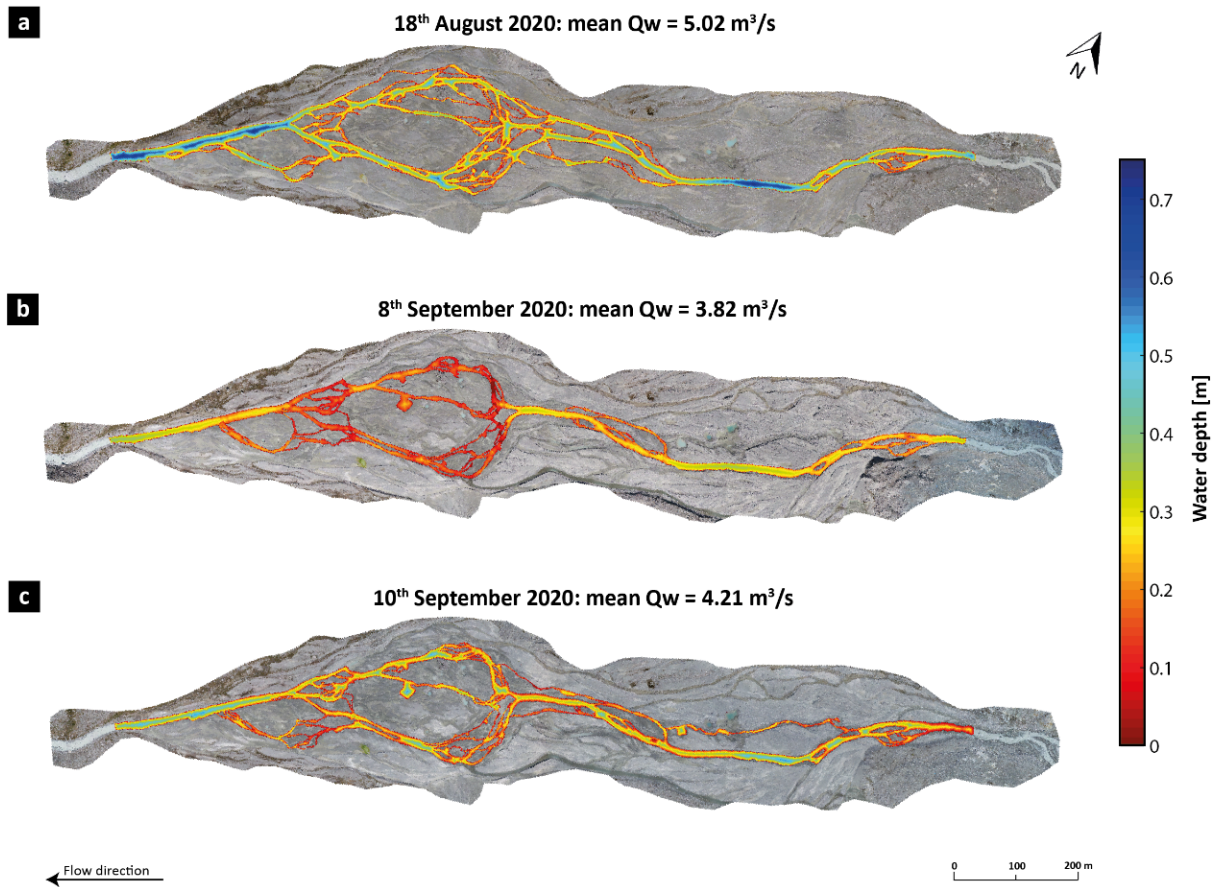


Figure 3.6: Predicted water depth corrected by the changing water stage occurred along the UAV surveys. Mean discharge rates during both UAV-survey and water depth acquisitions are: 5.29 m³/s on the 18th of August, 2.98 m³/s on the 8th of September and 3.11 m³/s on the 10th of September (Figure 3.1).

Water depth predictions (Figure 3.6) are higher in regions characterized by a straight fluvial configuration, notably in the the most upstream and downstream parts of the study area. In contrast, predictions are more variable and shallower in the braided sectors, although increasing depths are recorded in regions coinciding with flow confluence regions.

Using the validation datasets, we evaluated the predictive capacity of the multiple linear regression models (Figure 3.1, Table 3.2 and Figure 3.7). The comparison against independent measurements shows that, as implicit in differing statistical success in the calibration results (Table 3.3), models have different predictive performances.
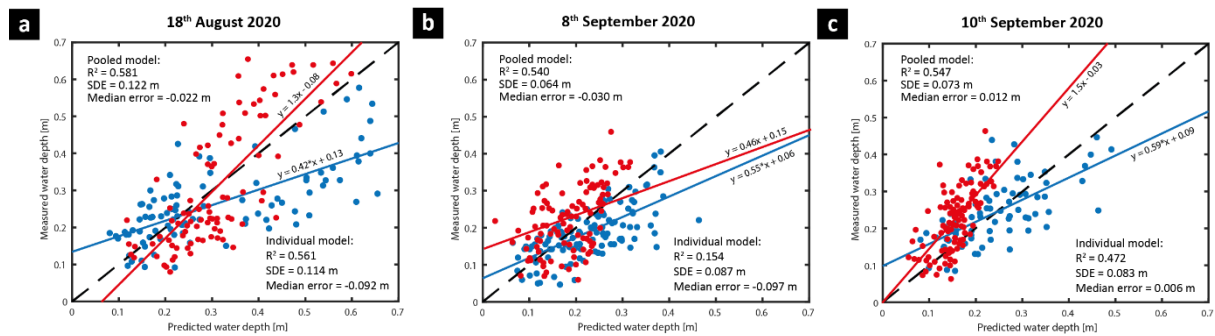
Figure 3.7: Validation plots comparing the predicted and the measured water depths observed in location showed in Figure 3.1 for individual (red) and pooled (blue) models.

The 18th of August and the 10th of September validation datasets had the highest $R^2$ values of respectively 0.561 and 0.472 (Figure 3.7a and Figure 3.7c). However, they both tend to over-estimate the measured water depths in shallower regions (up to ca. 0.27 m and ca. 0.05 m, respectively) and to under-estimate deeper ones, especially for the 10th of September. The residual errors for the latter have a wider range (Figure 3.8a). The model for the 8th September is the one with the lowest $R^2$ (0.154, Figure 3.7b) and has an opposite relation compared to that described for the other two datasets with under-estimation for shallower regions (up to ca. 0.27 m) and over-estimation for deeper ones.

Figure 3.8 shows the residual errors associated with validation points (Figure 3.1 and Table 3.2). On the 8th of September, errors are between ca. -0.25 m and +0.1 m, with some outliers falling outside these limits mostly located in secondary channels in the braided sector. On September 10th, the error range is similar but more symmetrical around zero (ca. -0.18 to +0.18 m) with larger errors mainly located in the main channel. The 18th August dataset has the widest distribution of error compared to the other two datasets with points having differences as low as -0.35 m and as big as +0.13 m: higher errors are generally in the main channel, while in the braided sector they are generally limited to -0.05 to -0.1 m. These results show that the individual models vary in both their precision and their bias.
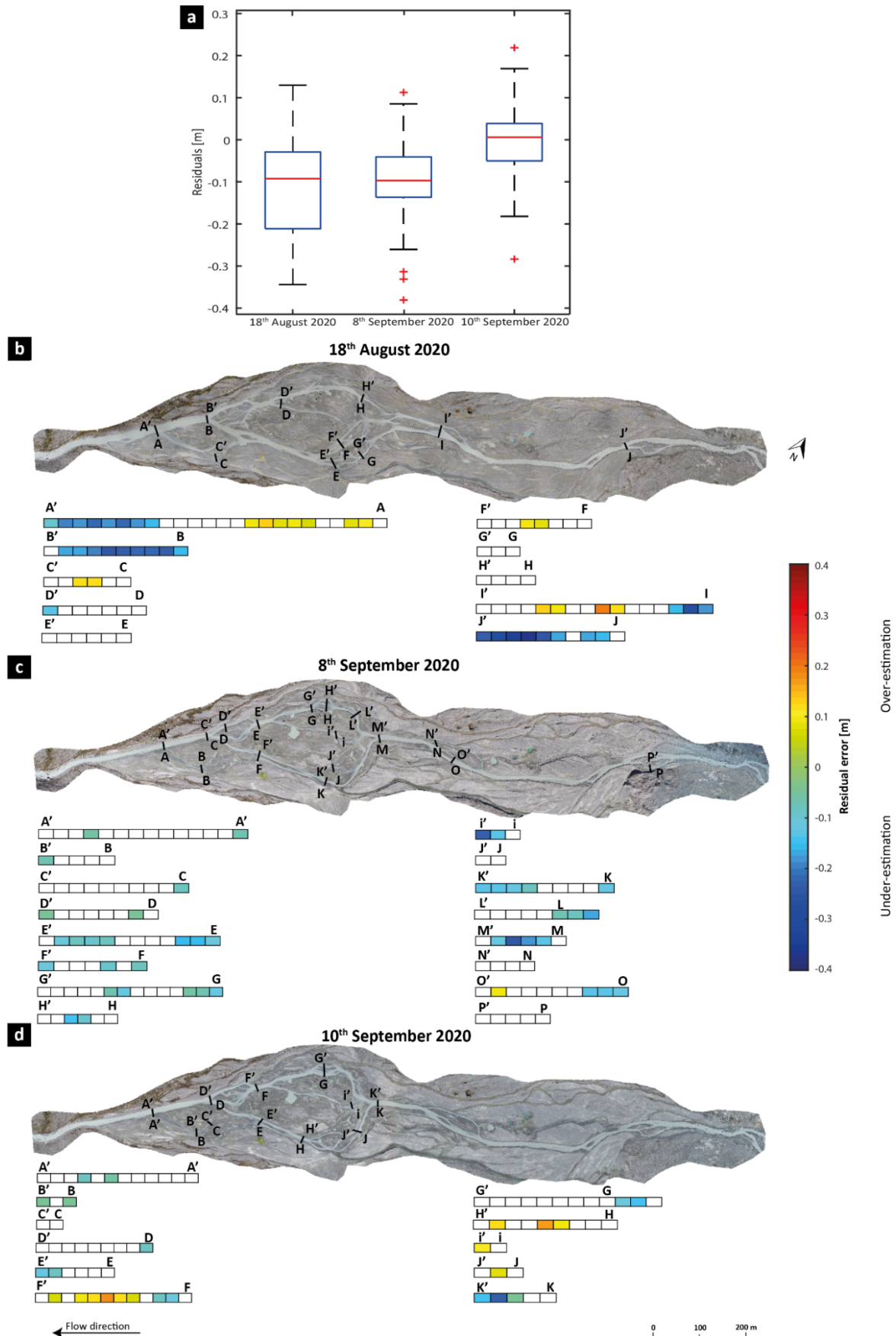
Figure 3.8: Boxplots (a) and spatial distribution of residual errors (b to d) for individual calibrated models. Errors in the interval defined by ± the standard deviation of error (SDE, Figure 3.7) are showed as white. Positive values highlight that the model under-estimate the measured water depth (predictions are shallower than measured data), while negative values refers to over-estimation (predictions are deeper than measured data).

### 3.2.3.2 Pooled model

Given mixed validation results when applying the modelling approach to individual datasets, we developed a single model and applied it individually to the three dates for which validation data are available. The correlation matrix and the VIF values for the merged calibration dataset were not collinear (Supplementary Information 3.4.5). Table 3.4 shows the application of the stepwise regression approach to define the generalized multiple linear regression model.

Table 3.4: Stepwise regression approach applied the merged 2020 datasets

| Step | Variable | Coefficient b | | | | | | Statistics | | |
|---|---|---|---|---|---|---|---|---|---|---|
| | | $b_0$ | $b_1$ | $b_2$ | $b_3$ | $b_4$ | $b_5$ | $R^2$ | SDE | p-value |
| 1 | Dist. nearest bank | 0.147 | 0.083 | | | | | 0.355 | 0.118 | $2\times10^{-26}$ |
| 2 | + Total width | 0.132 | 0.073 | 0.001 | | | | 0.560 | 0.115 | $3\times10^{-10}$ |
| 3 | + Convergence | 0.128 | 0.076 | 0.052 | 0.001 | | | 0.648 | 0.113 | $8\times10^{-8}$ |

The most significant explanatory variables retained differ from those found when applied individually (Table 3.3); distance from the nearest river bank; total inundated width; and distance from the nearest convergence region. The resultant $R^2$ of 0.648 suggests a statistically significant relation between the retained predictors and the response variable. The standard deviation of error was ±0.113 m (Table 3.4).

The qualitative assessment of water depth distribution is in line with that described above for the individual calibrated models (Figure 3.9): deeper water in the upstream and downstream parts of the study area where the river is more confined; shallower in the braided sector with more variability in regions affected by flow convergence. Predicted depths are generally higher for the August dataset, confirming that the generalized model is able to discriminate between higher and lower flow conditions (Figure 3.1 and Figure 3.9a). However, the comparison between water depth maps issued using individual calibrated and pooled models reveals that for the pooled model, predictions are slightly shallower for the 18th of August dataset, deeper for the 8th of September, while consistent for the 10th of September (Figure 3.6 and Figure 3.9).
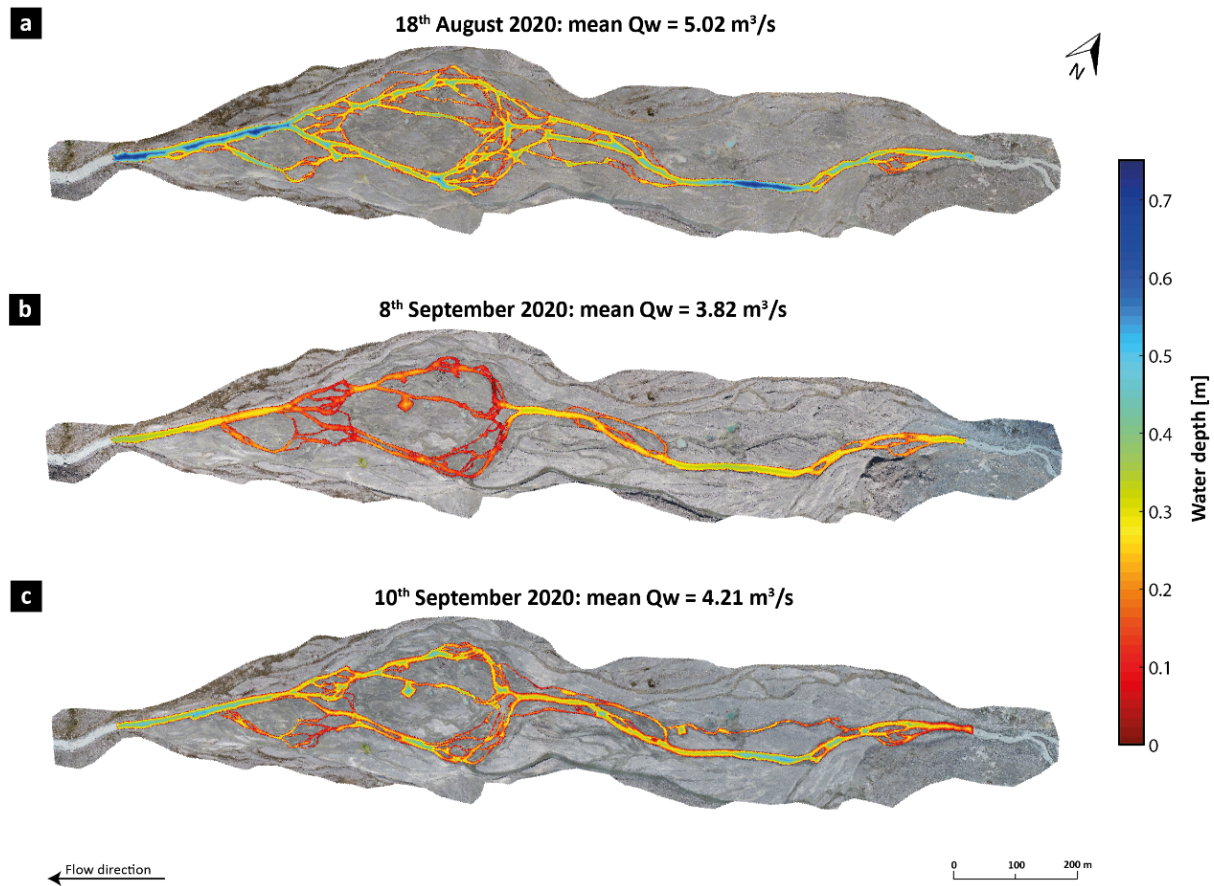
Figure 3.9: Spatial distribution of water depths issued from the application of the pooled model. Obtained water depths were corrected by the changing water stage occurred along the UAV surveys. Mean discharge rates during both UAV-survey and water depth acquisitions are: 5.02 m³/s on the 18th of August, 3.82 m³/s on the 8th of September and 4.21 m³/s on the 10th of September (Figure 3.1).

The validation analyses show that the pooled model produces better results than individual models with the obtained $R^2$ values between 0.5 and 0.6 for all datasets (Figure 3.7). Despite this, relations all have a common tendency to slightly under-estimate shallower depths and to over-estimate deeper ones, especially for the 18th of August (Figure 3.7a and Figure 3.10a). The better performance of the pooled model is also confirmed by the residual errors, which are smaller compared to the individual models with median errors more generally centred on zero and the error range and the outliers more contained (Figure 3.8a and Figure 3.10a). The pooled calibration approach reduces the errors in the downstream end of the floodplain where the channel is straight, but also in secondary channels composing the most braided sector (Supplementary Information 3.4.6). Especially for the 18th of August dataset, occasional and significant under-estimations are still found in confined flow regions.
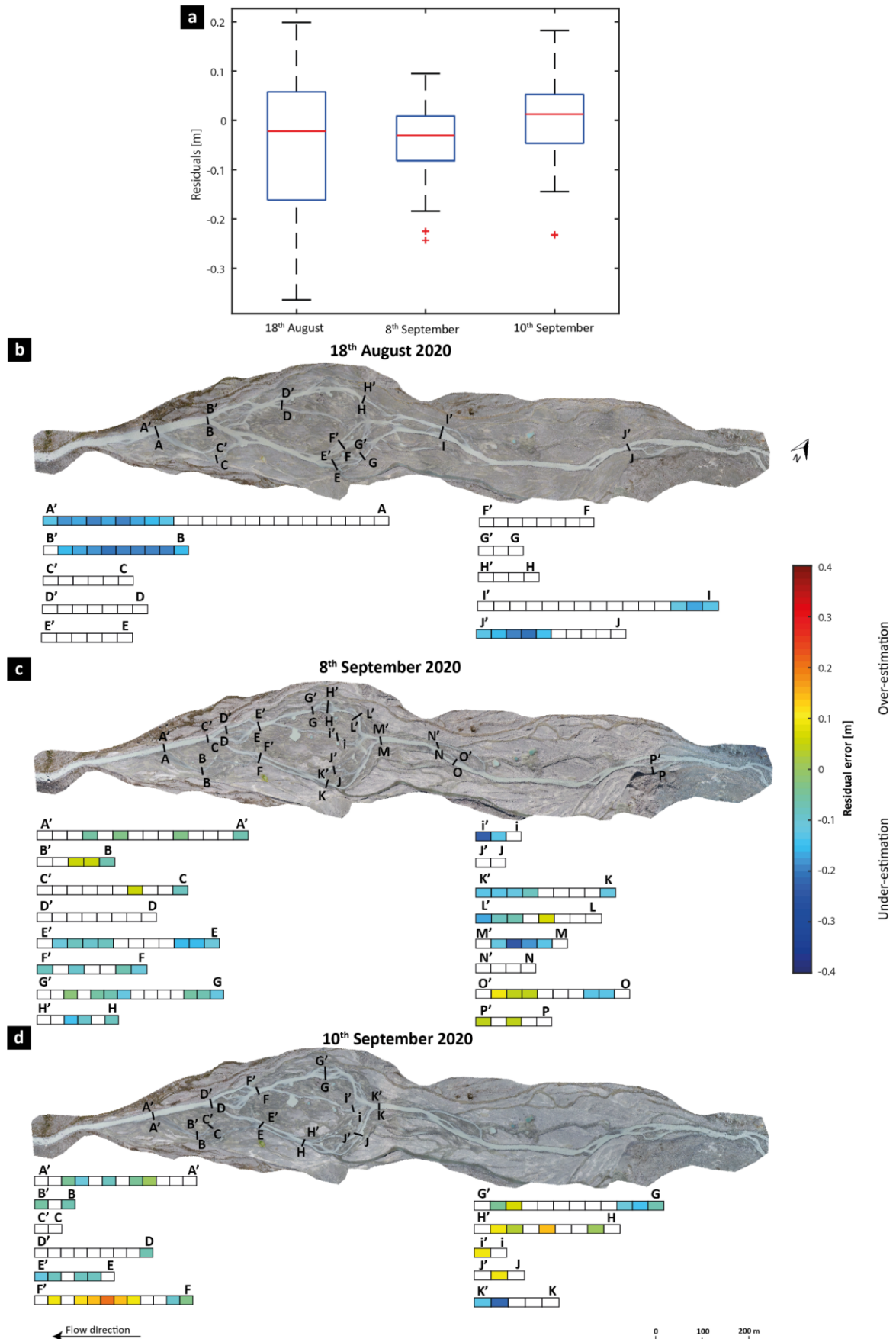
Figure 3.10: Boxplots (a) and spatial distribution of residual errors (b to d) for pooled model. Errors in the interval defined by ± the standard deviation of error (SDE, Figure 3.7) are showed as white. Positive values highlight that the model under-estimate the measured water depth (predictions are shallower than measured data), while negative values refers to over-estimation (predictions are deeper than measured data).

109

### 3.2.3.3 Model inter-comparison

Table 3.5 compares the prediction capacity for both specific and pooled models. The latter appears to improve the relationships between the measured and the predicted water depths increasing all $R^2$ values, while the residual errors improves for two of the three datasets.

Table 3.5: Comparison between validation R-squared valued and residual error obtained with the application of individually calibrated models and the generalized one.

| Date | Statistics | Individual model | Pooled model | % Difference |
|---|---|---|---|---|
| 18th August 2020 | $R^2$ | 0.561 | 0.581 | |
| | Median [m] | -0.092 | -0.022 | -70.21 |
| | SDE [m] | 0.114 | 0.122 | +12.54 |
| 8th September 2020 | $R^2$ | 0.154 | 0.540 | |
| | Median [m] | -0.097 | -0.030 | -68.64 |
| | SDE [m] | 0.086 | 0.064 | -25.90 |
| 10th September 2020 | $R^2$ | 0.472 | 0.547 | |
| | Median [m] | 0.006 | 0.012 | -60.32 |
| | SDE [m] | 0.083 | 0.073 | -10.84 |

Differences in water depths between the individual and the pooled models primarily impact single channel zones (Figure 3.11). In these regions, differences for the 18th of August are between ca. +0.05 m and +0.30 m and for the September dates they are between -0.20 m to -0.05 m. In secondary channels within the more braided section the differences are smaller, between ca. -0.1 m and +0.1 m in all datasets. Thus, although the pooled model produces more reliable results than the individual model (Table 3.5), model performances are more similar for braided zones. In deeper areas the pooled model performs much better (see Supplementary Information 3.4.6 for comparisons).
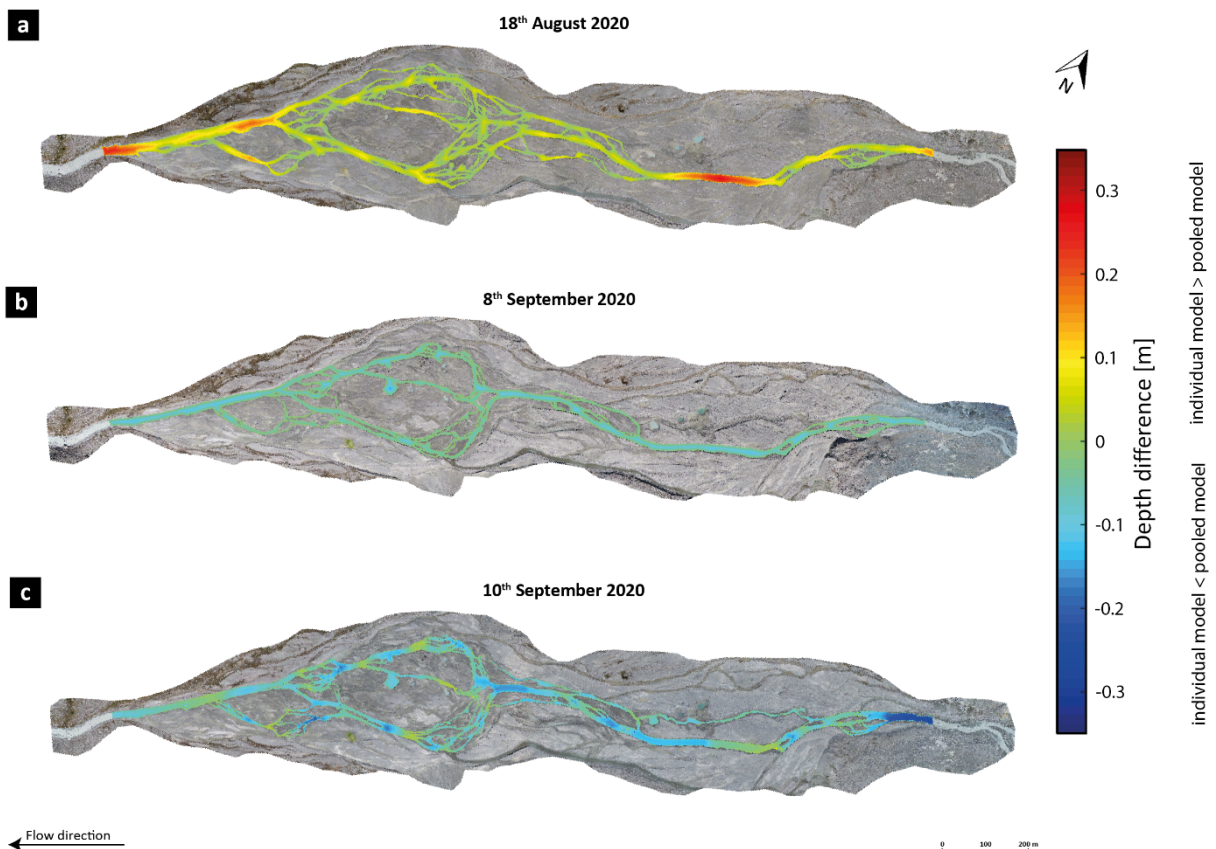


Figure 3.11: Depth of difference maps computed by subtracting predictions issued from the individual models from those given by the pooled one.

### 3.2.3.4 Uncertainty and spatial patterns of levels of detection

The spatial distribution of elevation uncertainty for both dry and wet surfaces were generated for both individual and pooled models following Eq. 3.5 (Figure 3.12).
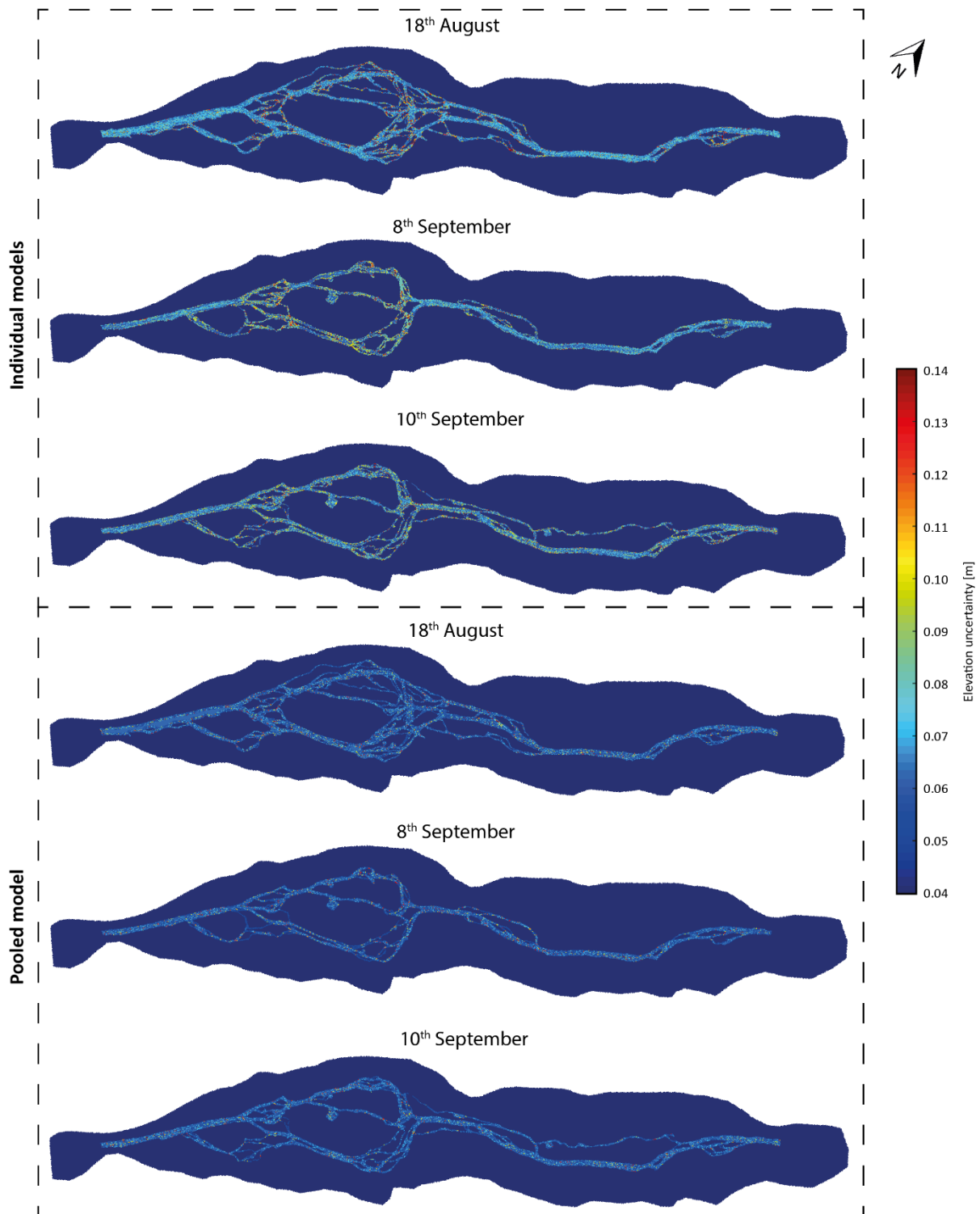


Figure 3.12: Spatial distribution of elevation uncertainty for water depth maps predicted using both individual and pooled models. Dry regions (in dark blue) have lower uncertainties compared to inundated regions.

Elevation uncertainties are higher for the individual models than for the pooled model. Individual models had elevation uncertainties between ±0.05 m and ±0.12 m for the 18th

August, between ±0.035m and ±0.08 m for the 8th of September and between ±0.04 m and ±0.09 m for the 10th of September dataset (Figure 3.13a). The pooled model had lower uncertainties of ±0.035 m to ±0.06 m in all datasets. These were not uniform in space, with the braided sector and narrower channels having higher uncertainties compared to single-thread and wider channels (Figure 3.12).
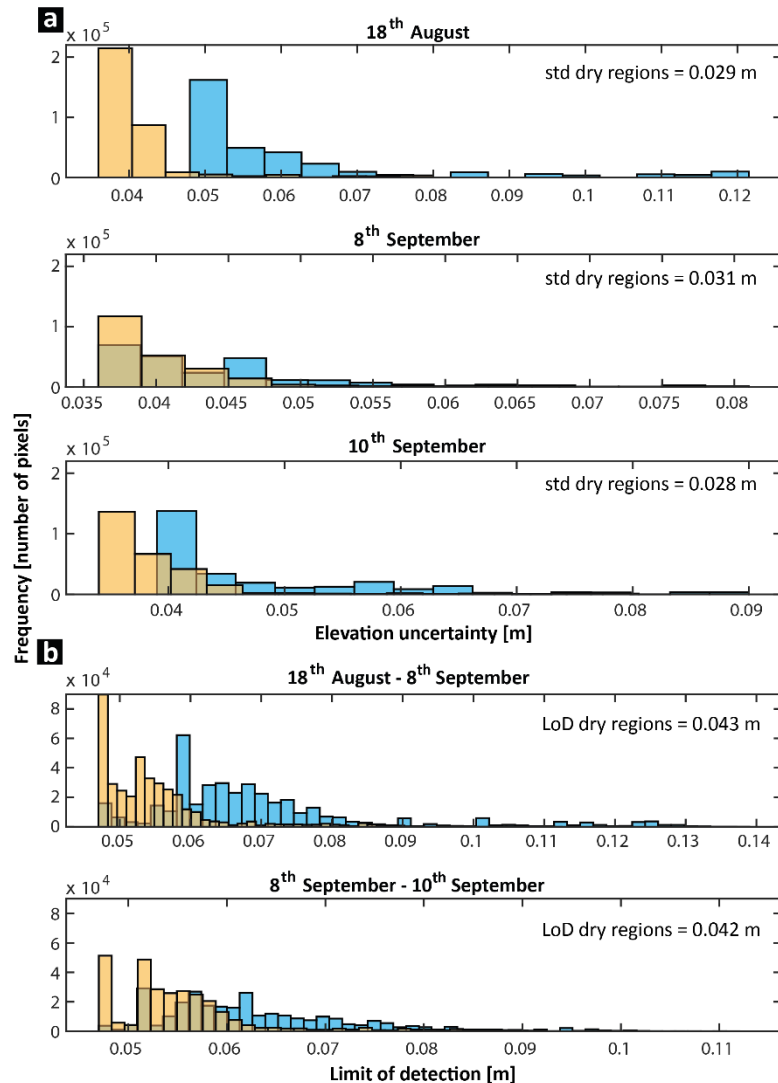


Figure 3.13: Histograms of the frequency (i.e. number of cells) for both (a) elevation uncertainty and (b) limits of detection for permanently inundated and transient regions. Light blue refers to results issued using the individual calibrated models, while the light orange one to those obtained using the pooled model.

The spatial distribution of LoDs (Eq. 3.6) is highly variable in space, and higher than when the individual calibrated models were used (Figure 3.13b). Given that wet areas are more uncertain (Figure 3.13a), elevation changes in zones permanently inundated were substantially higher. For the individual models, these are ±0.045 m to ±0.14 m for changes between the 18th of August and the 8th of September and between ±0.045 m to ±0.11 m for the period between the 8th September and the 10th September. These are substantially higher than the uncertainties for dry to dry elevation changes (±0.042 and ±0.043 m). However, limits of detection associated with the pooled model are lower, ranging between ±0.045 m and ±0.09 m, and only marginally higher than the mean $D_{50}$ of 0.06m. Thus, implementation of the pooled model reduces elevation uncertainty and improves the detection of morphological change.
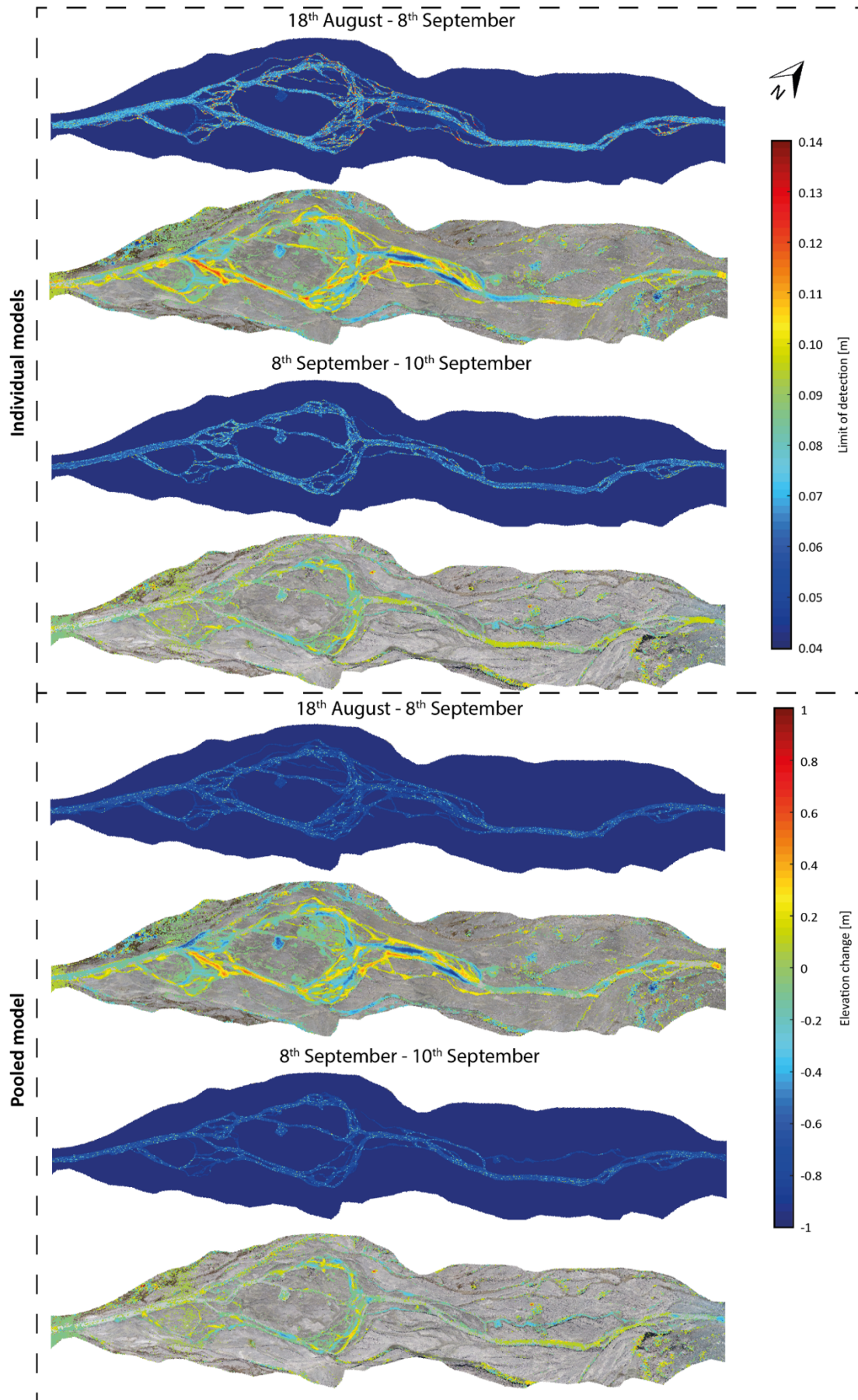
Figure 3.14: Spatial distribution of limits of detection (upper maps) for water depth prediction maps obtained using both individual and pooled models, and associated significant elevation changes (lower maps).

### 3.2.3.5 Volumetric change estimates

Table 3.6 shows the volume change estimates for regions staying inundated and/or dry within surveys, but also for transient areas (i.e. inundated to dry or dry to inundated). During the investigated period, the proglacial forefield went through net erosion in areas that were both dry (but became inundated at higher discharges) and both inundated on the survey dates presented here. Irrespective of the model used to predict water depth distributions, the vast majority of the erosion took place in inundated regions, or in areas inundated on one of the two dates concerned with contributions to the total volumetric change of up to 69.8%. Transient regions going from wet to dry are associated with deposition (Table 3.6). Volumetric changes for transient regions (wet-dry or dry-wet) account for more than half of the total volumetric changes at the forefield scale. Dry only regions, as might be expected, witness relatively less change (up to 15.8% of the total volumetric change). It seems that at the seasonal scale, in this case, significant morphodynamic re-organization was spatially-restricted to specific areas of the proglacial margin. Volume of change estimates from elevation difference maps are slightly higher when the pooled model is considered for determining water depth distribution, confirming observations related to Figure 3.11.

Table 3.6: Volumetric change estimates [m$^3$] in dry, inundated and transient (i.e. dry to wet and wet to dry) regions issued from DoD maps involving DEMs of both dry and wet areas (Figure 3.14).

| Model | Period | Total volumetric change [m$^3$] | Sectorial volumetric change [m$^3$] | | | |
|---|---|---|---|---|---|---|
| | | | Before | | | |
| | | | Wet | Dry | | |
| individual | 18th August - 9th September | 3.322 x 10$^3$ | -1374 (37.4%) | -710.3 (21.4%) | Wet | |
| | | | 1011 (26.4%) | -434.2 (15.8%) | Dry | |
| | 9th September - 10th September | 555.2 | -66.07 (11.9%) | -366.2 (66.0%) | Wet | |
| | | | 114.6 (20.6%) | -8.438 (-1.5%) | Dry | After |
| Pooled | 18th August - 9th September | 3.436 x 10$^3$ | -1374 (40.0%) | -724.1 (21.1%) | Wet | |
| | | | 903.8 (26.3%) | -434.2 (12.6%) | Dry | |
| | 9th September - 10th September | 557.3 | -49.23 (8.8%) | -389.2 (69.8%) | Wet | |
| | | | 110.32 (19.8%) | -8.605 (1.5%) | Dry | |

### 3.2.4 Discussion

### 3.2.4.1 Evaluation of specific and pooled models for water depth prediction

The predictive models we develop for water depths in shallow, turbid, glacier-fed braided streams, especially that for the pooled dataset, are encouraging (Table 3.5). Single calibration models did differ between themselves in terms of predictors and performances (Table 3.3). The distance from the nearest bank variable was common to all models but three of the remaining four variables (total width, distance from convergence, distance from divergence) did not appear systematically in the models, while curvature did not appear in any of them. These differences between models likely reflect either between-date differences in where and how much data were collected and/or different discharge magnitude at the moment of data acquisition (Figure 3.1, Table 3.2). The extension or the contraction of the proglacial outwash plain due to discharge variation, may have enhanced (or decreased) the importance of certain variables in explaining the measured water depth distributions.

Analysis of $R^2$ values (Figure 3.7) and both magnitude and spatial distribution of standard deviations of error (Figure 3.8) through the validation process also reveals that models have different predictive capacities. We emphasise that our methodology does not involve the removal of outliers during the calibration process. Braided rivers are complex and non-linear geomorphic systems, with a wide range of water depths (Ashmore, 1988; Phillips, 2003), making it difficult to identify outliers. The resulting predictive capacities for the individual models (Table 3.3) are more encouraging than their validation results (Figure 3.7). For instance, the validation relation for the 8th September had a low $R^2$ (0.154, Figure 3.7b) likely because the model struggles to reconstruct the proper bathymetry of braided reaches having shallower depths (Figure 3.7b and Figure 3.8c). In the same way, the model for the 10th of September has a better validation $R^2$ of 0.472 (Figure 3.7c); albeit with some error remaining, including significant predicted under-estimation, much of it located in the main channel rather than in secondary channels composing the most braided sector (Figure 3.8d).

The main problem with the individual models is that they have different retained variables and regression coefficients making their application to dates when no calibration data were available a challenge. The pooled calibration approach produced a single model with three predictors (distance from nearest river bank, total inundated width, and distance from nearest flow divergence region), a final $R^2$ value of 0.648 and a SDE of $\pm 0.113$ m (Table 3.4). Its application using the 2020 datasets produced encouraging results as the validation $R^2$ values were substantially higher than for individual models (Figure 3.7) and the residuals had a lower range of magnitude; the $R^2$ was close to 0.6 for each of the three validation dates, with residual errors of ca. $\pm 0.1$ m (Figure 3.10 and Table 3.5). Predictions and residual errors were better for the September datasets than for the August one likely because of the lower flow conditions (Figure 3.1 and Figure 3.10a). The distributions of residual error were generally within $\pm 0.1$ m for secondary channels, increasing to ca. -0.4 m to +0.3 m in regions characterized by single straight channels (Figure 3.8). Thus, despite the occurrence of a certain degree of error in the predicted water depths, a multiple linear regression constructed using a greater number of samples collected during different discharge and morphological conditions has a better performance compared to daily models (Table 3.5; Supplementary Information 3.4.6).

The final water depth distributions resulting from the pooled model make qualitative sense. The study area is composed of three sectors each having different fluvial patterns: a highly braided sector in the middle of the proglacial floodplain bounded by a straight channel configuration upstream towards the glacier terminus and downstream at the forefield end (Figure 3.1). The pooled model produces water depth distribution maps (Figure 3.9) that reflect this configuration; water depths are higher for straight stream transects where flow is confined into a single channel, while much lower in the most braided regions (Figure 3.9). Secondary flow, as represented by channel curvature, does not seem to be important in explaining water depth distributions as no models included it (Table 3.3 and Table 3.5). A possible explanation could be related to the high ratio of channel width to water depth, which may not be sufficient to allow development of significant secondary circulation in this system (Nezu et al., 1985).

Water depths are also very heterogeneous in the braided stream sector because of the recurrence of flow divergence and convergence regions (Figure 3.6 and Figure 3.9). Previous studies of the morphodynamics of braided streams show that flow divergence regions are mainly characterized by upstream bar deposition because of flow velocity reduction; in junctions, scouring may occur due to increasing stream power related to an enhancement in flow velocity, also eventually reinforced by secondary circulation if channel geometry permits (e.g. Lisle et al., 1991; Ashworth, 1996; Powell, 1988; Schuurman and Kleinhans, 2015).

On this basis, both the quantitative and the qualitative elements sustain the hypothesis that the heuristic-approach presented here can be used to estimate spatially-distributed water depth patterns in a turbid braided stream (Figure 3.7 to 3.10 and Table 3.5).

### 3.2.4.2 Use of water depth maps for DEM construction and estimation of change volumes

Incorporation of the bathymetric maps into the dry area DEMs allowed us to create complete DEMs for the three dates and to also produce spatially-explicit maps of elevation uncertainty. For the pooled model, elevation uncertainties were ±0.035 m to ±0.06 m in all datasets, comparable to the $D_{50}$ of the study area. The resulting levels of detection in permanently inundated areas was between ±0.045 m and ±0.09 m. Thus, whilst reworking and deposition patterns could be detected for dry-dry changes that were smaller than the mean $D_{50}$ (i.e. 0.06 m), this rose to $1.5D_{50}$ for wet-wet changes. Dry-wet and wet-dry changes lie between these two extremes. This is an encouraging result for using these DEMs for change detection and estimation of volumetric change.

Volumetric change estimates suggest that regions permanently dry in both surveys (but that could be inundated between surveys) contributed less to the total volume change over both temporal scales (1.5% to 15.8%, Table 3.6). Regions permanently wet were those affected by higher reworking over long timescales (37% to 40%, Table 3.6). Transient regions passing from dry to wet recorded more changes over short timescales (66% to 70%, Table 3.6). During the investigated period the proglacial forefield experienced a net phase of incision reflected in both long-term (i.e. 18th August to 8th September) and short-term (i.e. 8th September to 10th September) volumetric quantifications.

Cumulative volumetric change estimates highlight different patterns according to the timescale of analysis: over short timescales the cumulative contribution of transient regions is much higher (>80%) compared to permanently wet and permanently dry regions; the latter become dominant (>50%) over longer timescales of analysis. These match previous observations of the importance of transient fluvial regions in braided rivers, such as bars, in acting as both sediment sinks and sources (e.g. Ashmore, 1982; Ferguson, 1987; Jagers, 2003; Ashmore, 2013). In proglacial margins geomorphic changes that occur underwater are not easily taken into account in volumetric change quantifications because high turbidity impedes measurement of underwater topography using current remote sensing approaches (e.g. Milan et al., 2007; Brasington et al., 2012; Beawert and Morche, 2014). As a consequence, this results in significant underestimation of total volumetric estimates.

### 3.2.4.3 Perspectives for development and application

The errors in depth estimation reported in Table 3.5 are better than the ±0.15 to ±0.30 m errors reported when applying the Beer-Lambert law to lower resolution imagery (i.e. Westaway et al. 2003; Lane et al., 2003; Fonstad and Marcus, 2005), and in line with those of ca. ±0.05 m and ±0.10 m issued from the application of two-media photogrammetry approaches (i.e. Westaway et al., 2001; Woodget et al., 2015; Dietrich, 2017). They are much bigger than the ±10 mm obtained with laser scanning (LiDAR) and multi-beam techniques (i.e. Smith and Vericat, 2014). However, the precisions of our results are better than those of Bures et al. (2019), where authors reported errors up to ±0.30 m, involving a comparable method based on morphometric variables to predict cross-sectional water depths in meandering steams.

Model sensitivities and errors for representing riverbed topography are likely dependent on other factors in addition to sampling strategy, including survey instrument precision, survey point quality, surface complexity and roughness, grid resolution and interpolation method

(Lane et al., 1994; Lane, 1998; Bangen et al., 2016). These affect water depths maps to different degrees irrespective of the used model. However, increasing the total amount of measured water depths during the calibration process and paying attention to their spatial distribution (i.e. main and secondary channels; depth ranges) seems to be of major importance (Lane, 1998). Further analyses have to be done in this regard, but testing of the model according to the above proposed conditions can be limited by the feasibility of collecting water depths measurements in deeper areas and during periods of relatively constant discharge.

The proposed methodology does not take into account the effects of bedforms smaller than bars on the riverbed, such as sand and gravel ripples or dunes and riffle-pool sequences, on water depth distribution (Gomez et al., 1989; Venditti et al., 2017; Dhont and Ancey, 2018). Such features are typical of alluvial rivers flowing on mobile beds (Cartigny et al., 2013). They may be between a few and 10s of centimetres in height in this kind of stream, even if normally always smaller than channel-scale bar forms (Dey, 2014; Venditti et al., 2017). Such bedforms have a riverbed bathymetric expression largely independent of the surficial planimetric configuration of the channel and so are not modelled in our study (Carling, 1999; Carling et al., 2005). These structures are likely to explain a certain degree of error between predicted and measured water depths, especially in secondary channels because of their higher sensitivity to the transition from subcritical to critical flow conditions (Figure 3.8 and Figure 3.10).

That said, despite these sources of uncertainties, both individual and pooled prediction models scale predicted water depths by discharge conditions (i.e. higher predicted water depths for datasets collected at higher flow conditions; Figure 3.6 and Figure 3.9).

Even if the results are encouraging, the model still suffers from methodological issues resulting in local large errors (Supplementary Information 3.4.7). To improve the overall reliability of the predictions, three improvements merit attention. First, as mentioned above, particular attention should be given to the field sampling strategy for collecting water depth measurements as it needs to take into account both shallow (i.e. secondary channels) and deep (i.e. the main channel) reaches of the investigated area for calibration. This may increase the number of variables retained in the multiple linear regressions, and/or improve the predictive capacity of the model. Second, adding more generic topographic and hydraulic variables (i.e. valley bottom slope distribution, local flow velocity,…) to the initial pool of variables could be beneficial to expand the number of factors that can potentially explain water depth distribution in the stepwise approach. Combining the proposed model with another one specifically designed for water depth prediction in straight channels might merit consideration. Third, detection of random errors in water depth prediction maps could be investigated by computing the continuous slope between inundated cells. If the slope within two boundary cells exceeds a given threshold, the local water depth could be considered erroneous. Finally, further improvements may be made to fully automate the algorithm, although the degree of manual correction needed is relatively restricted (i) to classification of turbid water to produce inundated maps, and (ii) to locate flow divergence and convergence regions.

The future application of outputs obtained from the application of our approach are not only limited to quantification of topographic change estimation. The geometrical analyses here go further than the analysis of stream nodes and links of Hiatt et al. (2020), notably in terms of curvature and convergence/divergence estimation, but also wider parameters related to braided rivers and their ecosystems. For instance, data from these analyses have been used to show how braided river morphodynamics condition the access to water for embryonic vegetation succession, notably linked to biofilm development (Roncoroni et al., 2023a). Spatial patterns of water depth and bed elevation are also central to hydraulic modelling whether for understanding spatially-distributed patterns of sediment transport using morphological (e.g.

Antoniazza et al., 2019) or hydraulic (e.g. Williams et al., 2016a,b; Reid et al., 2019) modelling and habitat analysis (e.g. Gabbud et al., 2019a).

### 3.2.5 Conclusions

This study addressed the question of whether the spatial distribution of water depths of shallow braided mountain streams can be estimated based upon five basic planimetric variables derived from heuristic statements of what might influence that distribution. We tested this for three individual datasets for summer 2020, as well as for a pooled model for all datasets. We used a split calibration-validation approach. Results showed that the proposed methodology is promising for obtaining reliable predictions, especially in proglacial streams where the application of remote sensing techniques (e.g. two-media photogrammetry, optical methods) is not suitable due to the high turbidity contents. Using models calibrated using different total water depth measurements and spatial distributions within main and secondary channels produced different results, we observed that the robustness of, and the variables included in, the models appear to be dependent upon survey design. That said, the pooled model involving all datapoints collected in the three datasets gave better results that individual models. However, regardless of the approach used to calibrate the predictive model, the obtained bathymetric maps respect discharge conditions and the basics hydraulic theories, in particular those related to hydraulic geometry and erosion and deposition patterns associated with, respectively, flow divergence and convergence regions.

In the same way, volumetric change estimates computed by integrating water depths maps into DEMs of dry regions suggest that a large proportion of geomorphic changes in these environments occur both underwater and in transient (i.e. zones passing from wet to dry, or vice-versa) zones. However, cumulative effects on the total volumetric change depend on the timescale under investigation: over long temporal scales stable regions contribute the most, while over short timescales are the transient ones which become dominant. These observations highlight the need for (1) a methodological approach to quantify volumetric changes in flooded areas situated in proglacial margins to obtain more reliable quantifications, but also (2) careful consideration of the validity of the proposed statistical approach for bathymetric mapping in turbid braided streams.

### 3.3 Chapter summary

This Chapter has demonstrated that it is effectively possible to predict water depth distribution in braided shallow streams using basic planimetric information and statistical approaches. The proposed methodology appears to be a viable alternative to other remote sensing techniques (e.g. two-media photogrammetry, optical methods) where their application is not suitable due to the high turbidity contents, such as in proglacial streams. The obtained bathymetric maps showed a distribution of water depths consistent with basic hydraulic theories, with deeper and shallower depths in flow divergence and convergence regions, respectively. Additionally, their integration into DEMs of dry regions revealed low uncertainties, suggesting change detection limits smaller than the mean $D_{50}$ for dry-dry changes and 1.5 times the mean $D_{50}$ for wet-wet changes. That said, investigation of model performance highlighted a high sensitivity of water depth estimates to both total number and spatial distribution of field collected data used for calibration. Future studies should consider this to enhance result quality (see Section 6.2).

This Chapter provides the possibility to thoroughly investigate the geomorphic response of a proglacial forefield to subglacial sediment evacuation at the entire floodplain scale, which is the aim addresses in Chapter 4.

## 3.4 Supplementary information

### 3.4.1 UAV surveys and SfM-MVS photogrammetric post-processing

Table S3.1: Acquisition date and time of UAV imagery, mean discharge during data acquisition and total number of collected images with respective total number of tie points in the SfM-MVS post-processing.

| Date | Acquisition time | Mean Qw [m³/s] | Total number of images | Number of images | Number of tie points |
|---|---|---|---|---|---|
| 18th August 2020 | 09:00 - 12:55 | 5.29 | 2629 | 2604 | 744'826 |
| 8th September 2020 | 09:40 - 12:11 | 2.98 | 1959 | 1949 | 582'564 |
| 10th September 2020 | 08:55 - 11:12 | 3.11 | 1849 | 1835 | 533'214 |

Table S3.2: Retained camera model parameters and total number of GCPs used for the bundle adjustment

| Retained parameters in the internal camera model | Number of used GCPs |
|---|---|
| Focal length | |
| Principal point offsets ($C_x$, $C_y$) | |
| Affinity and orthogonally parameters ($B_1$, $B_2$) | 52 (68% of the total) |
| Radial distortions ($K_1$, $K_2$, $K_3$) | |
| Decentering distortions ($P_1$, $P_2$) | |

### 3.4.2 Explanatory morphologic variables
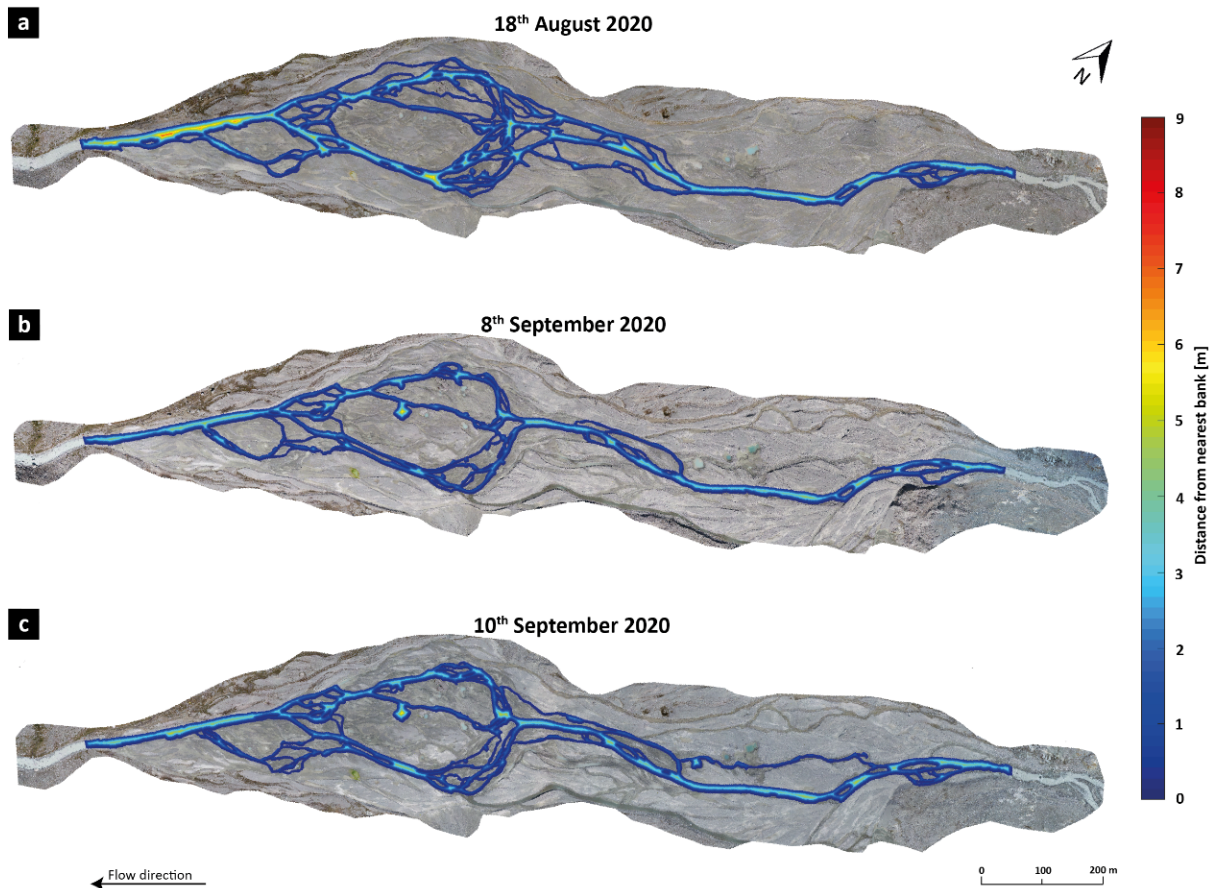


Figure S3.1: Distance from nearest river bank spatial distribution for each dataset under investigation.
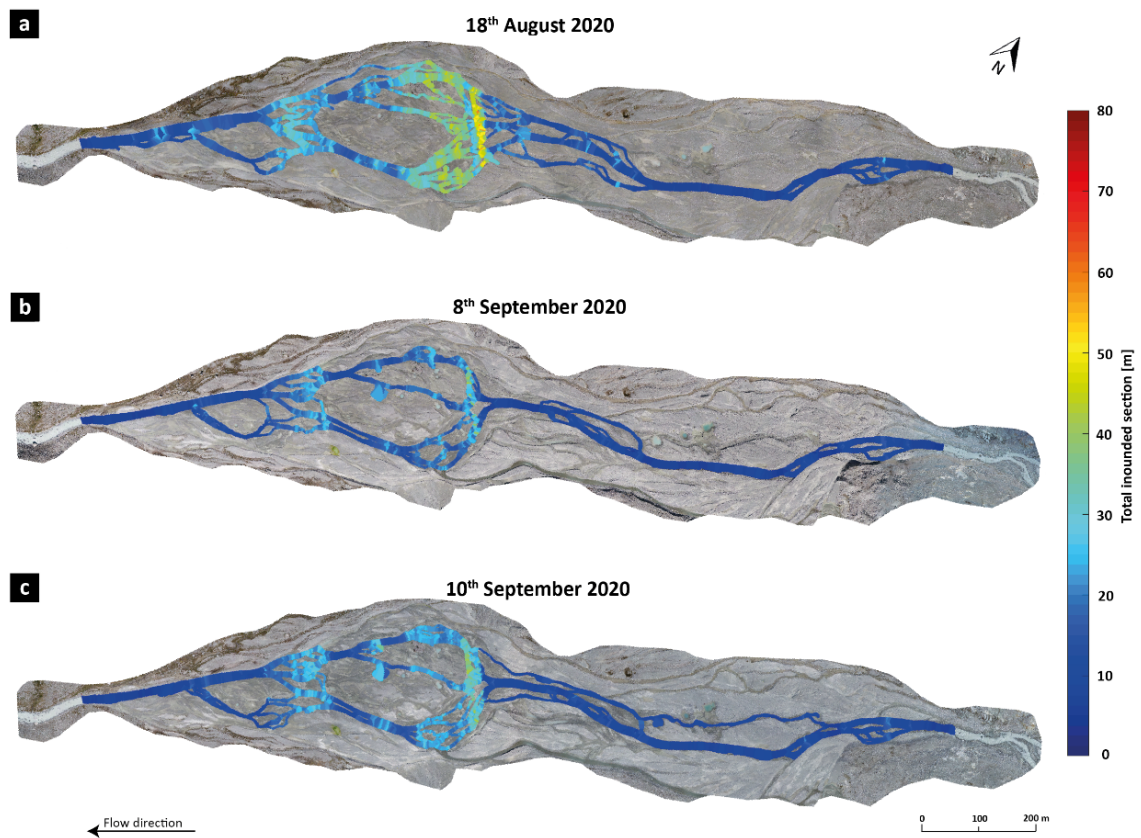
Figure S3.2: Total inundated width quantification for the entire floodplain according to each dataset under investigation.
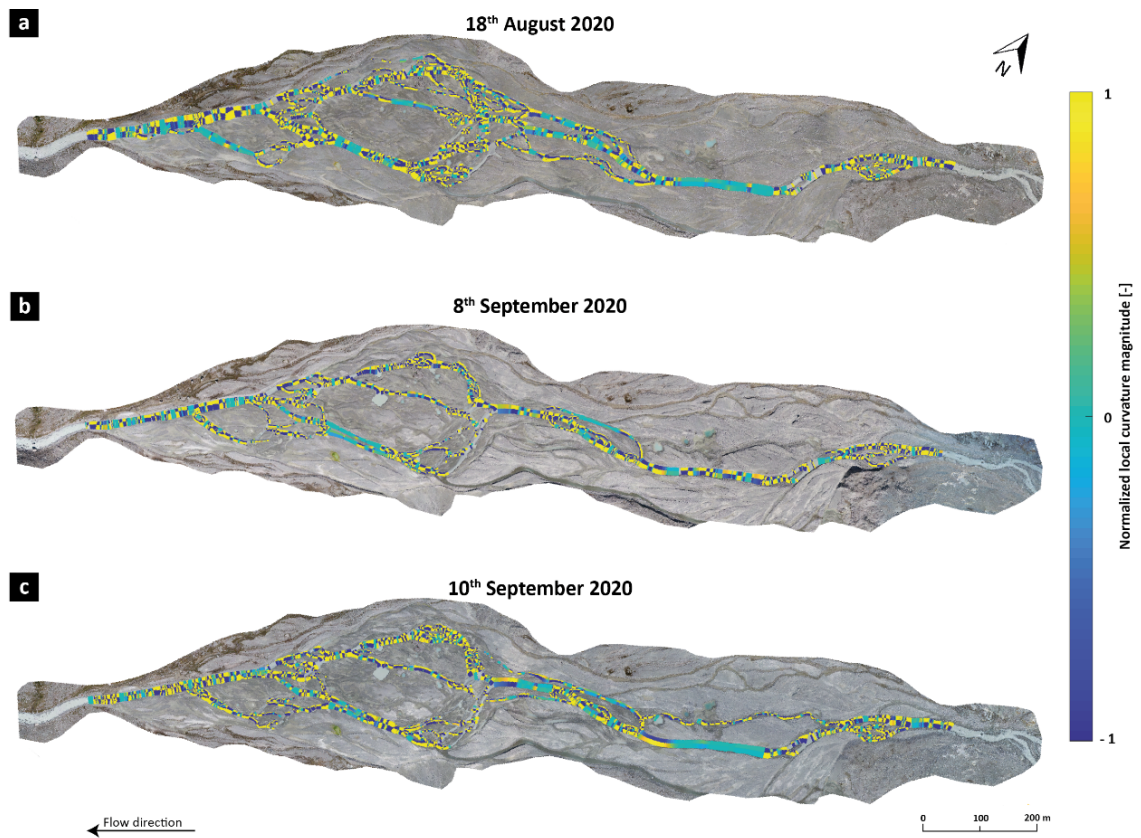


Figure S3.3: Local curvature magnitude and direction for each dataset under investigation. Curvature magnitude values are normalized between 1 and -1 to better show their spatial distribution.
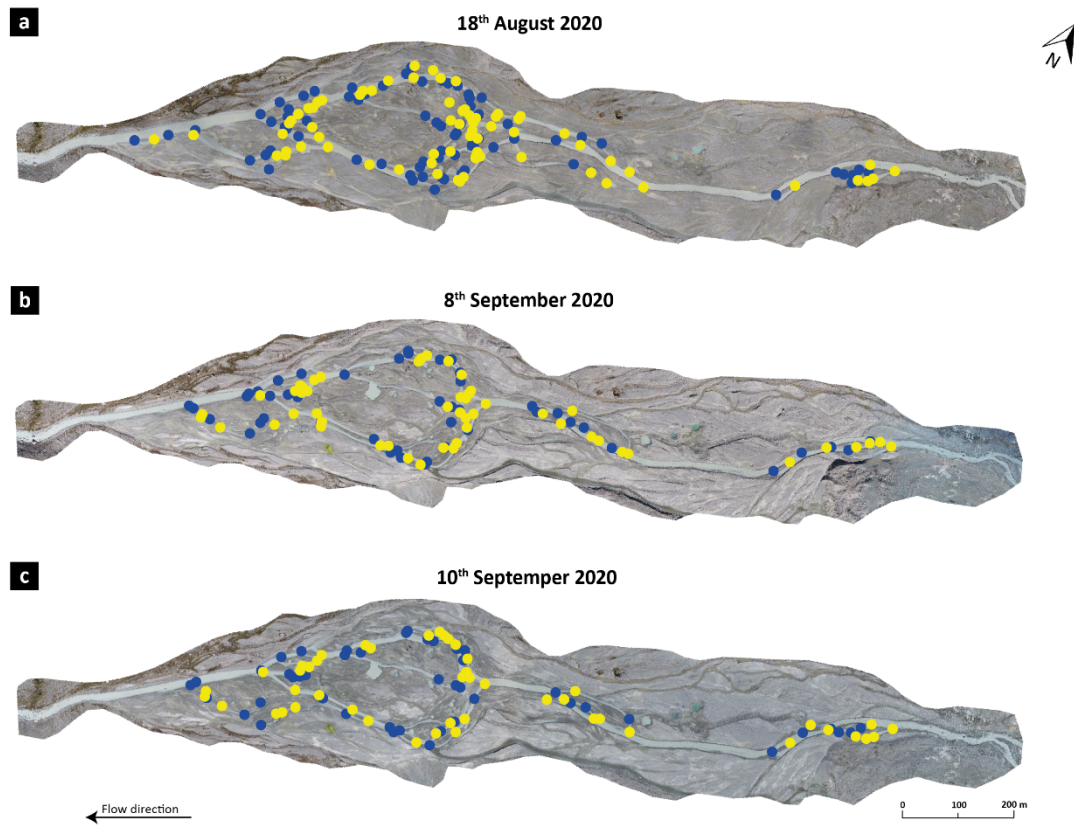
Figure S3.4: Spatial distribution of divergence (yellow dots) and convergence (blue dots) for every dataset under investigation.

### 3.4.3 Correction of predicted water depths

Predicted water depth distribution were corrected by the changing water stage resulting from the increasing subglacial runoff which may have taken place during both UAV and dGPS surveys, having a duration of ca. 3 hours. As a water pressure sensor is installed at the end of the forefield, we were able to correct the water depth predictions by integrating an approximation of the temporal change in water stage along the UAV survey. Knowing the starting and ending time of the drone surveys, as well as the associated water depth at those specific moments, we generated a matrix representing the linear evolution of water stage trough time. This latter is then subtracted from the obtained water depth prediction matrices in order to standardize them by the time.
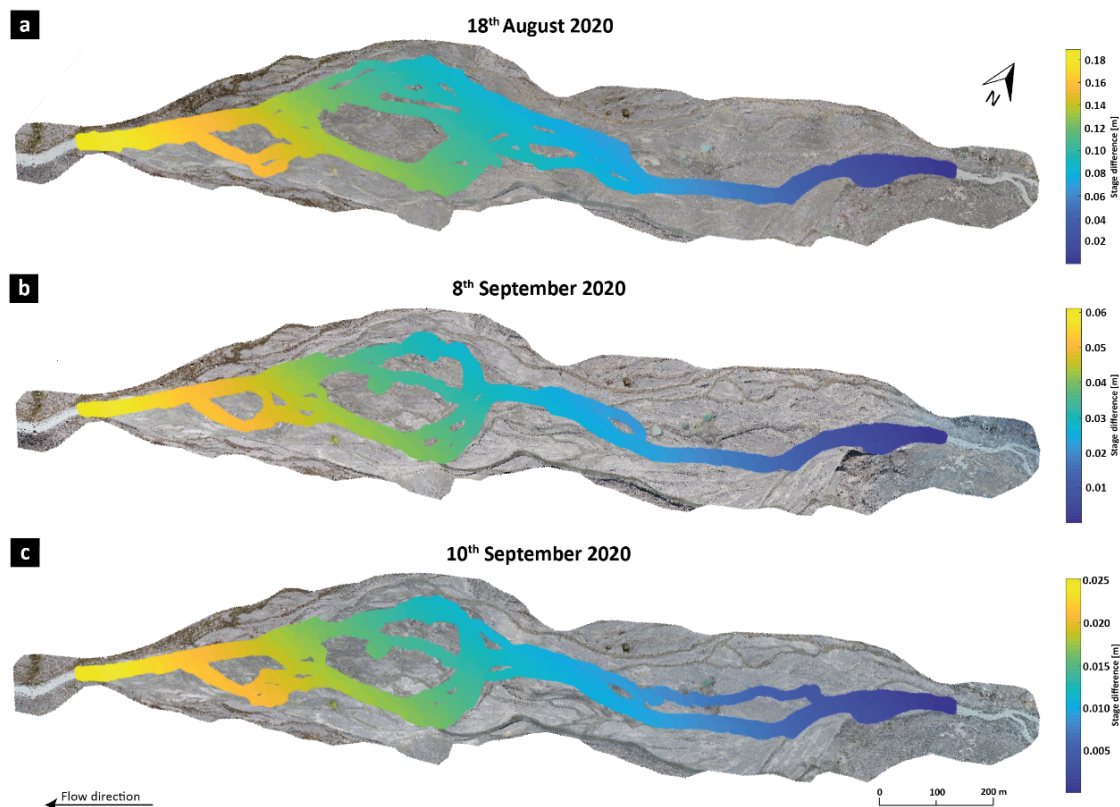
Figure S3.5: Predicted stage difference between the dGPS sampling time and the end of UAV flights.

### 3.4.4 Statistical models of water depth: preliminary analysis of morphometric variables, model calibrations and predictions

Table S3.3: Correlation matrix and VIF values related to the candidate explanatory variables.

| | | Correlation matrix | | | | | |
|---|---|---|---|---|---|---|---|
| | Variable | 1. Distance from nearest bank | 2. Total inounded width | 3. Curvature magnitude and direction | 4. Distance from nearest flow divergence | 5. Distance from nearest flow convergence | VIF |
| **18th August 2020** | 1 | 1 | -0.322 | 0.020 | 0.361 | 0.248 | 1.165 |
| | 2 | | 1 | 0.050 | -0.742 | -0.589 | 2.128 |
| | 3 | | | 1 | 0.094 | 0.031 | 1.041 |
| | 4 | | | | 1 | 0.461 | 3.412 |
| | 5 | | | | | 1 | 2.416 |
| **8th September 2020** | 1 | 1 | -0.338 | -0.072 | 0.370 | 0.418 | 1.264 |
| | 2 | | 1 | 0.070 | -0.589 | -0.546 | 1.508 |
| | 3 | | | 1 | -0.075 | 0.009 | 1.043 |
| | 4 | | | | 1 | 0.469 | 4.513 |
| | 5 | | | | | 1 | 4.152 |
| **10th September 2020** | 1 | 1 | -0.113 | -0.233 | 0.313 | 0.342 | 1.210 |
| | 2 | | 1 | 0.473 | -0.489 | -0.495 | 1.716 |
| | 3 | | | 1 | -0.179 | -0.181 | 1.375 |
| | 4 | | | | 1 | 0.350 | 3.350 |
| | 5 | | | | | 1 | 3.712 |

Table S3.4: R-squared values between the measured water depth and the explanatory variables.

| Date | Variable | | | | |
| --- | --- | --- | --- | --- | --- |
| | 1. Distance from nearest bank | 2. Total inounded width | 3. Curvature magnitude and direction | 4. Distance from nearest flow divergence | 5. Distance from nearest flow convergence |
| 18th August 2020 | 0.375 | 0.172 | 0.001 | 0.366 | 0.145 |
| 8th September 2020 | 0.225 | 0.367 | 0.029 | 0.268 | 0.313 |
| 10th September 2020 | 0.434 | 0.099 | 0.009 | 0.261 | 0.182 |

### 3.4.5 Correlation matrix and VIF values for the calibration of the pool model

Table S3.5: Correlation matrix and VIF values for the 2020 merged dataset

| Variable | 1. Distance from nearest bank | 2. Total inounded width | 3. Curvature | 4. Distance from nearest flow divergence region | 5. Distance from nearest flow convergence region | VIF |
| --- | --- | --- | --- | --- | --- | --- |
| 1 | 1 | -0.181 | -0.099 | 0.313 | 0.317 | 1.124 |
| 2 | | 1 | 0.210 | -0.484 | -0.505 | 1.408 |
| 3 | | | 1 | -0.059 | -0.067 | 1.056 |
| 4 | | | | 1 | 0.113 | 1.024 |
| 5 | | | | | 1 | 1.206 |

## 3.4.6 Visual comparison between measured and predicted water depths
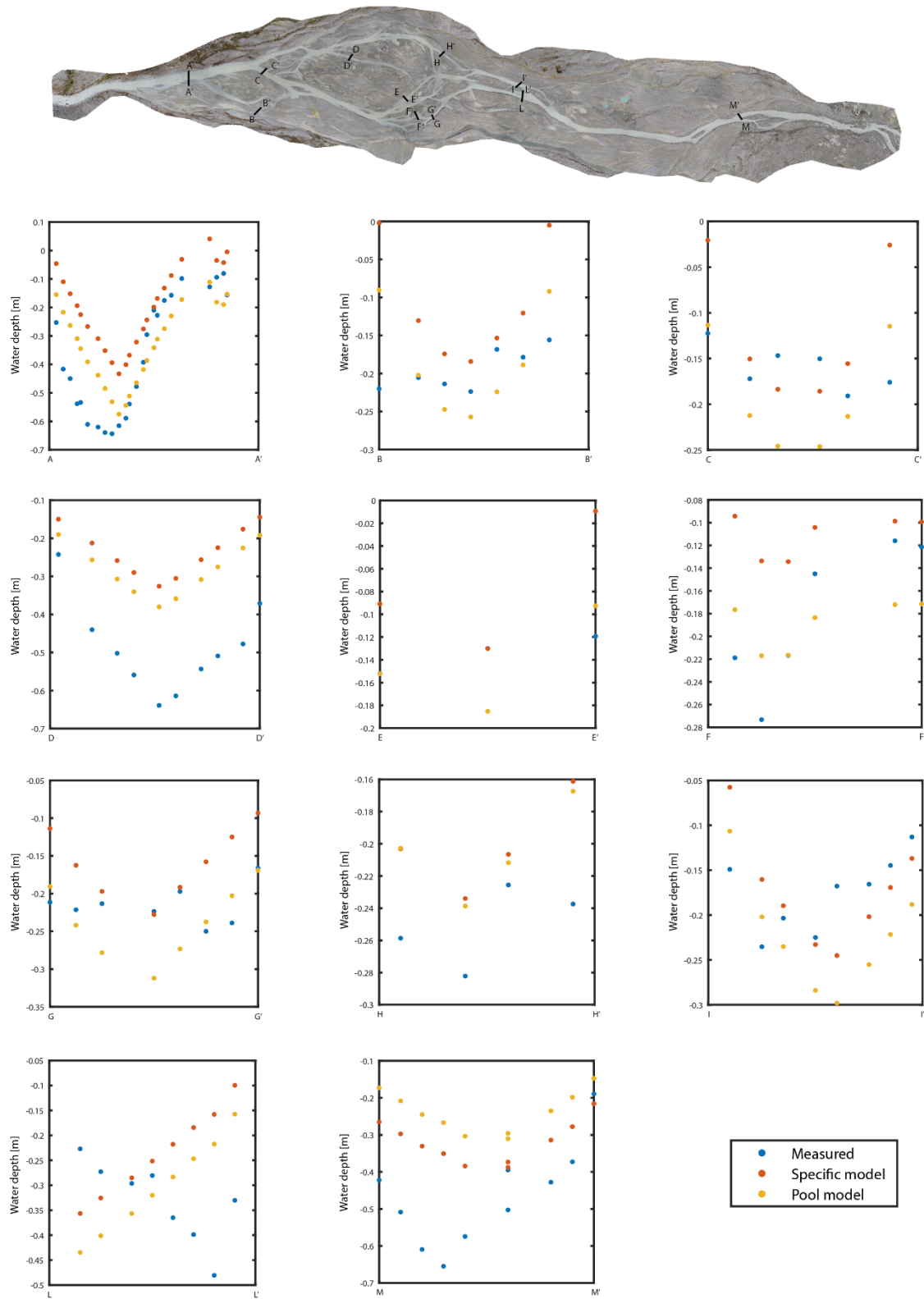


Figure S3.6: Comparison between measured water depths (blue dots) and predictions issued from the specifically calibrated (orange dots) and the generalized model (orange light dots) for transects composing the 18th August 2020 validation sub-dataset.
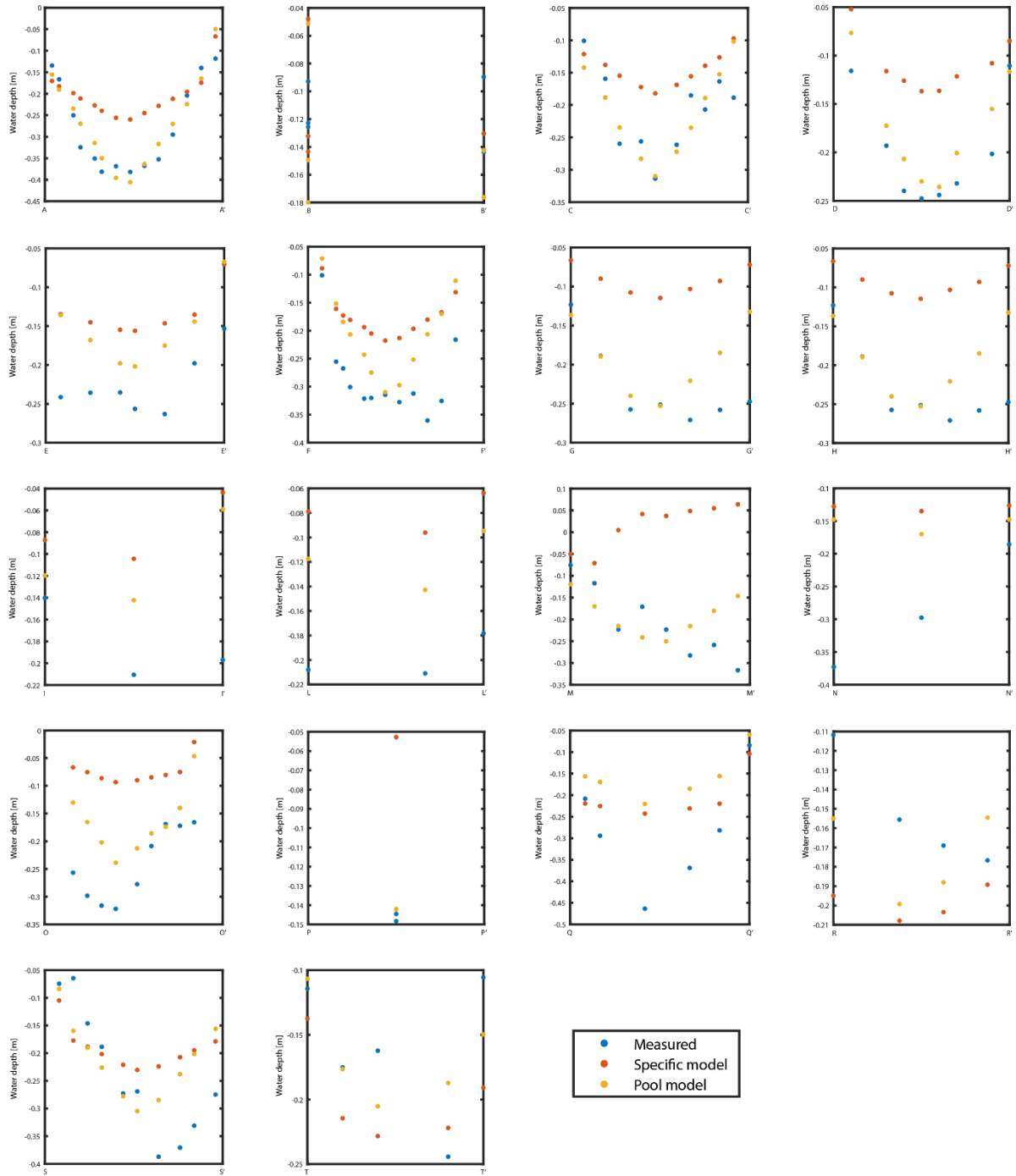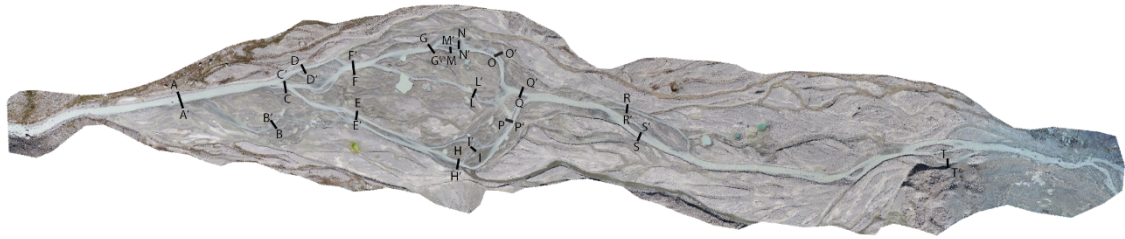
Figure S3.7: Comparison between measured water depths (blue dots) and predictions issued from the specifically calibrated (orange dots) and the generalized model (orange light dots) for transects composing the 8th September 2020 validation sub-dataset.
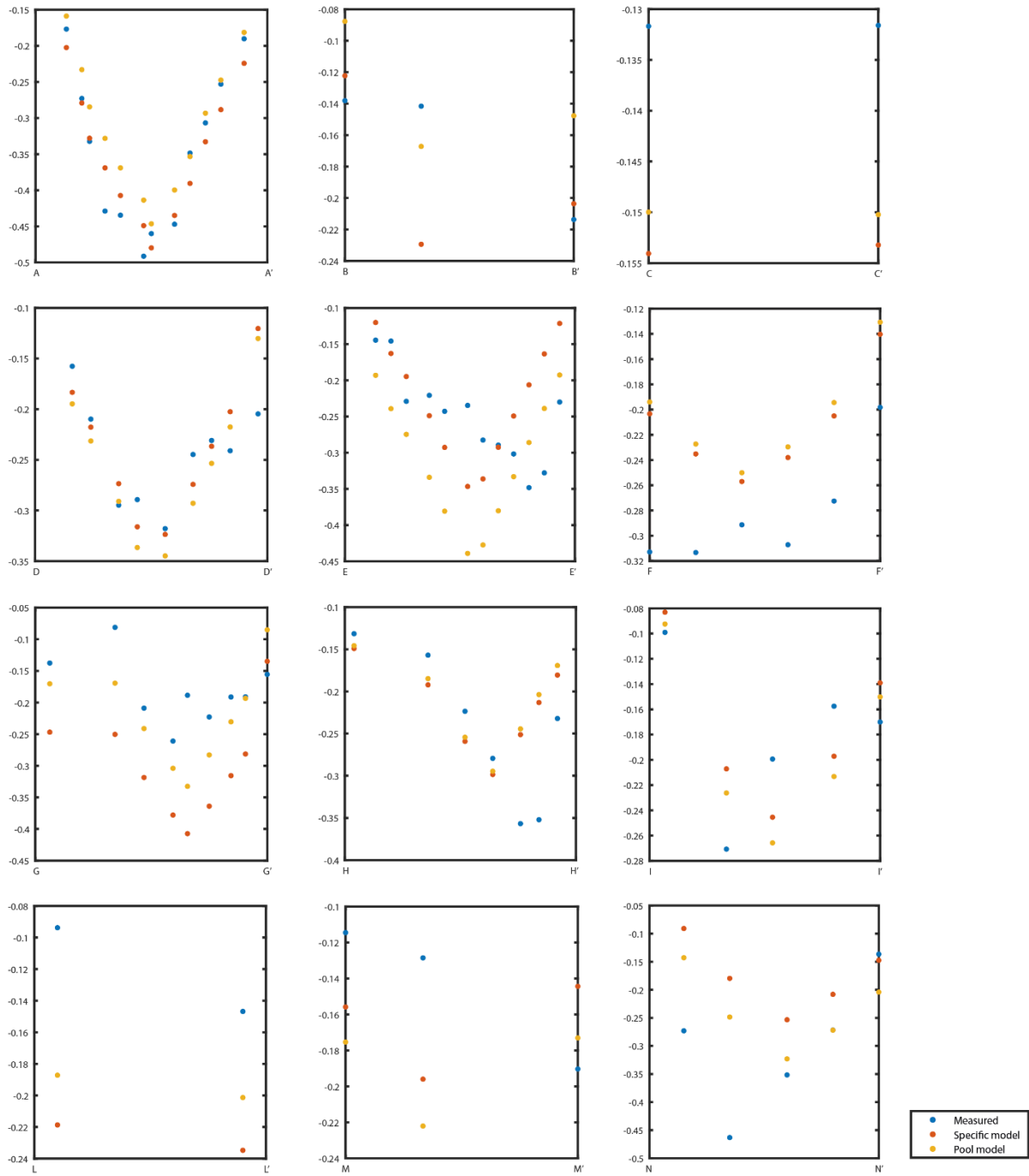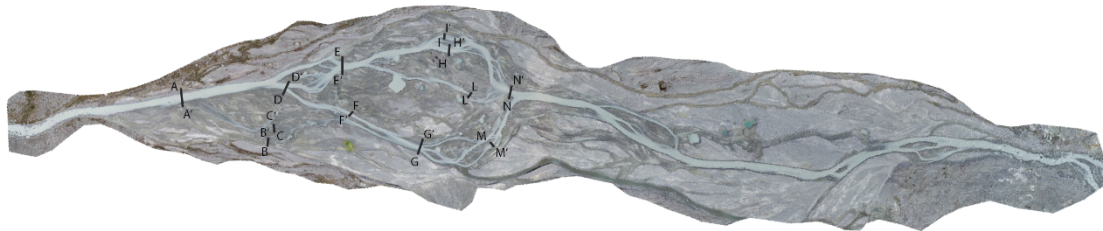
Figure S3.8: Comparison between measured water depths (blue dots) and predictions issued from the specifically calibrated (orange dots) and the generalized model (orange light dots) for transects composing the 10th September 2020 validation sub-dataset.

# Chapter 4: Rates of evacuation of bedload sediment from an Alpine glacier control proglacial stream morphodynamics

## 4.1 Chapter overview

The findings of Chapter 2 show that proglacial forefield morphodynamics filter the subglacial sediment export signal, especially that related to bedload, but without addressing in details the geomorphic mechanisms driving this filtering. To fill this gap, Chapter 4 attempts to answer to the third research question of the thesis: "How do forefields geomorphologically respond to subglacial sediment export? And which are the implications for the longitudinal sediment connectivity"? The study is based on the temporal and spatial comparison of sediment budget and water discharge data (Chapter 2), proglacial stream configuration, surficial morphological changes in dry and wet regions (Chapter 3), and modificationa of grain-size distribution under varying subglacial sediment supply and transport capacity conditions.

This contribution has been submitted for consideration to Journal of Geophysical Research: Earth Surface and it is currently under peer-review as: Mancini, D., Roncoroni, M., Dietze, M., Jenkin, M., Müller, T., Ouvry, B., Miesen, F., Pythoud, Q., Hofmann, M., Lardet, F., Nicholas, A. & Lane, S.N. (submitted – minor revision). Rates of evacuation of bedload sediment from an Alpine glacier control proglacial stream morphodynamics. *Journal of Geophysical Research: Earth Surface*.

## 4.2 Rates of evacuation of bedload sediment from an Alpine glacier control proglacial stream morphodynamics

### 4.2.1 Introduction

Proglacial margins are increasing in size following rapid glacier retreat. In the Swiss and Austrian Alps alone, ca. 930 km$^2$ of deglaciated terrain have been created since the end of the Little Ice Age (Carrivick et al., 2018). If there is lateral accommodation space and valley slope is not sufficient to allow the river to evacuate all the sediment supplied to it, active, fluvially-reworked forefields may develop in the proglacial margin. Such systems are thought to be amongst the most dynamic and active landscapes on Earth because of their sensitivity to varying discharge and sediment supply in both space and time (Ashmore, 1988, 1991a; Lane et al., 1996), conditions which themselves have become more intense since deglaciation (Lane et al., 2017; Huss and Hock, 2018; Lane and Nienow, 2019; Zhang et al., 2023).

Braided stream mechanisms for both sand- and gravel-systems have traditionally been studied in relatively small-scale field settings (e.g. Ashworth and Ferguson, 1989; Lane et al., 1996; Brasington et al., 2000; Williams et al., 2011), scaled laboratory experiments (e.g. Ashmore, 1982, 1991a,b; Ferguson and Ashworth, 1992; Germanoski and Schumm, 1993) and numerical simulations (e.g. Nicholas, 2013; Schuurman and Kleinhans, 2015; Williams et al., 2016a,b). Such research has resulted in a good understanding of braiding processes, but less attention has been given to how they respond to subglacial processes (Carrivick and Heckmann, 2017). Subglacial discharge (Riihimaki et al., 2005; Gimbert et al., 2016; Lane and Nienow, 2019) and sediment supply (Lane et al., 2017; Perolo et al., 2019) both evolve systematically during the melt season of Alpine glaciers. Forefield river response is likely then a function of the ratio of glacier-driven sediment supply to meltwater-driven transport capacity, both at the daily- to weekly-scale but also over longer timescales (Lane et al., 1996; Collins, 2008). Incision has been observed immediately in front of glaciers where a commonly single-thread subglacial stream enters the proglacial forefield and capacity exceeds supply; providing the sediment that may cause supply to exceed capacity further downstream and hence

aggradation (Germanoski and Schumm, 1993; Marren, 2002; Beylich et al., 2009; Roussel et al., 2018). As glaciers retreat, the hinge point between upstream erosion and downstream deposition is thought to migrate upstream (Marren, 2002; Marren and Toomath, 2013, 2014). If supply can match or exceed capacity, aggradation may be present throughout the whole forefield along with highly braided stream networks (Curran et al., 2017).

Whilst the temporal and spatial variability in sediment transport in these environments is driven by external forcing it is also impacted by autogenic reorganization of the proglacial river itself (Coulthard et al., 2005; Coulthard and Van de Wiel, 2007; Marren and Toomath, 2014) notably with the progressive reworking of riverbed deposits (e.g. Ashmore, 1991b; Ferguson and Ashworth, 1992; Cudden and Hoey, 2003; Kasprak et al., 2015). It impacts particle advection lengths and attenuates the downstream transport of sediment (Ganti et al., 2014; Mancini et al., 2023a). In proglacial environments, the transport signal evolves with distance from being a function of subglacial sediment evacuation rates to being a function of reworking of the forefield itself (Jerolmack and Paola, 2010). Mancini et al. (2023a) tested this hypothesis for both suspended sediment and bedload flux using continuous records collected in an active proglacial forefield. They found strong filtering (i.e. dampening and delaying) of the subglacial sediment export signal for bedload, but not suspended sediment whose signal passed almost unimpeded through the forefield. Proglacial forefield morphodynamics thus modify the longitudinal connectivity of sediment flux between glacier margins and downstream geomorphic systems.

Evidence suggests proglacial forefields filter the signal of bedload exported from glaciers, but the interaction between braided stream morphology, sediment fluxes and topographical constraints is only partially understood (Davies, 1987; Warburton, 1996; Maizels, 2002; Ashmore et al., 2011). This is because measuring bedload transport continuously over long time periods (e.g. a glacial melt season) and quantifying the space-time dynamics of the proglacial river are both difficult. The development of passive environmental seismology for continuous bedload monitoring makes it possible to get continuous season-scale bedload transport data (e.g. Burtin et al., 2011; Dietze, 2018; Dietze et al., 2019; Mancini et al., 2023a). Developments in remote sensing, notably combining low-cost UAV platforms combined with SfM (Structure-from-Motion)-MVS (Multi-View-Stereo) photogrammetry software to create Digital Elevation Models (DEMs), is allowing high-frequency quantification of morphodynamic changes (e.g. Fonstad et al., 2013). This paper harnesses both of these developments.

Given the relatively small influence of proglacial filtering on the suspended sediment signal (Mancini et al., 2023a), we hypothesize (1) that subglacial bedload export drives both geomorphic and morphodynamic responses of the proglacial stream which, in turn, control the downstream bedload flux. Following Collins (2008), a higher ratio between upstream bedload supply and transport capacity promotes aggradation as the stream evolves towards a more braided configuration. This results (2) in decreasing supply rates to downstream as the increasing presence of flow divergence regions buffers the downstream transport of coarser particles which may also be detected in surface coarsening (Mosley; 1983; Ashmore, 1988; Kaspark et al., 2015; Antoniazza et al., 2019). In contrast, when capacity exceeds supply, we hypothesis (3) that net loss of bedload sediment causes the proglacial stream to evolve towards a less complex configuration (Germanoski and Schumm, 1993). We test these hypotheses for an Alpine proglacial margin in front of the Glacier d'Otemma, south-west Switzerland, for two entire melt seasons (2020 and 2021).

## 4.2.2 Methodology and methods

### 4.2.2.1 Study area

The forefield of the Glacier d'Otemma (southern-western Swiss Alps) is located at 2,450 m a.s.l. and is ca. 1 km long by ca. 200 m wide, including an active braided stream network

(Figure 4.1). Upstream and downstream of the forefield, flow is confined into a single channel due to the combination of narrower valley sections and a steeper valley slope, the latter leading to a bedrock-dominated riverbed. A decadal-scale analysis of the evolution of its valley sidewall systems following glacial debuttressing confirmed that sidewall sediment supply is decoupled from the active forefield (Mancini and Lane, 2020). As already highlighted in other studies in the same region (i.e. Roncoroni et al., 2023a; Muller et al., 2024), other potential source of sediment and water could be considered geomorphologically and hydrologically negligible in this study.

The mean channel width of the straight section is ca. 10 m at the forefield inlet and ca. 8 m at the forefield outlet. Within the forefield, the longitudinal slope is between ca. 1% in the upper and ca. 0.45% in the lower section. The riverbed is dominated by a mixture of gravels and sands. The in-stream grain size fines from upstream ($D_{50}$ of ca. 78 mm and $D_{84}$ of ca. 92 mm, sample size 345) to downstream ($D_{50}$ of ca. 37 mm and $D_{84}$ of ca. 48 mm, sample size 348). The grain size in zones non-inundated at low flow also decreases from a $D_{50}$ of ca. 100 mm close to the glacier terminus to ca. 30 mm in the most braided sector downstream.

Data were collected for two melt seasons with different climatic conditions: summer 2020 from the 8 July [Day of the Year (DOY) 190] to the 27 August [DOY 240] which was warmer and drier; and summer 2021 from the 12 July [DOY 193] to the 21 August [DOY 233] which was wetter especially in the first part of the melt season (Supplementary Information 4.4.1).
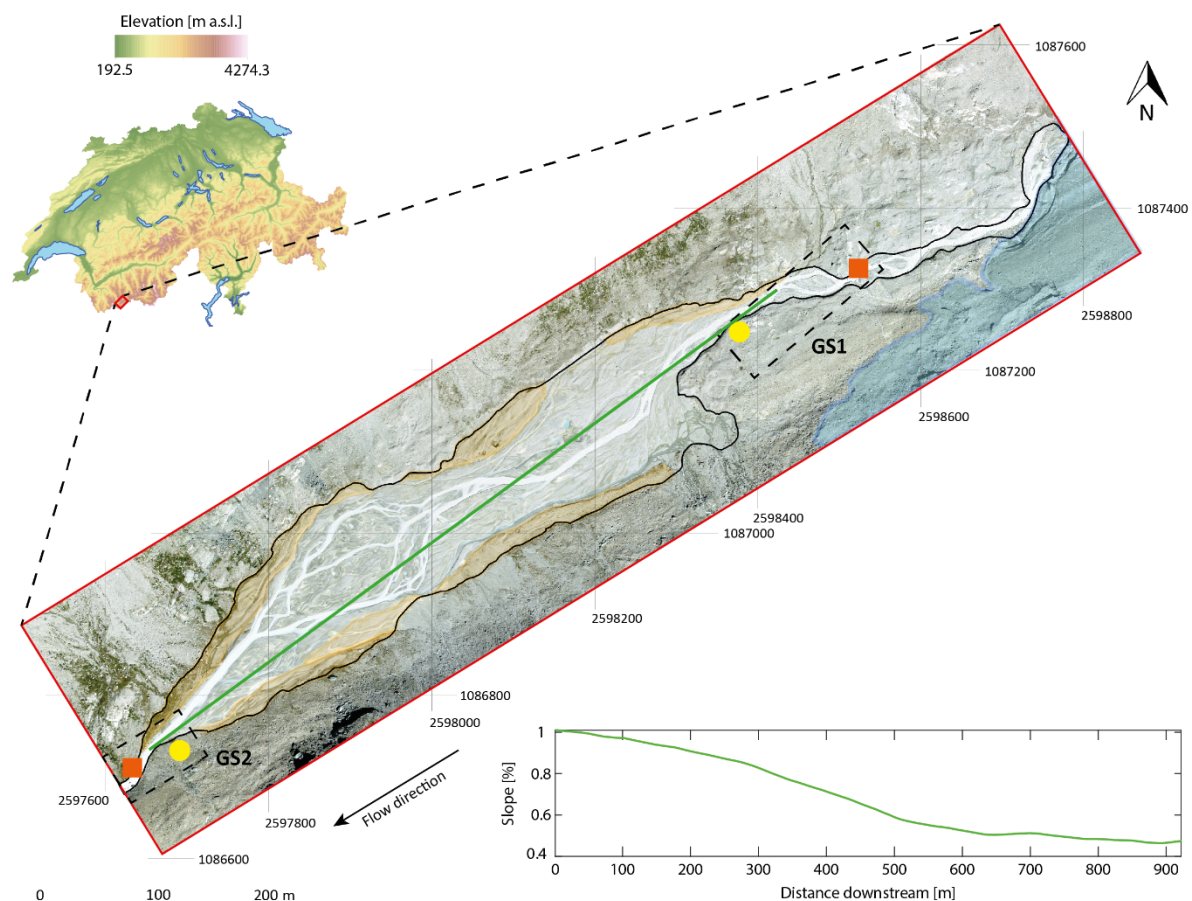


Figure 4.1: Location of the Glacier d'Otemma proglacial forefield and spatial location of monitoring stations GS1 and GS2. Orange squares refer to turbidity and water pressure sensors, while yellow dots highlight geophones. The solid black line refers to the limit of the proglacial forefield, while the dashed ones to the extent of the monitoring stations. The shaded orange polygons show the terrace systems, while the light blue one the glacier. The green line highlights the downstream slope transect. Coordinates are in the Swiss CH1903+/LV95 geographic coordinate system. Source of the orthomosaic: Swisstopo (2020).

### 4.2.2.2 Methods

The relationship between upstream boundary conditions and proglacial forefield response was investigated by combining continuous sediment flux quantification, water discharge measurements and repeated daily UAV surveys (Figure 4.2). Turbidity sensors, geophones and water pressure sensors were deployed at the glacier terminus (Gauging Station [GS] 1) and at the forefield outlet (GS2) for the continuous monitoring of water stage and both suspended sediment and bedload transport (Figure 4.1) (Section 4.2.2.2.1). The measured bedload transport rates (S) at GS1 were compared to the potential bedload transport capacity (C) estimated using a hydraulic transport model based on the instantaneous discharge to investigate the geomorphic response of the proglacial forefield to under- and over-subglacial sediment supply conditions (Section 4.2.2.2.2). If S is higher than C, deposition in the forefield is expected; while in the opposite case erosion is expected. Aerial images of the floodplain, covering the spatial extent shown in Figure 4.1, were collected daily during low flow conditions using an Uncrewed Airborne Vehicle (UAV). Photogrammetric post-processing was used to generate DEMs and orthomosaics of the floodplain for the two melt seasons (Section 4.2.2.2.3). The DEMs allowed determination of volumetric change estimates over time for the entire proglacial forefield (Section 4.2.2.2.4). Orthomosaics were used to manually classify the floodplain into inundated and dry regions, a condition needed (i) to extract basic planimetric information on the proglacial stream over time, such as daily braiding indices, total number of bars and bars total area and perimeter length, and (ii) to determine the spatial distribution of water depths through the application of a statistical model (Section 4.2.2.2.4 and Section 4.2.2.2.5). Orthomosaics were also calibrated to produce grain-size maps of dry regions at the floodplain scale to investigate surficial texture change over time (Section 4.2.2.2.6). All datasets used in this study have been published and we explain where they can be obtained below.
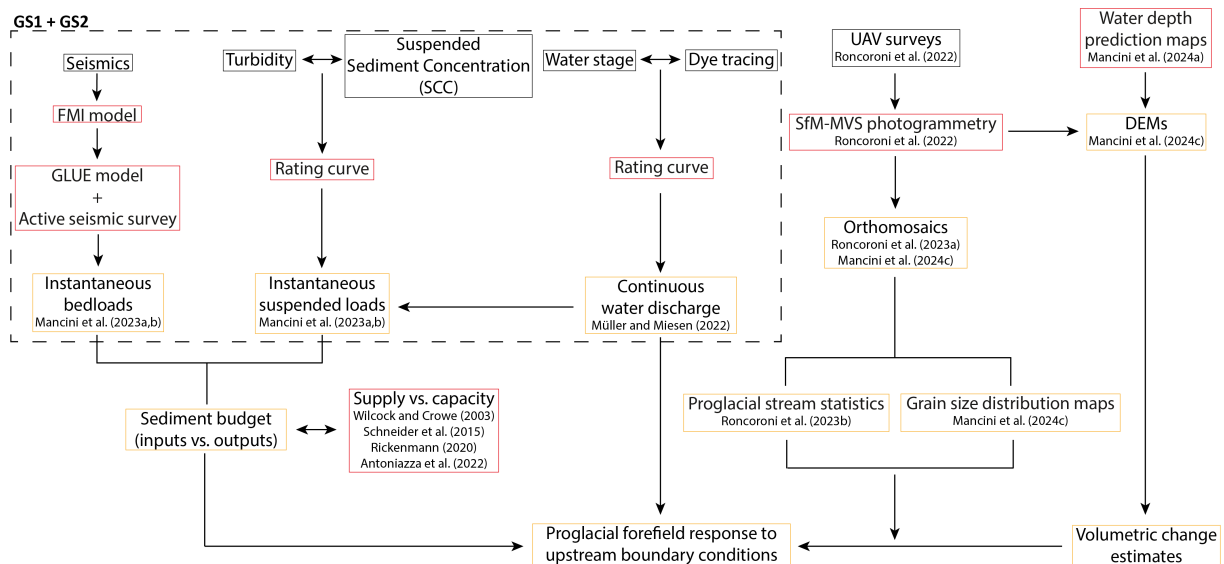


Figure 4.2: Overview of the methodological approach used in this study. Black boxes are the technique used in the field, the red ones those used for the post-processing of the collected data, and the orange ones the final outputs. The dashed box represents the data measured directly in the field at GS1 and GS2 (Figure 4.1).

### 4.2.2.2.1 Sediment supply to and export from the proglacial forefield

The methods and datasets acquired at GS1 and GS2 have been published in open access format for discharge in Müller and Miesen (2022) and for continuous suspended sediment and bedload fluxes in Mancini et al. (2023a,b).

Daily total suspended sediment load and bedload at the upstream and downstream stations were calculated by cumulating instantaneous loads (unit kg/s) and multiplying these

by the measurement resolution of 120 seconds. The loading was converted into daily volumes and corrected for porosity for comparison with volume of change estimates using:

$$V = \frac{M}{\rho_S \; x \; E}$$

<div align="right">Eq. 4.1</div>

where:

V = daily transported volume [m³];
M = daily mass of transported sediment [kg];
$\rho_s$ = density of sediment [kg/m³] = 2650 kg/m³ (Bezinge et al., 1989); and
E = porosity = (1 - 0.85) = 0.15 (Carling and Reader, 1982)

## 4.2.2.2.2 Sediment supply and potential transport capacity

The geomorphic response of the proglacial forefield was investigated for under- and over-subglacial sediment supply (S) conditions compared to the actual theoretic potential capacity (C) of the proglacial stream.

We estimated C for the relatively straight stream pattern just upstream from the start of the braided sector (GS1) using shear-stress based sediment transport equations developed for Alpine streams (Schneider et al., 2015; Rickenmann, 2020; Antoniazza et al. 2022) based upon the modified Wilcock and Crowe (2003) approach. The latter allows to compute potential transport rates for particles larger than 0.004 m, which correspond to fine gravel. Consequently, we assume this size is the interface between suspended load and bedload in our study area.

The potential transport rates over the entire channel width were determined from (Antoniazza et al., 2022):

$$Q_b = b * \rho_S * W^* * \frac{(g*r_h*S)^{1.5}}{R*g}$$

<div align="right">Eq. 4.2</div>

where: $Q_b$= potential bedload transport rate [kg/s]; $b$ = average channel width [m] (i.e. 10 m); $W^*$= dimensionless transport rate over the entire channel width defined as

$$W^* = 0.002 \left(\frac{\tau^*_{D50}}{\tau^*_{rD50}}\right)^{16.1} for \left(\frac{\tau^*_{D50}}{\tau^*_{rD50}}\right) < 1.143 \; and \; D > 4 \; mm$$

<div align="right">Eq. 4.3</div>

$$W^* = 14 \left(1 - \frac{0.85}{\left(\frac{\tau^*_{D50}}{\tau^*_{rD50}}\right)^{0.7}}\right)^{4.5} for \left(\frac{\tau^*_{D50}}{\tau^*_{rD50}}\right) \geq 1.143 \; and \; D > 4 \; mm$$

<div align="right">Eq. 4.4</div>

$\tau^*_{D50}$= dimensionless bed shear stress defined as

$$\tau^*_{D50} = \frac{r_h S}{R D_{50}}$$

<div align="right">Eq. 4.5</div>

$\tau^*_{rD50}$= dimensionless reference bed shear stress defined as

$$\tau^*_{rD50} = 0.56 S^{0.5}$$

<div align="right">Eq. 4.6</div>

$D_{50}$= median of the surface grain-size distribution (i.e. 0.078 m); $r_h$= hydraulic radius [m] defined as

$$r_h = \frac{(b+mh)h}{(b+2h*\sqrt{1+m^2})}$$

<div align="right">Eq. 4.7</div>

$h$ = measured water depth [m]; $m$ = increase in channel width with depth defined as

$$m = \frac{h}{\tan(45)} = 1 \qquad\qquad \text{Eq. 4.8}$$

$S$ = channel gradient [-]; $R$ = relative sediment density [-] using sediment ($\rho_s$) and water ($\rho_w$) densities set at 2650 kg/m$^3$ and 1000 kg/m$^3$, respectively; and $g$ = gravitational acceleration 9.81 [m/s$^2$].

Topographical and sedimentological parameter values are available in Mancini et al. (2023a). Forefield evolution was investigated looking at the relationship between theoretic bedload transport capacity (C) estimates and field-collected bedload sediment supply (S) issued from geophone measurements.

**4.2.2.2.3 Repeat Digital Elevation Models (DEMs) and orthomosaics of the proglacial forefield**

Aerial images of the braidplain were collected once a day during low flow conditions using a DJI Phantom 4 Pro. The survey time in 2020 to do this was long (ca. 3.5 hours) with the potential for changing conditions (light, water discharge, etc.) during data collection. Hence, in 2021 we deployed two UAVs (DJI Phantom 4 Pro) simultaneously. Data collection involved a systematic approach consisting in subdividing the forefield in four sectors, each of that was surveyed using two orthogonal rectancular grids (camera at nadir and flight height of 80 m) and two circular flights (camera pointing in direction of the center and flight height of 60 m) according to best practices given in James et al. (2020) to minimize propagation of systematic errors. Post-processing of collected datasets was performed photogrammetrically in Agisoft Metashape (version 1.5.5) with the aid of field-collected ground control points (GCPs) to generate a time-series of georeferenced orthomosaics and DEMs of the floodplain for the two melt seasons. The orthomosaics had a resolution of 0.05 m and the DEMs of 0.2 m. Details of data collection and post-processing are available in Roncoroni et al. (2022). Orthomosaics were used to manually classify the floodplain into inundated and dry regions, a condition needed to (i) to extract basic planimetric information on the stream (section 4.2.2.2.5), (ii) to define the surficial grain size distribution (section 4.2.2.2.6) and (iii) to estimate the spatial distribution of water depths through the application of a statistical model developed in Mancini et al. (2024a). Validation tests for a subset of available data demonstrated that the model was able to reproduce water depth distribution for braided mountain streams (Mancini et al., 2024a). Elevation uncertainties for permanently inundated and transient regions range from ±0.035 m to ±0.060 m, with associated limits of detection between ±0.045 m and ±0.090 m. These limits are slightly higher than those for permanently dry regions (i.e. ±0.042 and ±0.043 m). Thus, reworking and deposition patterns could be detected for changes smaller than the mean $D_{50}$ (0.06 m) in dry zones; but 1.5 $D_{50}$ in permanently inundated zones. Geomorphic changes in transient regions lie between these two cases. Water depth maps were integrated into DEMs of dry regions to obtain DEMs of the entire proglacial forefield (Westaway et al., 2003). These datasets are available in Roncoroni et al. (2023b) and in Mancini et al. (2024c).

**4.2.2.2.4 DEMs of difference and volume of change estimates**

DEMs were classified according to a contingency table of pixel evolution between surveys (i.e. permanently dry, permanently inundated or transient wet to dry or dry to wet) using the inundation maps described above (see Mancini et al., 2024a). The heuristic model of water depth resulted in spatial variation in the uncertainty of individual water depths; thus, in inundated regions, DEM elevation uncertainty was computed spatially as the sum in quadrature of both water depth prediction and water surface as (Lane et al., 2003):

$$EU_{ij} = \pm\sqrt{\sigma d_{ij}{}^2 + \sigma e_{ij}{}^2} \qquad\qquad \text{Eq. 4.9}$$

where:

$EU_{ij}$ = elevation uncertainty in cell (*i,j*);

$\sigma d_{ij}$ = standard deviation of water prediction error in cell (*i,j*) derived from prediction uncertainty bounds;

$\sigma e_{ij}$ = standard deviation of water surface error in cell (*i,j*), taken as the dry DEM uncertainty.

For dry regions we used a spatial homogeneous uncertainty value defined by as the standard deviation of error computed comparing 170 field-measured and photogrammetrically reconstructed elevations of stable areas. Thus, Eq. 4.9 is simplified as $EU_{ij} = \sigma e_{ij}$.

DEMs of difference (DoDs) were determined for the active floodplain, the latter defined as the alpha shape of the area experiencing at least one day of morphodynamic change across the two melt-seasons (Roncoroni et al. 2023a). Differences were filtered according by the limits of detection (LoDs) set at 95% confidence to highlight only statistically significant geomorphic changes. These were computed as (Brasington et al. 2003; Lane et al., 2003):

$$LoD_{ij} = \pm t \sqrt{(EU_{ij}^1)^2 + (EU_{ij}^2)^2}$$

Eq. 4.10

where:

$LoD_{ij}$ = limit of detection in cell (*i,j*) [m];

$t$ = Student's confidence interval threshold (1.96 at 95%), superscripts represent times 1 and 2, respectively.

Water depth uncertainties and LoDs for both inundated and dry regions in 2020 and 2021 are available in Supplementary Information 4.4.2 and Supplementary Information 4.4.3.

Sectoral volumetric change maps were produced from spatially filtered DoD maps and total volumetric change estimates computed following Lane et al. (2003) as:

$$V = d^2 n \sum DoD$$

Eq. 4.11

where:

V = Volume [m³];

d = cell size (i.e. 0.20) [m];

n = number of raster cells in DoD; and

DoD = DEM$_{t2}$-DEM$_{t1}$ spatially filtered by LoDs (Eq. 4.10).

The associated uncertainties in volume estimates ($\sigma v_{ij}$) were derived as (Lane et al. 2003):

$$\sigma v_{ij} = \left( \sum_{i=1}^{I} \sum_{j=1}^{J} \left[ d_{ij}^2 \left( EU_{1ij}^2 + EU_{2ij}^2 \right)^{0.5} \right]^2 \right)^{0.5}$$

Eq. 4.12

To conserve mass, the total daily volumetric difference from the monitoring stations (GS1-GS2) should match the volumetric change derived from the DEMs of difference. However, given the simplicity and the assumptions on which the bathymetric model relies on, there is likely to be error and some divergence between the two approaches. We consider this below.

### 4.2.2.2.5 Metrics describing forefield morphodynamics

Daily inundation maps comprised binary matrices (1 for dry and 0 for flooded regions) allowed extraction of temporal statistics on forefield morphodynamics. The total inundated area was calculated by multiplying the sum of cells having a value of 0 by the pixel area (i.e. 0.0025 $m^2$). Braiding indices were calculated using a channel count index by determining the number of channels in cross-sections perpendicular to the main valley direction (Howard et al., 1970; Hong and Davies, 1979; Mosley, 1982; Ashmore, 1988; Chew and Ashmore, 2001; Egozi and Ashmore, 2008):

$$Bc = \frac{\sum_{i}^{n_s} n_c^i}{n_s}$$ 

Eq. 4.13

where:

$Bc$ = braiding index;
$i$ = cross-section;
$n_c$ = total number of channels; and
$n_s$ = total number of cross-sections.

Inundation maps were used to determine bar characteristics (e.g. bar area) for those bars greater in area than 10 pixels (0.025 $m^2$). Obtained temporal braiding index and mean bar area values were normalized to better highlight the temporal occurrence of high and low peaks when compared to subglacial sediment export magnitudes, and to ease the comparison between fluvial variables. We also generated a summary inundation map following Roncoroni et al. (2023a) to give number of days that each pixel in the forefield was permanently inundated.

### 4.2.2.2.6 Surface grain-size data

Grain-size maps of dry regions at the forefield scale were generated using a texture-based approach, calibrated against field collected grain-size samples (Lane et al., 2020). Such an approach assumes that there is a relationship between image properties (e.g. zonal standard deviation of a grey-scale image) and parameters describing the particle sizes present (e.g. $D_{50}$) (Carbonneau et al., 2004, 2005). Delimitation of individual grains and extraction of grain-size properties (e.g. Butler et al., 2001) is not possible with the available resolution of the orthomosaics. The detailed methodology used to produce grain size maps is available in Supplementary Information 4.4.4.

Calibration data were collected twice for both melt seasons (8 July and 11 August in 2020; 17 July and 8 August in 2021) in 30 randomly-selected stable sites of the floodplain using grid-by-number sampling (Wolman, 1954). The four corners of a 1 m x 1 m square were measured with a differential GPS (dGPS) and grains were manually sampled at 0.10 m grid intersections within each square. The b-axis of each sampled grain was measured. Those smaller than 0.002 m were recorded as 0.002 m. Squares were split equally between calibration and validation datasets.

The dGPS coordinates were used to identify the corresponding image segment for each grid for which the standard deviation of its greyscale pixel was determined to represent image texture. This was related to $D_{50}$ in the form y = a$D_{50}$+b. The calibration results are shown in Table 4.1. The estimates of $D_{50}$ were then assessed for the validation datasets. Table 4.1 suggests a good agreement between measured and predicted grain-sizes with $R^2$ values equal or higher than 0.6, negligible mean errors (i.e. bias) and standard deviations of error of between ±2 and ±8 mm. As the calibration used sampled grains (b axes) there is no need to correct for the fact that the surface expression of grains is not necessarily the b-axis as is the case when

grain boundaries are mapped directly from imagery (Adams, 1979). These relations were then used to transform entire orthoimages into grain-size maps.

Table 4.1: Calibration equations of field-collected grain sizes and image standard deviation to produce grain size distribution maps. Validation was performed using independent data. The error column refers to the mean and standard deviation of the error between the measured and the predicted grain-size values.

| Date | Calibration equation | Validation | | |
|---|---|---|---|---|
| | | $R^2$ | Error [m] | |
| | | | Mean | STDV |
| 8 July 2020 n = 30 | $y = 1.653 D_{50}$-1.618 ($R^2 = 0.796$) | 0.601 | 0.003 | 0.004 |
| 11 August 2020 n = 30 | $y = 1.459 D_{50}$-4.875 ($R^2 = 0.626$) | 0.761 | -0.001 | 0.004 |
| 17 July 2021 n = 20 | $y = 0.709 D_{50}$+3.137 ($R^2 = 0.826$) | 0.643 | -0.001 | 0.002 |
| 8 August 2021 n = 20 | $y = 2.971 D_{50}$-4.569 ($R^2 = 0.909$) | 0.743 | 0.002 | 0.008 |

The UAV data collection strategy was designed to minimize the effects of changing light conditions between datasets, but such effects could not be completely avoided. To correct these artifacts, we re-calibrated the grain-size maps using 15,000 image-estimated $D_{50}$ values sampled in stable zones characterized by different grain sizes where the surficial granulometry should not have changed between surveys (Supplementary Information 4.4.4). The corrected grain-size maps were visually checked leading to some datasets being excluded due to residual texture-related errors (most commonly when lighting conditions had evolved within a survey, such as due to changing cloud cover). At the end of this filtering, a total of 6 (26 July [DOY 208] to 27 August [DOY 240]) and 4 (22 July [DOY 203] to 12 August [DOY 225]) datasets for, respectively, 2020 and 2021 were retained and used to investigate the spatial patterns of grain-size changes. As with the DoDs, we limited the grain-size difference maps to the extent of active floodplain. Following Lane et al. (2020) we identified a limit of detection for grain-size changes, computed from 350 points randomly sampled in stable zones (Supplementary Information 4.4.4). These datasets are published in Mancini et al. (2024c).

Grain-size difference maps were compared to elevation difference maps, both spatially and by converting them into bi-dimensional frequency plots. The sub-daily and weekly grain-size and elevation of difference maps were masked by inundation maps (see Section 4.2.2.2.5) to exclude the wetter surface from the analysis. To produce bi-dimensional frequency plots, elevation changes were classed at cm resolution between -0.55 m and +0.55 m; and grain-size changes at a cm resolution between -0.065 and +0.065 m. This analysis allowed determination of the relationship between erosion/deposition and fining/coarsening and its visualization.

### 4.2.3 Results

### 4.2.3.1 Total sediment loads at GS1 and GS2 and their relationship with transport capacity

The proglacial margin experienced different total sediment transport loads in the two melt seasons under investigation (Figure 4.3). The daily mean amounts of glacier subglacial sediment load (GS1 in Figure 4.1) were 719.4±120 t (2020) and 1,052.2±462 t (2021), while the downstream export at the forefield outlet (GS2 in Figure 4.1) was much lower, with daily means of 533.7±21 t (2020) and 571.7±68 t (2021). These data imply net aggradation, greater in 2021 than 2020 (Figure 4.3). Only one day, DOY 234 in 2020 recorded the proglacial margin as a sediment source.

Daily suspended sediment loads (Ls) had a strong Pearson correlation with discharge at both GS1 (r = 0.695, p<0.05, in 2020 and r = 0.786 p<0.05, in 2021) and GS2 (r = 0.651, p<0.05, in 2020; r = 0.768, p <0.05 in 2021) suggesting these are hydrologically driven in both locations. Daily bedload transport rate (Lb) correlations with discharge were only significant at GS1 in 2021 (r = 0.466, p>0.05, in 2020; r = 0.681, p<0.05, in 2021), while at GS2 they are lower in both melt seasons (r = 0.425 in 2020, p>0.05; r = 0.286 in 2021, p>0.05). Weaker correlations between discharge and daily bedload rates within the proglacial forefield imply a greater probability that on a daily basis there is imbalance between S and C. Cumulative load uncertainties for both Ls and Lb are provided in Supplementary Information 4.4.5.
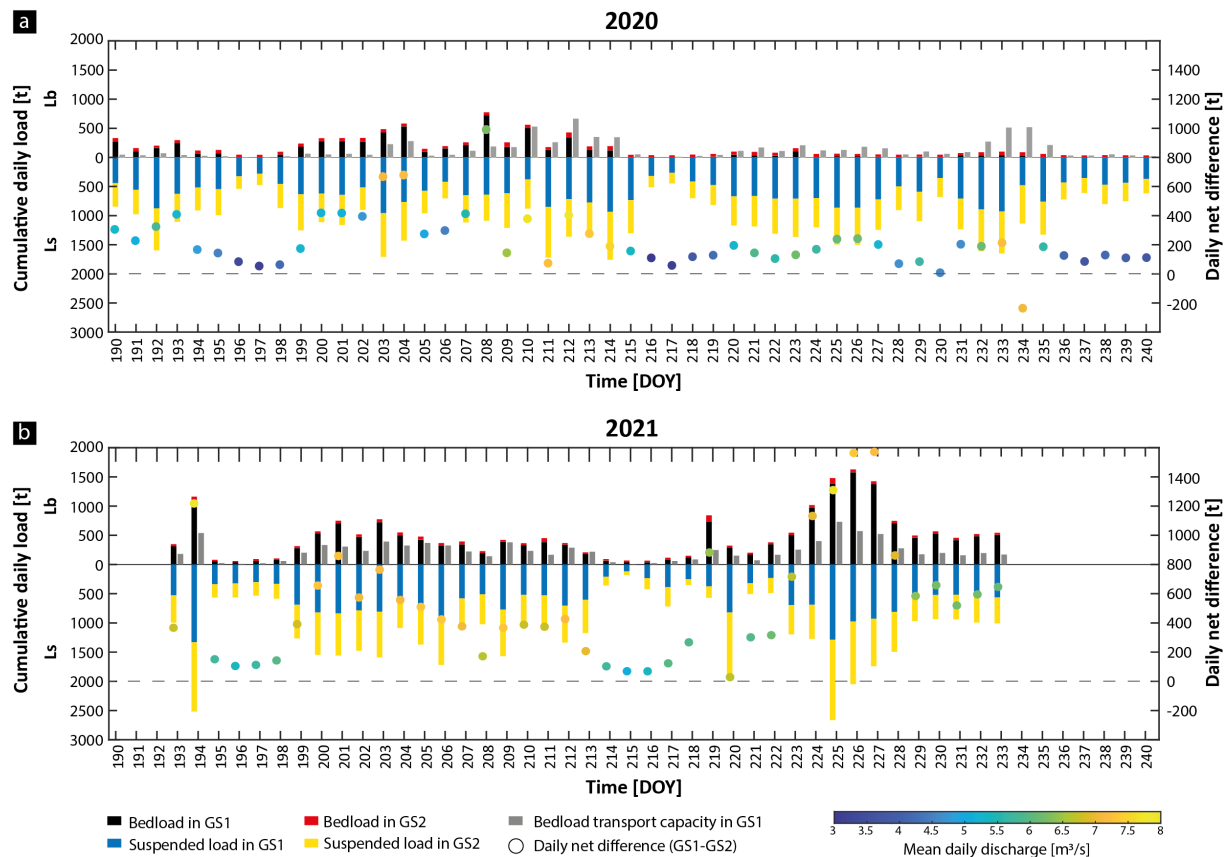


Figure 4.3: Daily cumulative sediment loads (suspended sediment [Ls] and bedload [Lb]) at GS1 and GS2, net load difference in relation to daily mean discharge rate, and bedload transport capacity measured in GS1 (Eq. 4.2) for melt season 2020 (a) and 2021 (b). Day of the year [DOY] refers to the number of days since the 1 January. Instantaneous and cumulative sediment quantifications and relative uncertainties are available in Supplementary Information 4.4.5, while discharge records in Müller and Miesen (2022).

In 2020, there were two differing periods in terms of bedload transport balance (Figure 4.3a). Between DOY 190 and ca. DOY 210 to 215, S exceeded C with the subglacial channels delivering coarser material than the proglacial stream could transport. This is reflected in the measured bedload balance with a total of 5,551 [3,813 to 8,357] t of bedload entering the forefield until DOY 215 at GS1 whilst 1,384 [1,344 to 1,921] t (24.9%) left the forefield at GS2. A total of ca. 4,168 [2,469 to 6,536] t of bedload accumulated in the proglacial margin. For the same period 2,560 [2,410 to 2,829] t of suspended sediment was stored in the forefield. After DOY 215, S became lower than C, ca. 452 [192 to 1,813] t (-91.8%) of bedload supplied at GS1 but ca. 1,157 [1,114 to 1,584] t leaving at GS2 and ca. 663 [240 to 965] t leaving the reach. However, suspended load continued to accumulate, with a net 3,470 [3,160 to 3,570] t of suspended sediment deposited. Thus, there was overall net deposition throughout 2020,

both bedload and suspended load until DOY 215 and then through suspended load deposition exceeding bedload loss after DOY 215.

In 2021, S generally remained higher than C which should result in a continuous phase of aggradation throughout the melt season (Figure 4.3b). Until ca. DOY 220, S was only slightly higher than C. Bedload inputs to GS1 were ca. 9,136 [3,274 to 13,600] t and loss through GS2 was ca. 1,116 [249 to 1,917] t (12.2%) implying that ca. 8,020 [3,025 to 11,653] t of bedload were stored in the proglacial margin. This compares with 2,100 [1,820 to 2,230] t of suspended load. From DOY 220, the difference between S and C increased; the total bedload supply to GS1 increased to ca. 9,743 [4,542 to 13,180] t, but the downstream export through GS2 reduced to 593 [163 to 1203] t. Consequently, ca. 9,150 [4,379 to 11,986] t of bedload were stored. This compares with 5,488 [4,628 to 6,178] t of suspended load.

**4.2.3.2 Forefield geomorphic and morphodynamic response**

To understand how the forefield is related to these changing sediment supply and export conditions, we considered the spatial (laterally-integrated) and temporal patterns of channel change together with the number of days the reach was inundated (Figures 4.4a and 4.4b), the temporal evolution of volume change (Figures 4.4c and 4.4d) and the cumulative volumes of sediment stored in the reach according to the DEMs and the load data (Figures 4.4e and 4.4f).
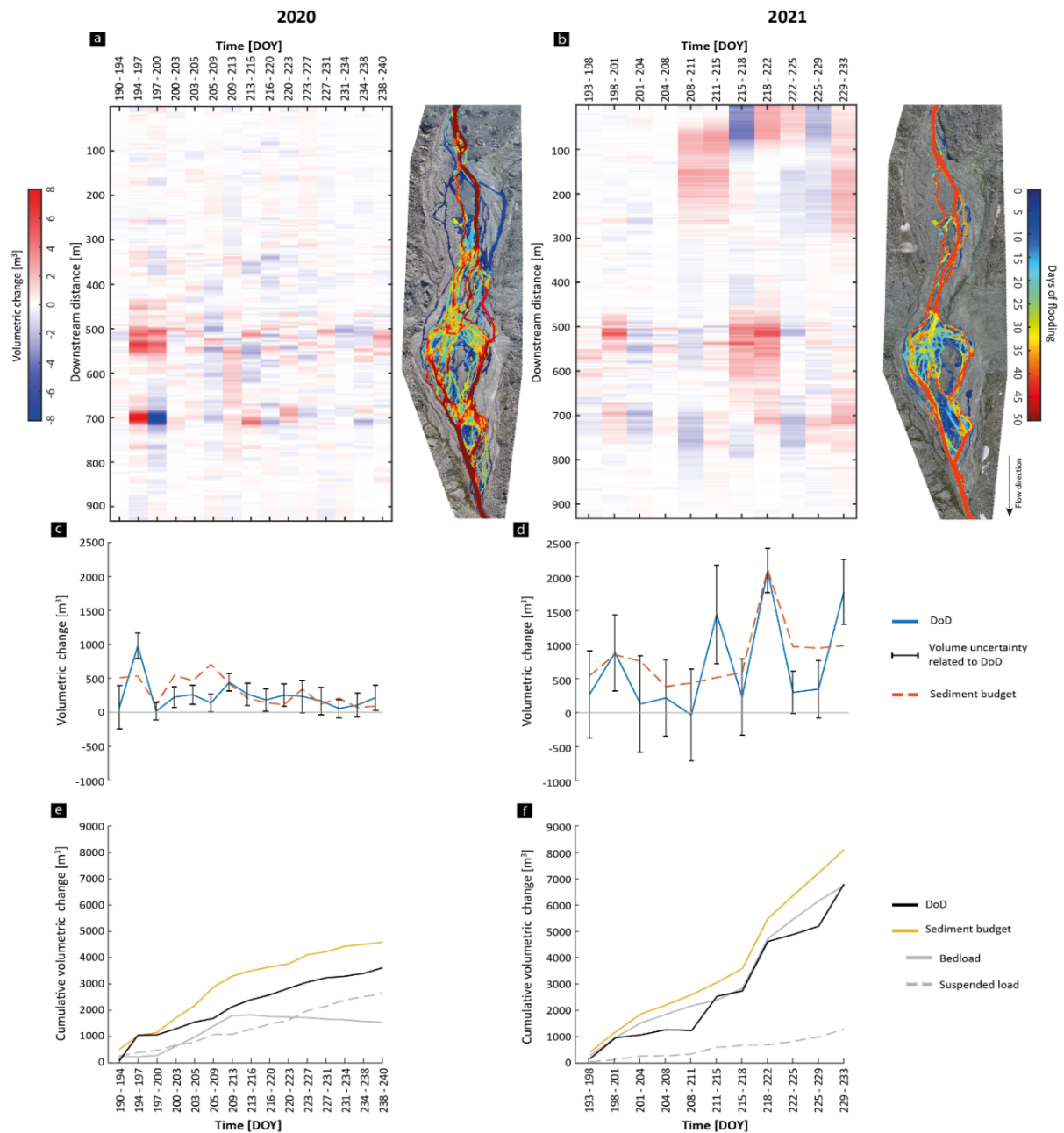
Figure 4.4: (a-b) 2D volumetric change maps in relationship with the spatial distribution of flooding frequencies in the two melt seasons; (c-d) volumetric changes issued from temporal DoD (blue line) and total volumetric sediment budget (GS1-GS2, orange dashed line); (e-f) cumulative sediment budget (GS1-GS2) according to DoD calculations and sediment load records (total sediment, suspended sediment and bedload). LoD values used in DoDs are available in Supplementary Information 4.4.2 (wet regions) and S4.4.3 (dry regions), field-collected instantaneous and cumulative transport rates for both suspended sediment and bedload (with uncertainties) in Supplementary Information 4.4.5, while elevation of change maps in Supplementary Information 4.4.6.

Rates of riverbed reworking were greater during summer 2021 as compared to 2020 (Figures 4.3, 4.4a, 4.4b and Supplementary Information 4.4.6). Geomorphic changes were most notable in the most braided sector. The upstream end of this braided sector was ca. 300 m downstream of GS1 in 2020 (Figures 4.4a and 4.4b), with a major flow divergence region and where there is a decrease in valley bottom slope (Figure 4.1). The braided zone is at its maximum width 550 m downstream (Figures 4.4a and 4.4b) and it then converges to be single thread by 800 m downstream.

Figure 4.5 shows the geomorphic responses to the balance of S and C for these two regions. For the two periods with S>C there were higher deposition rates most notably between 500 and 700 m downstream in the braided sector. During 2020, there was an avulsion to the true right between 300 m and 500 m downstream and the most intense deposition between 500 m and 700 m was downstream of the post-avulsion channel (Figure 4.5a). For the period in 2020 where C>S there is clear evidence of incision in the main channel from GS1 through to 500 m downstream (Figure 4.5b). Qualitatively, deposition patterns appear to coincide with flow divergence regions and erosion patterns with regions of maximum channel curvature and flow convergence areas (Figure 4.5 and Supplementary Information 4.4.6). One large bar, 550 to 650 m downstream remained present throughout the study, with reworking happening around it (Figure 4.5).
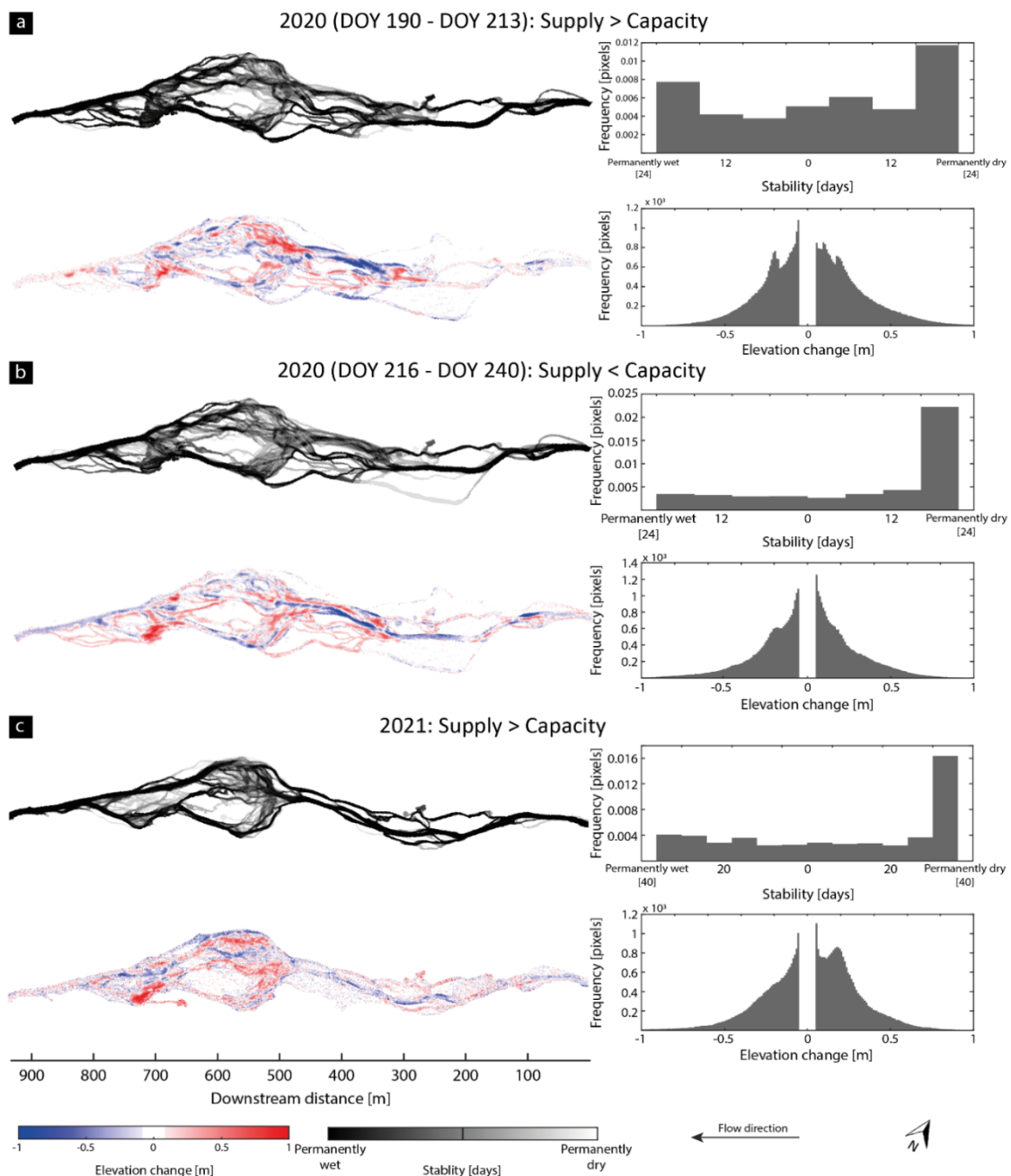


Figure 4.5: Seasonal frequency of inundation (upper), elevation of change (lower) maps and associated frequency histograms for different supply-transport conditions in melt season 2020 (a and b) and 2021 (c). Inundation maps are issued from flooding frequency maps (Figure 4.4a, 4.4b and Supplementary Information 4.4.7), while elevation of change maps for smaller temporal intervals are available in Supplementary Information 4.4.6. LoD values are available in Supplementary Information 4.4.2 and 4.4.3.

Both volumetric and the load-based methods suggest that the forefield is storing subglacially-exported sediment (Figures 4.4e and 4.4f). The temporal evolution of volumetric changes follows the same trend as the sediment budget (Figures 4.4c and 4.4d), but with a relative tendency for the DEM method to underestimate the volume of sediment being stored in the reach.

Channel patterns respond to these volumetric changes. In 2020 until DOY 215, when S>C, the total number of channels, the normalized braiding index and the number of bars increased (Figures 4.3a and 4.6). Bars became smaller with a concomitant increase in the number of flow convergence and divergence regions, (Figure 4.6c, Supplementary Information 4.4.7).
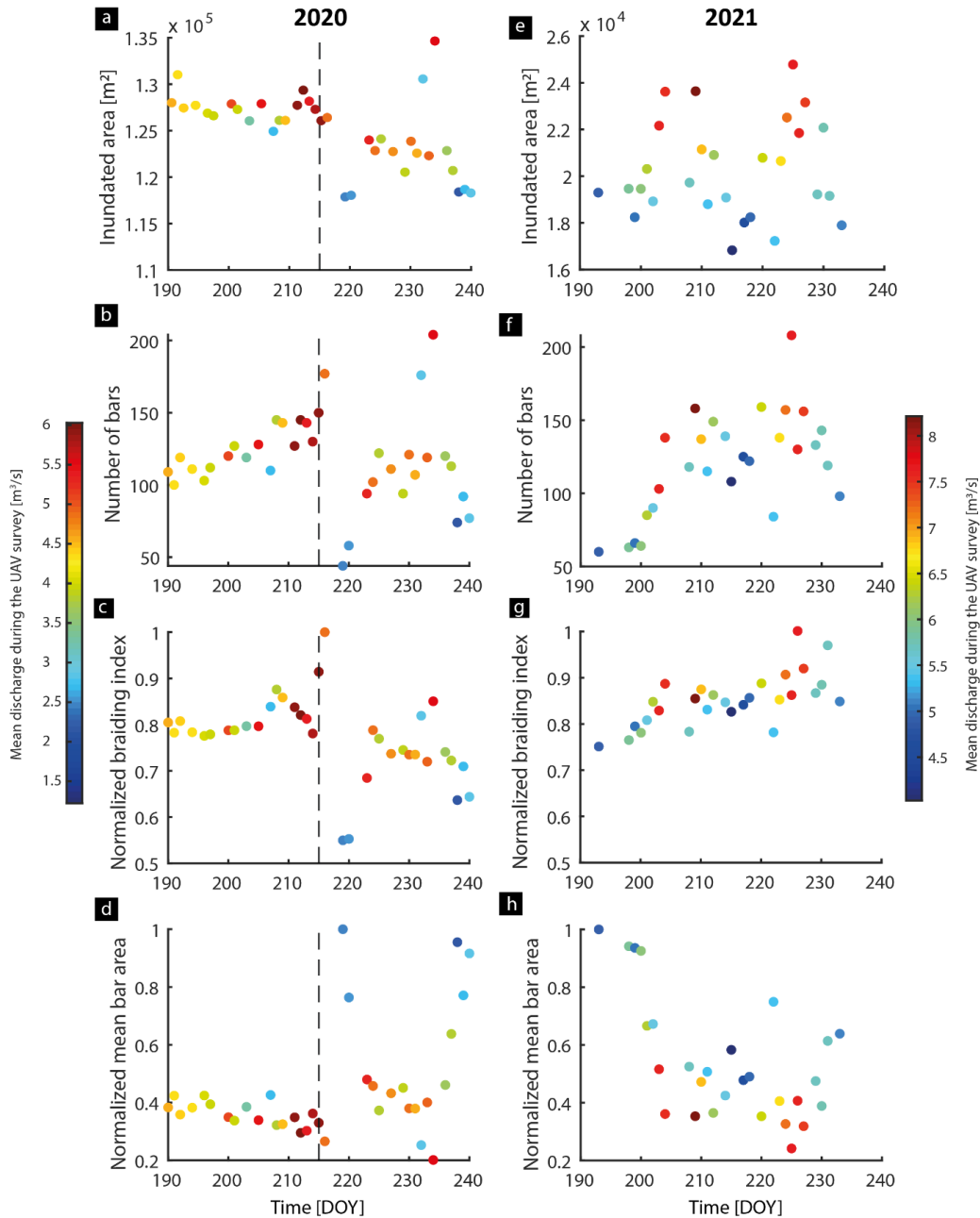


Figure 4.6: Proglacial stream statistics for melt seasons 2020 and 2021. Total inundated area (a and e), number of bars (b and f), normalized braiding index (c and g) and normalized mean bar area (d and h). Absolute braiding index values are comprised between 2 to 4.5 (2020) and 3 to 4.5 (2021), while absolute bar area between 100 to 600 m² (2020) and 80 to 350 m² (2021).

Despite the sensitivity to changes in discharge, the inundated area was high during this period (ca. $1.27 \times 10^5$ m$^2$) and ca. $3.7 \times 10^4$ m$^2$ (ca. 19.2% of the active floodplain) experienced reworking processes (Figure 4.6a, Figure 4.7a and Supplementary Information 4.4.7). During this period the proglacial forefield underwent a total aggradation of ca. 2,300 m$^3$ most of which was associated with zones passing from wet to dry (ca. 3,320 m$^3$, Figure 4.8a). Dry (during measurement) regions had erosion and deposition in balance. The downstream supply to GS2 was sustained by transient regions passing from dry to wet and by permanently inundated areas be reworked, respectively, ca. 350 m$^3$ and ca. 530 m$^3$ of material (Figure 4.8a).
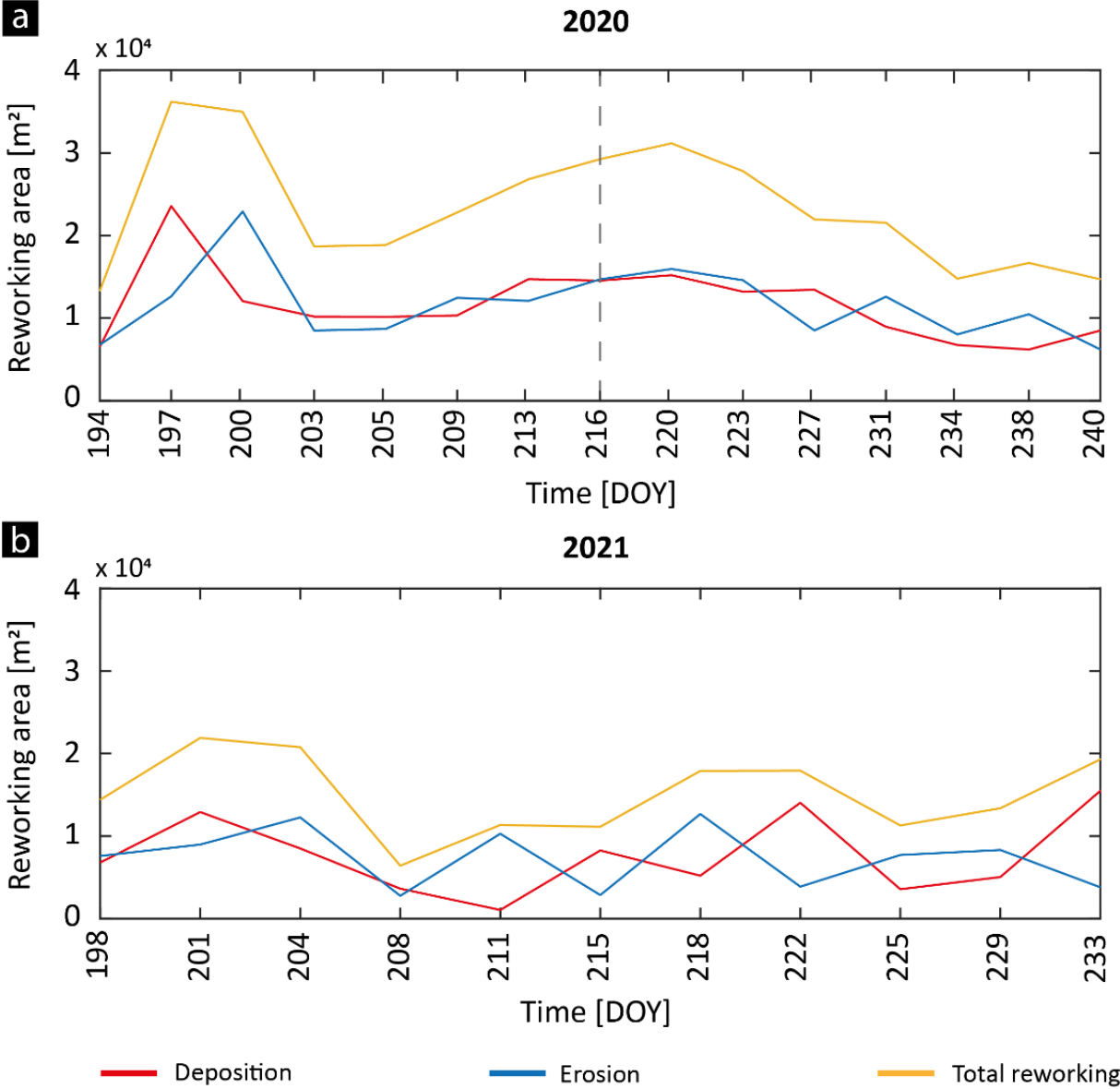


Figure 4.7: Reworked area (deposition, erosion and total) associated to volumetric change quantifications (Figure 4.4 and Figure 4.5) for melt season 2020 (a) and 2021 (b). The dashed gray line in (a) mark the change from S>C to S>C conditions. Elevation surface maps used to retrieve the reworking extent are available in Supplementary Information 4.4.6.

When C>S from DOY 215 in 2020 and there was channel incision upstream (Figure 4.5b); eroded sediment as well as that supplied from the glacier was insufficient to maintain the same braiding intensity in the braid zone; bars increased in size and total number and the braiding index decreased with the flow increasingly confined to fewer channels (Mann-Kendall tests at $p < 0.05$ confirmed monotonic trends; Figures 4.6a to 4.6d and Supplementary

Information 4.4.7). The total area being reworked progressively decreased to ca. $1.4 \times 10^4$ m$^2$, constituting around 7.3% of the total active floodplain (Figure 4.7a). The sediment budget data suggest that the forefield continued to act as a sink for suspended load (ca. 1,600 m$^3$) but, at the same time, ca. 250 m$^3$ of bedload was removed from the proglacial margin system (Figure 4.4e). The morphological method suggests a total aggradation of ca. 1,350 m$^3$ (Figure 4.4c). Erosion occurred in regions passing from dry to inundated (ca. 600 m$^3$), while the contribution of permanently inundated areas was limited to 200 m$^3$. Deposition occurred in regions becoming dry to a total of ca. 2,200 m$^3$ (Figure 4.8a).
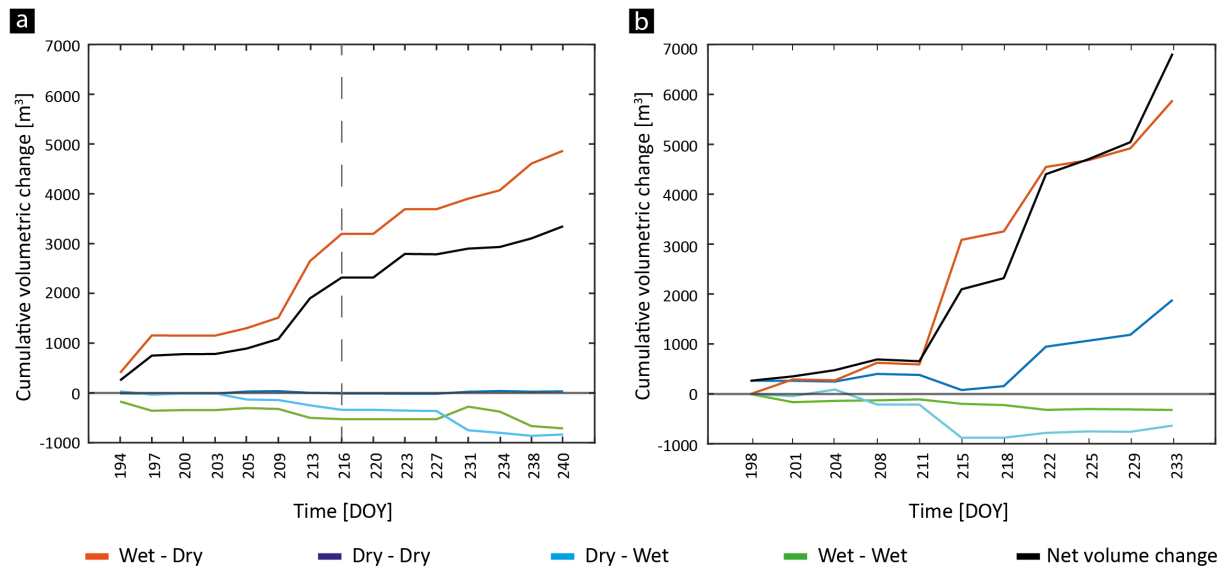


Figure 4.8: Cumulative volumetric contribution of permanently inundated (green line), permanently dry (blue line) and transient regions passing from inundated to dry (red line) or dry to inundated (light blue line) to the total volumetric change (black line) in 2020 (a) and 2021 (b). The dashed gray line in (a) mark the change from S>C to S>C conditions. DoD maps used to extract the total number of cells associated to these regions are available in Supplementary Information 4.4.8.

In 2021, S was continuously higher or comparable to C. Despite a larger variability due to higher daily discharge amplitudes, the seasonal-scale geomorphic response of the proglacial forefield was similar to the first part of the 2020 melt season with progressively increasing braiding and numbers of bars and falling mean bar area (Mann-Kendall tests at $p < 0.05$ confirmed monotonic trends; Figures 4.6f to 4.6h). However, the area affected by geomorphic processes was more confined compared to 2020 which, except between DOY 208 and DOY 215, remained constant at around $2.1 \times 10^4$ m$^2$ (ca. 10.9% of the active floodplain). The proglacial margin stored ca. 6,800 m$^3$ of sediment according to morphological calculations and 8,100 m$^3$ according to sediment load data across the entire season (Figure 4.4f). Of this total ca. 50% occurred in the second part of the melt season (ca. DOY 220 to DOY 234) during high rates of subglacial sediment supply (Figure 4.4b). Thus, while volumetric changes were more limited in space, their magnitude was higher compared to 2020. Deposition dominated in regions experiencing inundation only during high flow conditions (i.e. permanently dry regions in Figure 4.8) and in those passing from wet to dry. Erosion was found in the permanently wet zones and those passing from dry to wet, the latter being dominant (Figure 4.8b). During the second half of the 2021 season, when S increases notably, deposition increased in zones that were previously not inundated upstream of the most braided sector and also through the construction of numerous small bars, accounting for, respectively, 85% and 15% of the total aggradation of ca. 6,100 m$^3$ in this period (Supplementary Information 4.4.6). The forefield configuration progressively evolved towards a more complex spatial configuration in terms of stream statistics (Figure 4.6). The periods DOY 194 to 213 and DOY 220 to 228 experienced increasing subglacial bedload evacuation rates, resulting in a

downstream increase in the total number of bars, a decrease in their emerged area and, consequently, a higher number of secondary channels (Mann-Kendall tests at $p < 0.05$ confirmed monotonic trends; Figures 4.3b and 4.6). The reverse occurred between DOY 214 and 219 and after DOY 229 due to decreasing subglacial supply of coarse particles likely due to colder atmospheric conditions (Mann-Kendall tests at $p < 0.05$ confirmed monotonic trends; Figure 4.3b, 4.6 and Supplementary Information 4.4.1).

### 4.2.3.3 Relationship to changes in surface grain-size distribution

Figure 4.9 shows the mean elevation change and surficial grain size change in both melt seasons (Supplementary Information 4.4.9). According to the gauging station data, forefield aggradation persisted throughout both melt seasons, although notable changes, particularly in 2020, were observed in terms of the associated size fractions. The relationship between vertical elevation and surficial grain size dimention (GSD) change (Figures 4.9a and 4.9b) shows that summer 2021 experienced more intense grain-size change.
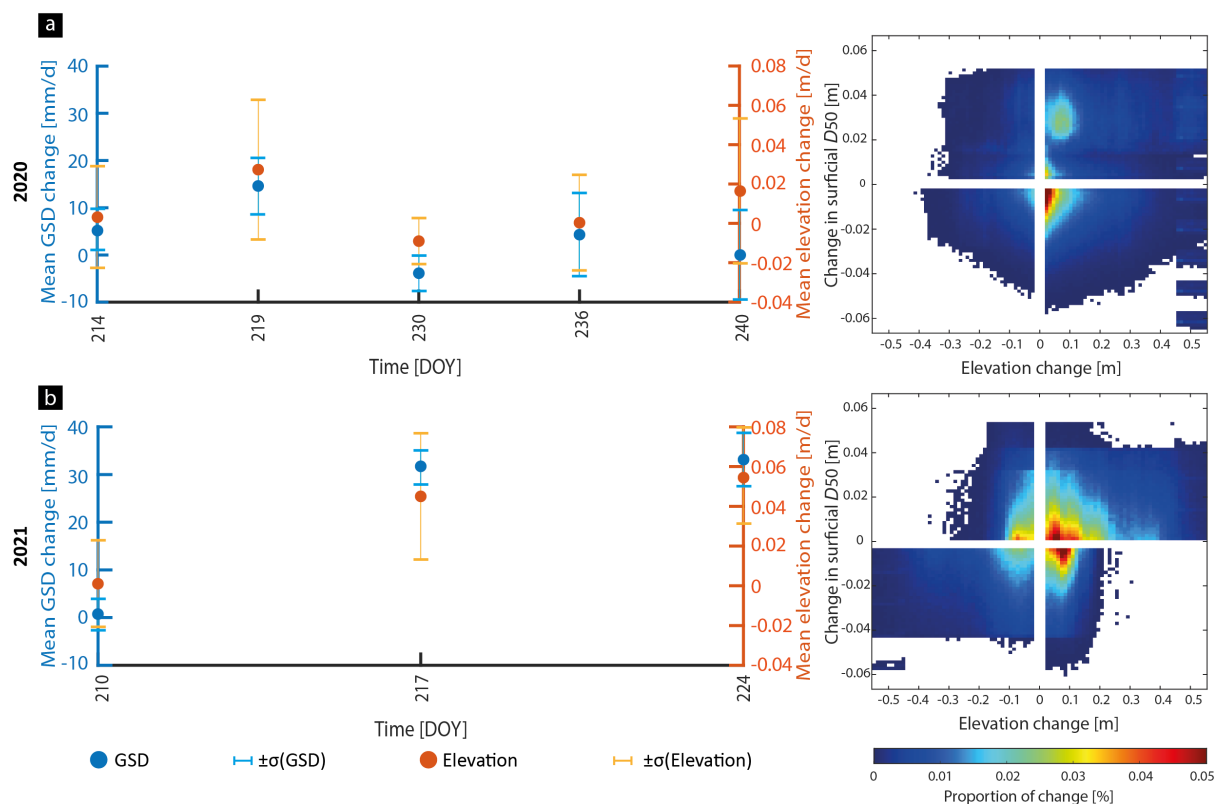


Figure 4.9: Mean surficial elevation and mean $D_{50}$ rate of change (per day) in 2020 (a) and 2021 (b) melt seasons, with respective proportional change at the seasonal scale.

In 2020, up to ca. DOY 219 when S>C, the mean elevation change tends to vary between ca. 0.01 m/d and 0.04 m/d and associated with a general coarsening of surficial sediment deposits of up to ca. 15 mm/d (Figure 4.9a). This situation is reflected in the forefield with coarsening on bar heads, especially where the stream initiates braiding, and with a progressive downstream fining towards the forefield outlet (Figure 4.10a). The situation changed when C became higher than S, with a net decrease of aggradation rates down to ca. -0.02 to 0.02 m/d and with grain size fining between ca. -5 mm/d to 1 mm/d (Figure 4.9a). However, the spatial distribution of change shows two different patterns: aggradation related to coarsening on the right side of the forefield where the stream is more dynamic, with general fining on the most stable left side (Figure 4.10b). In contrast, in 2021 the evolution related to the mean grain size and elevation change relationship is positive, highlighting the importance

of the ratio between coarse and fine sediments exported from subglacial channel in determining the spatial configuration of surficial deposits (Figure 4.9b).
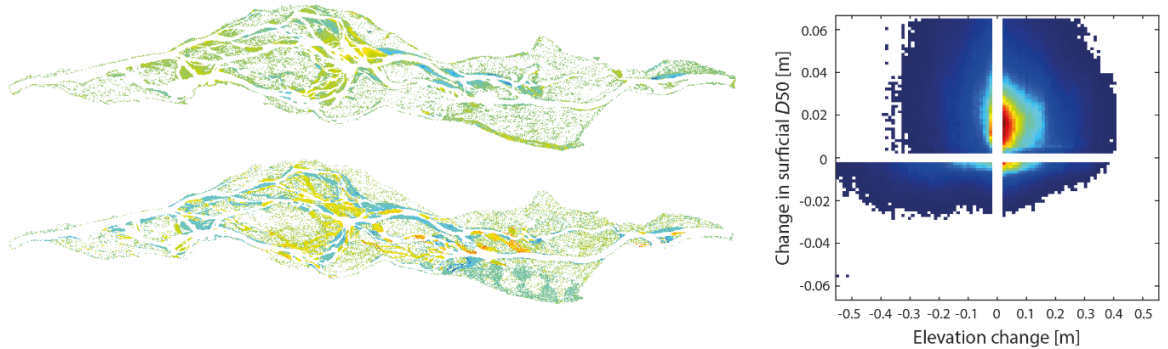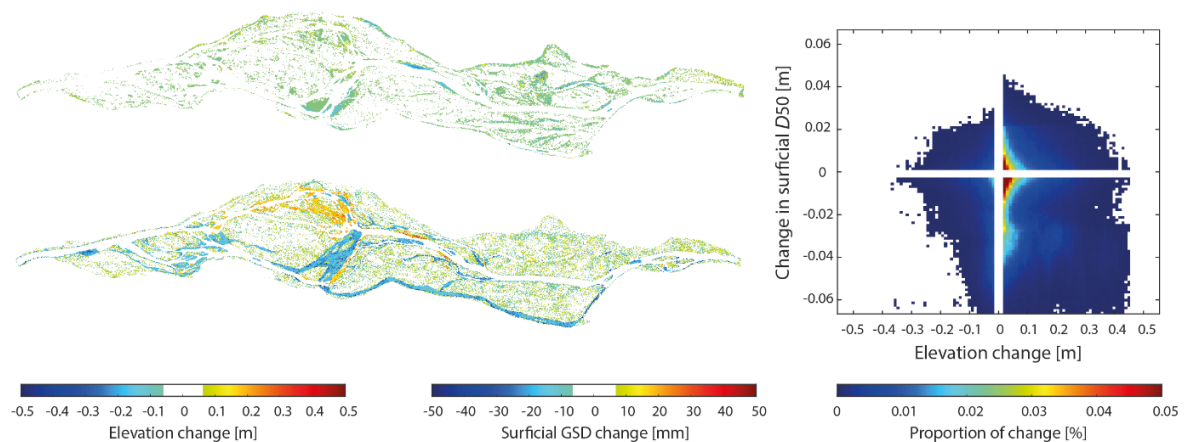


Figure 4.10: Elevation change (upper maps), surficial grain-size change maps (lower maps) and proportion of change (total number of cells) considering both variables for different sediment supply (S) and transport capacity (C) conditions shown in Figure 4.3. In (a) the example for the 26 July (DOY 208) to the 1 August (DOY 214) 2020 period having $S_{ti}$ exceeding $C_{ti}$, while in (b) the example for the 23 (DOY 236) to the 27 August (DOY 240) 2020 period characterized by the contrasting condition. Used LoD values are given in Supplementary Information 4.4.4, while comparison over shorter periods are available in Supplementary Information 4.4.9.

### 4.2.3 Discussion

#### 4.2.3.1 Proglacial geomorphic response to upstream boundary conditions

Quantification of sediment flux dynamics from the continuous monitoring of river loads and the repeated elevation difference maps gave comparable results in cumulative terms over long timescales (Figure 4.4). This coherence not only validates the method presented in Mancini et al. 2024a) for estimating river-bed elevations in the inundated zones of proglacial streams, but also gives confidence to seismically inferred bedload flux quantifications (Mancini et al., 2023a; Figure 4.3). That said, sediment budgets obtained from the two methods differ, which could arise from four possible reasons. First, the bathymetric model used to generate DEMs of both dry and wet regions currently accounts for approximately 50% and 60% of the spatial variability in water depth (Mancini et al., 2024a). Mancini et al. noted that this may be due to an insufficient number of water depth measurements and their correction for changing water stage condition during the calibration process. Consequently, some prediction errors may propagate into estimates of temporal volume changes derived from DEMs of differencing. Second, the seismic method may have a lower sensitivity to fine sediment fractions (0.002-0.008 m) transported either in suspension or as bedload depending on flow conditions (Wilcock et al., 2009). The net change estimates for suspended and bedload (i.e. the sediment budgets)

were lower than those from the DEMs of difference. As there is clear downstream fining in the reach, there may be finer material in transport downstream, such that the seismic method under-estimates how much bedload has left the reach. This would explain why the sediment budgets have higher estimates of aggradation. Third, the use of LoD thresholds in temporal volumetric changes from DEMs of difference maps to remove non-statistical elevation changes may lead to underestimation (Anderson, 2019). This is because not all elevation changes falling within the LoD range can be attributed to the propagation of random errors due to the photogrammetric process, and some of them may still reflect real geomorphic changes. Finally, fourth, the sediment density and porosity values used to convert sediment transport loads into volumes (Eq. 4.1) are not based on direct field measurements, but rather on the literature. The use of a single values retrieved in different geomorphic settings, combined with the spatially in grain size distribution in the study area (Figure 4.1), may be another source of error for the discrepancy between the two quantifications (Manger, 1963; Frings et al., 2011; Tabesh et al., 2022).

Changes in the upstream supply of sediment, i.e. from the glacier, elicit a clear morphodynamic response and the bedload supply matters more than suspended sediment (Figure 4.6; Ashmore, 1991b; Nicholas et al., 1995). Where supply exceeds capacity at the entrance of the forefield, as for the first part of 2020 and for the entire 2021 melt season, the forefield aggrades where valley slope was lowest (Figures 4.4). As long as supply exceeded capacity, braiding indices were maintained or increased; the total number of bars tended to decrease; bars became smaller and total inundated area increased (Figure 4.6; Ashmore, 1991b; Nicholas et al., 1995). In parallel, there was a general coarsening of surface grain size at the forefield scale, but limited to bar head regions (Figure 4.10a). As in this case all supplied sediment was subglacially-exported, it appears that bedload supply by the glacier drives the braiding process. In 2021 the subglacial sediment supply rates were higher than transport capacity for most of the summer season and was associated with substantial deposition in the steeper upstream part of the forefield (Figure 4.4b). Aggradation is known to lead to increasing braiding intensity, with reduction of the valley bottom slope upstream and an increase downstream, in the region where deposition occurs (Germanski and Schumm, 1993; Curran et al., 2017; Roussel et al., 2018). In proglacial forefields, our data show that the balance between changes in bedload sediment supply and transport capacity drive aggradation process and the resulting channel patterns.

When supply is lower than transport capacity, as was the case for the second part of the 2020 melt season, erosion dominated closer to the glacier terminus with stream incision (Figure 4.5b; Lisle et al., 1993). The proglacial margin continued to act as a sink for suspended sediments, but significant bedload was removed from the forefield (Figures 4.3a and 4.4e). Given the extremely low rates of bedload transport supply to the forefield (Figure 4.3a), the bedload leaving the system is likely to have been released by changes in channel pattern and incision (Germanowski and Schumm, 1993; Marren, 2002; Roussel et al., 2018). The proglacial forefield evolved towards a less complex and a geomorphologically more stable configuration characterized by fewer channels and increasing bar areas, likely to promote the longitudinal connection of sediment flux (Figure 4.6). Flood inundation maps showed that the forefield was still affected by some large-scale re-organization events, but these were confined to specific sectors (Figures 4.5b). Changes in surficial grain size distribution maps suggest a general surficial fining due to continued deposition of fines. This is evident as fines constitute a larger proportion of the total volumetric loads, and coarsening patterns occur in the most dynamic sectors (Figure 4.10b; Asselman and Middelkoop, 1995).

The above observations confirm our initial hypotheses that with ongoing glacier retreat, forefield response is a function of the ratio of sediment supply to sediment transport capacity

(Collins, 2008; Kaser et al., 2010; Guillon et al., 2018; Zhang et al., 2022): the dividend of increased runoff during glacier retreat may increase sediment transport capacity drastically, but morphodynamic response depends on whether or not there is concomitant increase in the supply of bedload-sized sediment due to increase in glacial sediment export. Results suggest a strong sensitivity of channel patterns to this balance (Figure 4.6). The forefield acted as a suspended sediment sink throughout, but bedload responded to the interactions between changing bedload sediment supply and changing sediment transport capacity (Figures 4.3 and 6). The regions which contributed the most to capturing subglacially-exported sediment are those transitioning from wet to dry, while the reworking from areas becoming inundated was less important (Figure 4.8). This suggests that reworking of deposited coarse particles was difficult once they were in place. This reworking also impacted strongly the bedload evacuation from the reach and explains the strong filtering for this reach reported by Mancini et al. (2023a). There is also a methodological issue to note. Figure 4.3 shows that the relationship between the transport capacity and discharge is not linear. There are days with higher discharge rates that are not always associated with largest bedload transport capacities. This discrepancy may be attributed to the constant $D_{50}$ value of 0.078 m used in the capacity model, which does not accurately reflect the entire range of bedload fractions effectively transported in proximity to GS1. Further studies are needed to better address the relationship between subglacial sediment evacuation and proglacial forefield response.

### 4.2.3.2 Implications for downstream sediment transport

The strong relationship between subglacial bedload export, morphodynamic activity and forefield geomorphic evolution contrasts with that of suspended sediment load (Figure 4.3). When upstream bedload supply is higher than the transport capacity lateral erosion appears to predominate over the vertical component as, due to aggradation, higher proportions of dry regions are reworked to maintain the discharge rate (Antoniazza et al. 2019). This phenomenon is particularly evident during the 2021 melt season (Figure 4.8b). At the same time, the increasing braiding intensity combined with the establishment of flow divergence regions, causes the forefield to become more of an obstacle to downstream transported particles (Ashmore, 1988; Ferguson and Ashworth, 1992; Kasprak et al., 2015). An aggrading proglacial margin likely increases its tendency to be a sediment sink (Figures 4.4e and 4.4f).

In contrast, when transport capacity become greater than upstream supply, as in the second half of 2020, the forefield contracts into fewer channels likely creates hydraulically more efficient channels, which in turn progressively reinforces the erosional tendency especially for the vertical component increase in bedload export from the proglacial forefield (Bertoldi et al., 2009; Egozi and Ashmore, 2009; Ashmore et al., 2011). Sediment reworking can only influence bedload export directly if discharge variations are sufficiently high to reach the characteristic critical discharge ($Q_c$) for a sufficiently long period of time ($t_{Q>Q_c}$) both to entrain and to export previously deposited bedload particles (Parker, 1976; Ashmore, 1982; Mancini et al., 2023a). In our case, this occurred at the beginning of August 2020 (ca. DOY 220) when daily hydrographs were already characterized by high daily maximum discharges giving both the competence to entrain sediment and the capacity to move it downstream (Figures 4.3a and 4.10b; Lane and Nienow, 2019; Mancini et al., 2023a).

### 4.2.3.3 Wider implications

Our results suggest that proglacial forefields respond to changes in bedload-sized sediment supply, with aggradation and enhanced morphodynamic activity, modifying the surficial grain size distribution, and storing and buffering the downstream flux of upstream delivered sediments. As glaciers retreat, the balances between bedload sediment supply, both its erosion by subglacial processes and its transport under the ice, and transport capacity will

both change (Li et al., 2021; Zhang et al., 2022, 2023) and are likely to lead to systematic shifts in river channel pattern. As glacial erosion rates have a dependence on ice thickness through the latter's control on ice velocity (Herman et al., 2015; Cook et al., 2020), there is likely to be a progressive decline in bedload supply. Whether this then translates into a systematic shift to transport capacity being greater than supply for Alpine glaciers will also depend on how glacial melt changes, the latter also declining as glaciers get smaller (Huss and Hock, 2018; Zhang et al., 2022, 2023). If it does, then our results suggest that there should be a progressive decline in the rates of reworking of proglacial braidplains as glaciers retreat. This observation explains the conceptual model of proglacial fluvial morphodynamics following glacier retreat of Gurnell et al. (1999).

Our results emphasize the critical role played by bedload supply in controlling river morphodynamics in this environment. If this declines as glaciers retreat, and capacity can exceed supply, then glacier-supplied sediment may be replaced by reworking of the braid plain, as happened in the second half of 2020. This has to be time-limited. Our data shows how it reduces the spatial extent of reworking whilst the concentration of flow into a set of smaller channels should lead to sediment sorting processes that make it progressively harder to release sediment. This is likely why as deglaciation continues, the sediment yield to downstream declines (Stoffel and Huggel, 2012; Lane et al., 2017; Delaney and Adhikari, 2020) so explaining at least part of the classical model of paraglacial response (Church and Ryder, 1972). In our case, given extreme decoupling of valley side walls from the braidplain by alluvial fans (Mancini and Lane, 2020), it is likely to be the primary explanation.

Further studies are now needed to understand the relationship between the supply to capacity ratio of coarse sediment, proglacial forefield morphodynamics, glacier retreat, and the influence of dead-ice buried within the forefield on sediment transport dynamics especially to establish robust predictions of sediment supply from glacierized basins in the actual context of rapid climate warming (Zhang et al., 2022). Such changes will also have important implications for the management of downstream sediment transport in hydropower plants (e.g. Carrivick and Tweed, 2021; Li et al., 2021) and for ecosystem stability in high mountain regions (e.g. Gabbud et al., 2019b; Miller and Lane, 2019; Roncoroni et al. 2023b). We showed a strong linkage between channel pattern and bedload supply/capacity. Research has also shown that the rates of embryonic ecosystem development in proglacial forefields appear to be very strongly sensitive to fluvial disturbance and access to water (Roncoroni et al., 2023a). If there is a progressive shift to capacity exceeding supply, then reduced disturbance may be countered by reduced access to water due to the development of larger bars (and greater distances to water; Roncoroni et al., 2023a) as well as incised channels and water table draw down (Müller et al., 2024). This is an area that merits further research.

### 4.2.4 Conclusions

In this study we investigated the geomorphic response of a glacially-fed proglacial forefield to deglaciation in two melt seasons experiencing different climatic and glacier-controlled hydrological and sediment supply conditions. The forefield was largely isolated from valley sidewall sediment supply and contained a braided river. During periods when bedload sediment supply from the glacier exceeds transport capacity there was aggradation, more intense bar construction, increasing channel instability and braiding intensity and coarsening of floodplain deposits. Coarsening was spatially focused upon flow divergence regions and bar tops. The forefield was also a sink for both bedload and suspended load sediment. In contrast, when the subglacial bedload export rates were lower than transport capacity, the forefield continued to act as a sediment sink for fine sediment reflected in the fining of surficial deposits. However, the system was net degradational, reflecting in particular the loss of significant bedload sized sediment. Changes in the balance between glacial sediment supply and

transport capacity resulted in rapid (timescale of days) changes in river morphodynamics. In the actual context of rapid climate change, these results have major implications for the prediction of sediment supply from glacierized catchments as the magnitude of forefield connectivity with downstream regions is likely to be driven by the interplay between sediment availability and transport capacity, either related to meltwater discharge and extreme precipitation events. Given recent work concerning the relationship between access to water, bar destruction and the intensity of ecosystem engineering by primary colonizers, it further suggests that this balance may impact ecosystem succession in proglacial forefields following their deglaciation.

## 4.3 Chapter summary

This study highlighted a strong control of the relationship between subglacial bedload evacuation rates and meltwater supply on proglacial forefield configuration. Periods with bedload export exceeding the stream's capacity to transport it were characterized by large scale morphodynamics processes, enhanced bar construction, and coarsening of surficial sediment deposits suggesting aggradation of both suspended and bedload particles. Conversely, when bedload export was lower then the transport capacity, the proglacial system evolved rapidly toward a less braided and dynamic state. Although, it continued to act as a sink for fine sediment, it became a source of bedload size particles. In this situation, fining dominated at the forefield scale, with isolated coarsening patterns observed in flow divergence regions highlighting difficulties in evacuating previously deposited coarser particles. Thus, the proglacial forefield configuration is highly sensitive to the balance between subglacial sediment supply and transport capacity, with significant implications for longitudinal connectivity with downstream regions.

These findings are based on a case study constrained by specific topographical, sedimentological and hydrological settings (Section 1.5 and 1.6). This Chapter highlights the need to extend this knowledge to forefields characterized by different boundary conditions. This is the research objective addressed in Chapter 5.

## 4.4 Supporting information

### 4.4.1 Climatic conditions during melt season 2020 and 2021

The melt-seasons 2020 and 2021 were associated with two different climatic conditions (Figure S4.1). The 2020 melt season had a mean temperature of ca. 7.7 °C characterized by a warming phase in July (mean of ca. 7.8 °C) followed by a short cold period (mean of ca. 4.3 °C) at the beginning of August, and again a warm and more stable phase lasting until end of August (mean of ca. 8.2 °C). In 2021, the mean atmospheric temperature was ca. 7.4 °C. The mid-June period was characterized by rapid warming (mean of c. 8.2 °C), followed by a general cooling trend (mean of ca. 6.9 °C) until mid-July, but with short very warm days for the altitude (2450 m a.s.l.) with temperatures up to ca. 15 °C. The rest of the melt season had very similar conditions to those of 2020 with a warming period until the end of July (mean of ca. 7.5 °C), a slightly longer cold period at the beginning of August (mean of ca. 5.3 °C) and a warmer phase in mid-August (mean of ca. 8.4 °C) with atmospheric temperatures reaching ca. 18 °C. In terms of precipitation, 2021 was affected by higher rainfall rates compared to 2020. In 2021 there was a particularly wet period (263 mm of precipitation) in the first half of July. In 2020, only a total of 76 mm was recorded across the whole melt season mainly distributed in multiple short-lived events. More details are available in Mancini et al. (2023a).
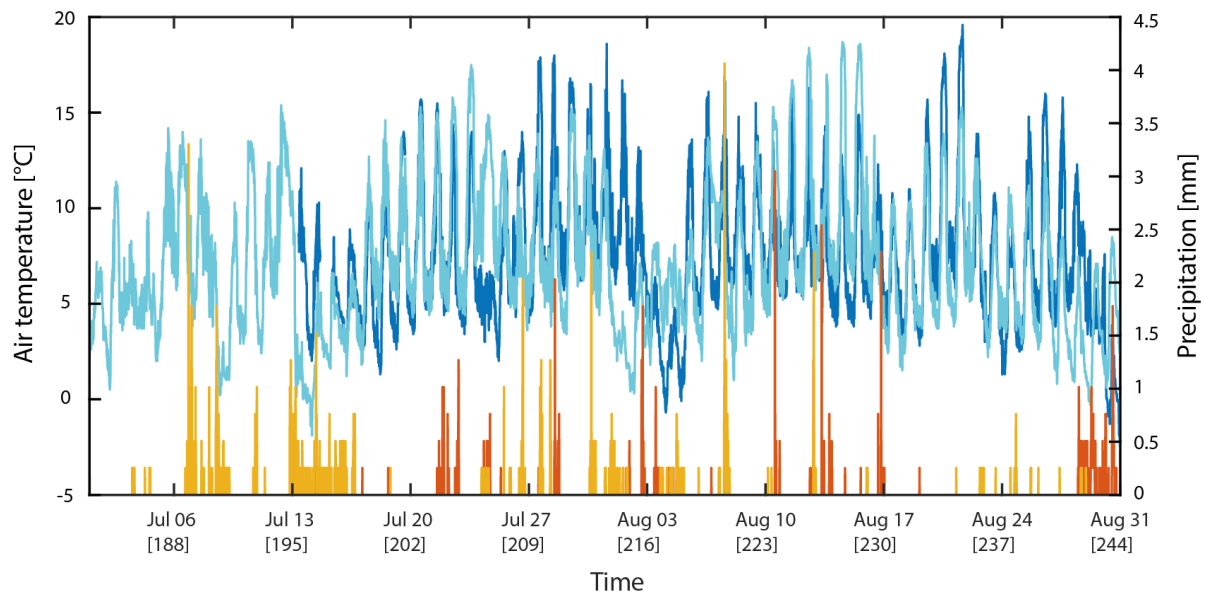


Figure S4.1: Climatic condition in the Glacier d'Otemma proglacial forefield during melt seasons 2020 and 2021 measured at a meteorological station located ca. 150 m upstream of GS1 (Figure 4.1). Dark and light blue (orange) lines refer to atmospheric temperature [°C] (cumulative precipitation [mm]) in 2020 and 2021, respectively. In square brackets is the time from the 1 January.

## 4.4.2 Surface uncertainties (wet and dry regions) and LoD values for inundated areas
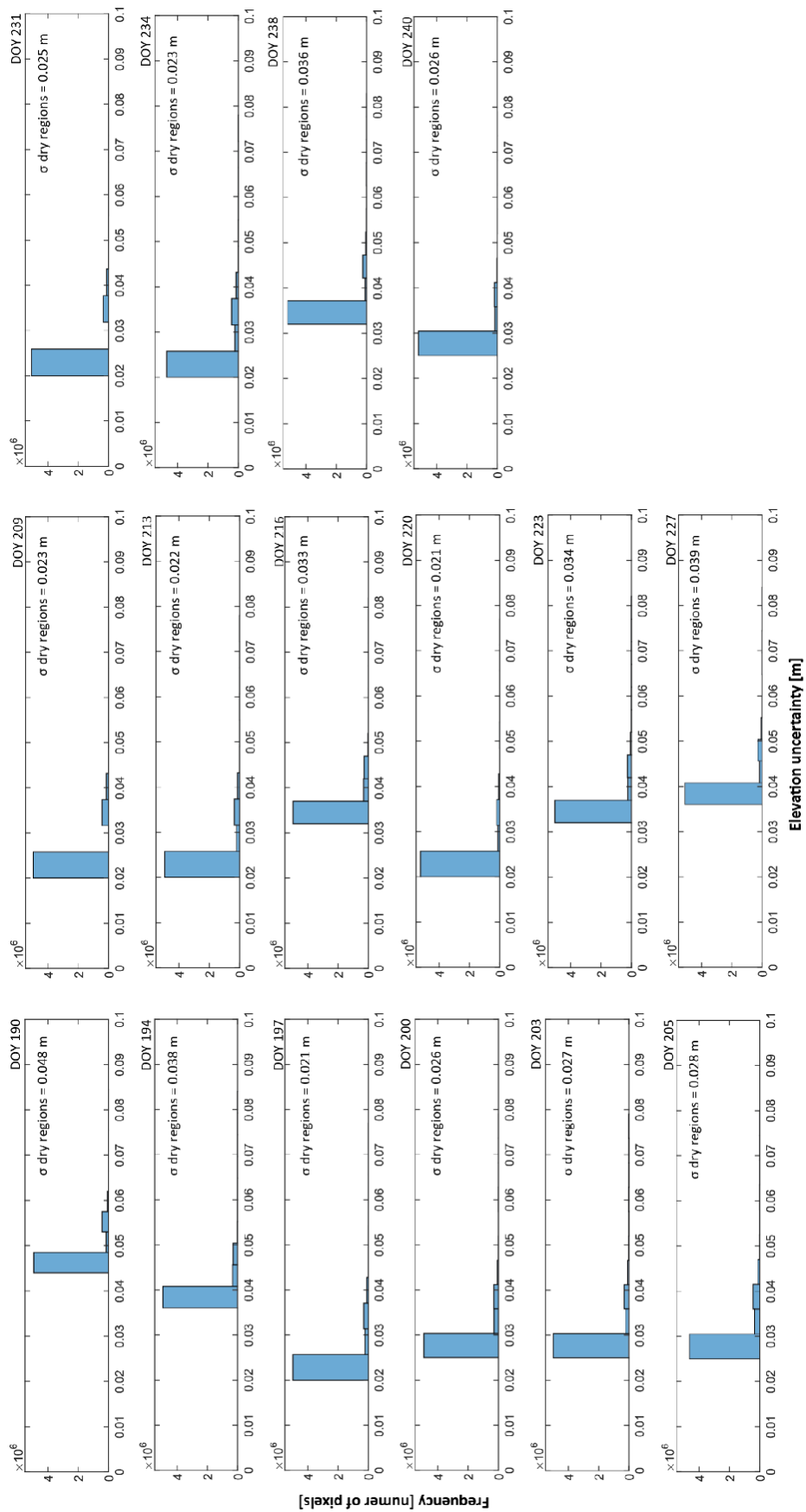


Figure S4.2: Elevation uncertainties distribution and standard deviation of error for, respectively, inundated and dry area in 2020 elevation of difference maps (Figure S4.8).
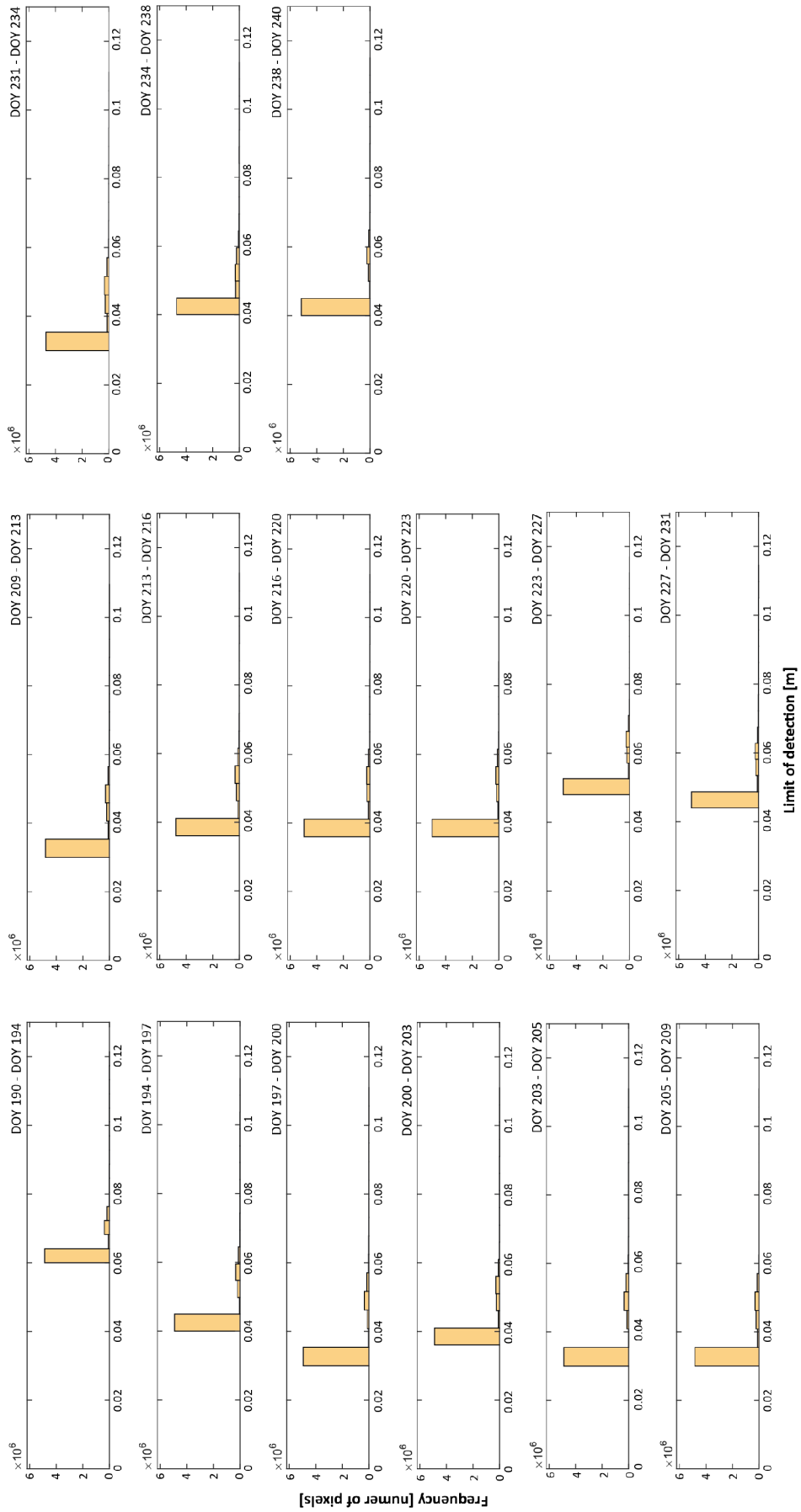
Figure S4.3: Limit of detection values (at 95%) for inundated area in 2020 elevation of difference maps (Figure S4.8).
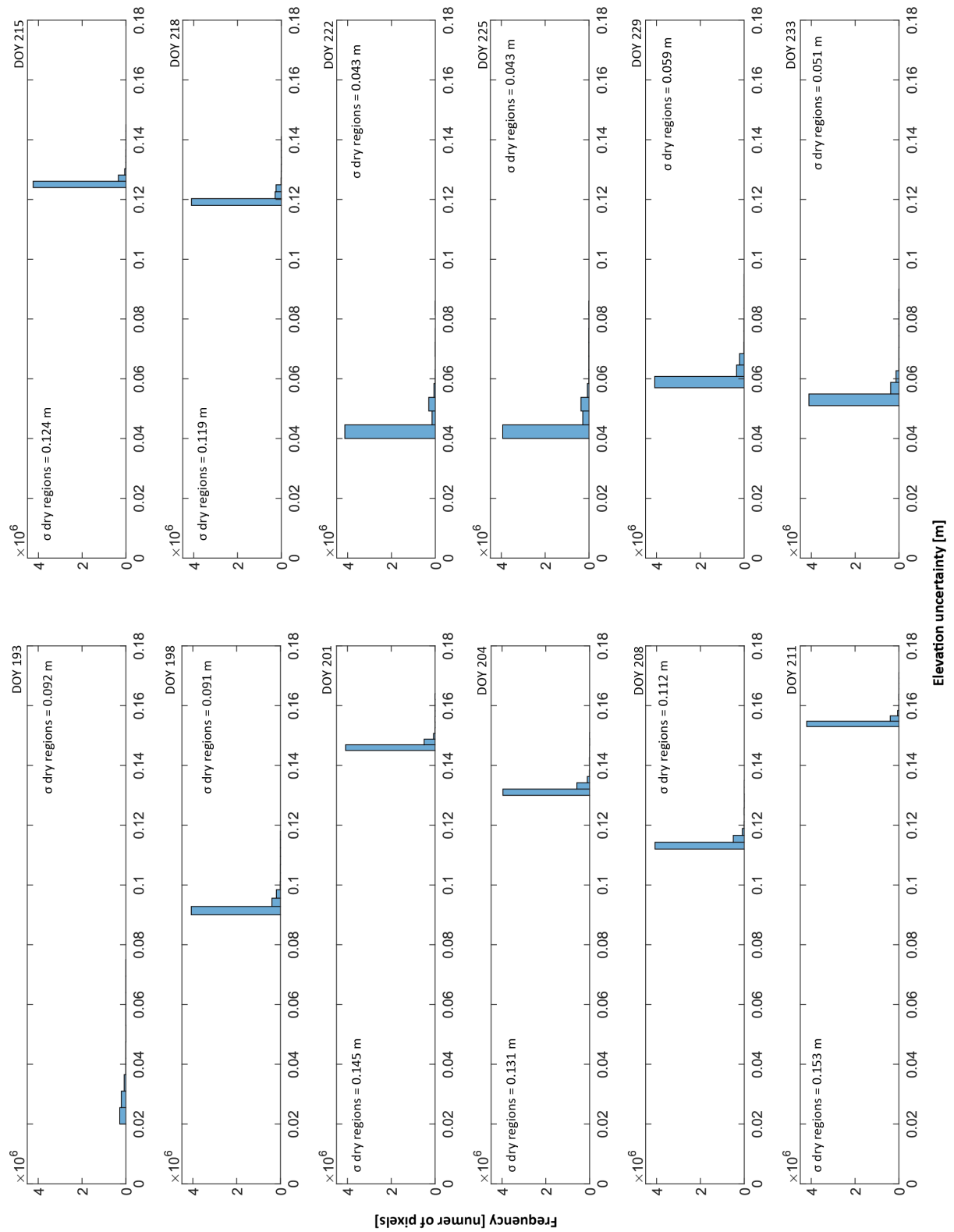
Figure S4.4: Elevation uncertainties distribution and standard deviation of error for, respectively, inundated and dry area in 2021 elevation of difference maps (Figure S4.9).
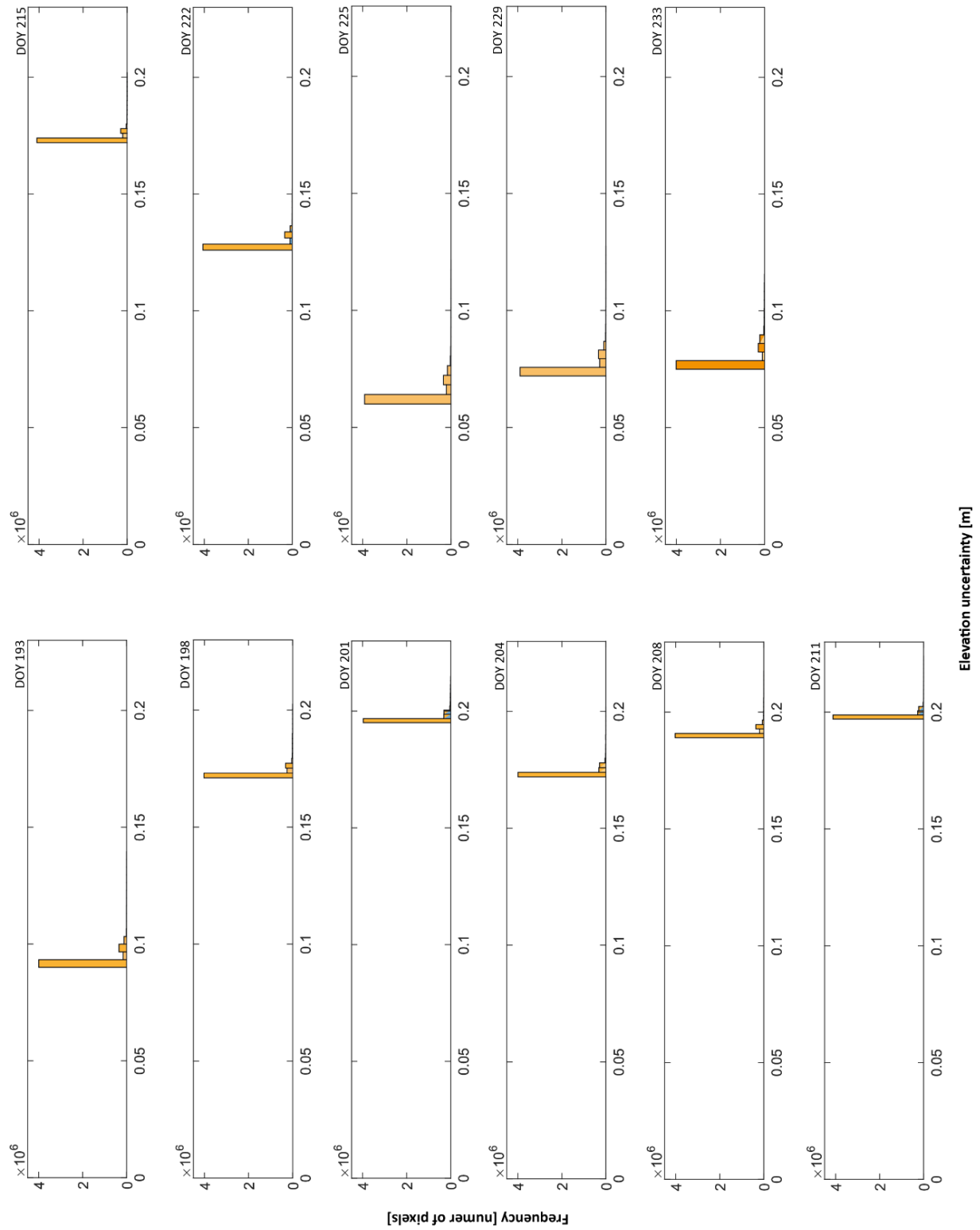
Figure S4.5: Limit of detection values (at 95%) for inundated area in 2021 elevation of difference maps (Figure S4.9).

### 4.4.3 LoD values for dry regions

Table S4.1: LoD values for permanently dry regions in elevation of difference maps (Figure 4.4, 4.5, S4.8 and S4.9).

| Year | Date | 95% LoD |
|---|---|---|
| 2020 | 8 July [DOY 190] – 12 July [DOY 194] | ±0.059 |
| | 12 July [DOY 194] – 15 July [DOY 197] | ±0.042 |
| | 15 July [DOY 197] – 18 July [DOY 200] | ±0.042 |
| | 18 July [DOY 200] – 21 July [DOY 203] | ±0.037 |
| | 21 July [DOY 203] – 23 July [DOY 203] | ±0.035 |
| | 23 July  [DOY 205] – 27 July [DOY 209] | ±0.034 |
| | 27 July  [DOY 209] – 31 July [DOY 213] | ±0.032 |
| | 31 July [DOY 213] – 3 August [DOY 216] | ±0.039 |
| | 3 August [DOY 216] – 7 August [DOY 220] | ±0.041 |
| | 7 August [DOY 220] – 10 August [DOY 223] | ±0.041 |
| | 10 August [DOY 223] – 14 August [DOY 227] | ±0.052 |
| | 14 August [DOY 227] – 18 August [DOY 231] | ±0.046 |
| | 18 August [DOY 231] – 21 August [DOY 234] | ±0.034 |
| | 21 August [DOY 234] – 25 August [DOY 238] | ±0.043 |
| | 25 August [DOY 238] – 27 August [DOY 240] | ±0.044 |
| | 8 July [DOY 190] – 31 July [DOY 213] | ±0.096 |
| | 31 July [DOY 213] – 27 August [DOY 240] | ±0.088 |
| 2021 | 12 July [DOY 193] – 17 July [DOY 198] | ±0.055 |
| | 17 July [DOY 198] – 20 July [DOY 201] | ±0.105 |
| | 20 July [DOY 201] – 23 July [DOY 204] | ±0.095 |
| | 23 July [DOY 204] – 27 July [DOY 208] | ±0.101 |
| | 27 July [DOY 208] – 30 July [DOY 211] | ±0.134 |
| | 30 July [DOY 211] – 3 August [DOY 215] | ±0.119 |
| | 3 August [DOY 215] – 6 August [DOY 218] | ±0.083 |
| | 6 August [DOY 218] – 10 August [DOY 222] | ±0.047 |
| | 10 August [DOY 222] – 13 August [J DOY 225] | ±0.047 |
| | 13 August [DOY 225] – 17 August [DOY 229] | ±0.048 |
| | 17 August [DOY 229] – 21 August [DOY 233] | ±0.046 |
| | 12 July [DOY 193] – 21 August [DOY 233] | ±0.089 |

### 4.4.4 Surface sedimentological analysis: detailed methodology

Grain-size distribution maps at the forefield scale were generated following the approach described in Lane et al. (2020), based on the image-texture approach of Carbonneau et al. (2004, 2005). Texture-based approaches assume that there is a relationship between image properties (e.g. the standard deviation of a grey-scale image) and parameters describing the particle sizes present (e.g. $D_{50}$) for a given spatial unit.

Grain size measurements were collected twice for both melt seasons (6 July and 11 August in 2020; 17 July and 8 August in 2021) in random sites of the Otemma floodplain following the Wolman (1954) method. We manually measured the b-axis of 100 grains located on a 1 m x 1 m grid. The corners of each grid were measured using a differential GPS. We measured 30 grids per date in 2020 and 20 in 2021 in sites chosen to cover the range of grain-sizes in the floodplain but focusing upon locations way from the most likely active channel zones. These grids were randomly assigned into a calibration and a validation dataset for each date. For each grid, the image was segmented to the grid corners and we calculated the image texture, taken here as the standard deviation of the greyscale image values (following Lane et al., 2020) for the grid. The calibration data were then used to determine a relationship between

image texture and the measured $D_{50}$ of the form y = a$D_{50}$+b; the calibration relation was then applied to the image data for the validation grids to evaluate the method.

The UAV data collection strategies were designed to minimize the effects of changing light conditions between datasets. However, it is likely that orthomosaics were characterized by artifacts affecting their textures. We assessed this effect by determining 15,000 grain-sizes using this method for stable non-inundated zones on different dates. In such zones, the surficial granulometry should not have changed over time. These were then used to construct a correction calibration for each date such that derived grain-sizes were equivalent to the reference date for which the calibration relation was calculated. Coefficients of the linear regressions between the corrected grain-size map and the reference, as well as the respective R-squared values, are available in Table S4.2.

Table S4.2: linear regression coefficients and final $R^2$ values used to correct $D_{50}$ maps for both 2020 and 2021 datasets.

| Reference | Date | Coefficients | | $R^2$ |
|---|---|---|---|---|
| | | a | b | |
| 8 July 2020 [DOY 190] | 26 July [DOY 208] | 0.780 | 5.768 | 0.864 |
| | 1 August [DOY 214] | 0.791 | 6.136 | 0.832 |
| | 6 August [DOY 219] | 0.793 | 4.656 | 0.904 |
| 11 August 2020 [DOY 224] | 17 August [DOY 230] | 1.023 | 4.024 | 0.871 |
| | 23 August [DOY 236] | 1.026 | 6.069 | 0.781 |
| | 27 August [DOY 240] | 1.019 | 3.859 | 0.824 |
| 17 July 2021 [DOY 198] | 22 July [DOY 203] | 0.916 | 0.018 | 0.812 |
| | 29 July [DOY 210] | 0.861 | 0.017 | 0.818 |
| | 5 August [DOY 217] | 0.823 | 0.013 | 0.840 |
| 8th August 2021 [DOY 220] | 12 August [DOY 224] | 0.705 | 0.022 | 0.744 |

Grain-size difference maps limited by the extent of the active floodplain used with the DEMs were produced at both seasonal and weekly scales. Following Lane et al. (2020) we identified a limit of detection for grain-size changes, computed from 350 points randomly sampled from stable zones where grain-size changes should be absent (Table S4.3).

Table S4.3: LoDs values used for the relationship between surficial elevation and $D_{50}$ changes shown in section 4.4.9.

| Year | Date | 95% LoD [m] | |
|---|---|---|---|
| | | DoD | GSD |
| 2020 | 25 July [DOY 207] – 1 August [DOY 214] | ±0.051 | ±0.075 |
| | 1 August [DOY 214] – 6 August [DOY 219] | ±0.034 | ±0.007 |
| | 6 August [DOY 219] – 17 August [DOY 230] | ±0.031 | ±0.009 |
| | 17 August [DOY 230] – 23 August [DOY 236] | ±0.038 | ±0.010 |
| | 23 August [DOY 236] – 27 August [DOY 240] | ±0.036 | ±0.006 |
| 2021 | 22 July [DOY 203]  – 29 July [DOY 210] | ±0.055 | ±0.013 |
| | 29 July [DOY 210]  – 5 August [DOY 217] | ±0.053 | ±0.012 |
| | 5 August [DOY 217] – 12 August [DOY 224] | ±0.047 | ±0.015 |

## 4.4.5 Sediment transport dynamics

Daily hydrographs have an asymmetrical shape characterized by a rapid increase during the rising limb up to rates of 10 m$^3$/s and a gentler decrease in the falling limb usually occurring around 6 pm (Figure S4.6a and S4.6c). The same dynamic is consequently also reflected in suspended sediment loads and concentrations. In the first case, suspended sediment loads at GS1 and GS2 co-varied strongly in both melt seasons (r = 0.661 in GS1 and

r = 0.612 in for 2020; r = 0.675 in GS1 and r = 0.652 in for 2021), so that suspended sediment concentration also tracked discharge (r = 0.663 in GS1 and r = 0.634 in for 2020; r = 0.694 in GS1 and r = 0.671 in for 2021). There is a consistent temporal pattern in suspended sediment dynamics consisting in (1) a rapid rise with discharge starting at ca. 9 am; (2) a suspended loads peak around 6 pm which is slightly higher at GS1 than at GS2; followed by (3) a sudden decline more important at GS2 than at GS1. This suggests that the proglacial forefield acts as a net sink for suspended sediment and this is reflected in the cumulative load plots (Figure S4.6b and S4.6d).
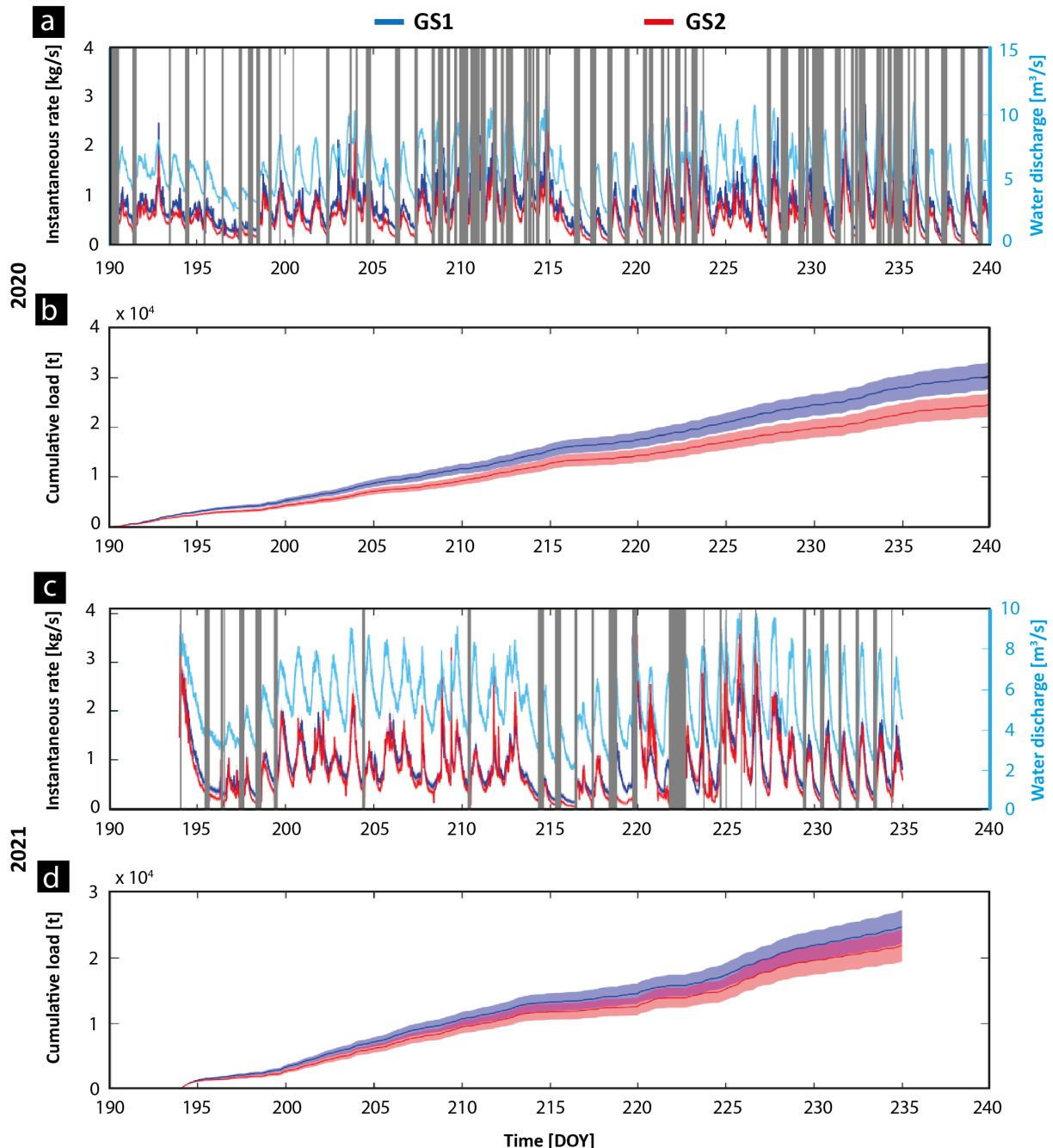


Figure S4.6: Mean water discharge, instantaneous suspended sediment transport rates and cumulative suspended loads in GS1 and GS2 for melt seasons 2020 (a and b) and 2021 (c and d). The grey areas in (a) and (c) highlight periods without sediment transport records; shaded blue and red area is the transport uncertainty.

Instantaneous bedload transport rates show more intra- and inter-yearly variability compared to suspended sediment rates (Figure S4.7). The intra-yearly variability close to the

glacier terminus is characterized by daily transport cycles closely related to discharge variation (r = 0.694 in 2020 and r = 0.670 in 2021). Bedload increases rapidly with the rising limb of the daily hydrograph, it peaks coinciding with water discharge maxima around 7 pm, then falls to low or even zero levels (Figure S4.7a and S4.7c). At GS2, bedload transport also rises with discharge but more slowly, to a variable degree and tends also to occur continuously even at low overnight discharges (Figure S4.7a and S4.7c). Thus correlations with discharge are lower variation (r = 0.462 in 2020 and r = 0.431 in 2021) and bedload co-varies between GS1 and GS2 less strongly than for suspended load.

At the seasonal scale, bedload transport at GS1 evolves similarly in both melt seasons (Figure S4.7a and S4.7c). There is (i) a phase comprised between the beginning and the end of July (DOY 190 to DOY 215) with daily cycles of transport with rates going from completely absence of transport up to rates of ca. 4.3 kg/s in 2020 and ca. 6 kg/s in 2021, (ii) followed by a phase (DOY 215 to DOY 220) in which no bedload transport is recorded because both MAATs and discharge rates drastically decreased, and (iii) a phase starting at the beginning of August (around DOY 220) characterized by the re-activation of daily cycles of bedload transport. Unlike suspended load (Figure S4.6) bedload is very sensitive to short duration periods of climatic degradation. There is one important difference between 2020 and 2021 despite no real climate differences and similarly intense diurnal discharge variation (Figure S4.1 and S4.7). In 2020, from early August (DOY 215) bedload transport rates reduced in magnitude and became more variable between days (Figure 4.3a). In contrast, in 2021 after a cold period at the turn between June and July (DOY 214 to 218) instantaneous bedload rates increased again with peaks continuing to co-vary with discharge (Figure 4.3b).

At GS2 bedload transport variability at the seasonal-scale was similar for both 2020 and 2021 with constant rates and occasional daily peaks of, respectively, ca. 0.7 kg/s and 1.5 kg/s (Figure S4.7a and S4.7c). Thus, whilst GS1 has some clear season changes, these were less clear at GS2. The cumulative bedload curves show this markedly with periods of faster and slower growth in bedload at GS1 but almost constant rates of accumulation at GS2. Substantially more bedload enters the forefield at GS1 than leaves at GS2.

The methods used to acquire and to analyses these records, as well as the resulting datasets themselves have been published for discharge in Müller and Miesen (2022) and for continuous suspended sediment and bedload fluxes in Mancini et al. (2023a,b).
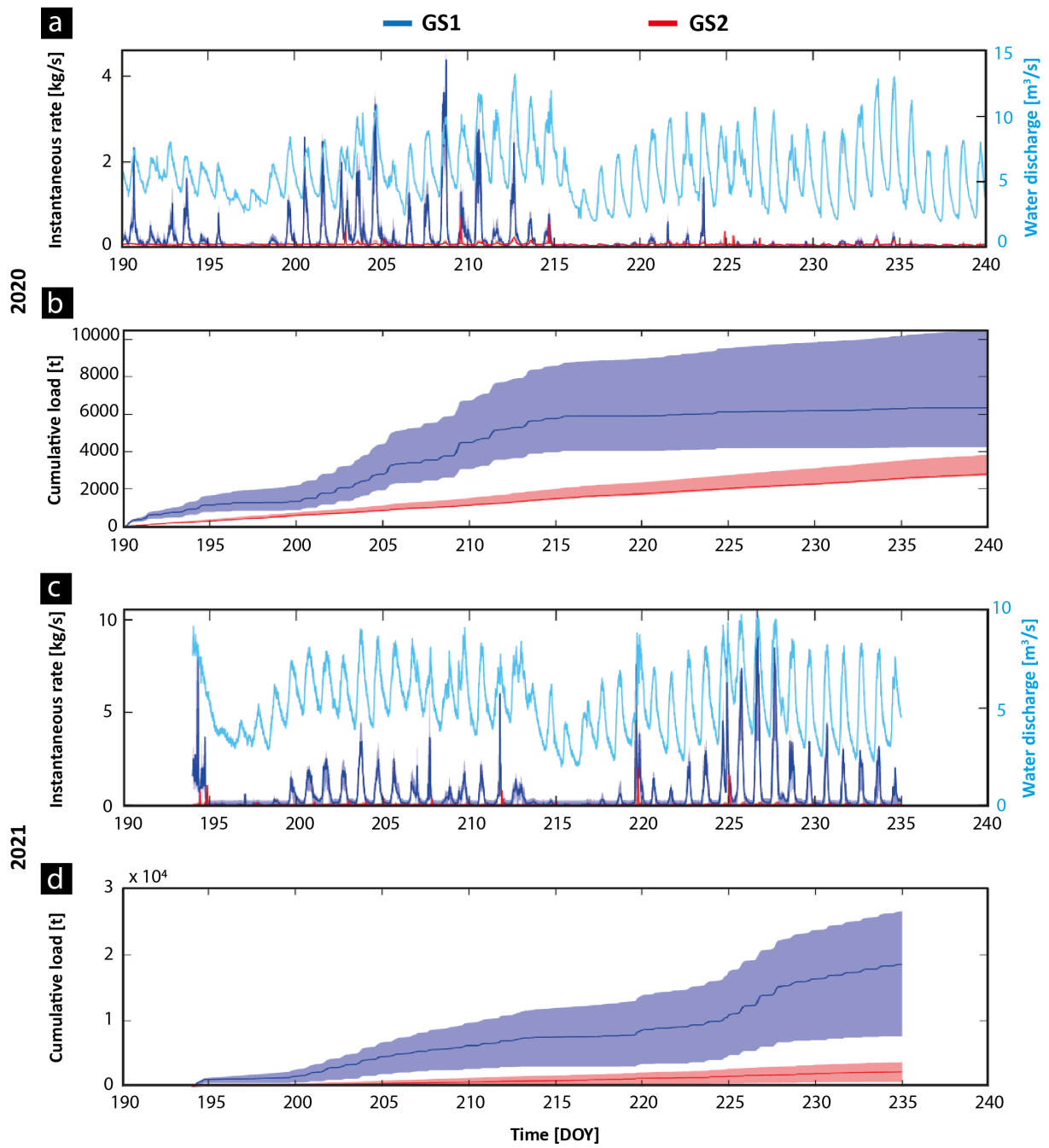
Figure S4.7: Mean water discharge, instantaneous transport rates and cumulative bed-loads in GS1 and GS2 for melt seasons 2020 (a and b) and 2021 (c and d). The shaded blue and red area refers to transport uncertainty.

## 4.4.6 Daily and sub-daily surface elevation changes (DoDs) for the 2020 and 2021 melt season

**a** 8ʰ July [DOY 190] - 12ᵗʰ July [DOY194]

**b** 12ᵗʰ July [DOY 194] - 15ᵗʰ July [DOY 197]

**c** 15ᵗʰ July [DOY197] - 18ᵗʰ July [DOY 200]

**d** 18ᵗʰ July [DOY 200] - 21ˢᵗ July [DOY 203]

**e** 21ˢᵗ July [DOY 203] - 23ʳᵈ July [DOY 205]

**f** 23ʳᵈ July [DOY 205] - 27ᵗʰ July [DOY 209]

**g** 27ᵗʰ July [DOY 209] - 31ˢᵗ July [DOY 213]

**h** 31ˢᵗ July [DOY 213] - 3ʳᵈ August [DOY 216]

Flow direction

**i** 3ʳᵈ August [DOY 216] - 7ᵗʰ August [DOY 220]

**j** 7ᵗʰ August [DOY 220] - 10ᵗʰ August [DOY 223]

**k** 10ᵗʰ August [DOY 223] - 14ᵗʰ August [DOY 227]

**l** 14ᵗʰ August [DOY 227] - 18ᵗʰ August [DOY 231]

**m** 18ᵗʰ August [DOY 231] - 21ˢᵗ August [DOY 234]

**n** 21ˢᵗ August [DOY 234] - 25ᵗʰ August [DOY 238]

**o** 25ᵗʰ August [DOY 238] - 27ᵗʰ August [DOY 240]

-1    -0.5    0    0.5    1
Elevation change [m]



Figure S4.8: Daily and intra-daily DEMs of difference maps accounting for both dry and wet regions in 2020. LoD for dry regions are reposted in Table S4.1. For inundated regions LoD values are spatially variable and illustrated in Figure S4.3.
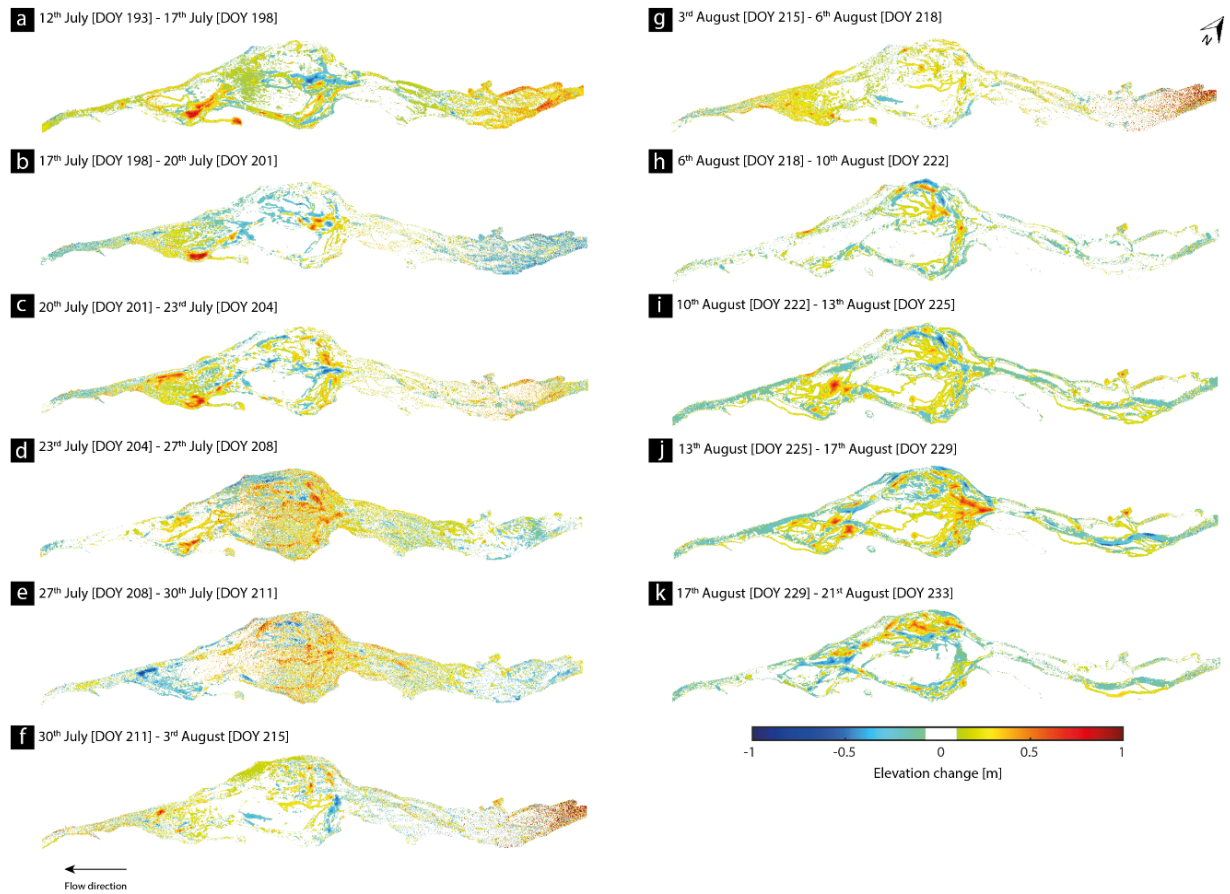
Figure S4.9: Daily and intra-daily DEMs of difference maps accounting for both dry and wet regions in 2021. LoD for dry regions are reposted in Table S4.1. For inundated regions LoD values are spatially variable and illustrated in Figure S4.5.

## 4.4.7 Flooding frequency maps for melt season 2020 and 2021



**a** 8th July 2020 [DOY 190] - 3rd August 2020 [DOY 216]
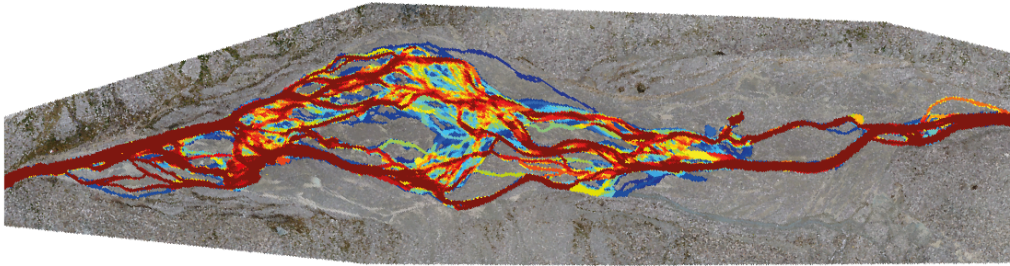
**b** 3rd August 2020 [DOY 216] - 27th August 2020 [DOY 240]
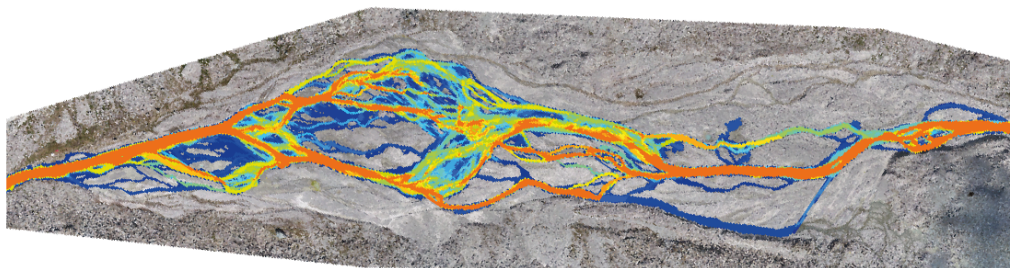
**c** 12th July 2021 [DOY 193] - 6th August 2021 [DOY 218]
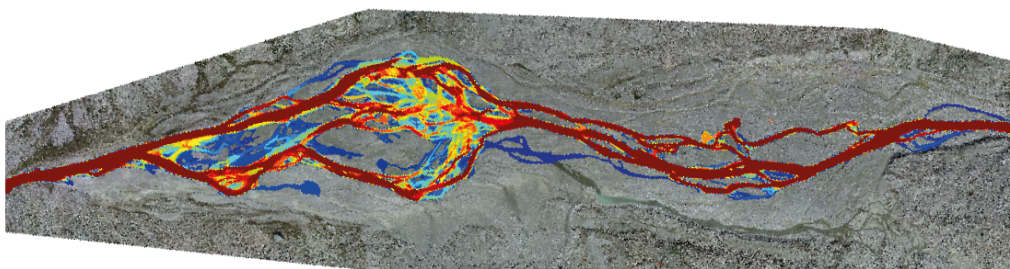
**d** 6th August 2021 [DOY 218] - 21st August 2021[DOY 233]
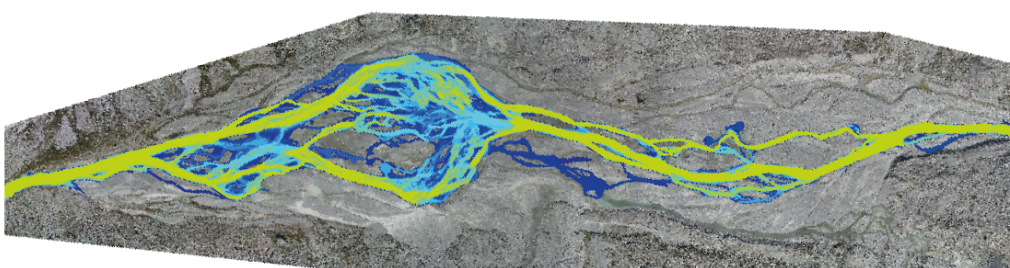
Flow direction

0    100    200 m

Figure S4.10: Flooding frequency maps for melt season 2020 (a and b) and 2021 (b and c) temporally subdivided according to the sediment supply-transport capacity relationship given in Figure 4.3.

## 4.4.8 Sectorial and total volumetric changes

Table S4.4: Sectorial volumetric contribution in DoD considering both inundated and dry regions shown Figure 4.8a.

| Period [DOY] | Total [m³] | Sectorial volumetric change [m³] | | | |
|---|---|---|---|---|---|
| | | Before | | | After |
| | | Wet | Dry | | |
| 190 - 194 | 253.01 | -173.79 [28.2%] | 29.86 [4.8%] | Wet | |
| | | 405.03 [65.6%] | -8.09 [1.4%] | Dry | |
| 194 - 197 | 496.23 | -184.09 [18.4%] | -64.02 [6.4%] | Wet | |
| | | 749.97 [74.7%] | -5.86 [0.5%] | Dry | |
| 197 - 200 | 30.83 | 13.45 [33.9%] | 21.38 [53.9] | Wet | |
| | | -3.84 [9.7%] | -0.99 [2.5%] | Dry | |
| 200 - 203 | 3.15 | -0.77 [16.4%] | 3.71 [79.2%] | Wet | |
| | | -0.078 [1.6%] | 0.13 [2.8%] | Dry | |
| 203 - 205 | 110.8 | 40.67 [11.4%] | -123.55 [34.6%] | Wet | |
| | | 150.17 [42.1%] | 42.72 [11.9%] | Dry | |
| 205 - 209 | 191.3 | -17.44 [7.1%] | -10.41 [4.2%] | Wet | |
| | | 210.66 [85.4%] | 8.19 [3.3%] | Dry | |
| 209 - 213 | 817.4 | -179.12 [12.3%] | -106.35 [7.3%] | Wet | |
| | | 1136.72 [78.1%] | -34.25 [2.3%] | Dry | |
| 213 - 216 | 417.8 | -26.49 [3.9%] | -89.85 [13.3%] | Wet | |
| | | 546.11 [80.9%] | -12.77 [1.9%] | Dry | |
| 216 - 220 | 0.51 | 0.03 [4.8%] | 0.49 [92.9%] | Wet | |
| | | -0.01 [0.7%] | -0.01 [1.6%] | Dry | |
| 220 - 223 | 475.6 | -0.09 [0.1%] | -16.54 [3.1%] | Wet | |
| | | 467.01 [95.7%] | -5.37 [1.1%] | Dry | |
| 223 - 227 | -8.12 | -0.99 [11.5%] | -7.29 [85.3%] | Wet | |
| | | 0.19 [2.3%] | 0.07 [0.9%] | Dry | |
| 227 - 231 | 114.23 | 252.48 [28.4%] | -387.88 [43.6%] | Wet | |
| | | 210.24 [23.6%] | 39.17 [4.4%] | Dry | |
| 231 - 234 | 33.46 | -99.51 [29.8%] | -50.93 [15.2%] | Wet | |
| | | 168.34 [50.4%] | 15.29 [4.6%] | Dry | |
| 234 - 238 | 172.87 | -290.77 [32.2%] | -61.13 [6.7%] | Wet | |
| | | 537.17 [59.5%] | -13.27 [1.6%] | Dry | |
| 238 - 240 | 244.54 | -45.97 [13.7%] | 27.51 [8.2%] | Wet | |
| | | 256.74 [76.4%] | 5.71 [1.7%] | Dry | |

Table S4.5: Sectorial volumetric contribution in DoD considering both inundated and dry regions shown in Figure 4.8b.

| Period [DOY] | Total [m³] | Sectorial volumetric change [m³] | | |
| --- | --- | --- | --- | --- |
| | | Before | | |
| | | Wet | Dry | |
| 193-198 | 267.1 | -13.65 [4.44%] | -6.81 [2.21] | Wet |
| | | 285.31 [92.72] | 2.05 [0.67] | Dry |
| 198-201 | 88.03 | -163.42 [32.77%] | -40.78 [8.18%] | Wet |
| | | 239.33 [58.82%] | -1.14 [0.23%] | Dry |
| 201-204 | 125.54 | 26.32 [13.80%] | 131.55 [68.97%] | Wet |
| | | -17.69 [9.28%] | -15.18 [7.96%] | Dry |
| 204-208 | 215.33 | 11.27 [1.38%] | -302.1 [36.88%] | Wet |
| | | 352.45 [43.02%] | 153.39 [18.72%] | Dry |
| 208-211 | -36.04 | 18.51 [25.35%] | -0.72 [0.99%] | Wet |
| | | 34.03 [46.59%] | -19.76 [27.06%] | Dry |
| 211-215 | 1444.51 | -89.05 [2.50%] | -665.57 [18.7%] | Wet |
| | | 2502 [70.28%] | -303.39 [8.52%] | Dry |
| 215-218 | 224.86 | -24.3 [8.92%] | 1.29 [0.48%] | Wet |
| | | 168.94 [61.97%] | 78.08 [28.64%] | Dry |
| 218-222 | 2088.45 | -96.07 [4.21%] | 97.28 [4.27%] | Wet |
| | | 1294.4 [56.77%] | 729.36 [34.75%] | Dry |
| 222-225 | 298.22 | 16.34 [5.48%] | 28.93 [9.71%] | Wet |
| | | 133.90 [44.93%] | 118.82 [39.87%] | Dry |
| 225-229 | 344.39 | -8.38 [2.23%] | -7.46 [1.99%] | Wet |
| | | 240.11 [63.91%] | 119.72 [31.87%] | Dry |
| 229-233 | 1776.08 | -10.77 [0.59%] | 124.23 [6.91%] | Wet |
| | | 961.64 [53.49%] | 700.89 [38.99%] | Dry |

After

163

## 4.4.9 Elevation and surficial grain size changes maps in 2020 and 2021
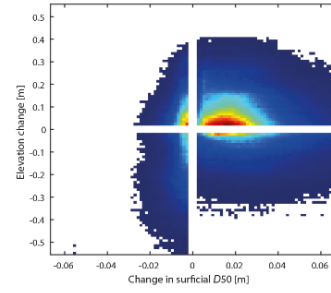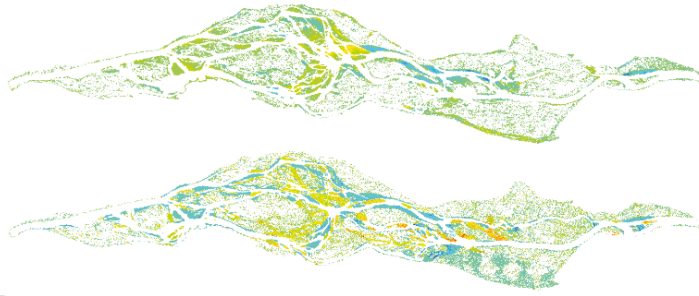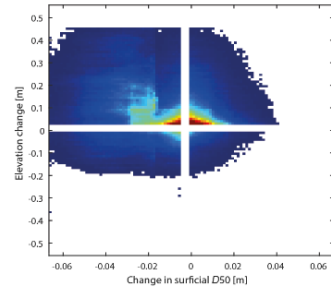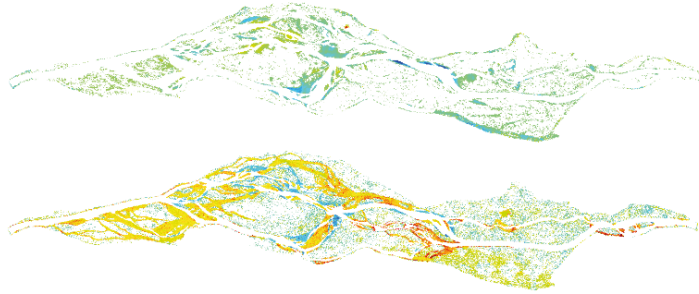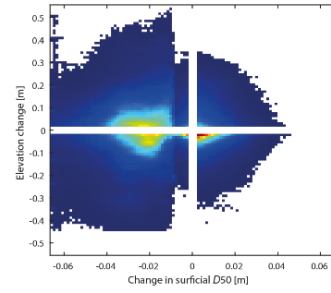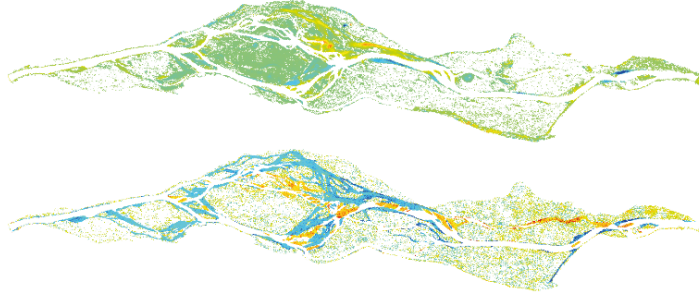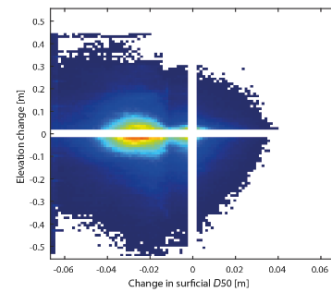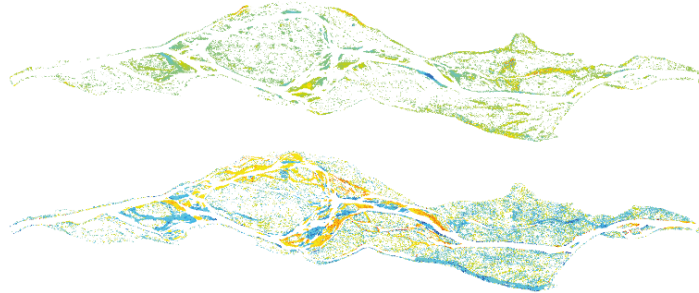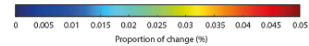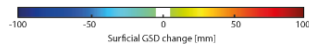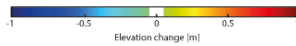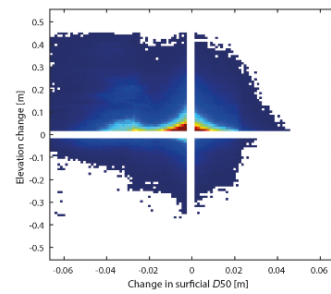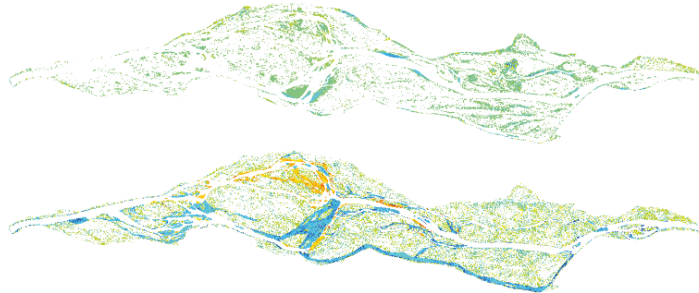


Figure S4.11: Elevation change (upper maps), surficial grain-size change maps (lower maps) and proportion of change (total number of cells) considering both variables for melt season 2020. Used LoD values are given in Table S4.3.
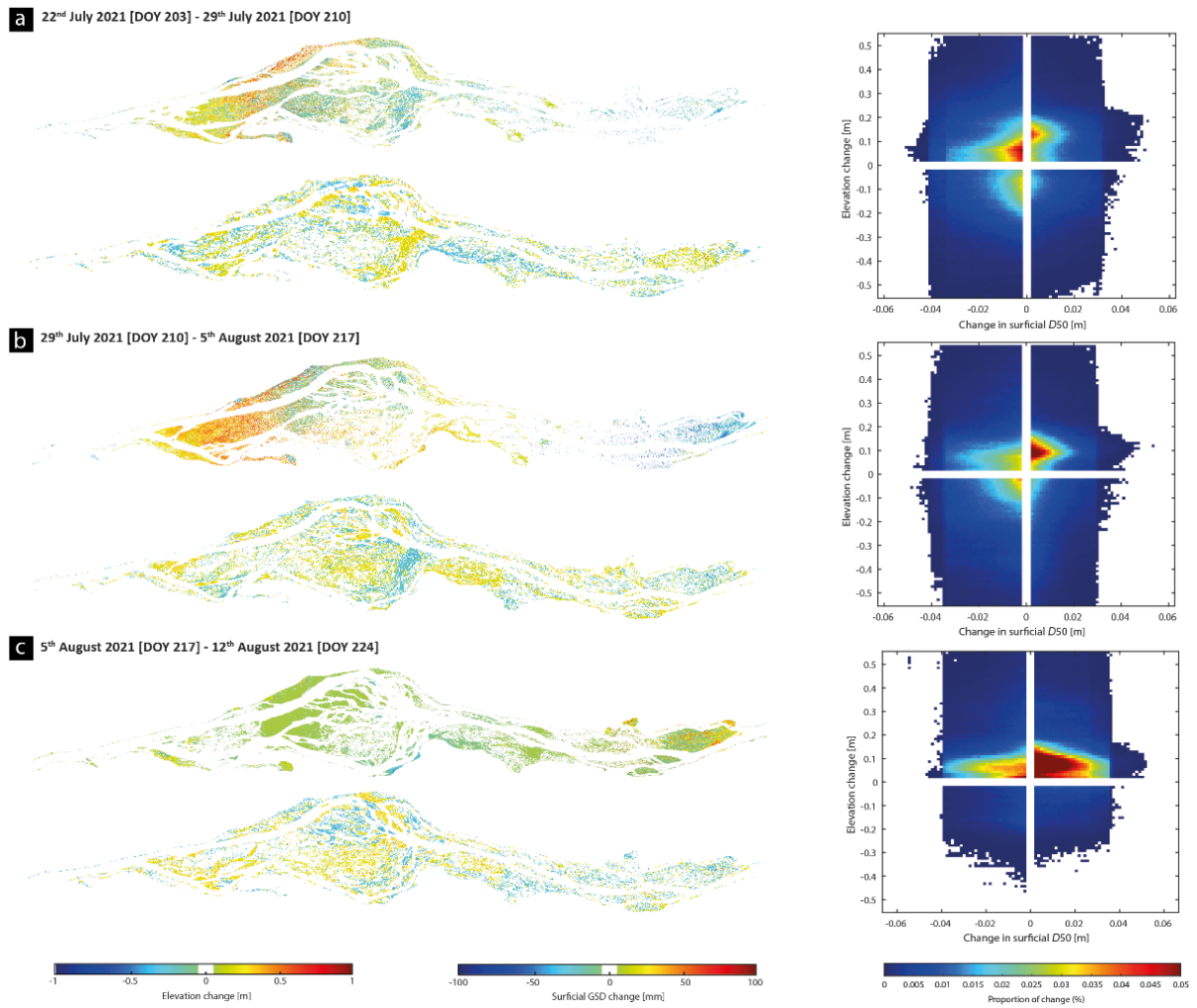
Figure S4.12: Elevation change (upper maps), surficial grain-size change maps (lower maps) and proportion of change (total number of cells) considering both variables for melt season 2021. Used LoD values are given in Table S4.3.

# Chapter 5: Simulations of proglacial forefield morphodynamics and their implications for the filtering of subglacial sediment export

## 5.1 Chapter overview

The results from Chapters 2 and 4 showed that the subglacial bedload export rates control the proglacial forefield morphodynamics which, in turn, directly affect the downstream bedload transport by filtering (i.e. dampening and delaying) the subglacial evacuation signal. This suggests that proglacial floodplains act as a buffer zone, strongly attenuating the sediment connectivity between glacier *termini* and downstream regions. Morphodynamic processes have less impact on the transport of suspended sediment, with the evacuation signal passing almost unimpeded through the braided system. This Chapter aims to generalize these findings by extending the investigation to proglacial forefield characterized by different geomorphic settings and sediment supply to transport capacity scenarios. It addresses to the research question "How the proglacial morphodynamic filtering reacts to changing topographical, sedimentological and hydrological boundary conditions?". This is achieved through the application of a 2D hydromorphological model calibrated and validated against field-collected data. Findings provide further insights on the future sediment transport dynamics in glacierized catchments experiencing changes in the balance between sediment supply and water availability due to glacier retreat.

The scientific manuscript derived from this contribution is ready to be submitted for consideration to *Earth Surface Processes and Landforms* as: Mancini, D., Nicholas, A., Roncoroni, M., Müller, T., Jenkin, M., Miesen, F., Dietze, M., Calvo, F. & Lane, S.N. (to be submitted to ESPL). Simulations of proglacial forefield morphodynamics and their implications for the filtering of subglacial sediment export.

## 5.2 Simulations of proglacial forefield morphodynamics and their implications for the filtering of subglacial sediment export

### 5.2.1 Introduction

A common feature of proglacial margins is a braid plain where a morphodynamically active braided river may develop (Smith, 1985; Maizels, 2002). Their formation is commonly associated with one or more conditions, notably (i) a high fraction of sediment transported as bedload (Leopold, 1992), (ii) a large lateral accommodation space producing a high width-to-depth ratio, and (iii) low river bank and river-bed resistance to sediment entrainment (Murray and Paola, 1994; Paola, 2001). Morphodynamic processes in braided river systems have been extensively studied using scaled-laboratory experiments (e.g. Ashmore, 1991a,b; Ashworth et al., 1996) and small-reach (e.g. Ashworth and Ferguson, 1989; Ferguson and Ashworth, 1992; Ferguson, 1993; Lane et al., 1996; Brasington et al., 2000; Wheaton et al., 2013) observations. Braiding has been shown to occur through central bar deposition, transverse bar conversion, chute cutoff, multiple dissection of lobes and avulsion (Ashmore, 1991a; Ferguson, 1993). There have been fewer studies of how braided river systems in proglacial margins respond to external forcing (Mao et al., 2019; Comiti et al., 2019; Engel et al., 2014) as this has hitherto been hard to measure (e.g. bedload supply); and how this forcing interacts with the autogenic response to strong filter (i.e. delay, dampen or shred) the downstream flux of sediment (Jerolmack and Paola, 2010; Mancini et al., 2023a, 2024d).

Collins (2008) proposed a conceptual model of proglacial forefield response to changes in upstream boundary conditions as a function of the ratio of sediment supply to sediment transport capacity. Where supply does not keep up with capacity, and in the absence of proglacial lakes, incision occurs close to the glacier termini; the resulting sediment liberated

may lead to distal aggradation where the rivers evolve from single thread to braided system (Germanowski and Schumm, 1993; Marren, 2002; Beylich et al., 2009; Roussel et al., 2009; Bogen et al., 2015). Marren and Toomath (2013) show that this behavior can be cyclical and form large terrace sets which buffer lateral supply of sediment to the river (Fryris, 2013). In contrast, if supply can keep up with capacity, local aggradation and more intense braiding is expected to occur (Lane et al., 1996; Collins, 2008). We would expect the influence of the supply-capacity ratio to be dependent upon geomorphological setting (Meizels, 2002; Marren, 2002; Curran et al., 2017). For instance, sediment transport capacity depends not only on river discharge but also longitudinal valley slope, such that steeper rivers for a given discharge would need greater sediment supply to create the conditions necessary for aggradation. Equally, valley width is likely to constrain the space available for braiding to occur. To date, there has been no systematic investigation of the interactions between sediment supply, river flow and the geomorphological setting on proglacial forefield morphodynamics and the flux of sediment to downstream.

This study takes a different approach, using a two-dimensional numerical model of river morphodynamics to generalize recent field measurements of the geomorphic response of the Glacier d'Otemma proglacial forefield to changing subglacial sediment export (Mancini et al., 2024d) to a wider set of conditions, hypnotizing that sediment transport is influenced by both supply to capacity ratio and topographic configuration of the proglacial margin. In the past, existing hydromorphodynamic models of braided rivers (Williams et al., 2016b) have been used to investigate fluvial controls on river patters, channel changes and bar dynamics (e.g. Nicholas, 2013a; Nicholas et al., 2013; Schuurman et al., 2013; Williams et al., 2016a), interactions between morphodynamic and ecological processes (e.g. Iwasaki et al., 2016; Stecca et al., 2022) and sediment displacement mechanisms (e.g. Kasprak et al., 2019) in both gravel- and sand-bed rivers. However, none of them have yet been applied to investigate the filtering of sediment signals in proglacial rivers. The model is calibrated and assessed using field data in Mancini et al. (2024d) and then used to quantify the effects of different exogenous forcing factors on the filtering process.

### 5.2.2 Methodology

### 5.2.2.1 The eRiDynaS model: summary

eRiDynaS is a 2D hydromorphodynamic physical-based model written in C++ incorporating improvements of the HSTAR model of Nicholas (2013b) and Nicholas et al. (2013) to include multiple suspended sediment and bedload grain-sizes and alternative hydrodynamic solvers. Here, only a brief description is given, but further details on the physical laws governing the numerical model are available in Nicholas (submitted) and in Supplementary Information S5.4.1. The model solves the shallow water equations using a Godunov-type finite volume scheme base on the Harten-Lax-Van Leer (HLL) approximate Riemann solver (Harten et al., 1983). The model is applied using a regular structured grid with a spatially uniform resolution ($\Delta x$, $\Delta y$), with topography initialized from a relatively flat domain configuration (see below). Each grid cell composing the model domain can be defined as either active riverbed (i.e. unvegetated) or floodplain (i.e. vegetated) depending on the characteristics of the study area and the simulation timescale (Nicholas et al., 2013). Changes in bed elevation and grain size composition throughout the domain are determined using the Exner mass balance equation applied to the active bed surface layer. The effects of gravity and secondary circulation on the motion of transported sediment in the direction of the local bed slope are included into the modelling following formulations of Ikeda (1982), Stuiksma et al. (1985) and van Rijn (1984, 1993). Sediment supply at the domain inlet for both suspended sediment and bedload are defined using rating curves:

$$qb_{,k} = fb_k Ab_n (1 \pm 0.5 f_{Spert}) Q_n^{Bb_n} \qquad \text{Eq. 5.1}$$

$$\psi_{,k} = f\psi_k A\psi_k (1 \pm 0.5 f_{Spert}) Q_n^{B\psi_n} \qquad \text{Eq. 5.2}$$

where $qb_{,k}$ and $\psi_{,k}$ are the coarse sediment supply rate and the fine sediment concentration in size fraction *k* at the inlet, $fb_k$ and $f\psi_k$ are the proportions of the total coarse and fine sediment supply in the size fractions (both of which sum up to 1), $Ab_n$, $Bb_n$, $A\psi_k$ and $B\psi_n$ are used-defined constants, $f_{Spert}$ is the fractional variability in the sediment supply generated using random numbers, the subscript *n* refers to the inlet number, and $Q_n$ is the discharge rate at the inlet. Suspended sediment transport (Qs) is modelled by solving an advection-diffusion mass balance, while the Meyer-Peter and Müller (1948) approach is used for bedload transport (Qb).

### 5.2.2.2 The eRiDynaS model: developments specific to this application

The eRiDynaS model was initially calibrated to the present-day hydrodynamics and morphological conditions of the Glacier d'Otemma proglacial forefield, a glacierized catchment located in the south-western Swiss Alps at an altitude of ca. 2'400 m a.s.l (Figure 5.1). It is a geomorphic system composed of an active braided proglacial stream, in an about 1000 m long and 200 m wide valley section, where in the most upstream and downstream regions flow is confined into a single bedrock-dominated riverbed channel due to the combination of narrower valley sections and a steeper valley slope (Mancini et al., 2023a, 2024d). The proglacial system is essentially supplied by sediment and melt-water delivered from subglacial channels, with only marginal influence from other sources (Mancini and Lane, 2020; Roncoroni et al., 2023a; Müller et al., 2024). Figure 5.1 shows the methodological approach used for calibrating and validating the model before its application to various boundary conditions.
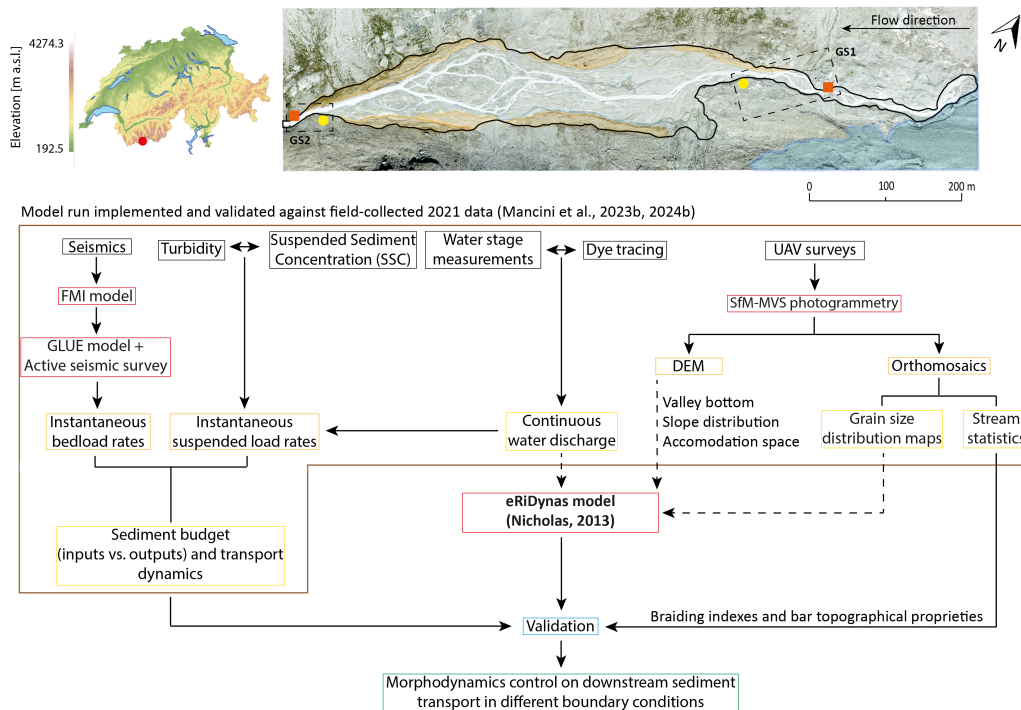


Figure 5.1: Location and spatial configuration of the Glacier d'Otemma proglacial forefield (45.935 N 7.414 E) and general methodological approach used to calibrate eRiDynas to present-day conditions, and to validate it (b). In (a) GS1 and GS2 refers to the location of the monitoring station used to collect continuous suspended sediment (via turbidity-discharge technique, orange squares) and bedload (via geophones, yellow circles) fluxes mobilized for calibrating the model. The shaded orange regions refer to the distribution of terrace systems and the blue shaded area to the glacier. In (b) the dashed lines refer to the field-collected data directly applied into the model.

Field-collected data describing the topographic, sedimentological and hydrological conditions during the 2021 melt season were used to produce a first calibrated simulation (Simulation 1) representing the actual fluvial conditions. Hydrologically, the 2021 melt season represents a condition typical of deglaciation where the subglacial sediment supply (S) is generally higher than the transport capacity (C) during the day, but the opposite may occur overnight (see below, Mancini et al., 2024d). The data used and protocols followed to produce them are available in Müller and Miesen (2022), Roncoroni et al. (2022, 2023a), Mancini et al. (2023a,b, 2024c, 2024d).

The initial model set up comprised a flat domain of 462x125 cells (i.e. half of the real-world extent) and a 1 m resolution subdivided into three regions with varying longitudinal valley bottom slopes, lateral accommodation space and substrate grain size composition reflecting the real-world configuration (Figure 5.2). The choice to use a smaller domain size compared to the study area was due to two reasons: (i) the aim was to replicate the general proglacial fluvial behavior in terms of sediment transport and morphodynamic processes, rather than the exact dynamics observed in the field; and (ii) to substantially decrease the computational time. However, the sufficiently fine lateral resolution allowed for resolving lateral variations in depths and fluxes across narrow and wider channels, providing a reliable representation of both sediment fluxes and morphodynamic changes within the domain. Depending on the simulation properties, each model run still took between 28 and 42 days to process four complete melt seasons.

The distribution of valley bottom gradients was extracted from the 26th July 2021 field-collected UAV-MVS photogrammetrically derived digital elevation model (DEM) of the proglacial forefield: the most upstream region (R1, 0 to 200 m) is characterized by a slope of 2.5%, the middle one (R2, 201 to 400 m) 1.88% and the most downstream one (R3, 401 m to 932 m) where most of the braiding develops by a gradient of 1.25% (Figure 5.2a). In each region, we included the constraining effects of terrace systems on forefield morphodynamics. These were represented by an elevation gain of 1 m between the different levels of the valley floor: in R1 the main channel was confined on both banks by a double (upstream, 0 to 50 m) and triple (downstream, 50 to 100) terrace system, while R2 and R3 by a double system (Figure 5.2a). The valley sidewalls were characterized by a coarser grain size (0.35 m corresponding to the maximum $D_{50}$ value measured in Figure 5.2c; see below) compared to the rest of the floodplain to minimize the occurrence of geomorphic processes and maintain the field-observed topographical configuration of the proglacial margin. We defined the regional lateral accommodation space where water is allowed to flow as the maximum width of the area experiencing at least one day of morphodynamic change across the melt season (Roncoroni et al. 2023a). The accommodation space evolves from 14 m for the first two sectors to 108 m for the third one (Figure 5.2b). The inlet and the outlet widths were set to 10 m, based on the mean widths measured during the 2020 melt season Mancini et al. (2023a). Slow rates of vegetation colonization in proglacial environments (Fickert, 2017; Fischer et al., 2019; Roncoroni et al., 2023a) meant that the entire braidplain, although deglaciated as many as 40 years ago, was void of vegetation (Mancini and Lane, 2020). Consequently, each cell composing the domain was defined as a riverbed (i.e. un-vegetated).
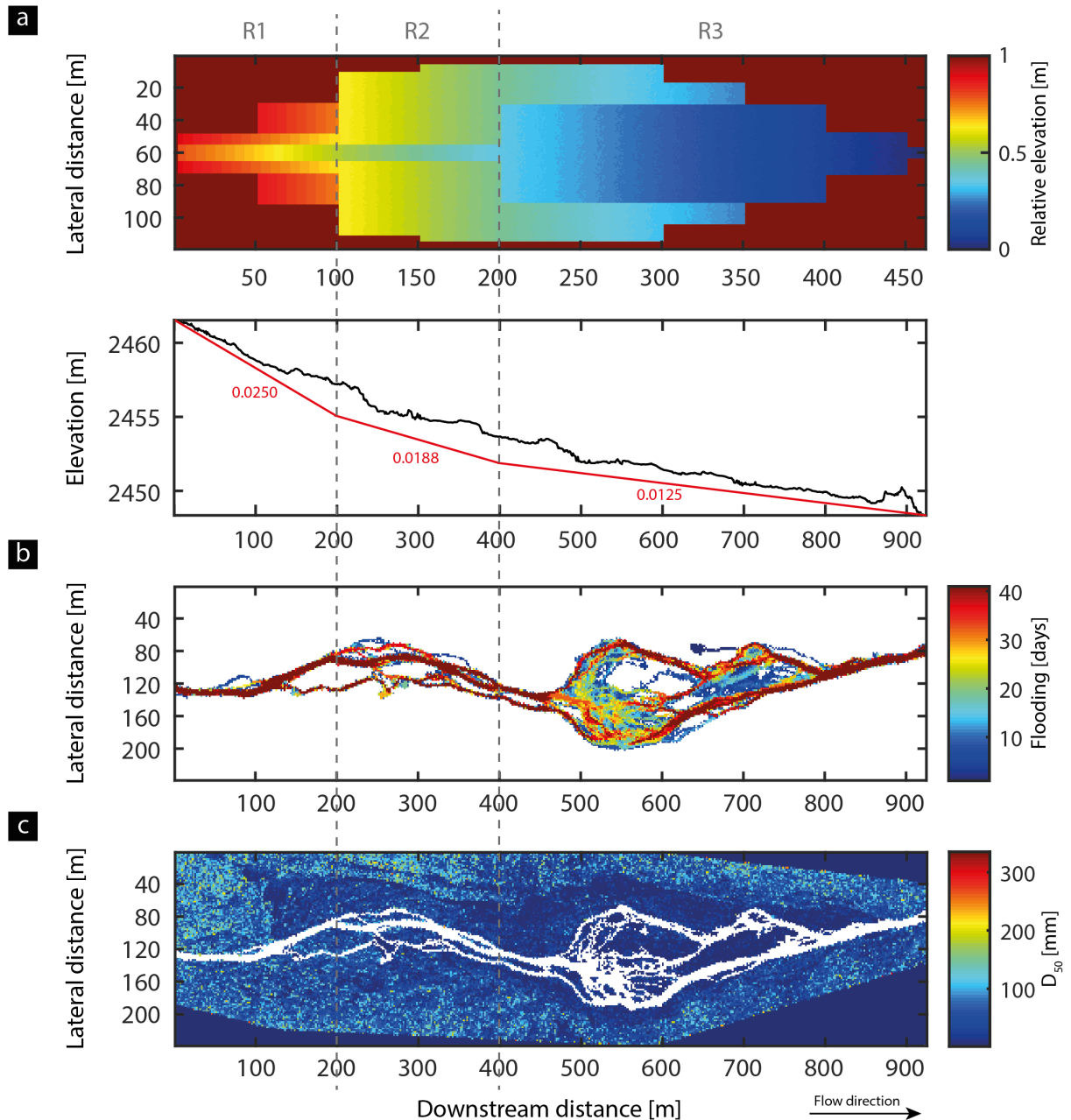
Figure 5.2: Topographical and sedimentological proprieties used to set up the three regions composing the model domain. (a) Initial configuration of the model domain and field-measured longitudinal elevation profile (black line) used to determine slope gradients (red line); (b) flood frequency maps showing the maximum lateral accommodation space in melt season 2021; and (c) surficial grain-site distribution on the 26th July 2021 (white areas have no grain size estimates because submerged, while the darker blue polygons at the edges of the figure are no-data regions). The downstream distance refers to the real-world distances. The red darker cells in (a) represents the valley sidewalls.

The size of transported suspended sediment and bedload (Eq. 5.1 and 5.2), as well as the fractions of substratum composition in the different regions were derived from the 26th July 2021 surficial $D_{50}$ grain size distribution map (Mancini et al., 2024d; Figure 5.2c). The assumption that surface grain size distribution reflected the sub-surface composition was made due to the reduced technical effort required in the field and the broader spatial coverage provided by the former method. A histogram with 15 classes was utilized to obtain the general spatial distribution of grain sizes characterizing the proglacial area (Figure 5.3a). Coarser sediment fractions were determined reclassifying the histogram into four classes: 0.01-0.032 m (-3 to -5 phi), 0.032-0.064 m (-5 to -6 phi), 0.064-0.1 m (-6 to -6.65 phi) and >0.1 m (>-6.65

phi) accounting for 24.6%, 54.8%, 16.4% and 3.8% of the entire grain size distribution at the forefield scale (Figure 5.3b). Their geometric means of 0.025 m, 0.043 m, 0.08 m and 0.13 m were used in the model as bedload grain size fractions. The choice of limiting the simulation to four grain size bedload fractions was made to manage computational costs. In contrast, a single grain size fraction of 0.001 m was employed for fine sediment. Due to limitations of grain size maps in representing fine $D_{50}$ value (i.e. silts and sands), its spatial abundance in the proglacial margin was assumed to reflect that of the 0.01 m fraction.
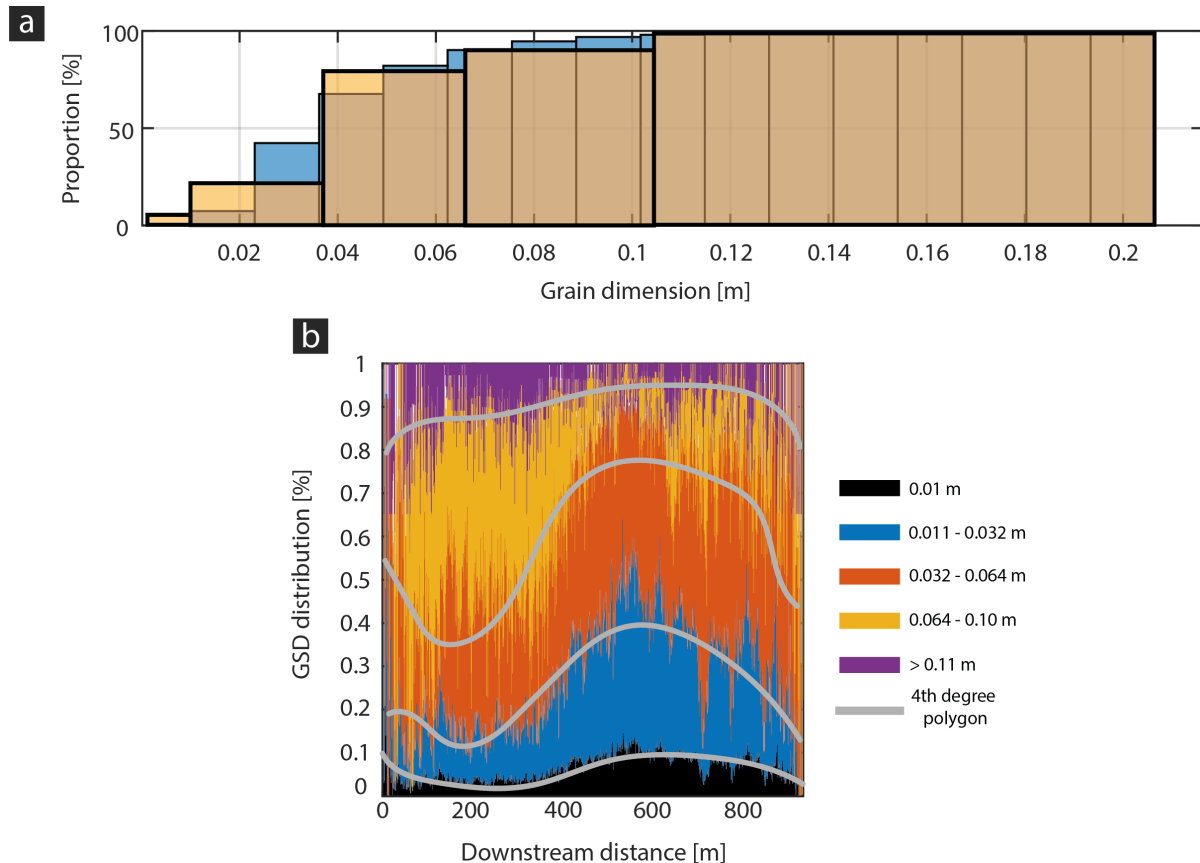


Figure 5.3: Characteristics of surficial grain sizes. (a) Proportional distribution of the surficial grain size distribution (Figure 5.2c) classified into 15 classes (blue) and four bedload classes retained in the simulation (orange); and (b) longitudinal spatial GSD distribution of the five retained classes within the proglacial margin with 4th degree polynoms used to model grain size distribution for the coarser classes.

The spatial distributions of the five granulometric classes (Figure 5.3a) were extracted from the grain size map shown in Figure 5.2c to compute their relative proportion in every sector. A 4th degree polynomial equation was fitted to the distributions of the four coarser granulometric class to generalize their downstream evolutions (Figure 5.3b). Simulated and observed results were similar (Figure 5.3b). Consequently, we represented the substratum of the most upstream region as completely composed of the coarser bedload fraction. The topographical and sedimentological characteristics in the three regions composing the model domain are summarized in Table 5.1. The differences between initial conditions in each region will influence both morphodynamic activity and sediment transport dynamics. Therefore, as explained below, the model was initially run to homogenize both topographical and sedimentological conditions within the model domain.

Table 5.9: Topographical and sedimentological conditions in the three regions composing the model domain.

| | Region | | |
|---|---|---|---|
| **Characteristics** | R1 | R2 | R3 |
| Slope [%] | 2.5 | 1.88 | 1.25 |
| Lateral space [m] | 14 | 14 | 108 |
| GSD composition [%] | | | |
| 0.02 m | 5 | 10 | 30 |
| 0.045 m | 20 | 40 | 40 |
| 0.08 m | 70 | 40 | 20 |
| 0.13 m | 5 | 5 | 0 |
| 0.001 m | 0 | 5 | 10 |

After the initial period of 10 simulation days with a constant discharge rate of 5.1 m³/s representing the average rate measured in 2021 to initialize the morphodynamic processes, daily hydrographs were implemented on the basis of field-data collected between mid-June (JD 161) to mid-September (JD 260) for representing melt seasons of 99 days each (Figure 5.4; Müller and Miesen, 2022). Measured daily minimum and maximum rates were extracted to define daily amplitude changes, then equally divided within every time steps t composing a day, and subsequently applied to an ideal sine wave to produce a simplified version of the seasonal hydrograph as:

$$Qt_{x,i} \begin{cases} min(t_{x,i}) + E_{x,i}\left(max(t_{x,i}) - min(t_{x,i})\right) \, if \, i < 0.5 \\ max(t_{x,i}) - \left((1 - E_{x,i})(max(t_{x,i}) - min\,(t_{x+1,i}))\right) \, if \, i > 0.5 \end{cases} \qquad \text{Eq. 5.3}$$

$$E_{x,i} = 0.5\left(1 + sin\left(2\pi\left(0.75 + \left(\frac{t_{x,i}}{86400}\right)\right)\right)\right) \qquad \text{Eq. 5.4}$$

where $Qt_{x,i}$ is the instantaneous discharge rate at timestep i (comprised between 0 and 1) at the simulation day x, and $E_{x,i}$ defines the ideal daily sine wave. Eq. 5.3 and 5.4 were repeated in loop to simulate discharge variation over multiple melt seasons.
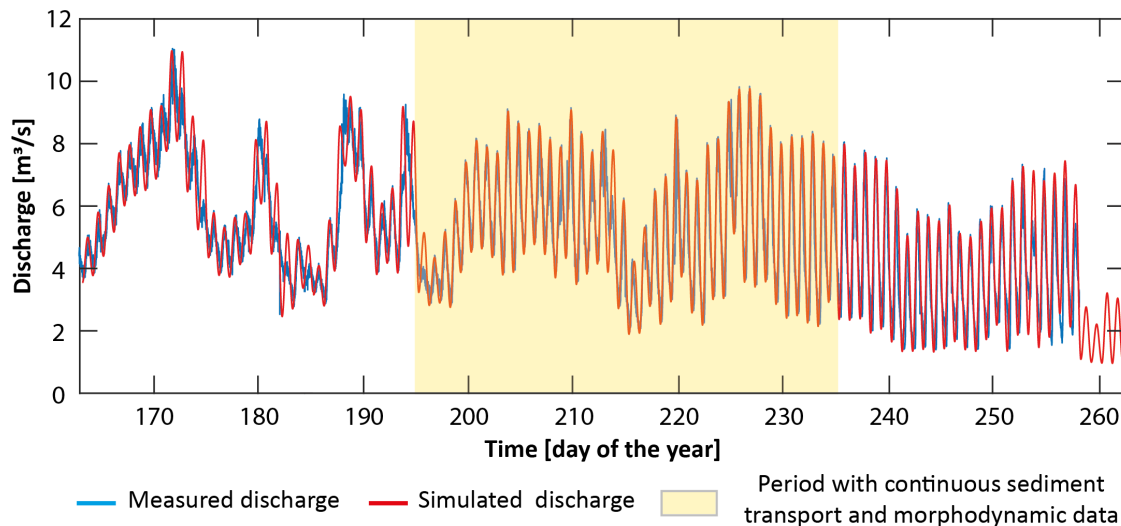


Figure 5.4: Measured (blue line; Müller and Miesen, 2022) and simulated (red line) water discharge time series. The orange shaded region is the period (day 194 to 234) with continuous field-collected suspended sediment and bedload transport quantification (Supplementary Information S5.4.2), as well as daily quantitative information on forefield morphodynamics (total number of bars, mean bar area and braiding index) which are used to evaluate model performance (see Section 2.3).

Subglacial sediment export rates for both suspended sediment and bedload transport were modelled using two distinct rating curves based on a power-law function of the form y = $ax^b$, where x is the water discharge (Eq. 5.1 and 5.2, Figure 5.5). Given that in the model Qs and Qb are, respectively, supply-limited and capacity-limited, their coefficient values were determined using two different approaches, both based on establishing an equilibrium condition at the model inlet. For Qs, multiple simulations with varying power-law values based on the field-collected data shown in Figure 5.5a, were run until coefficient values slightly above the threshold for deposition were identified. However, for Qb, the model was initially run by setting the sediment transport condition at the inlet to enforce an equilibrium condition state. The resulting bedload fluxes were then used to extract the values for the power-law function (Figure 5.5b).
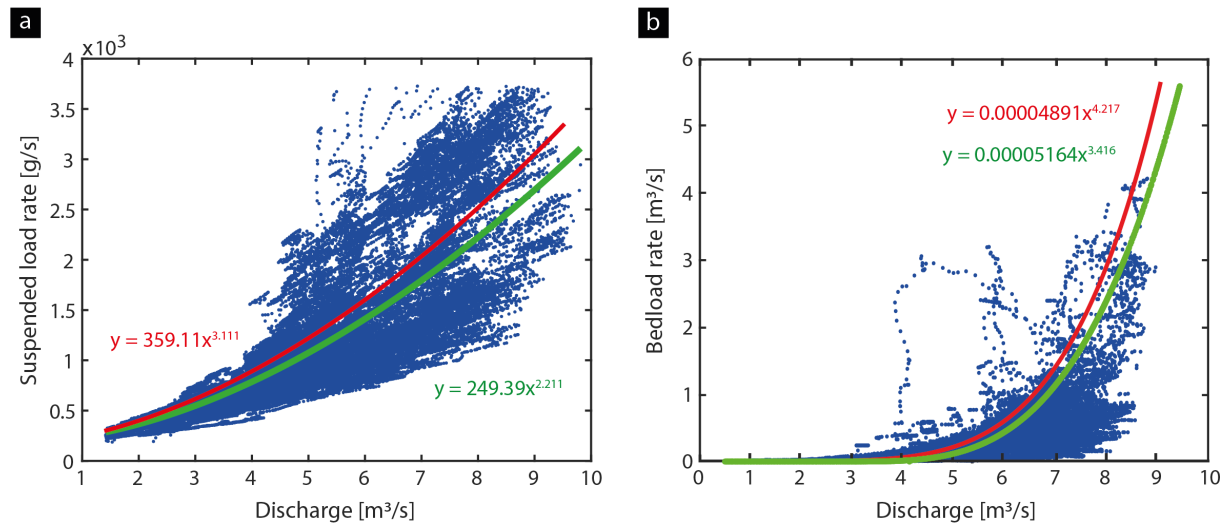


Figure 5.5: Field-collected sediment rating curve (blue dots and red lines) for both (a) suspended sediment and (b) bedload at the inlet (GS1, Figure 5.1) associated to the 2021 melt season. Rating curves coefficient values were determined by fitting sediment loads and water discharge rates using a robust regression based on the iteratively-reweighted least square (IRLS) method after Beaton and Turkey (1974), also known as bi-square method. Green lines refer to the used rating curves used in the calibrated model S1.

### 5.2.2.3 Model assessment

The calibrated model (Simulation S1) was initially run for two entire melt seasons (i.e. 0 to 198 simulation days) repeating the 2021 discharge time-series. This allowed the model domain, through sediment mixing and erosion-deposition patterns due to downstream sediment transport, to no longer be influenced by the initial topographical and sedimentological conditions. Model performance was then evaluated on the second simulated melt season by comparing the measured and simulated data in terms of (i) the sediment budget of the forefield for both cumulated suspended sediment load and bedload fluxes; and (ii) the statistics of proglacial forefield morphodynamics over time (i.e. total number of emerged bars, their mean area and the braiding index). Field-collected data refers to the period comprised between Julian day 194 to 234 (i.e. second simulated melt season) of the 2021 melt season (Figure 5.4). The purpose of this assessment was to evaluate if the model was effectively able to reproduce generally similar fluvial dynamics, in terms of sediment transport and morphological evolution, compare to those observed in the field. Then, once evaluated the similarities, Simulation 1 was continued for a total of four melt seasons (i.e. until simulation day 396) to establish a reference situation describing the simulated baseline fluvial behavior.

Collection techniques and data used to estimate sediment fluxes in the proglacial forefield are available in Mancini et al. (2023a) and Mancini et al. (2023b), respectively. The temporal planimetric information on proglacial morphodynamics and the grain size distributions

are based on analysis of daily SfM-MVS derived orthomosaics from UAV imageries collected in early mornings during low water stage conditions (Roncoroni et al., 2022, 2023a, Mancini et al., 2024c,d).

**5.2.2.4 Numerical simulations using changing boundary conditions**

The boundary conditions in Simulation 1 were modified at the end of the second simulated melt season (simulation day 198) to investigate the response of the forefield to external perturbations. Scenarios were designed to quantify the impacts of subglacial sediment supply (S) and transport capacity (C), as well as the topographic influences (Table 5.2). In Simulation 2, the transport capacity was increased by multiplying the field-measured discharge rates by 1.5, while maintaining the same sediment supply rates for both Qs and Qb measured in 2021 (i.e. same total sediment supply as Simulation 1 despite the increase in discharge rate). In Simulation 3, the Qs and Qb supply are increased by 20% without altering the discharge rates. Simulation 4 followed the same conditions as Simulation S1 until midway through the melt season (i.e. 243 day), at which point a bedload exhaustion scenario was simulated to reproduce the conditions of summer 2020 when bedload export from the glacier suddenly stopped in mid-August (Mancini et al., 2023a, 2024d). Simulation 5 and 6 had the same discharge and sediment supply rates for both Qs and Qb as Simulation 1, but with modifications to the wider valley-form compared to that shown in Figure 5.2. Simulation 5 was characterized by a 25% increase in the model domain dimensions (length and width), while Simulation 6 also included a doubling of the regional slopes.

Table 5.2: Simulation aims ("purpose"), duration, common variables ("similarity") and modified ("model change") conditions compared to Simulation 1. Dc refers to the flat domain configuration having characteristics shown in Figure 5.2 and 5.3. Qb, Qs and Qw to the 2021 field-measured sediment fluxes and discharge rates. Topographical constraints involve valley bottom length (L), lateral width (W) and slope (S).

| Simulation | Purpose | Duration [days] | Similarity with Simulation 1 | Model change |
|---|---|---|---|---|
| S1 | Reference | 0 - 396 | - | - |
| S2 | | 198 - 396 | Dc + Qs + Qb | 1.5 x 2021 Qw |
| S3 | Proglacial filtering response | 198 - 396 | Dc + Qw | +20% for Qs and Qb |
| S4 | | 198 - 396 | Dc + Qw + Qs | Exhaustion of Qb |
| S5 | | 0 - 396 | Qw + Qs and Qb | Increased L + W |
| S6 | | 0 - 396 | | Increased L + W + S |

The relationship between S and C over time was established by comparing the instantaneous sediment influx at the domain inlet with the theoretical potential capacity determined using the same approach used in the model as:

$$Qb = b * \rho_s * qb \qquad \text{Eq. 5.5}$$

where:

$Q_b$ = potential bedload transport rate [kg/s];
$b$ = average channel width [m] (i.e. 10 m);
$\rho_s$ = sediment set at 2650 kg/m$^3$;
$qb$ = transport rate [m$^2$/s] determined using the Meyer-Peter transport law approach described in Eq. S5.18 and S5.19 of the Supplementary Information S5.4.1 for $D_m = D_k$ = 0.069 m.

The effects of changing boundary conditions on the longitudinal connectivity of the proglacial forefield were investigated using sediment budgets, flood frequency and elevation of difference maps following Mancini et al. (2024d). Simulated Qs and Qb flux at both model inlet and outlet, DEMs and inundation maps are in Mancini et al. (in prep). Movies showing

simulated morphodyamic evolution of the stream in the different simulations are available online as Supporting Information.

### 5.2.3 Results

### 5.2.3.1 Assessment of model performance

The temporal comparison between field-collected and simulated instantaneous sediment transport rates for both suspended sediment and bedload transport for the second simulated melt season of Simulation 1, as well as the associated cumulative sediment budgets in the 40-day period having direct field measurements, are shown in Figure 5.6.
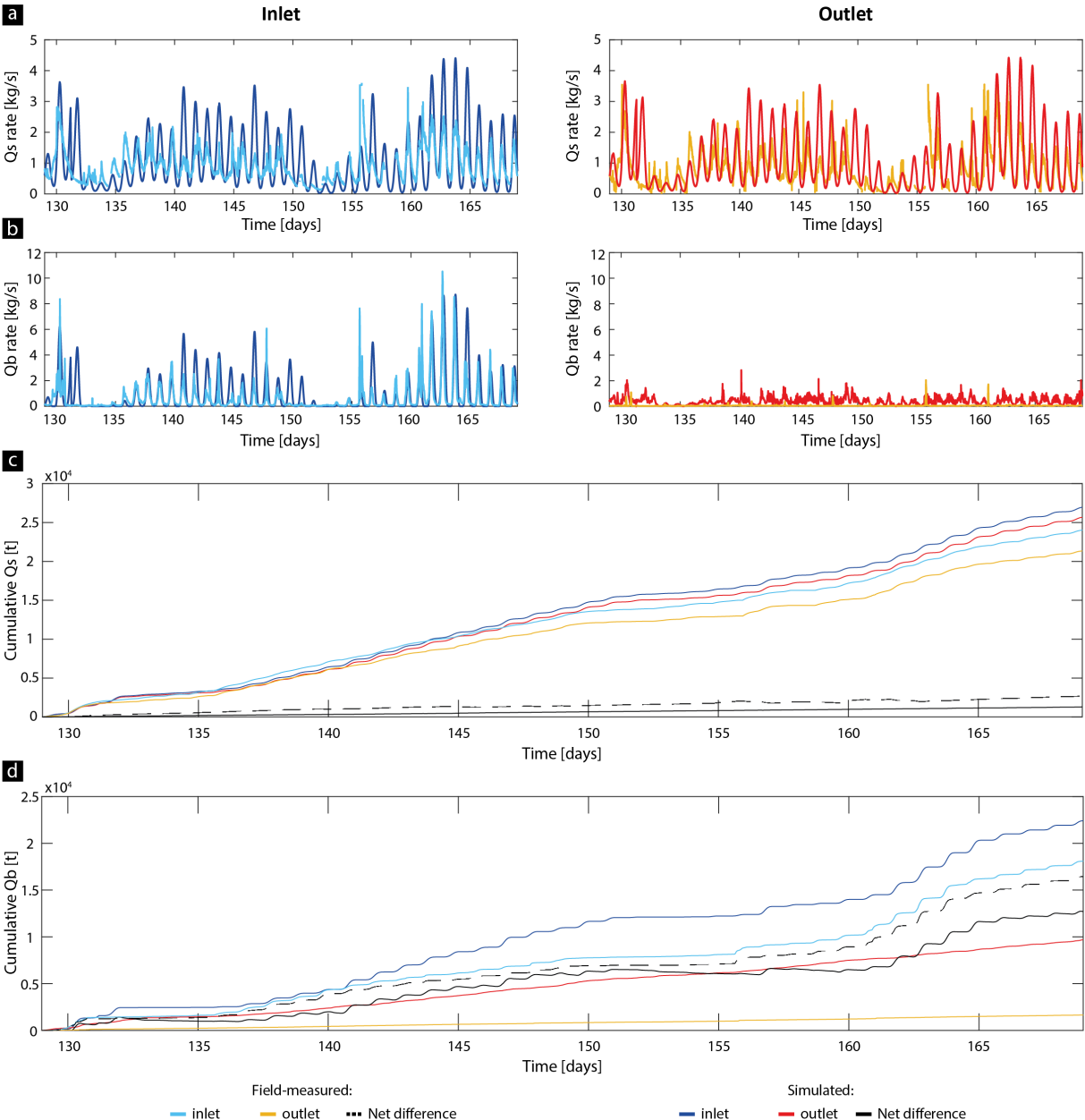


Figure 5.6: Comparison between 2021 field-collected and simulated (Simulation 1, second melt season) instantaneous transport rates (a and b) and cumulative fluxes (c and d) for both suspended sediment and bedload. Sediment transport uncertainties for field measurements are in Supplementary Information S5.4.2.

For the 40-day period having in common the same instantaneous discharge rates (i.e. simulation day 129 to 169), modelled sediment transport timeseries have similar magnitudes as the field-collected ones. Field-measured Qs range between ca. 0.13 kg/s to ca. 3.6 kg/s for

both forefield inlet and outlet region, while Simulation 1 outputs are comprised between ca. 0.09 kg/s and ca. 4.2 kg/s (Figure 5.6a). $Q_b$ supply at the model domain scale is consistent with real world conditions, as also highlighted by rating curve coefficient values and the similar critical discharges of ca. 3.7 $m^3$/s and ca. 3.9 $m^3$/s (Figure 5.5b), with only a slight underestimation of the maximum rate of ca. 8.9 kg/s compared to ca. 10.5 kg/s associated to field records (Figure 5.6b). However, at the model outlet, $Q_b$ rates for both measured and simulated rates fall within the range of ca. 0.1 kg/s and 3.2 kg/s (Figure 5.6b).

The integration of instantaneous sediment transport rates over time during summer 2021 highlights that a total of ca. 2600 t of $Q_s$ and of 16400 t of $Q_b$ particles were stored in the proglacial forefield, while Simulation 1 outputs shows a deposition of ca. 1200 t and ca. 12700 t, respectively (Figure 5.6c and 5.6d). This means that in terms of sediment budget the deposition in the proglacial margin is 53.9% lower for $Q_s$ and of 25.4% higher for $Q_b$ than the real-world. That said, as discussed further below, the validity of the model is still justified by the similar mean deposition rates per unit area consisting in dividing the cumulative net differences by the forefield area of ca. 93'200 $m^2$ (real world, Figure 5.1) and 57'875 $m^2$ (model domain, Figure 5.2a). For $Q_b$, field-measured and modelled deposition rates of, respectively, 0.17 $t/m^2$ and 0.21 $t/m^2$ show a similar behavior. However, for $Q_s$, the field-measured deposition rate of 0.029 $t/m^2$ was higher than the model's rate of 0.022 $t/m^2$, and the discrepancy was also slightly larger compared to that of $Q_b$.

Statistics of real-world and simulated proglacial forefield configuration also show a similar morphodynamic evolution over time (Figure 5.7). The number of bars is between ca. 75 and ca. 220 units, the mean area ranges from ca. 20 to ca. 200 $m^2$, while the braiding index between ca. 2.3 to 5.5. Daily field observations fall within those ranges with only fewer occasional outliers where the model is not able to reproduce the associated stream configuration.
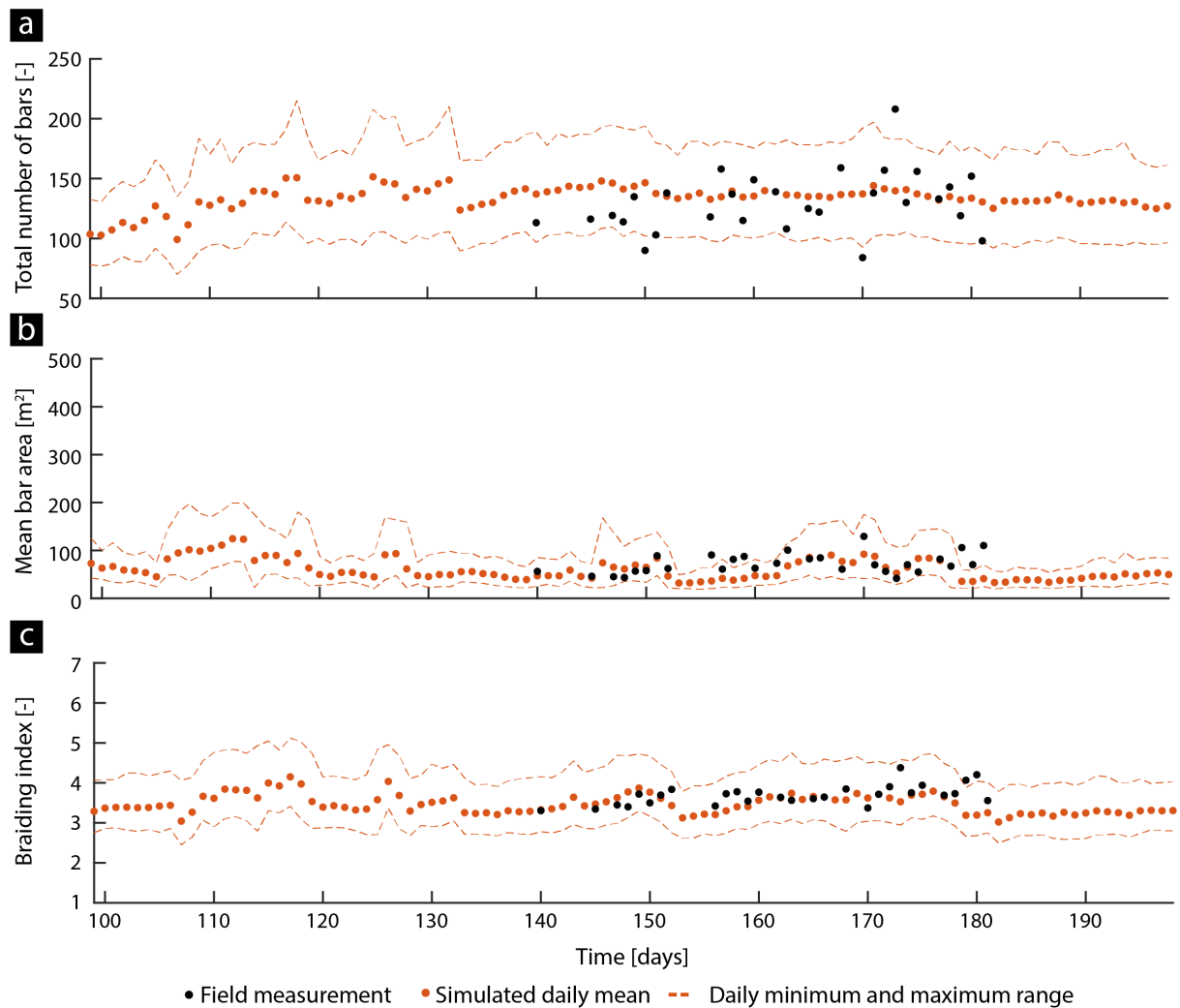
Figure 5.7: Comparison between 2021 field-measured and simulated (Simulation 1, second melt season) proglacial forefield morphodynamic statistics in terms of total number of bars (a), mean bar area (b) and braiding index (c) over time.

### 5.2.3.2 Fluvial and geomorphic responses of the proglacial forefield to changing boundary conditions

Figure 5.8 shows the inlet supply (S) to capacity (C) conditions over time measured along the four simulated melt seasons in the calibration run (Simulation 1) and the different simulated scenarios (Table 5.2).

The S to C conditions collected during melt season 2021 describe a situation where S was constantly higher than C over the day, except on days of low glacier meltwater discharge, with an opposite situation occurring overnight and in the early mornings and evenings. These conditions were replicated in Simulation 1, 5, 3 and 6 over four melt seasons, although in the last two simulations the overall magnitude is, respectively, higher due to the enhanced sediment supply at the inlet, and weaker due to the increasing valley bottom slope promoting increased flow velocity. Simulation 4 showed a transitioning behavior with S higher than C until halfway through the melt season, followed by a second phase (starting from ca. day 290) with C dominating over S because of the cessation of sediment delivery at the domain inlet. In contrast, Simulation 2 from ca day. 198 was entirely dominated by a condition where C permanently exceeded S as a result of increasing discharge rates.
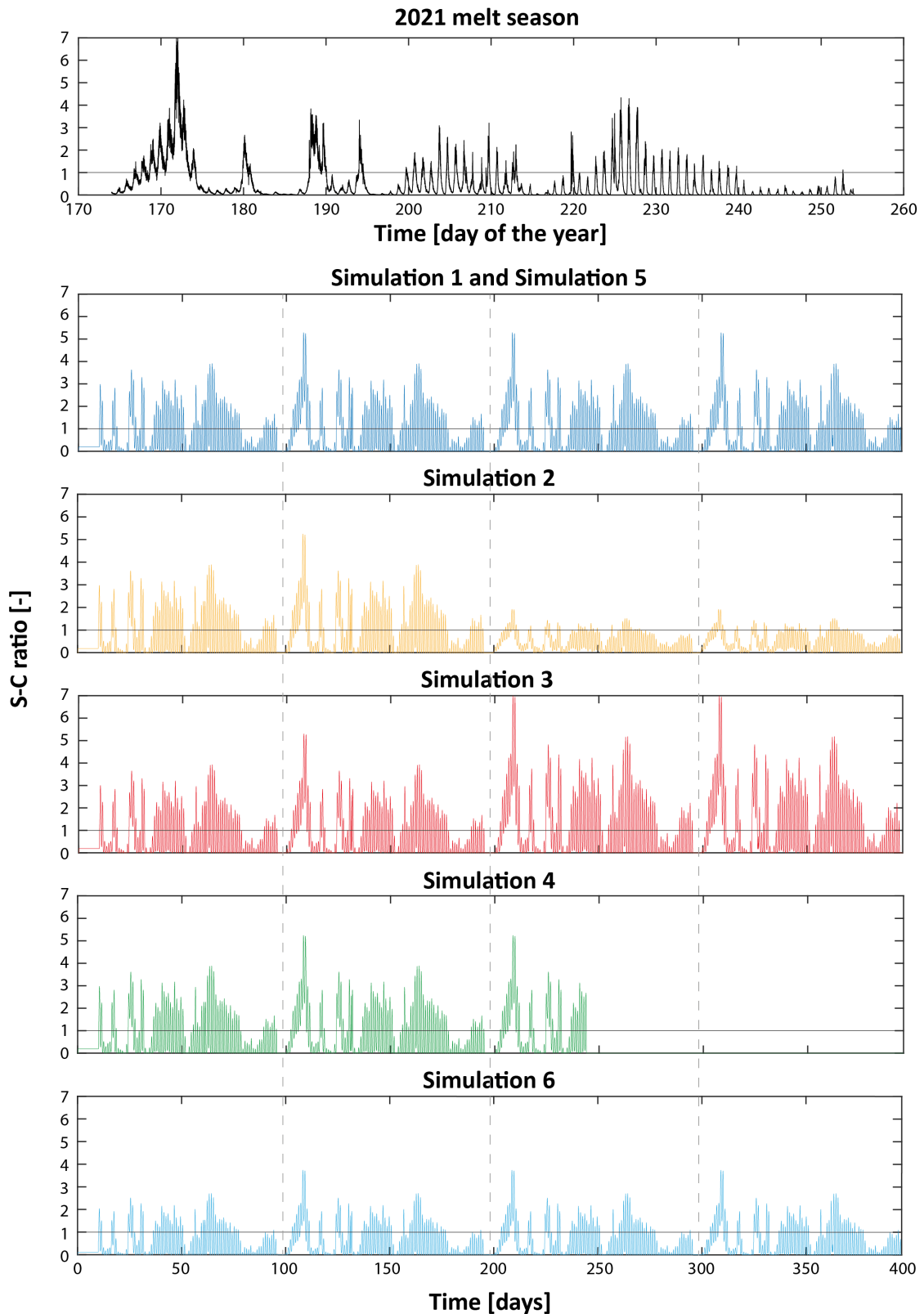
Figure 5.8: S to C ratio over time recorded during the 2021 melt season (Mancini et al., 2024d), the baseline Simulation 1 based on field-collected data and the different scenarios involving varying boundary conditions (Table 5.2). Starting from the third melt season Simulation 2 is characterized by an increase of 1.5 times the instantaneous 2021 discharge rates; Simulation 3 is affected by an increase of sediment supply of +20% for both suspended sediment and bedload fractions; Simulation 4 involves the same sediment supply as Simulation 1 until day 243 after which it was introduced a sudden decline in bedload supply. Simulation 5 and 6 were both run for four entire melt seasons using the Simulation 1 conditions over an extended domain area, with the last case additionally having steeper valley bottom. The grey dashed vertical lines refer to the limits between simulated melt seasons, while the horizontal solid black lines to the conditions where S is equal to C.

The changing boundary conditions applied to the proglacial forefield resulted in different fluvial and geomorphic responses (Figure 5.7 to 5.10 and Table 5.3).

Table 5.3: Daily mean value (x̄) and standard deviation (σ) of the total number of bars (BN), mean bar area (BA) and braiding index (BI) for the different simulation runs (Table 5.2, Figure 5.9 and 5.12).

| | | Period [days] | | | | | | | | | | | |
|---|---|---|---|---|---|---|---|---|---|---|---|---|---|
| | | 1 – 198 | | | | | | 198 – 396 | | | | | |
| Variable | | BN | | BA | | BI | | BN | | BA | | BI | |
| | | x̄ [units] | σ [units] | x̄ [m²] | σ [m²] | x̄ [-] | σ [-] | x̄ [units] | σ [units] | x̄ [m²] | σ [m²] | x̄ [-] | σ [-] |
| Simulation | S1 | | | | | | | 120.49 | 26.43 | 52.15 | 30.32 | 3.28 | 0.52 |
| | S2 | 125.63 | 29.73 | 55.43 | 26.09 | 3.36 | 0.58 | 16.84 | 20.77 | 14.42 | 9.07 | 0.95 | 0.44 |
| | S3 | | | | | | | 165.18 | 29.98 | 104.99 | 51.99 | 4.39 | 0.61 |
| | S4 | | | | | | | 33.51 | 35.11 | 25.09 | 34.32 | 1.91 | 0.79 |
| | S5 | 186.34 | 46.06 | 64.82 | 29.16 | 4.82 | 1.14 | 158.39 | 28.37 | 94.81 | 27.28 | 4.33 | 0.98 |
| | S6 | 97.88 | 19.83 | 62.21 | 22.66 | 2.89 | 0.38 | 100.71 | 9.36 | 57.11 | 28.13 | 2.79 | 0.27 |

In Simulation 1, with S higher than C (Figure 5.8), morphodynamic activity was intense characterized by high magnitude stream statistics over the four melt seasons (Figure 5.9 and Table 5.3). This fluvial behavior geomorphologically translated with enhanced erosion rates in the steeper region closest to the glacier where the stream flow confined into a single confined channel (ca. 0 m and 100 m; Figure 5.10a), and downstream deposition of the reworked material in the most unstable and braided sector of the proglacial margin (ca. 100 m and 450 m; Figure 5.10a).
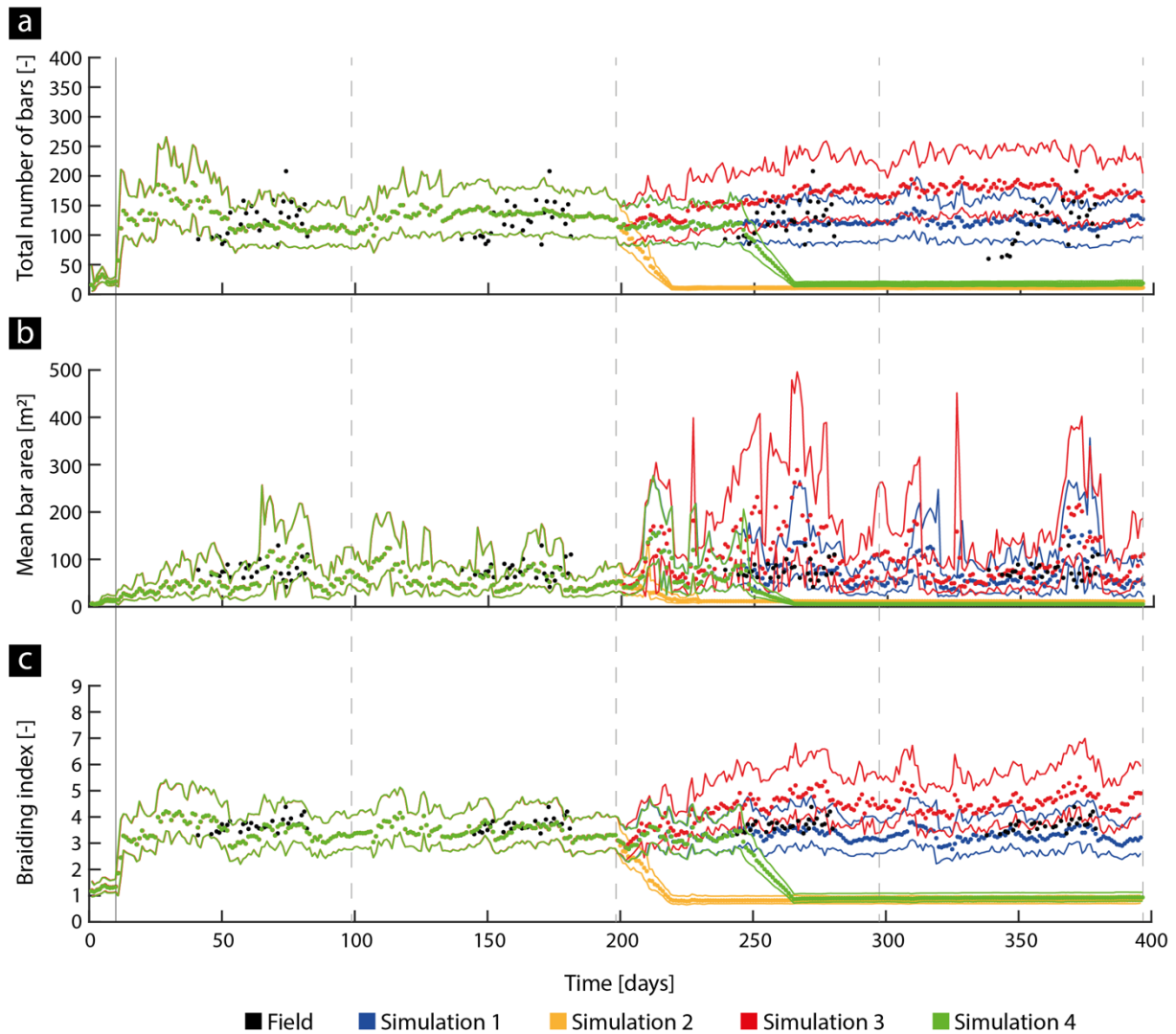
Figure 5.9: Proglacial stream morphodynamics statistics in terms of mean daily total number of bars (a), their mean area (b) and braiding index (c) over the third and fourth simulated melt seasons compared to field-data for Simulations 1, 2, 3 and 4 (Table 5.2). Dots refer to the daily mean value, while lines to the daily minimum and maximum value averaged over the whole model domain. The solid black vertical line defines the start of the four simulated melt seasons and the grey dashed lines the limits between simulated melt seasons.

In Simulation 2, the decrease in the S to C ratio following the increase in discharge rates at day 198 caused a rapid shift by day 220 into a more stable and straighter configuration (Figure 5.8, 5.9 and 5.10b). There was a systematic decline in the total number of bars, the mean bar area and the braiding index (Table 5.3). At the same time, the proglacial forefield shifted from an aggrading to a degrading geomorphic system with enhanced riverbed reworking rates along the entire proglacial margin (Figure 5.10b).
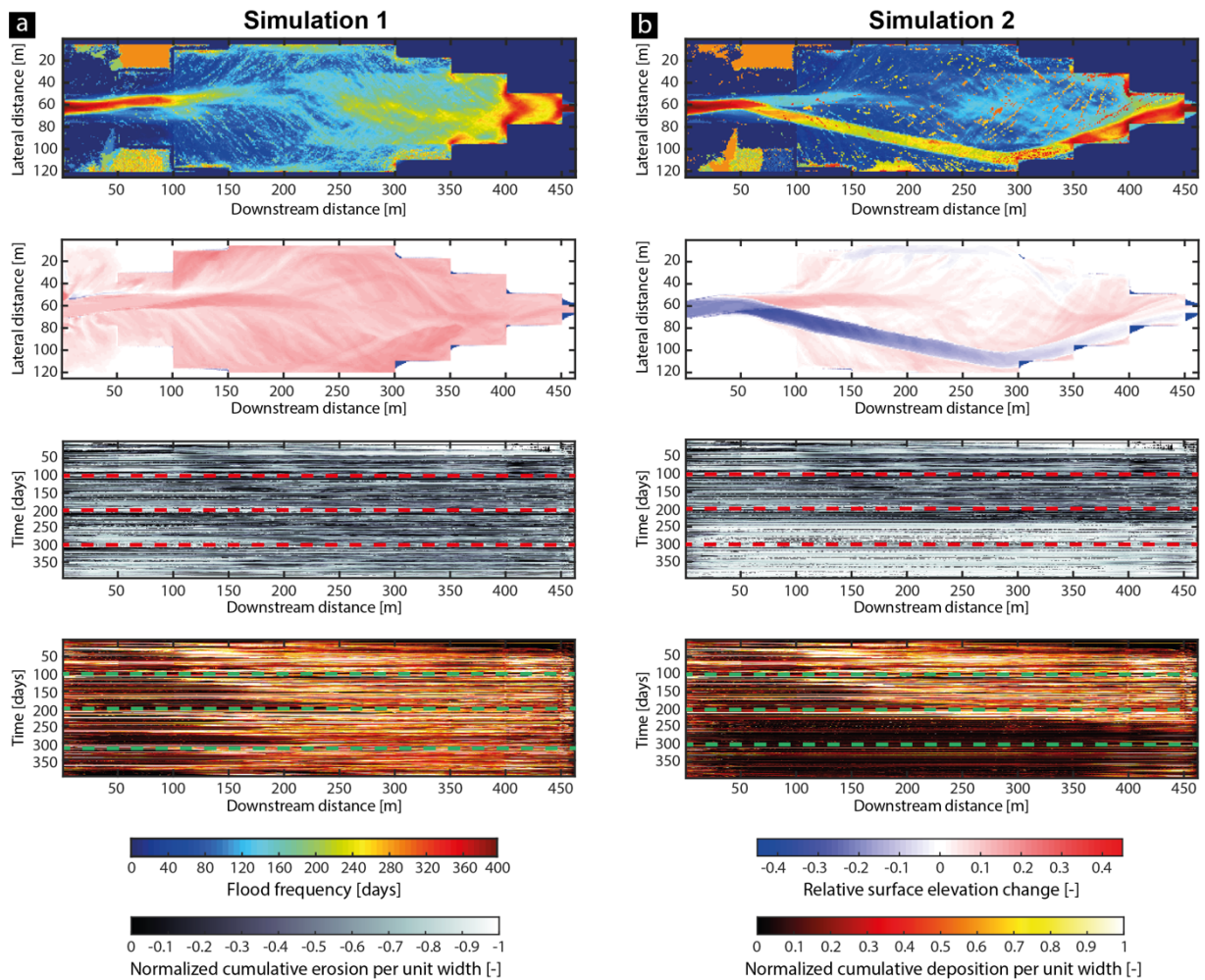
Figure 5.10: Spatial distribution of flooding frequency, relative vertical surface elevation change and 2D normalized cumulative erosion and deposition for Simulations 1 and 2 (Table 5.2) over the four melt seasons. Normalization is based on the local active width. Red and green dashed lines define the melt season limits.

In Simulation 3 the S to C ratio was reversed starting from day 198 by increasing the sediment supply rates for both Qs and Qb (Figure 5.8). This perturbation led to the development of the same fluvial response observed in Simulation 1, but with a higher magnitude (Figure 5.10 and 5.11a). The proglacial forefield gradually developed a more pronounced braided pattern characterized by numerous bigger bars with more intense morphodynamic activity (Figure 5.9). Bars became larger, the number increased and the braiding drastically increased (Table 5.3). There was net aggradation, notably in the central sector of the proglacial margin (ca. 50 m to 400 m; Figure 5.11a). In contrast to Simulation 2, the deposited material was probably not originating from the reworking of the riverbed in the straight reach close to the inlet as there is no net increase in erosion rates (Figure 5.10b and 5.11a). Thus, this sector acted as a conveyor of supplied sediment directly into the most unstable part of the proglacial margin.

Simulation 4 followed the geomorphic evolution observed for Simulation 1 until the end of the first half of the third melt season (ca. day 245) with S>C (Figure 5.8). Then, when Qb supply at the inlet was reduced leading to the establishment of S<C conditions, the same fluvial response observed for Simulation 1 occurred (Figure 5.10 and 5.11b). The system rapidly responded to the disturbance with the forefield evolving into a less morphodynamically intense state which culminated around day 263 with formation of a single and confined channel (Figure 5.9). This is also highlighted by the decrease in the number and size of bars and the braiding

index (Table 5.3). The development of a single channel, as occurred in Simulation 2, promoted the occurrence of large erosion rates at the forefield scale especially during the fourth melt season (Figure 5.11b).
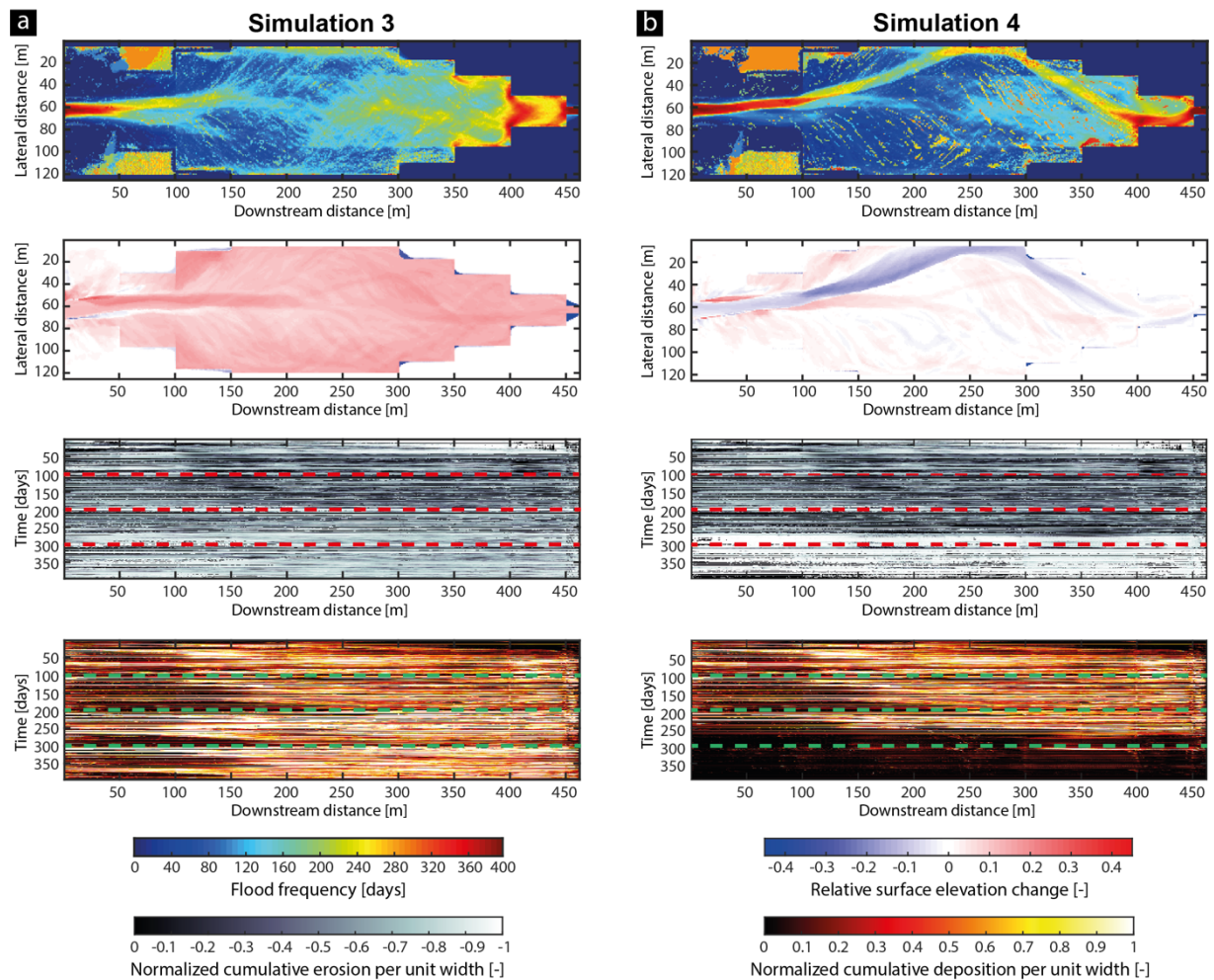


Figure 5.11: Spatial distribution of flooding frequency, relative vertical surface elevation change and 2D normalized cumulative erosion and deposition for Simulation 3 and 4 (Table 5.2) over the four melt seasons. Normalization is based on the local active width. Red and green dashed lines define the melt season limits.

Simulation 5 involved the same S and C conditions as Simulation 1, but with different valley conditions (Table 5.2 and Figure 5.8). The extended proglacial floodplain allowed the establishment of a fluvial system characterized by enhanced braiding intensity and more intense morphodynamic activity (Figure 5.12). The instability, as for Simulation 1 and 3, was mainly located in the flatter and wider region of the proglacial margin where aggradation dominated (ca. 150 m to 550 m; Figure 5.13a), while the confinement of flow in the most upstream region promoted riverbed erosion and downstream transfer of sediment as Simulation 1 (ca. 0 m to 150 m; Figure 5.13a).
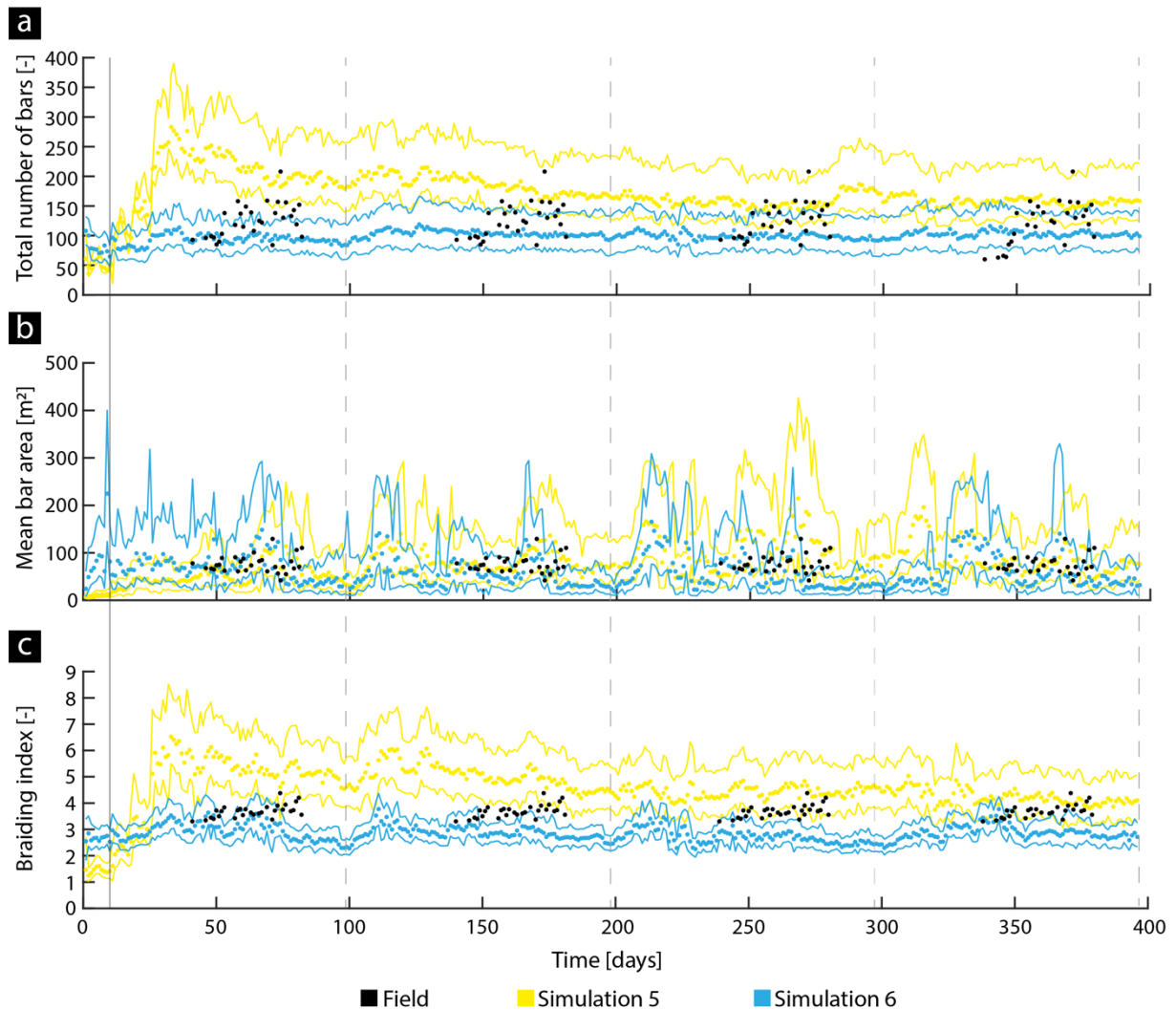
Figure 5.12: Proglacial stream morphodynamics statistics in terms of total number of bars (a), their mean area (b) and braiding index (c) over the third and fourth simulated melt seasons compared to field-data for Simulation 5 and 6 (Table 5.2). The solid black vertical line defines the start of the four melt seasons simulated and the grey dashed lines the limits between simulated melt seasons.

Simulation 6 involved a steeper valley bottom than Simulation 5 producing an enhancement of the transport efficiency and, consequently, a drastic decrease in the S to C ratio (Table 5.2; Figure 5.8). The proglacial stream responded to this perturbation by decreasing the magnitude and the variability of its morphodynamic activity (Figure 5.12). The forefield evolved into a more stable braided configuration with a lower braiding index, fewer bars and smaller bars (Table 5.3). A larger proportion of the floodplain region experienced riverbed erosion close to the inlet promoting channelization (ca. 0 m to 150-300 m; Figure 5.13b) and, consequently, there was a smaller downstream zone where reworked material was deposited (Figure 5.13b). This difference in geomorphic response was due to the decreased morphodynamic activity promoted by the steepening of the valley because the forefield evolved into a more stable braiding system (Figure 5.12 and Table 5.3).
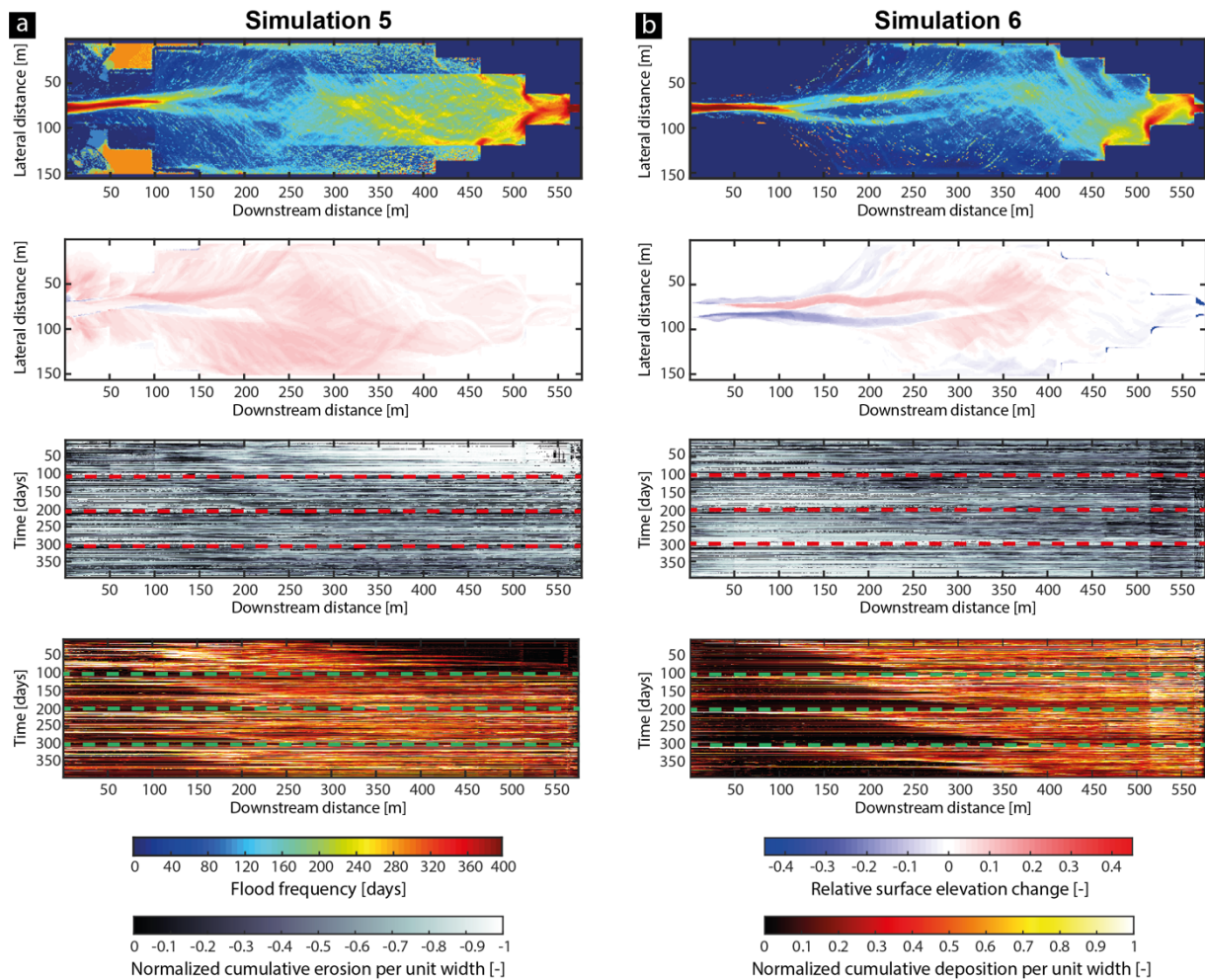
Figure 5.13: Spatial distribution of flooding frequency, relative vertical surface elevation change and 2D normalized cumulative erosion and deposition for Simulation 5 and 6 (Table 5.2) over the four melt seasons. Normalization is based on the local active width. Red and green dashed lines define the melt season limits.

### 5.2.3.3 Magnitude of the proglacial forefield morphodynamic filtering on downstream sediment connectivity

Figure 5.14 shows the cumulative flux of suspended sediment and bedload fluxes at both the domain inlet and outlet, as well as the net spatial difference. In the reference Simulation 1, until the end of the second melt season (i.e. day 198) a total of ca. 107'640 t of suspended sediment ($Q_s$) and of ca. 89'165 of bedload ($Q_b$) were supplied at the inlet. Equivalent values of these fluxes simulated at the outlet were ca. 97'495 t (90.58% of the total load) of $Q_s$ and ca. 27'270 t (30.58%) of $Q_b$. In the third and fourth melt seasons (i.e. day 198 to 396) the total supply of $Q_s$ was ca. 116'000 t, of which ca. 89'000 t (73%) left the geomorphic system. Thus, the net sediment budget for $Q_s$ is ca. 27'000 t (Figure 5.14a). However, ca. 104'600 t of coarse sediment were supplied to the inlet and ca. 58'300 t (56.8 %) were recorded at the domain outlet meaning that ca. 46'300 t were deposited in the floodplain (Figure 5.14b). In the other simulations the response of the sediment budget to the changing boundary conditions in the third and fourth simulated melt seasons depended on the S to C ratio, especially for bedload transport.

Compared to the sediment budget of $Q_s$ recorded for Simulation 1, Simulation 3 experienced increased aggradation (ca. +69%, 18'690 t), while Simulation 2 and 4 exhibited a reduction in deposition of ca. -51% (13'600 t) and ca. -24% (6'500 t), respectively (Figure 5.14a). The changing topographic configurations of the proglacial margin system also had

185

important repercussions for Qs dynamics. Over four melt seasons, Simulation 1 was associated with a total amount of deposited Qs of ca. 32'700 t. In Simulation 5 the extended forefield increased aggradation to ca. 61'450 t (46.8% more than Simulation 1), while the opposite evolution was recorded in Simulation 6 with a deposition of ca. 12'060 t (63.2% less than Simulation 1 and 83.3% less than Simulation 5) following the introduction of a steeper valley bottom (Figure 5.14a).
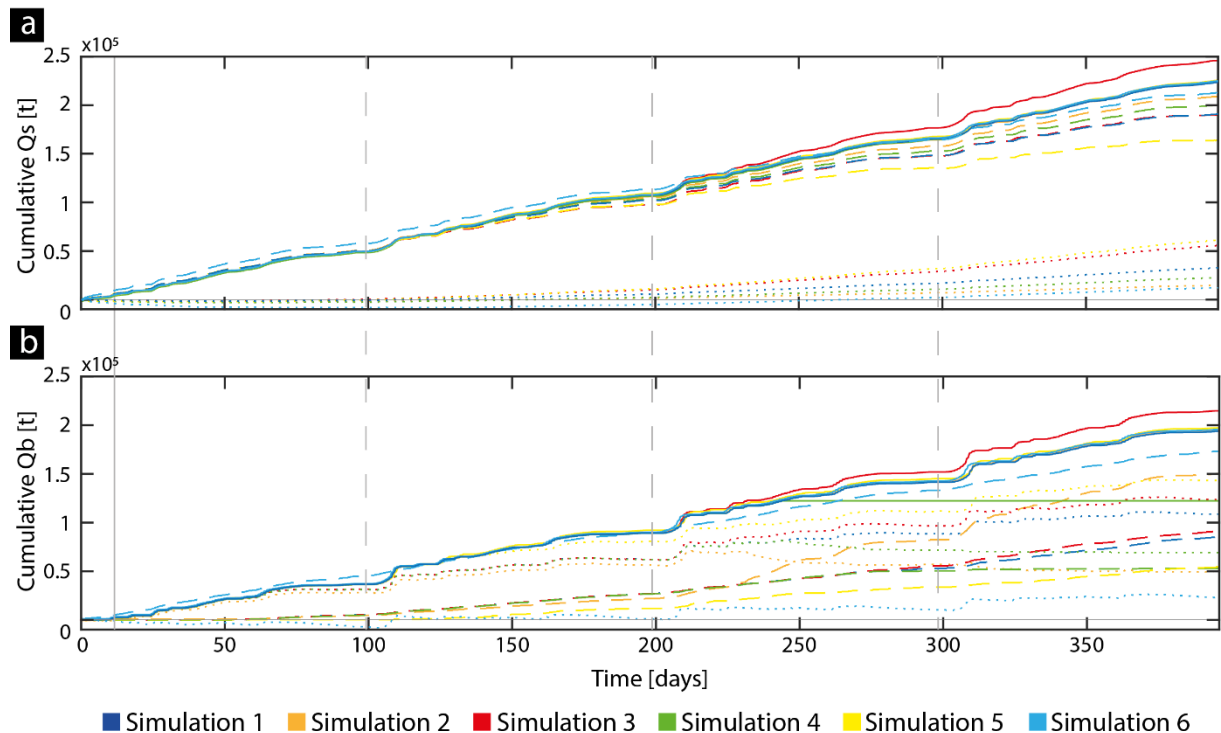


Figure 5.14: Cumulative suspended sediment (a) and bedload (b) fluxes at the domain inlet (solid lines) and outlet (dashed lines) for Simulation 1 and simulations having different S to C conditions (Table 5.2). Dotted lines refer to the net difference between inputs and outputs. The solid grey vertical line defines the period of time having steady discharge rates (5.1 m3/s) at the beginning of the simulations, while the gray dashed ones to limits of the simulated melt seasons. Instantaneous sediment transport rates are in Supplementary Information S5.4.3.

The evolution of the sediment budget for Qb was more dependent on the supply to capacity ratio. When the S to C ratio was increased, the magnitude of the proglacial margin increased as well (Figure 5.8). In Simulation 3, the increase of the total amount of Qb supplied to the system (to 125'400 t) increased aggradation by 8% as compared to Simulation 1 as only ca. 60'400 t (48.8% of the total) was able to leave the proglacial margin (Figure 5.14b).

Where C was higher than S, the opposite behavior occurred with the forefield becoming a sediment source (Figure 5.8 and 5.14b). In Simulation 2 the increase of C was immediately followed by a progressive increase in Qb export rates at the outlet. This coincided with the rapid transition from a braided to a straight channel which, after a transitioning period of balanced mass balance between day 260 and 300, became higher than the input rates. In terms of fluxes, 104'600 t of coarse material was supplied to the inlet (as for Simulation 1) and ca. 111'700 t were recorded at the outlet, suggesting that the forefield lost ca. -7'100 t of sediment (Figure 5.14b). This loss is ca. 8.4% more than the total amount of supplied sediment and it was related to the degradation of the forefield itself.

The sediment budget in Simulation 4 reflected the changing S to C ratio (Figure 5.8). Compared to the reference Simulation 1, over the third and fourth melt seasons, 33'210 t of Qb were supplied to the forefield, of which 26'050 t (78.4 % of the input load) were also

recorded at the outlet, highlighting that the ability of the proglacial margin in buffering coarser sediments was less compared to the other simulations (Figure 5.8c and 5.14b).

Simulations involving different topographic conditions than Simulation 1, but still with S>C, experienced both net aggradation with different degree of buffering on downstream Qb fluxes (Simulation 5 and 6 in Table 5.2, Figure 5.8). The extended forefield area in Simulation 5 aggraded by ca. 142'900 t (24.1% more than Simulation 1) due to the enhanced morphodynamic activity (Figure 5.12 and 5.14b). However, the steepening in the valley bottom slope in Simulation 6 promoted the development of a less braided and more stable stream pattern which eased sediment export from proglacial margin system as the 22'200 t of sediment deposited Qb were 20.4% and 15.5% of those recorded in Simulation 1 and 5, respectively (Figure 5.12 and 5.14b).

### 5.2.4 Discussion

### 5.2.4.1 Evaluation of model performance

Despite some discrepancies in the temporal evolution, Simulation 1 showed an overall good agreement between the simulated and the field-measured data (Figure 5.6 and Figure 5.7). In particular, the decision to use the simulated channel morphology at the end of the second melt season in Simulation 1 (i.e. day 198) as the initial conditions for all subsequent simulations (Table 5.2) was dictated by the better agreement in terms of deposition rates per unit area, along with a more similar temporal morphological evolution especially in terms of braiding index and total number of bars, compared to field observations (Supplementary Information S5.4.2 and S5.4.3).

During the second simulated melt season of Simulation 1 (i.e. day 99 to 198) similar Qs and slightly higher Qb flux rates at the domain inlet were observed compared to field records (Figure 5.4a and 5.6b). The cumulative loads over time fall within the uncertainty ranges of the 2021 field measured data suggesting that the numerical simulation correctly represented the real-world subglacial boundary conditions (Figure 5.6c and 5.6d; Supplementary Information S5.4.2). Sediment fluxes at the domain outlet, particularly for Qb, are slightly higher than field-records as shown by the cumulative loads over time (Figure 5.6c and 5.6d; Supplementary Information S5.4.2). However, field-recorded and modelled mean deposition rates per unit area showed similar values suggesting that, despite different sizes, the model was able to correctly simulate the proglacial forefield morphodynamic filtering on downstream transported bedload particles (Jerolmack and Paola, 2010; Ganti et al., 2014; Mancini et al., 2023a). For suspended sediment the simulated rates were lower than those based on field-data, a situation that can be explained by the use of a too fine (i.e. 0.001 m) sediment grain size used for representing Qs, as well as by an insufficient amount of fine sediment in the initial substrate composition leading to low mobilization rates of fines during the reworking of the floodplain (Figure 5.3c and Table 5.1).

Given the above, the model reproduces the general natural morphodynamic behavior of the proglacial forefield (Figure 5.7). That said, field-measured stream statistics are based on the spatial configuration in early morning (i.e. low flow conditions), but the associated values rarely match the lower bounds of daily modelled statistics. This may be related to uncertainties in the morphodynamic statistics linked to the manually generated masks of the inundated area potentially affected by high uncertainties (Roncoroni et al., 2023a), or the lack of representation of buried-ice processes in the used numerical model (Paster et al., 2022). Ground-ice patches, of which presence is confirmed in the study area (Müller et al., 2024), have the potential to reduce the magnitude of the morphodynamic activity constraining the proglacial streams in well-defined channels, with repercussion on the planimetric statistics of the stream (Hambrey,

1984). Further considerations on proglacial buried-ice processes on fluvial dynamics are given below.

### 5.2.4.2 Impact of boundary conditions upon proglacial filtering magnitude

Simulation results confirm the findings in Mancini et al. (2024d) showing that subglacial sediment supply, and particularly bedload sized sediment, determine the geomorphic response of the proglacial forefield which, in turn, controls the filtering magnitude on downstream transported sediments (Jerolmack and Paola, 2010; Ganti et al., 2014; Mancini et al., 2023a). In conditions where S is greater than C, the proglacial forefield increases its morphodynamic activity attenuating the downstream transport of coarser sediment particles and aggrading the proglacial margin. Conversely, where C is higher than S the opposite situation occurs with the transition of the proglacial stream to a less braided pattern promoting the evacuation of subglacially-exported bedload particles and the vertical incision of the proglacial stream (Figure 5.10b, 5.11b and 5.14b). These results shows that bedload transport dynamics is dependent on the S to C conditions that, by modifying the local configuration of the stream, can change the hydraulic efficiency of the stream in transporting sediment (Germanoski and Schumm, 1993; Marren, 2002; Curran et al., 2017; Roussel et al., 2018; Mancini et al., 2024d). The main mechanism for the proglacial filtering is the morphodynamic activity, particularly bar construction processes, with higher magnitudes of attenuation of subglacially-exported bedload particles when the forefield shows enhanced braiding (Figure 5.9; Ashmore, 1988; Ferguson and Ashworth, 1992; Kaspark et al., 2015; Curran et al., 2017). In contrast, for suspended sediment transport dynamics, the effects of changing S and C conditions are less evident with, except for a low degree of deposition, the subglacial export signal passing almost unimpeded though the proglacial margin (Figure 5.14a). However, as showed in Simulation 5, the magnitude of the buffering on fines increases with the braiding intensity (Figure 5.12 and 5.14a).

Topographical constraints are also important in determining the strength of filtering. Given a scenario where S is higher than C, the increasing width of the proglacial margin system was associated with enhanced braiding intensity and, as already described above, the buffering and deposition of subglacially-exported bedload particles (Figure 5.12 to 5.14). In contrast, the steepening of the valley bottom led to the confinement of the flowing water into fewer and hydrologically more efficient channels promoting sediment transport and river-bed incision (Figure 5.13b and 5.14b). These results suggest that the proglacial filtering of subglacially-exported coarse material is not only dependent on the on the S to C ratio, but also on local topographic settings (Schumm, 1981, 1985; Weber and Pasternack, 2017). Simulations characterized by floodplain aggradation showed incision-deposition patterns similar to those reported by Marren and Toomath (2013) because the narrower region located close to the glacier terminus constrained the flow into straight channels promoting the downstream transfer of sediments and consequent deposition in wider sectors (Figure 5.10a, 5.11a and 5.13). Perturbing the boundary conditions, by either a change in the S or C magnitude, led to a rapid response in the of the stream towards a new steady state to maintain the fluvial system in equilibrium with the new conditions (Figure 5.9, 5.12 and 5.14).

### 5.2.4.3 Longitudinal sediment connectivity following glacier retreat

A key question following deglaciation is how the internal functioning of proglacial margins might evolve to control the downstream flux of sediment (Stoffel and Huggel, 2012; Li et al., 2021; Zhang et al., 2022, 2023). As glaciers retreat, the total amount of sediment generated by its erosion is expected to decrease due to the weaker ratio between ice thickness and basal sliding velocity (i.e. "peak sediment", Herman et al., 2015; Cook et al., 2020). At the same time, meltwater rates will increase until glaciers become too small to sustain them (i.e.

"peak water", Huss and Hock, 2018; Zhang et al., 2022, 2023). These two processes will interact not only between each other, but also with the expansion of the proglacial margin following deglaciation. These modifications will have a chain effect on both fluvial patterns and sediment transport dynamics (Zhang et al., 2022).

Compared to a reference scenario based on field-measured conditions with S higher than C (Simulation 1), the simulated scenarios allow hypotheses of how proglacial margins might react to subglacial and topographic conditions in the near future. According to Zhang et al. (2022), the actual glacier peak water may cause an increase in the S to C ratio and the forefield is likely to evolve following Simulation 3 with increasing braiding intensity and morphodynamic activity leading to aggradation for both fine and coarse subglacially-evacuated sediments. In a second phase, when the mass of ice becomes too low to support high subglacial erosion rates (i.e. "peak sediment" event), the proglacial stream will progressively evolve into a geomorphically more stable state characterized by lower braiding and reworking events (Simulation 4). At this point, the reaction of the forefield is likely highly dependent on a complex relationship between proglacial discharge, even due to meltwater or precipitation events, the input of sediment from para- and peri-glacial processes and the geomorphic stability due to vegetative colonization. If the input of sediment is high enough, repetition of a behavior more similar to Simulation 3 might be expected; in the opposite case, a transition toward a more stable state as shown in Simulation 2 might be expected.

In this latter scenario the sediment delivered to downstream regions is expected to increase over short timescales before to becoming constrained by the changing topographical configuration of the proglacial margin and decreasing discharge rates due to glacier recession. Deglaciation leads to an expanding proglacial floodplain greater space for morphodynamic processes and a progressive upstream extension of aggradation patterns. This likely promotes a more intense filtering of subglacially-exported coarse material as with Simulation 5 (Figure 5.10a and 5.11). However, this only occurs if the configuration of the newly-deglaciated terrain is sufficiently flat for establishing a braided stream pattern (Schumm, 1981, 1985), or if there is exposition of areas prone to deposition such as depressions and over-deepenings (Swift et al., 2021; Müller et al., 2024). In contrast, if the deglaciated valley bottom is steeper, headward erosion processes may occur promoting riverbed incision close to the glacier terminus and deposition of reworked sediment further downstream in the proglacial margin as in Simulation 6 (Figure 5.10b; Germanoski and Schumm, 1993; Curran et al., 2017; Roussel et al., 2018). In both cases, decreasing meltwater discharge rates due to deglaciation are likely to reduce particle advection lengths, promoting sorting of downstream transported sediment due nto reduced frequencies of reworking, thus reducing the total downstream export from proglacial margins (Mancini et al., 2023a).

The near-future evolution of the proglacial margin filtering will have repercussion for the supply of sediment towards downstream regions (Stoffel and Huggel, 2012), for the management of hydropower plants (Milner et al., 2017) and for aquatic ecosystems (Miller and Lane 2019; Roncoroni et al., 2023a).

**5.4.4.4 Limitations and perspectives**

To study the evolution of the proglacial filtering to different boundary conditions, several assumptions were made. Sediment delivery from sidewalls is not considered as the model has been calibrated on a proglacial margin characterized by a high disconnectivity between the valley sidewalls and the valley bottom due to the presence of large alluvial cones (Figure 5.1; Mancini and Lane, 2020). This process has been reported more widely (e.g. Lane et al., 2017) but it is possible that there are systems where debuttressing of glaciers from their valley sidewalls leads to increased sediment delivery (Church and Ryder, 1972).

The presence of buried-ice patches in the floodplain may strongly attenuate the geomorphic disturbances slowing down morphodynamic processes, either by reducing the lateral erosion or by forming stable kettle holes, but also generate sediment pulses due to bank failure related to the melting of ice (Hambrey, 1984; Orwin and Smart, 2004; Paster, 2022). For long temporal scales of analysis, other important variables to consider are the progressive vegetative colonization of glacial forelands and glacial-bed overdeepenings which may have the potential to, respectively, constraint lateral erosion and to modify the subglacial sediment export dynamics (Miller and Lane, 2019; Swift et al., 2021). These aspects will theoretically have important implications for both maintenance and magnitude of the proglacial filtering.

### 5.2.5 Conclusion

In this study the fluvial and geomorphic responses of proglacial forefields were simulated using the 2D hydro-morphodynamic physically-based model eRiDynaS. The model was calibrated and validated against continuous field-collected suspended sediment and bedload transport records, as well as proglacial stream statistics (i.e. daily total number of bars, their mean area and the braiding index of the forefield) over time. The calibrated model was applied to different hydrological, sedimentological and topographical conditions to investigate the response of the proglacial morphodynamic filtering to varying boundary conditions. The results showed a relationship between proglacial forefield morphodynamic intensity and sediment transport dynamics is controlled by the supply to capacity ratio acting of subglacially-exported bedload particles. In conditions where subglacial sediment supply is greater than transport capacity, the proglacial forefield develops more intense braiding promoting deposition of coarser particles. In contrast, if capacity can keep up with supply, flow becomes confined into fewer straight channels promoting riverbed erosion and the transfer of sediment through the proglacial margin system. The adjustment of the proglacial stream towards a new steady state following changes in these boundary conditions is rapid. However, suspended sediment transport is less dependent on this relationship with only small proportions of the total subglacially-exported amount of fines deposited in the forefield. Simulations showed the importance of topographic conditions following glacier retreat for longitudinal sediment connectivity. Increasing the size of proglacial margins under conditions where supply is higher than transport capacity leads to enhanced deposition rates, while in the opposite case riverbed reworking and downstream sediment transfer take over. These findings are important for improving the scenarios of suspended sediment and bedload transport dynamics in Alpine glacierized catchments, particularly in the actual context of rapid expansion of proglacial environments characterized by changes in the balance between subglacial sediment supply and meltwater availability, for better predicting sediment management in hydropower plants.

### 5.3 Chapter summary

This final Chapter aimed to bring together the findings obtained in Chapter 2 to 4 by investigating the proglacial filtering response in glacierized catchments under different topographical, hydrological and sedimentological boundary conditions.

Numerical simulation results confirmed, as shown in Chapter 4, that the magnitude of the proglacial filtering is related to the intensity of the morphodynamic processes of the proglacial streams which, in turn, are controlled by the subglacial sediment supply to transport capacity conditions. In scenarios where sediment supply was higher than the transport capacity, such as at the beginning of a deglaciation phase or for large deglaciating glaciers, the forefield experienced aggradation and enhanced braiding. Conversely, when the transport capacity exceeded the sediment supply, a situation typical of smaller glaciers in advanced

stages of deglaciation, the forefield contracted into fewer channels transitioning to a degradational state with improved longitudinal sediment connectivity.

In general, the proglacial filtering of subglacially-evacuated bedload particles was more sensible to changes in the supply to capacity conditions, while that for suspended sediment was more affected by topographical variations that promote enhanced braiding intensity. The topographic configuration of the proglacial margin also proved to be critical in determining the strength of the proglacial filtering, with larger proglacial margins providing greater buffering of downstream transported sediment. This suggests that the magnitude of filtering in proglacial forefields varies between glacierized catchments, and it is expected to evolve depending on changes in water and sediment availability due to deglaciation.

## 5.4 Supporting information

### 5.4.1 *eRiDynaS*: model description

5.4.1.1 Overview

eRiDynaS is a two-dimensional (grid-based) River Dynamics Simulator that incorporates equations representing water flow, multi-fraction sediment transport, bank erosion and floodplain processes. Initial channel and floodplain morphology (e.g., river slope, width and depth) and grain size characteristics (for bedload and suspended load) must be specified to define a channel-floodplain system with a simple initial configuration. The river system then evolves during the simulation to develop a self-formed channel and floodplain with morphology that is a product of the imposed model boundary conditions and process representation. Each grid cell in the domain is classed as either channel (unvegetated) or floodplain (partially vegetated). Cells can be converted between these two classes through a range of mechanisms as a simulation proceeds. Process equations and parameter values may differ between channel and floodplain cells, and as a function of floodplain age. The model represents a development of the approach presented by Nicholas et al. (2013).

5.4.1.2 Hydrodynamics

Two alternative approaches for modelling flow conditions are available in *eRiDynaS*. The simpler approach (herein referred to as the IF solver) is based on the inertial formulation of the shallow water equations presented by Bates et al. (2010). The more sophisticated approach (herein referred to as the MC solver) is based on a solution of the full shallow water equations using an approach based on a Godunov-type scheme (van Leer, 1979), which is a commonly used method in hydrodynamic (e.g., Liang et al., 2008) and morphodynamic models (e.g., Nicholas et al., 2013). Both schemes are used to calculate the flow depth $h$ and the unit discharge in $x$ and $y$ directions ($qx$, $qy$). The flow depth within each grid cell is calculated by applying the conservation of mass equation to sum the discharge entering and leaving the grid cell:

$$\frac{\partial h}{\partial t} + \frac{\partial qx}{\partial x} + \frac{\partial qy}{\partial y} + \delta = 0$$

Eq. S5.1

where $t$ is time, and the final term ($\delta$) in the balance equation can be used to represent vertical losses due to floodplain drainage (infiltration). The two alternative flow solvers use different approaches to calculate the unit discharge terms $qx$ and $qy$. The more sophisticated MC solver represents the spatial transport of momentum, which is neglected by the IF solver. To benefit from the advantages afforded by this improved process representation, it must typically be implemented on a grid with a higher spatial resolution than that used with the simpler scheme. In the study, the MC solver approach was used.

*IF Solver*

Unit discharges in $x$ and $y$ directions are calculated at cell faces using the inertial formulation of the shallow water equations presented by Bates et al. (2010) and modified by de Almeida et al. (2012), recast to use a Chezy roughness law. This can be expressed in the $x$ direction as:

$$\frac{\partial qx}{\partial t} + gh\frac{\partial(h+z)}{\partial x} + \frac{g|qx|qx}{C^2h^2} = 0$$

Eq. 5.2

where $C$ is the Chezy roughness coefficient, and $g$ is acceleration due to gravity. This relation is rearranged to calculate the unit discharge at the face, $f$, between each pair of grid

cells. For example, the $x$ direction flux at the end of the current model time step, $qx_f^{t+\Delta t}$, is updated from its current version, $qx_f^t$, as:

$$qx_f^{t+\Delta t} = \frac{(\theta_M qx_f^t + (1 - \theta_M)qx_*^t) - gh_f S\Delta t}{1 + g\Delta t qx_f^t/(C^2 h^2)}$$

Eq. S5.3

where $qx_*^t$ is the average value of the unit discharge at the faces upstream and downstream of face $f$, $S$ is the water surface slope across the face, and $\theta_M$ is a parameter of the numerical scheme. The flow depth at the face is evaluated as the difference between the water level in the upstream cell and the higher of the two bed elevations on either side of the face. An equivalent expression is used to calculate the $y$ direction mass fluxes. The parameter $\theta_M$ is a weighting coefficient with a value between 0 and 1. In the original scheme proposed by Bates et al. (2010) $\theta_M = 1$. In the q-centered scheme of de Almeida et al. (2012) $\theta_M = 0.9$ was found to lead to significant improvements in model stability for simulations of flooding in the case of a static bed. The model time step ($\Delta t$) is determined using a simplified Courant-Friedrichs-Lewy criterion (where $\alpha$ is a parameter that should be less than c. 0.75 in order to maintain model stability, and which has a default value of 0.5 here), and $h_{max}$ is the maximum flow depth in the model domain.

$$\Delta t = \alpha \frac{\Delta x}{\sqrt{gh_{max}}}$$

Eq. S5.4

*MC Solver*

The MC solver applies a finite volume scheme in which unit discharges in $x$ and $y$ directions are calculated at cell centres by solving the depth-averaged shallow water equations written in the form:

$$\frac{\partial qx}{\partial t} + \frac{\partial(qx^2/h)}{\partial x} + \frac{\partial(qx\,qy/h)}{\partial y} + gh\frac{\partial(h+z)}{\partial x} + \frac{1}{\rho}\frac{\partial(h\tau_{xy})}{\partial y} + \frac{1}{\rho}\frac{\partial(h\tau_{xx})}{\partial x} + \frac{\tau_{bx}}{\rho} - F_x = 0 \quad \text{Eq. S5.5}$$

$$\frac{\partial qy}{\partial t} + \frac{\partial(qy^2/h)}{\partial y} + \frac{\partial(qx\,qy/h)}{\partial x} + gh\frac{\partial(h+z)}{\partial y} + \frac{1}{\rho}\frac{\partial(h\tau_{yx})}{\partial x} + \frac{1}{\rho}\frac{\partial(h\tau_{yy})}{\partial y} + \frac{\tau_{by}}{\rho} - F_y = 0 \quad \text{Eq. S5.6}$$

where $\rho$ is fluid density; $\tau_{xy}$, $\tau_{yx}$, $\tau_{xx}$ and $\tau_{yy}$ are turbulent stresses; $\tau_{bx}$ and $\tau_{by}$ are bed shear stresses in $x$ and $y$ directions; $F_x$ and $F_y$ are momentum fluxes due to secondary flows; and all other variables are as defined above. Bed shear stresses are modelled using a quadratic friction law:

$$\frac{\tau_{bx}}{\rho} = \frac{g}{(Ch)^2}qx\sqrt{qx^2 + qy^2}$$

Eq. S5.7

$$\frac{\tau_{by}}{\rho} = \frac{g}{(Ch)^2}qy\sqrt{qx^2 + qy^2}$$

Eq. S5.8

Because the terms in equations S5.5 and S5.6 associated with turbulence stresses and secondary flow have a very small influence on simulated morphodynamics, the model can be implemented with these terms neglected. This approach was implemented in the simulations reported in the current study. When included, these terms are represented using the approaches described by Nicholas et al. (2013).

In the MC solver, the mass and momentum equations are solved by explicit time integration using a Godunov-type finite volume scheme based on the Harten-Lax-Van Leer (HLL) approximate Riemann solver (Harten et al., 1983). The HLL solver is implemented by

interpolating variables to cell faces using the monotone upwind scheme for conservation laws approach to variable reconstruction with a Monotonized Central slope limiter (van Leer, 1979), thus achieving second-order accuracy in space. The solver can be implemented using two alternative approaches to represent the water surface slope (term 4 in equations S5.5 and S6). The simpler approach treats the water surface pressure gradient as a source term in the momentum equation, expressed using a central difference approximation. In the alternative approach, the pressure gradient term is split into a bed slope source term and a pair of momentum fluxes associated with the flow depths at cell faces, which are evaluated using the Riemann solver. This approach involves writing the water surface slope term (e.g., in the $x$ direction) as:

$$gh\frac{\partial(h+z)}{\partial x} = gh\frac{\partial z}{\partial x} + \frac{g}{2}\frac{\partial h^2}{\partial x}$$

Eq. S5.9

The momentum fluxes (represented by the second term on the right hand side of equation S5.9) are calculated by the HLL solver, after reconstructing the water surface elevations, flow depths and bed levels using the Surface Gradient Method of Zhou et al. (2001); see also Aureli et al. (2008). This approach ensures a well-balanced solution in the presence of variable bottom topography and at wet-dry interfaces.

Second-order accuracy in time is achieved using a predictor-corrector scheme to update cell centred flow variables ($h$, $qx$ and $qy$) at the mid-point and end of each model time step. The model hydrodynamic time step $\Delta t$ is again defined to satisfy a Courant-Friedrichs-Lewy stability criterion:

$$\Delta t = min\left(\alpha\left(\frac{\Delta x}{(\sqrt{gh}+|qx/h|)}\right), \alpha\left(\frac{\Delta y}{(\sqrt{gh}+|qy/h|)}\right)\right)$$

Eq. S5.10

When using either flow solver, channel roughness can be represented using one of three approaches: (i) A constant Chezy friction value, $C$; (ii) A relative roughness model that determines Chezy as a function of the flow depth, $h$, and a constant roughness lengthscale, $ks$; or (iii) A relative roughness model where the length scale is the maximum of $ks$ and the local bed material mean diameter, $D_m$:

$$C = a(h/ks)^b$$

Eq. S5.11

$$C = a(h/\max[ks,D_m])^b$$

Eq. S5.12

Floodplain roughness is modelled by defining the floodplain Chezy coefficient $C_F$ as a piecewise function of floodplain age, or using an approach based on the work of Baptist et al. (2007):

$$C_F = \left(\frac{1}{C^2} + B_v h\right)^{-0.5} \qquad H_v \geq h$$

Eq. S5.13a

$$C_F = \left(\frac{1}{C^2} + B_v H_v\right)^{-0.5} \qquad h > H_v$$

Eq. S5.13b

where $h$ is the flow depth, $C$ is the Chezy coefficient of the bare surface determined using equations S5.11 and S5.12, $H_v$ is the vegetation height, and $B_v$ is the vegetation blockage factor, which is a function of stem density, $m$, expressed in stems per unit area, stem diameter, $D_s$, and a bulk drag coefficient, $C_D$:

$$B_v = C_D m D_s/2g$$

Eq. S5.14

## 5.4.1.3 Sediment transport

*eRiDynaS* represents both bedload and suspended load transport by incorporating a capacity driven approach (for coarse sediment fractions) and an advection-diffusion approach (for fine fractions). Vertical layering of sediment is represented by an active surface layer with constant thickness ($L_{Act}$), a series of substrate layers with constant thickness ($L_{Sub}$), and an exchange layer (between the active layer and upper substrate layer) with a variable thickness ($L_{Ex}$). Coarse sediment (capacity-based) transport calculations begin by determining the sediment transport rate in each grid cell using one of several alternative transport formulae. Three different transport laws are available, but the Meyer-Peter and Müller approach was used in this study.

o    A generic velocity-based transport law, in which transport rates are calculated as a power law function of the depth-mean velocity in excess of a grain size dependent threshold.

$$qb_k = f_k f_b \Omega (\epsilon_F V - V cr_k)^\beta \qquad \text{Eq. S5.15}$$

$$V cr_k = C\sqrt{R\tau_{cr}^* D_m^\chi D_k^{1-\chi}} \qquad \text{Eq. S5.16}$$

where $qb_k$ is the volumetric sediment transport rate per unit width for the $k^{th}$ size class, $f_k$ is the fraction of size class $k$ in the active bed layer, $f_b$ is the fraction of the grid cell that is unvegetated (which is 1 in the case of channel cells), $\Omega$ is a constant with a default value of 0.001, $V$ is the depth mean velocity in the grid cell, $\beta$ is an exponent with a default value of 3, $\epsilon_F$ is a transport efficiency factor, which can be used to approximate the effect of form drag, $V cr_k$ is the critical entrainment velocity of sediment in size class $k$, $C$ is the Chezy roughness, $R$ is the submerged specific gravity of sediment, $\tau_{cr}^*$ is the critical dimensionless shear stress for entrainment, $D_m$ is the geometric mean sediment diameter in the active layer, $D_k$ is the mean sediment diameter in size class $k$, and $\chi$ is a hiding factor. By varying the exponent $\beta$ and constant $\Omega$ it can approximate the behavior of several other sediment transport relations.

o    The Engelund-Hansen (1967) total load sand-silt transport law, which has been modified to include a simple treatment of relative size effects (in the denominator), such that transport rates are a function of both the individual grain diameter and the geometric mean diameter.

$$qb_k = f_k f_b \Omega \frac{V^5}{C^3 D_m^\chi D_k^{1-\chi}} \qquad \text{Eq. S5.17}$$

where $qb_k$ is the volumetric sediment transport rate per unit width for the $k^{th}$ size class, $f_k$ is the fraction of size class $k$ in the active bed layer, $f_b$ is the fraction of the grid cell that is unvegetated (which is 1 in the case of channel cells), $\Omega$ is a constant with a default value of 0.0059, $V$ is the depth-mean velocity in the grid cell, $C$ is the Chezy roughness, $D_m$ is the geometric mean sediment diameter in the active layer, $D_k$ is the mean sediment diameter in size class $k$ and $\chi$ is a hiding factor.

o    Meyer-Peter and Müller gravel transport law, expressed here in a form that includes relative size effects.

$$qb_k = f_k f_b \Omega (D_k(\epsilon_F \tau^* - \tau_{cr}^* (D_m/D_k)^\chi))^{1.5} \qquad \text{Eq. S5.18}$$

$$\tau^* = \frac{(V/C)^2}{RD_k} \qquad \text{Eq. S5.19}$$

where $qb_k$ is the volumetric sediment transport rate per unit width for the $k^{th}$ size class, $f_k$ is the fraction of size class $k$ in the active bed layer, $f_b$ is the fraction of the grid cell that is unvegetated (which is 1 in the case of channel cells), $\Omega$ is a constant with a default value of 32.2, $V$ is the depth mean velocity in the grid cell, $C$ is the Chezy roughness, $\tau_*$ is the dimensionless shear stress, $\epsilon_F$ is a transport efficiency factor, which can be used to approximate the effect of form drag, $R$ is the submerged specific gravity of sediment, $\tau_{cr}^*$ is the critical dimensionless shear stress for entrainment, $D_m$ is the geometric mean sediment diameter in the active layer, $D_k$ is the mean sediment diameter in size class $k$, and $\chi$ is a hiding factor.

5.4.1.4 Sediment transport direction and adjustments for curvature effects

Coarse sediment transport rate components in $x$ and $y$ directions are calculated based on the local depth-mean flow direction, which is adjusted in channel cells to account for the effects of streamline curvature:

$$qbx_k = qb_k\cos(\tan^{-1}(Vy/Vx) - \tan^{-1}(\epsilon_A h/R_C)) \qquad \text{Eq. S5.20}$$

$$qby_k = qb_k\sin(\tan^{-1}(Vy/Vx) - \tan^{-1}(\epsilon_A h/R_C)) \qquad \text{Eq. S5.21}$$

where $qbx_k$ and $qby_k$ are the $x$ and $y$ components of the volumetric transport rate per unit width for the $k^{th}$ size fraction, $Vx$ and $Vy$ are the $x$ and $y$ velocity components (Figure S5.1), $h$ is the flow depth, $R_C$ is the streamline radius of curvature at the cell centre, and $\epsilon_A$ is a parameter that controls the magnitude of the curvature effect on sediment transport (this effect tends to steer sediment towards the inside of bends, leading to the construction of point bars).
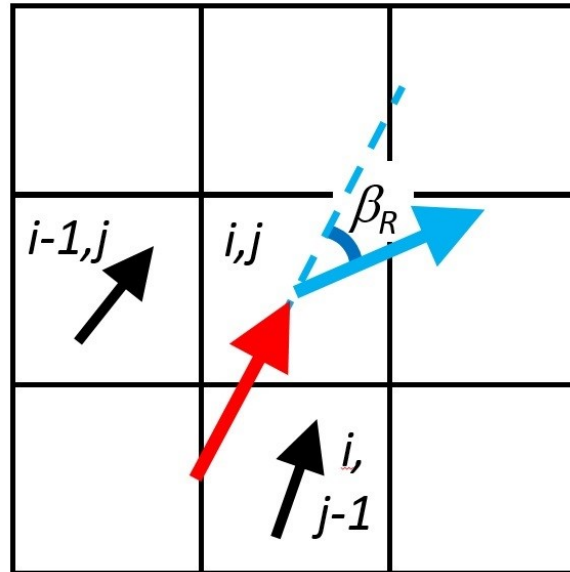


Figure S5.1: Calculation of streamline radius of curvature using geometric scheme.

Streamline radius of curvature values can be modelling using two approaches. The first of these calculates curvature from the spatial gradients in the flow field as:

$$R_C = \frac{|V^3|}{V_x V_y \left(\frac{\partial Vy}{\partial y} - \frac{\partial Vx}{\partial x}\right) + V_x^2 \left(\frac{\partial Vy}{\partial x}\right) - V_y^2 \left(\frac{\partial Vx}{\partial y}\right)} \qquad \text{Eq. S5.22}$$

The alternative approach adopts a geometric method to calculate the local radius of curvature as a function of the angular deviation, $\beta_R$, between the local flow vector in cell ($i,j$)

and the upstream flow vector (respectively, the blue and red vectors shown in Figure S5.1). In this approach, the radius of curvature is calculated as:

$$R_C = \max\left(\frac{2\Delta x}{\beta_R}, 10h_{i,j}, \Delta x\right)$$

Eq. S5.23

where $\Delta x$ is the grid resolution, $\beta_R$ is the angle through which the flow rotates between the upstream and downstream vectors, and the sign of the curvature indicates the direction of rotation (i.e. clockwise or anticlockwise). The flow direction in cell ($i,j$) is determined from the $x$ and $y$ components of the flow velocity in the cell. The upstream flow direction is approximated by taking a weighted average of the $x$ direction unit discharge values in the cells that are upstream of ($i,j$), and an equivalent weighted average $y$ direction unit discharge in these cells. These weighted average $x$ and $y$ direction unit discharge values ($qx_{up}$ and $qy_{up}$) then define the mean upstream flow direction. The two upstream cells (indicated by black vectors in the image below) are selected based on the sign of the $x$ and $y$ components of the flow in cell ($i,j$).

The weighting of these two vector components is determined from the flow orientation at ($i,j$), thus for the case shown in Figure S5.1:

$$qx_{up} = \left(\frac{Vx_{i,j}}{V_{i,j}}\right)^2 qx_{i-1,j} + \left(\frac{Vy_{i,j}}{V_{i,j}}\right)^2 qx_{i,j-1}$$

Eq. S5.24

$$qy_{up} = \left(\frac{Vx_{i,j}}{V_{i,j}}\right)^2 qy_{i-1,j} + \left(\frac{Vy_{i,j}}{V_{i,j}}\right)^2 qy_{i,j-1}$$

Eq. S5.25

The geometric approach to calculating curvature may be better suited to cases involving coarse grids with narrow channels. Both of the approaches to calculating curvature described above can be combined with a non-equilibrium method that allows the spatial evolution of the curvature to be modelled by solving a transport equation for the spiral motion intensity of the flow. This approach is presented in Nicholas et al. (2013) and Deltares (2018), but was not implemented in the model simulations carried out in this study, and hence is not described here.

5.4.1.5 Sediment transport adjustments for bed slope effects

Topographic steering of coarse sediment transport by the local bed slope is modelled following the principles outlined by Ikeda (1982) and others, summarized by van Rijn (1993). Sediment transport rates are adjusted to account for the bed slope in both the longitudinal and transverse directions (i.e. parallel and perpendicular to the flow). These bed slopes are calculated as:

$$S_{Long} = \frac{\partial z}{\partial x}\frac{qbx}{qb} + \frac{\partial z}{\partial y}\frac{qby}{qb}$$

Eq. S5.26

$$S_{Tran} = \frac{\partial z}{\partial y}\frac{qbx}{qb} - \frac{\partial z}{\partial x}\frac{qby}{qb}$$

Eq. S5.27

where $z$ is the bed elevation, and $qbx$ and $qby$ are the $x$ and $y$ components of the sediment transport $qb$ calculated by equations S5.20 and S5.21. These sediment transport components are adjusted to account for the effect of the bed slope parallel to the sediment transport direction:

$$qbx' = qbx(1 + \Gamma LongSLong) \qquad \text{Eq. S5.28}$$

$$qby' = qby(1 + \Gamma LongSLong) \qquad \text{Eq. S5.29}$$

where $qbx'$ and $qby'$ are the adjusted transport rates, and $\Gamma_{Long}$ is an order one coefficient. The coarse sediment fluxes at cell faces, $f$, in the $x$ and $y$ directions, $qbx_{f,k}$ and $qby_{f,k}$, are then calculated as the sum of the longitudinal and transverse flux components, and a third flux (last term on the right hand side of equations S5.30 and S5.31) which is independent of the adjusted transport rates:

$$qbx_{f,k} = qbx'_{Up,k} - qby'_{Low}\Gamma_{Tran}S_{Tran}f_{Src,k}M + \Pi(S_x^*)f_{Src,k} \qquad \text{Eq. S5.30}$$

$$qby_{f,k} = qby'_{Up,k} + qbx'_{Low}\Gamma_{Tran}S_{Tran}f_{Src,k}M + \Pi(S_y^*)f_{Src,k} \qquad \text{Eq. S5.31}$$

where $qbx'_{Up,k}$ and $qby_{Up,k}'$ are sediment fluxes for the $k^{th}$ size fraction in the cell on the upstream side of the face, $qby'_{Low}$ and $qbx'_{Low}$ are the $y$ and $x$ components of the total sediment flux in the lower of the two cells (in terms of bed height), $\Gamma_{Tran}$ is an order one coefficient, $S_{Tran}$ is the transverse bed slope, $f_{Src,k}$ is the fraction of the sediment in the active bed layer in the source cell in the $k^{th}$ size class, $\Pi$ is a user defined constant, $S_x^*$ and $S_y^*$ are the excess bed slope in the $x$ and $y$ directions (i.e. the bed slope minus a threshold bed slope), and $M$ is a mobility factor that can be approximated by:

$$M = Vcr_m/V \qquad \text{Eq. S5.32}$$

where $Vcr_m$ is the critical velocity for entrainment of the geometric mean particle size. Alternatively, the effect of the mobility factor can be neglected by setting $M=1$. The final terms on the right hand side of equations S5.30 and S5.31 are introduced to modify the representation of sediment fluxes on steep topographic slopes and limit the development of very large depth gradients at the channel margins. These terms are only non-zero where the topographic slope between the cells exceeds the threshold gradient and can be neglected by setting $\Pi = 0$.

Topographic effects on bedload transport can be particularly challenging to account for when simulating processes in large rivers that necessitate the use of a coarse resolution model grid on which steep slopes are difficult to represent. For example, on grids with resolutions of 50-100 m, even rapid flow shallowing (e.g., where water depths tend to zero as flow is directed onto bar heads) is typically associated with weak adverse bed slopes. To address this situation, and to limit the transport of sediment on such adverse bed slopes, a maximum adverse bed gradient ($S_{Max}$) can be defined (approximately equivalent to a maximum reduction in the flow depth between two cells in the longitudinal flow direction), above which the bedload flux is set to zero.

Equations S5.30 and S5.31 are applied to calculate the coarse sediment fluxes at faces between pairs of channel cells. When only one of the two cells is wet, the term representing the transverse slope effect can be replaced by an alternative expression that is written in the form of the treatment of bank erosion processes (see below). This is equivalent to treating the face between the wet and dry channel cells as an unvegetated river bank.

$$-qby'_{Low}\Gamma_{Tran}S_{Tran}f_{Src,k}M = \Gamma_{Bank}(V - Vcr)^\omega \frac{\partial z}{\partial x} \qquad \text{Eq. S5.33}$$

$$qbx'_{Low}\Gamma_{Tran}S_{Tran}f_{Src,k}M = \Gamma_{Bank}(V - Vcr)^{\omega}\frac{\partial z}{\partial y}$$

<div align="right">Eq. S5.34</div>

where $\Gamma_{Bank}$ is a user-defined constant, $V$ is the depth-mean velocity in the wet channel cell, $V\,cr$ is the critical velocity for sediment entrainment from the dry cell, and $\omega$ is a user-defined exponent.

### 5.4.1.6 Supply-limited transport of fine sediment

The transport of fine (suspended) sediment can be modelled by solving an advection-diffusion mass balance relation of the form:

$$\frac{\partial \psi_k h}{\partial t} + \frac{\partial qx\psi_k}{\partial x} - \frac{\partial}{\partial x}\left(D_H h \frac{\partial \psi_k}{\partial x}\right) + \frac{\partial qy\psi_k}{\partial y} - \frac{\partial}{\partial y}\left(D_H h \frac{\partial \psi_k}{\partial y}\right) + D_R - E_R - B_R \quad = 0 \text{ Eq. S5.35}$$

where $\psi_k$ is the concentration of suspended sediment in the $k^{th}$ size fraction, $D_H$ is a horizontal diffusivity, $D_R$ is the rate of sediment deposition, $E_R$ is the rate of sediment erosion from the bed, and $B_R$ is the rate of sediment supply by bank erosion in adjacent grid cells. Since advection is likely to be the dominant mode of sediment transport and because the model is intended to be suitable for use on coarse resolution grids, the option exists to neglect the diffusive transport terms.

The diffusive fluxes in equation S5.35 are represented using a central difference scheme. The advection terms can be represented using either first or second order upwind numerical schemes when using the MC flow solver. When using the simpler IF flow solver these terms are represented using a first order upwind scheme. Deposition and erosion of sediment at the bed are represented as:

$$D_R = \left(1 - \left(\frac{V}{V_D cr_k}\right)^2\right)w_{sk}T_e\psi_k \qquad V < V_D cr_k \qquad \text{Eq. S5.36}$$

$$E_R = \left(\left(\frac{V}{V_E cr_k}\right)^2 - 1\right)S_R f_k f_b \qquad V > V_E cr_k \qquad \text{Eq. S5.37}$$

where $V_D cr_k$ and $V_E cr_k$ are the critical velocity for the deposition and erosion of fine sediment in size fraction $k$, $w_{sk}$ is the particle fall velocity for size fraction $k$, $T_e$ is the trapping efficiency of the surface, which is 1 for channel cells, but may be higher for floodplain cells (see below), $S_R$ is a scour rate constant, $f_k$ is the fraction of size class $k$ in the active bed layer, and $f_b$ is the fraction of the grid cell that is unvegetated (which is 1 in the case of channel cells). The generation of sediment by bank erosion, represented in equation S5.35 by $B_R$, is discussed below.

### 5.4.1.7 Bank erosion

Faces in the model domain that separate channel grid cells from floodplain grid cells are treated as river banks. At these faces, the transverse component of sediment transport (i.e. that associated with the lateral bed slope) is not calculated using the procedure described above. Instead, the transfer of sediment from the floodplain to the channel cell is represented as lateral bank erosion. The bank erosion process involves two stages: (i) Calculation of sediment fluxes from the floodplain to the channel, which result in removal of mass from the

floodplain cell; and (ii) Conversion of the floodplain cell into a channel cell once sufficient sediment has been removed from the floodplain. For bank erosion to occur, the water depth in the near-bank grid cell must exceed a threshold depth ($h_{Bank}$) and the bank height ($H$) must exceed a minimum critical bank height ($H_0$). Bank erosion rates are then calculated as:

$$qs_k = f_{k,F}\Theta_v (V_C - Vcr)^\omega H(1 - \zeta f_{SC,F}) \qquad \text{Eq. S5.38}$$

where $qs_k$ is the bank erosion sediment flux for size class $k$, $f_{k,F}$ is the fraction of sediment in the active layer of the floodplain cell in size class $k$, $f_{SC,F}$ is the fraction of silt and clay sized sediment in the river bank as a whole, $V_C$ is the depth-mean velocity in the channel cell, $Vcr$ is the critical velocity for bank material entrainment, $\omega$ is a user-defined exponent, $H$ is the bank height, $\Theta_v$ is the bank erodibility, which is a function of floodplain age (see below), and $\zeta$ is an empirical constant.

Coarse sediment (modelled using the capacity-based approach) that is eroded from the floodplain cell is deposited in the adjacent channel cell. In contrast, fine sediment (modelled using a supply-limited approach) enters the water column in the channel cell (via the $B_R$ term in equation S5.35). The volume of sediment that is removed from the floodplain cell is tracked, but the height of the floodplain surface is not lowered as a result of bank erosion. This approach (see Nicholas et al., 2013) is adopted because bank erosion is assumed to occur laterally, rather than vertically. When the volume of sediment eroded from the floodplain cell exceeds a threshold value, the floodplain cell is converted to channel and the elevation of the cell is lowered to the level required to conserve mass. The threshold erosion volume for floodplain to channel conversion depends on the height of the river bank (i.e. on the elevation difference between the floodplain cell and the lowest adjacent channel cell). For low river banks, the threshold erosion volume equals that required to lower the floodplain to the height of the adjacent channel cell (i.e. 100% of the floodplain sediment must be removed). As river bank height increases the threshold erosion volume is defined by a declining proportion of the total bank height. This approach is based on the assumption that sediment removal from the floodplain cell leads to progressive steepening of the bank, and that the critical bank angle for failure declines as the bank height increases, thus:

$$VOL = H\Delta x^2 p \qquad \text{Eq. S5.39}$$

$$p = 1 - \left(\frac{L_B}{\Delta x}\right)\left(\frac{0.75\left(\frac{H}{H_{MIN}} - 1\right)}{0.75 + \left(\frac{H}{H_{MIN}} - 1\right)}\right) \qquad \text{Eq. S5.40}$$

where $VOL$ is the threshold erosion volume that must occur for conversion of the floodplain cell to a channel cell, $H$ is the bank height, $\Delta x$ is the cell resolution, $p$ is the proportion of the bank that must be eroded in order for the conversion of the floodplain cell to a channel cell, $L_B$ is the horizontal length of the bank zone, which must be less than or equal to the cell resolution, and $H_{MIN}$ is a minimum bank height below which the floodplain must be lowered to the level of the channel bed (100% of the floodplain eroded). The ratio of the typical bank length $L_B$ to the grid cell size $\Delta x$ is also defined by the user as an input parameter. This parameter is intended to account for the fact that if the model grid resolution is coarse relative to the length of the bank, then the volume of sediment that must be removed from the floodplain cell before it can be converted to channel will be larger because the bank may need to go through more than one failure cycle before this occurs.

During each model time step the elevation of channel and floodplain cells and the grain size composition of the active layer in each cell is adjusted by integrating the sediment fluxes into and out of the grid cell during the time step. The active layer is assumed to have a fixed vertical thickness. Net aggradation of the bed results in sediment being passed from the active layer to the sediment exchange layer below (to maintain a constant active layer thickness). Similarly, net degradation of the bed results in sediment being removed from the exchange layer and incorporated within the active layer, to compensate for the sediment removed. If the exchange layer thickness exceeds a critical value, the exchange layer is split into two parts, one of which becomes a new layer at the top of the stack of substrate layers. If the exchange layer thickness falls below a minimum critical value, the current topmost substrate layer is incorporated within the exchange layer. The bed is assumed to have a constant porosity that is the same for all grain size fractions.

When implementing model mass balance calculations, sediment fluxes (and hence rates of elevation change) are multiplied by a morphological scaling factor (*MSF*) which is defined by the user and held constant over the course of the simulation. This approach is equivalent to implementing the model using different time steps for the hydrodynamic and morphodynamic aspects of the calculations. It has the effect of accelerating rates of morphological change, thus enabling more efficient simulation of long-term river and floodplain evolution. This is a relatively common approach used in morphodynamic modelling of fluvial and coastal environments (e.g., Ranasinghe et al., 2011; Nicholas et al., 2013; Morgan et al., 2020).

5.4.1.8 Floodplain processes

Floodplain cells are assumed to contain vegetation, the age of which increases progressively from the point in time when the cell was first converted to floodplain. Vegetation effects are represented by defining the changes in vegetation properties associated with vegetation succession as a set of piecewise linear functions. In addition to inducing a change in surface roughness (see above), vegetation has a number of effects on flow and sediment transport processes. Floodplain cells are considered to be characterized by an unvegetated fraction, $f_b$, that is used in bedload transport calculations, and a vegetated fraction, $f_v$, that is a function of floodplain surface age, such that $f_b=1-f_v$. The fine sediment trapping efficiency (see equation S5.36) of floodplain cells can be defined to be higher than that of channel cells. The bank erodibility parameter, $\Theta_v$, is also defined as a function of floodplain age. In addition to these effects, a simple drainage scheme can be implemented, which is applied only in floodplain cells, so that ponded flood water is able to leave the floodplain before the next overbank event at a defined drainage rate that is applied over a specified fraction of each flood hydrograph (during low flow conditions). Curvature corrections to the sediment transport direction are not applied in floodplain cells.

The conversion of channel cells to floodplain is assumed to occur as a result of the onset of vegetation colonization, which can be represented using one of two approaches. In the simplest approach, the cell is assumed to be colonized if the time since the cell was last inundated by water deeper than a threshold depth exceeds the time required for colonization. In the more sophisticated approach, the fraction of the time that grid cells are wet and dry is calculated during a hydrologic time window. The cumulative times that cells are wet and dry are then calculated over this time period. In order for a channel cell to be colonized by vegetation, the time that the cell was dry must exceed a threshold colonization time, and the time that the cell was wet must exceed a second threshold inundation time. The latter condition reflects the fact that in some environments colonization is dependent upon the dispersal of

seeds to inundated areas. In addition to these conditions, the second colonization scheme can be implemented by defining a colonization probability, which sets the probability that an individual grid cell will be colonized if it meets the conditions described above.

Model grid cells may be converted from floodplain to channel as a result of several mechanisms, including: Bank erosion (see above); burial by sediment (where the floodplain surface experiences aggradation by more than a threshold amount); surface scour (where the floodplain surface experiences degradation by more than a threshold amount); vegetation uprooting (where the floodplain flow velocity exceeds a critical velocity for vegetation scour); and mortality for hydrological reasons (where the floodplain surface is inundated for a time greater than a threshold duration or where the floodplain surface is dry for a time greater than a threshold duration). Each of these processes is represented by thresholds that are a function of floodplain age.

## 5.4.1.9 Boundary conditions

Water flow into the domain at inlets is defined as a series of discharge hydrographs of constant duration. Hydrographs can be represented using one of two simple shapes: either a symmetrical hydrograph based on a sine curve or an asymmetric hydrograph with a steep rising limb and gentle recession limb (Figure S5.2).
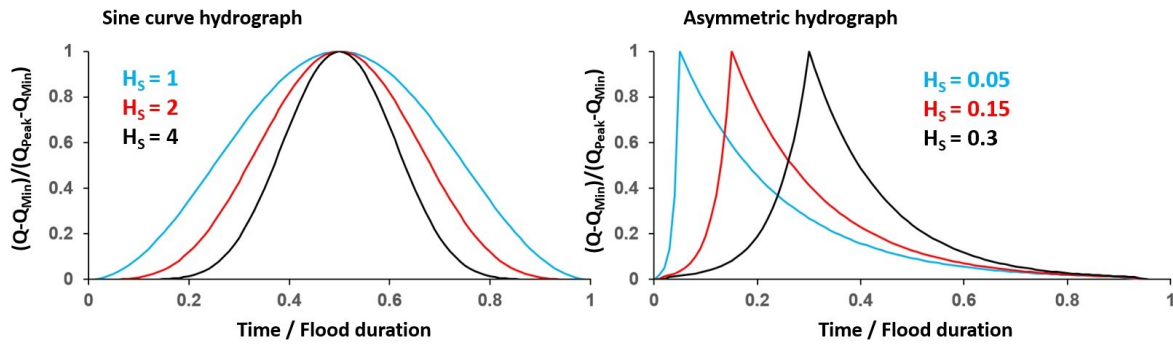


Figure S5.2: Alternative synthetic hydrograph shapes used at inlet boundaries.

Both hydrograph types are described using a shape parameter ($H_S$). For the sine curve hydrograph, the shape parameter controls the peakedness of the hydrograph. For the asymmetric hydrograph the shape parameter defines the fraction of the flood event represented by the rising limb of the hydrograph. Each flood is represented by a minimum discharge ($Q_{Min}$) and a peak discharge ($Q_{Peak}$), which varies between floods. The relationship between the relative discharge ($Q-Q_{Min}$)/($Q_{Peak}-Q_{Min}$) and the dimensionless flood time is shown below for examples of the two hydrograph types. Before each simulation begins a series of random flood peaks is generated. Floods are assumed to have a constant duration ($T_{Flood}$). The first flood can be preceded by a time period ($T_{Lead}$) with constant discharge ($Q_{Initial}$).

Sediment supply to the model domain is defined using rating curves, as follows:

$$qb_{IN,k} = fb_k Ab_n(1 + f_{Spert}(R - 0.5))Q_n^{Bb_n} \qquad \text{Eq. S5.41}$$

$$\psi_{IN,k} = f\psi_k A\psi_n(1 + f_{Spert}(R - 0.5))Q_n^{B\psi_n} \qquad \text{Eq. S5.42}$$

where $qb_{IN,k}$ and $\psi_{IN,k}$ are the coarse sediment supply rate in size fraction $k$ and the fine sediment concentration in size fraction $k$ at the inlet, $fb_k$ and $f\psi_k$ are the proportions of the total

coarse sediment supply and the total fine sediment supply in these size fractions (both of which sum separately to 1), $Ab_n$, $Bb_n$, $A\psi_n$ and $B\psi_n$ are user-defined constants, $f_{Spert}$ is the fractional variability in the sediment supply, $R$ is a pseudo-random number in the range 0 to 1 generated for each flood event, and subscript $n$ refers to the inlet number. The rating curve boundary condition for coarse sediment supply can also be over-ridden to force sediment transport rates at the inlet to be defined by the coarse sediment transport capacity. In this situation, the bed elevation and bed sediment grain size distribution in the first row of interior grid cells at the boundary are not allowed to adjust (i.e. an equilibrium bed condition is applied at the inlet).

The total discharge and sediment supply that is defined at inlets using the procedures described above must be distributed across the cells at the inlet. This is achieved by first defining the shape of the inlet cross section and how the shape changes through time. These things are controlled by the inlet timescales ($\Delta T_{0,n}$) and ($\Delta T_{1,n}$), and the inlet elevation scale ($\Delta Z_n$). The inlet section is represented with a thalweg (local elevation minimum) that migrates back and forth across the inlet over time. When the thalweg is located at either the extreme left or right sides of the channel, the inlet is treated as a simple laterally inclined plane with an elevation difference between the left and right sides of the inlet that is equal to $\Delta Z_n$. When the thalweg is not located at the edge of the inlet section, the channel bed on either side of the thalweg is represented using two inclined planes that meet at the thalweg. The duration of the inlet bed oscillation varies randomly over the course of the simulation between the two timescales ($T_{Flood}\Delta T_{0,n}$) and ($T_{Flood}\Delta T_{1,n}$). The discharge entering the model domain is distributed across the inlet in proportion to the height difference between the channel bed and the water level. Bedload supply to the model domain is distributed to account for the sediment fluxes out of the first row of model grid cells and to satisfy the mass balance requirements associated with the imposed oscillating bed level at the inlet.

At outlets from the model domain the discharge leaving the domain is calculated for each grid cell by applying a normal flow approximation based on the flow depth in the grid cell and the boundary outlet slope ($S_{OUT,n}$), where $n$ is the outlet number. Coarse sediment fluxes out of outlet boundary grid cells are derived by assuming that the bed elevation and grain size distribution at the outlet are fixed.

5.4.1.10 Computational needs

The model is built using a combination of openMP and MPI programming interfaces, enabling parallelization, and it was executed on the HPC infrastructure of the University of Lausanne. This cluster comprises 96 nodes equipped with AMD ZEN2/3 CPUs providing a total of 4608 compute cores and 54 TB of memory. Depending on the simulation proprieties, each model run took a processing time comprised between 28 and 42 days to process four complete melt seasons.

## 5.4.2 Field-collected 2021 instantaneous and cumulative suspended sediment (Qs) and bedload (Qb) fluxes with associated uncertainties
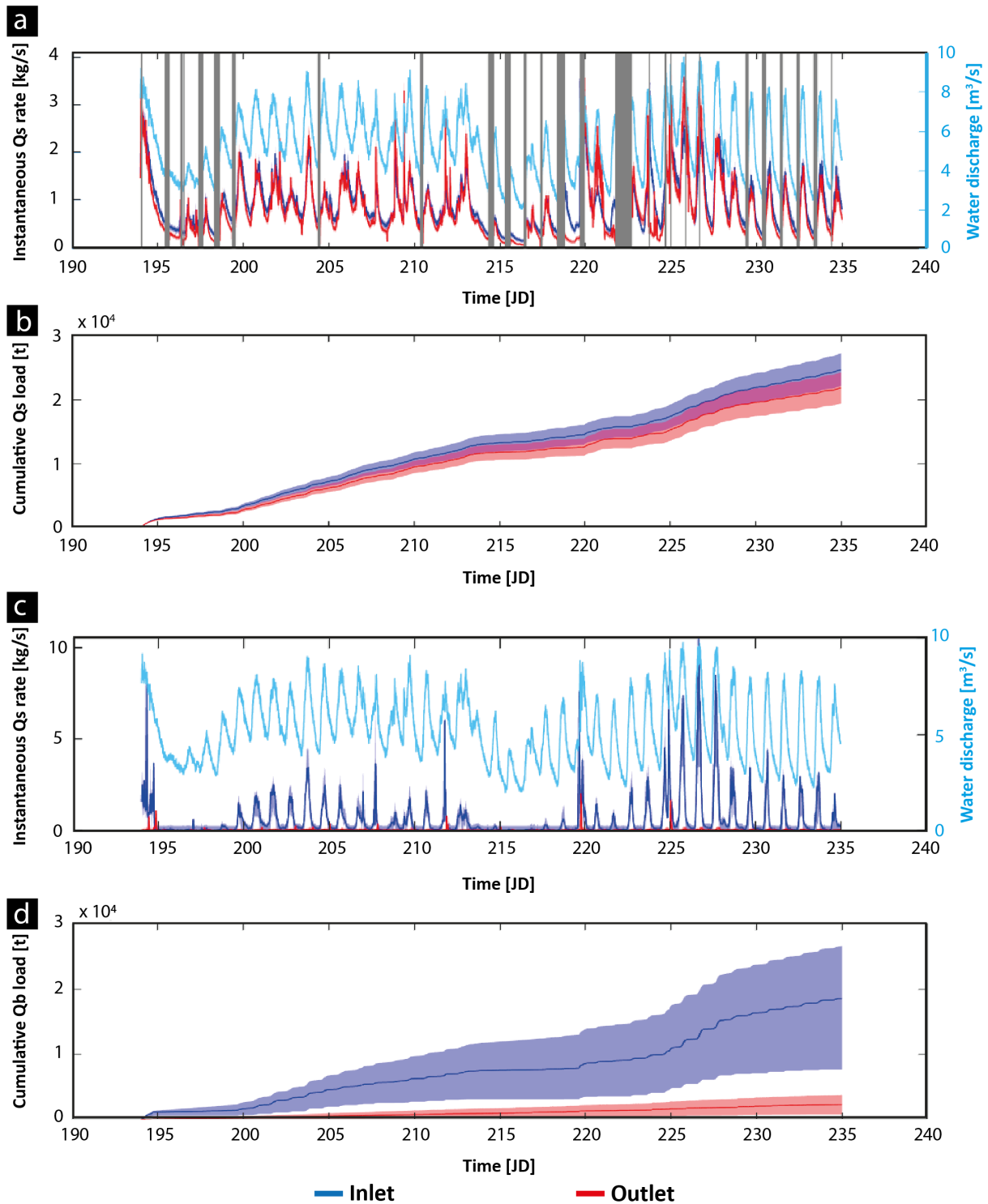


Figure S5.3: Field-collected instantaneous and cumulative sediment fluxes at both proglacial margin inlet (GS1, blue lines) and outlet (GS2, red lines) for both suspended sediment (a and b) and bedload (c and d) (Figure 5.1). Shaded areas refer to the transport uncertainties computed using techniques described in Mancini et al. (2023a). Light blue lines in (a) and (c) refer to the measured instantaneous discharge rates (Müller and Miesen, 2022).

### 5.4.3 Instantaneous and cumulative sediment fluxes over four melt seasons for simulations S1 to S6 (Table 5.2)
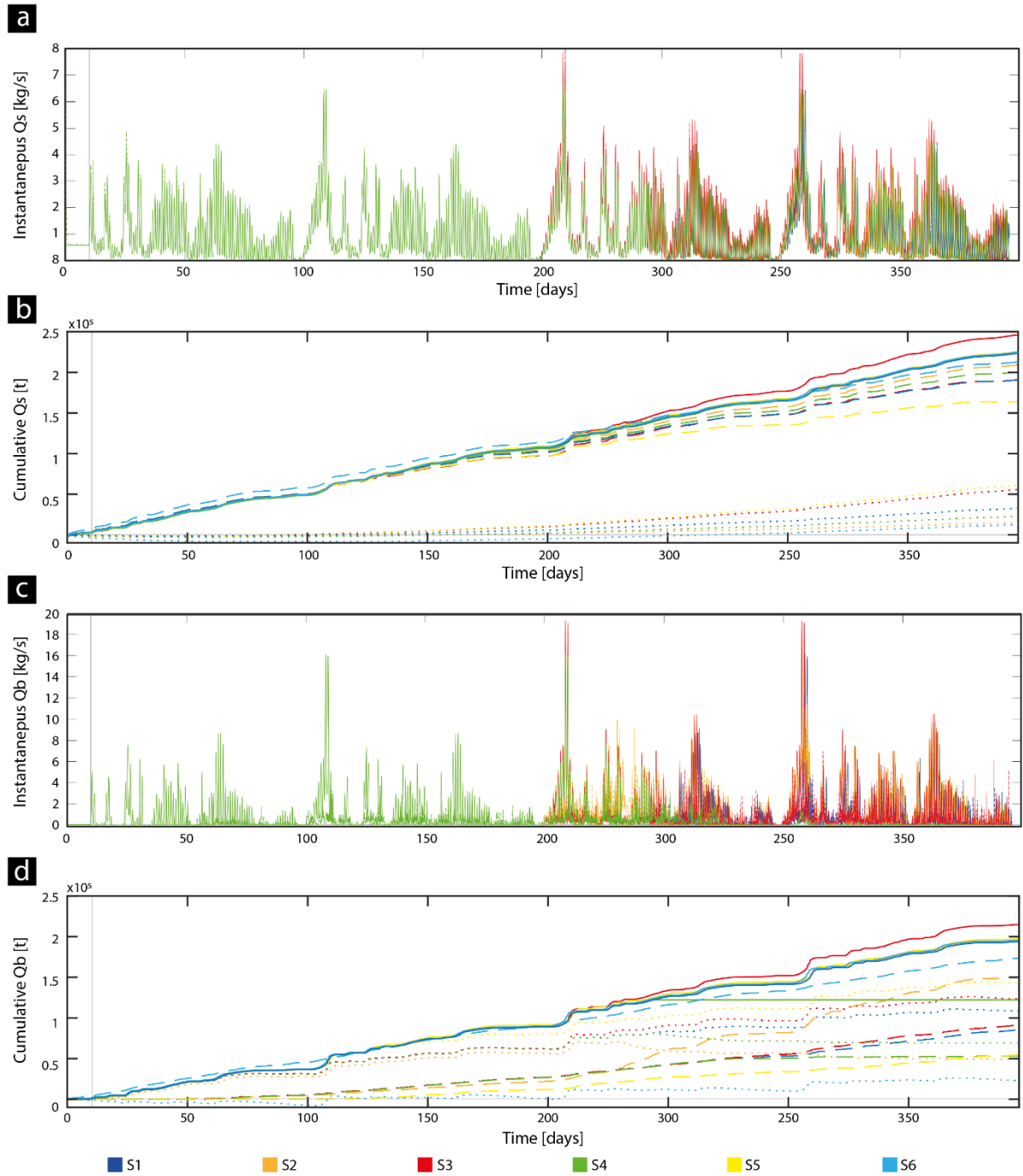


Figure S5.4: Simulated instantaneous and cumulative suspended sediment and bedload transport fluxes over four melt seasons. The vertical gray line defines the temporal limit between the use of a constant (i.e. 5.1 m³/s) and the field measured discharge rates in simulations.

# Chapter 6: Synthesis, limitations and perspectives for future studies

## 6.1 Synthesis

This PhD thesis aimed to investigate the geomorphic response of proglacial forefields to subglacial sediment export, and to assess the effects of proglacial morphodynamics on sediment flux to downstream. These aims were achieved through three inter-related chapters, each one focused on a specific research question (Section 1.3). The Chapter summarizes the main findings of the PhD thesis.

### 6.1.1 Do forefields filter the signal related to subglacial sediment export? If yes, over what timescales does this filtering occur?

The deployment of environmental seismology in proglacial zones (Chapter 2), and their combination with a calibrated turbidity-based record of suspended sediment concentration allowed the first continuous, melt-season scale quantification of how a proglacial margin filters the signal of the export of both bedload and suspended load export. The seismically-derived bedload flux timeseries were produced applying a geophysical inversion method called Fluvial Model Inversion (FMI) developed in Dietze (2018), incorporating geophysical models for estimating the seismic signals generated by water turbulence (Gimbert et al., 2014) and bedload transport (Tsai et al., 2012). This latter is based on a set of 15 parameters describing both topographical and sedimentological proprieties of the reach under investigation. Commonly, these parameter values are determined using either a Graphical User Interface (GUI; Dietze, 2018; Dietze et al., 2019a) approach or through the performance of an *in-situ* active seismic survey (Bakker et al., 2020; Lagarde et al., 2021). A new parameterization approach was used here, based on the Generalized Likelihood Uncertainty Estimation (GLUE; Beven and Binley, 1992; 2014). Given an un-calibrated model having large potential parameter ranges and at least one observation relative to the object for which the model was built for, GLUE uses a Monte Carlo approach to find a set of plausible values minimizing the difference between predictions and observations. Its implementation may not only ease the calibration of geophysical inversion methods, but also allow sediment transport quantification for regions where the active survey is not feasible. By considering all parameter values falling within the standard deviation bounds outputted from GLUE were used to produce one of the first seismically inferred bedload transport uncertainties.

The time-series of bedload and suspended load was then used to investigate the role of proglacial forefield in filtering the subglacial sediment export signal related to suspended sediment and bedload evacuation (Chapter 2). The results showed that: (i) the subglacial sediment export signal can be strongly modified by morphodynamic processes; and that (ii) the signal related to bedload export is significantly dampened and delayed compared to the suspended sediment signal, which pass almost un-impeded through the proglacial margin. The timescales over which the filtering operated was sub-daily. Cross-correlation of particle propagation velocities and critical discharge for sediment entrainment suggested that the physical explanation for the filtering was the particle advection lengths (Ganti et al., 2014; Pelosi and Parker, 2014): it is not generally possible for bedload sediment to move fast enough through the entire proglacial forefield in a single diurnal discharge cycle, while particles transported in suspension are less affected by discharge fluctuation.

These findings have wider implications as subglacial sediment export estimates are used to parameterize subglacial erosion models (e.g. Herman et al., 2015). This requires that glaciers are effectively able to evacuate all the eroded sediment (Alley et al., 1997) and that

there is no lag between the export of sediment and where it is measured downstream. However, sediment transport monitoring stations (e.g. water intakes) are often located kilometers downstream of glacier termini (e.g. Herman et al., 2015). Further, these studies have tended to focus on suspended load erosion models and overlooked bedload, as the latter has been so difficult to measure.

### 6.1.2 Is it possible to predict water depth distribution in high turbid, shallow, mountain braided stream using basic planimetric information?

Chapter 3 proposes a new heuristic-based approach for determining the spatial distribution of riverbed elevations in turbid braided rivers, so dealing with the classic challenge of making DEMs of such rivers. The approach was heuristic in the sense that it was based upon quantifying basic relationships that we might expect to describe qualitatively in a river. For instance, we might expect a river to be deeper further away from the nearest river bank. We used five heuristic statements, each represented by a morphometric variable (i.e. distance from the nearest riverbank, total inundated width along a line tangential to the local flow direction, local curvature magnitude and direction, and distance from the nearest flow divergence and convergence regions) extracted from orthomosaics and inundation maps of the proglacial forefield using image processing techniques. These variables were parametrized into a multiple linear regression against samples of field-collected water depths measured at discrete river cross-sections using a stepwise approach. Tests on a subset of field-collected datasets showed that up to 60% of the spatial variability in water depths could be detected with elevation uncertainties comprised between ±0.045 m and ±0.09 m, which is 1.5 times the mean $D_{50}$ detected in the study area. These observations not only highlight the potential of this new method for predicting large scale spatial distribution of water depths, but also confer a high reliability to associated volumetric change estimates issued from DEMs of differencing maps combining both wet and dry regions. An important by-product was high resolution orthoimagery that could also be used to quantify river morphodynamics (e.g. changes in channel pattern). The data then allowed us to quantify the geomorphic response, erosion and deposition patterns, at daily frequency, to improve understanding of what drives the filtering processes reported in Chapter 2.

### 6.1.3 How do forefields geomorphologically responds to subglacial sediment export? And what are the implications for the longitudinal sediment connectivity?

Chapter 4 aimed to understand the relationship between the proglacial filtering described in Chapter 2 and the fluvial morphodynamics in the proglacial margin. The data associated with Chapter 3, notably the orthoimagery, were used: (i) to extract inundation maps at daily resolution and hence to describe the temporal evolution of proglacial stream statistics including total inundated area, braiding index and total number of bars and their morphology (area and perimeter)  (Roncoroni et al., 2023a); and (ii) to obtain grain-size distribution maps following calibration of a statistical model developed in Carbonneau et al. (2004, 2005) and Lane et al. (2020). These were combined with the DEM-derived information on morphological change described in Chapter 3.

The volumetric in-stream and out-of-stream geomorphic changes at the entire forefield scale (i.e. both dry and wet regions) compared well with the sediment budget quantifications issued in Chapter 2, so giving confidence in both the heuristic bathymetric method (Chapter 3) and the environmental seismology approach (Chapter 2). Results confirmed the role of the proglacial forefield as a sediment sink, storing large amounts of subglacially-exported sediments because of the filtering effect highlighted in Chapter 2. A closer investigation cross-

correlating the relationship between subglacial suspended sediment and bedload supply (S), stream transport capacity (C) determined applying a theoretical shear-stress based sediment transport model (Wilcock and Crow, 2003; Schneider et al., 2015; Rickenmann, 2020) and the proglacial stream dynamics found a strong influence of subglacial bedload evacuation rates on forefield configuration (Schuum, 1985; Germanoski and Schuum, 1993; Collins, 2008). In periods where S exceeded C, the proglacial forefield was characterized by a more complex configuration having higher inundated area, total number of bars and braiding indices with important amounts of subglacial bedload supply deposited in the proglacial margin. However, as soon as the glacier exhausted all available subglacial bedload stocks and C became more important than S, the forefield contracted into fewer channels and larger quantities of bedload sized particles were exported from the proglacial forefield system.

These results suggest that subglacial bedload rates drive bar construction processes in the proglacial margin, so defining the configuration of the proglacial stream, and hence the magnitude of proglacial filtering. Significant supply of subglacial bedload particles produces higher braiding indices and, consequently, flow divergence regions which are largely known to be depositional features (e.g. Ashmore, 1988; Ferguson and Ashworth, 1992; Karsprak et al., 2015). In contrast, in the absence of bedload supply and bar construction processes, the contraction of the floodplain produces hydraulically more efficient channels promoting erosion (Bertoldi et al., 2009; Egozi and Ashmore, 2009; Ganti et al., 2014). The first spatially-extensive repeat datasets of surficial grain-size maps showed that the surface grain-size distribution of the proglacial forefield also followed the S-C relationship, with coarsening in periods where C keeps up with S and fining when C takes over. However, in the last case, results also shows spatially isolated coarsening patterns coinciding with bar heads (i.e. flow divergence regions) highlighting the difficulties of the proglacial forefield in evacuating coarser particles out of the proglacial system (e.g. Powell, 1998; Kasprak et al., 2015). Taken together the above findings show that forefields effectively have the potential to disconnect the transfer of sediment from the glacier terminus to downstream regions as previously highlighted in Carrivick et al. (2018, 2019), but this effect strongly depends on upstream conditions (Lane et al., 1996; Collins, 2008). This last statement is verified under probabilistic scenarios involving different S, C and topographic forcings in Chapter 5.

The above findings will have important implications for the management of sediment in hydropower plants (e.g. Carrivick and Tweed, 2021; Li et al., 2021) and for the ecosystem stability in high mountain regions (e.g. Gabbud et al., 2019b; Miller and Lane, 2019; Roncoroni et al., 2023a). As glaciers retreat, the balance between subglacial bedload and melt-water supply will change (Li et al., 2021; Zhang et al., 2022, 2023). Smaller glaciers will become thinner resulting in lower subglacial erosion rates and, consequently, reduced bedload supply to proglacial margins (Herman et al., 2015; Cook et al., 2020). However, whether or not this translates into a systematic shift to transport capacity being greater than supply for Alpine glaciers will also depend on changes in glacial melt-water availability, which concurrently also tend to decline as glaciers get smaller (Huss and Hock, 2018; Zhang et al., 2022, 2023). If it does, glacier-supplied sediment may be first replaced by reworking of the braid plain, followed by a progressive decline as glaciers retreat combined with sediment sorting processes that make it progressively harder to release sediment. This will result in increasing geomorphic stability, promoting ecosystem development (e.g. Gurnell et al., 1999), and decreasing downstream sediment yields out of the proglacial system (Church and Ryder, 1972). This aspect is likely to generate an interesting debate in the near future concerning the management costs and the effective profitability of hydropower for the Swiss Energy Strategy 2050 (Pelto, 2011; Ehrbar et al., 2018; Farinotti et al., 2019; SCCER-SoE, 2019; Schaefli et al., 2019).

**6.1.4 How does the proglacial morphodynamic filter react to changing boundary (topographical, sedimentological and hydrological) conditions?**

Chapter 5 aimed to generalize the above findings to a wider set of topographical, sedimentological and hydrological settings (Section 1.5). This work uses the 2D hydromorphological numerical model eRiDynaS, developed and tested in Nicholas (2013a,b) and (Nicholas et al., 2013). The model was calibrated and validated against field-collected data in terms of sediment transport and budgeting dynamics over time for both suspended sediment and bedload, as well as looking at the forefield morphodynamic metrics, to reproduce the observed real-world fluvial behavior (Chapter 2 and 4). Once done, it allowed investigation of the geomorphic responses and the implications for downstream sediment transport in proglacial margins under changing boundary conditions. Four scenarios were addressed: (i) proglacial forefields characterized by a steeper valley bottom slope having both wider and longer accommodation space, (ii) increased transport capacity (C), (iii) reduced subglacial sediment supply (S), and (iv) a time-varying C-S ratio.

The results showed that active proglacial margins effectively buffer the longitudinal sediment connectivity between the glaciers and the downstream regions, with a magnitude that is controlled by the S to C ratio, confirming the hypothesis of Collins (2008) and the field measurements in Chapter 4. Where S was higher than C, more intense morphodynamic activity developed, resulting in increased braiding intensity and smaller mid-channel bars (Nicholas et al., 1995; Lane et al., 1996). This fluvial configuration reduced the downstream flux of subglacially-evacuated bedload particles because the numerous flow divergence regions became regions of flow velocity reduction further promoting the deposition of the coarse particle sediment sizes (Kaspark et al., 2015; Antoniazza et al., 2019). These fluvial features decreased the advection lengths associated with bedload transport such that the proglacial forefield became aggradational (Jerolmack and Paola, 2010; Ganti et al., 2014). However, where C kept up with or even exceeded S, the opposite occurred with the development of a hydrologically more efficient proglacial stream with the flow confined to fewer channels. This change in fluvial pattern converts the proglacial forefield into a sediment source maintaining a high longitudinal sediment connectivity between glaciers and downstream regions for two inter-related reasons (Ganti et al., 2014). First, both subglacially-exported bedload and suspended sediment are more easily transferred out of the proglacial margin system because of the lower number of bars buffering their downstream transfer (Kaspark et al., 2015; Antoniazza et al., 2019). Second, the hydraulic efficiency promotes the vertical incision of the proglacial stream in the floodplain reworking and re-mobilizing large amounts of previously deposited sediments (Germanowski and Schumm, 1993; Marren, 2002; Roussel et al., 2018). Fine sediments are less impacted by the morphodynamic intensity, and the consequent fluvial patterns associated with the changing balance between S and C. In both cases, compared to coarser particles, they are more rapidly evacuated out of the proglacial margin with relatively small effects on the sediment budget.

Simulations involving different forefield topographic forcings (i.e. floodplain length, width and slope) also showed the important of non-fluvial and non-glaciological constraints on the longitudinal sediment connectivity of proglacial margins. Flatter and larger proglacial forefields are likely to develop more active proglacial braided steams resulting, as already mentioned above, in floodplain aggradation. However, the opposite situation occurs if the outwash plain in front of the retreating glacier is characterized by a steeper valley bottom as the proglacial stream develops into fewer channels having higher hydraulic efficiency promoting the downstream transport of sediment.

These observations allow inference of the consequences of longitudinal sediment connectivity in proglacial margins following the onset of glacier recession, as it is the size of glaciers which will determine the subglacial erosion rates and the total amounts of meltwater delivered to proglacial streams (Herman et al., 2015; Cook et al., 2020). In the near future, and already in present-day conditions for certain smaller and lower-altitude glaciers, a decrease in the glacier meltwater rates (i.e. "peak water") followed by a decrease in the total amount of evacuated sediments (i.e. "peak sediment") (Zhang et al., 2022). Thus, over a short temporal scale from now, S is likely to become progressively higher than C for a period determined by the ability of the glacier to erode its own bed and by laterally-source sediment delivery to the outwash plain, such as from permafrost degradation and reworking of unconsolidated morainic deposits (Lane et al., 2017). Under those conditions the downstream delivery rates from proglacial margin is expected to increase, but the high braiding intensity of proglacial forefields will compensate for the increasing amounts of subglacially-exported sediments which can potentially leave the system (Kaspark et al., 2015; Antoniazza et al., 2019). This effect would also be amplified by the increasing spatial extent of proglacial margins and increasing space available for morphodynamic processes.

However, over longer timescales, even if the proglacial margin will increase in area, if S cannot keep up with C a chain of effects may result leading to establishment of better longitudinal connectivity. Decreasing subglacial sediment export rates will lead to reduced morphodynamic activity of proglacial streams, enhanced sediment fluxes towards downstream regions and increased biogeomorphic stability as the riverbed incision will be concentrated in specific areas (Schumm, 1985; Germanoski and Schumm, 1993; Miller and Lane, 2019; Roncoroni et al., 2023a). Therefore, terrace systems will appear in the proglacial floodplain promoting channelization, lower proglacial filtering magnitude and enhanced downstream sediment delivery rates (Germanowski and Schumm, 1993; Marren, 2002; Roussel et al., 2018). Whether or not this stability extends into biogeomorphic succession is not yet established; but vertical incision likely also causes water table drawdown which has been shown to restrict embryonic vegetation succession in this kind of environment (Roncoroni et al., 2023a).

These results are important for hydropower. For example, the Swiss Energy Strategy 2050 aims increase the to increase energy production from hydropower to compensate the progressive de-activation of nuclear power plants (Martinez-Jaramillo et al., 2023). An increase of the downstream sediment transport from both subglacial and proglacial systems may generate a surplus of sediment reaching the infrastructures for hydropower production, such as water intakes and dams, exceeding the sediment retention capacity for which they were originally designed for (Milner et al., 2017). Under this scenario, hydropower companies will need to rethink their infrastructures and sediment management strategies to secure future energy production.

## 6.2 Limitations and perspectives

The thesis addressed three inter-related research questions (Chapters 2 to 5) justified by a detailed literature review given in Chapter 1. Their answers provided important findings for better understanding the relationship between glacier retreat and proglacial forefields, as well as the implications for the downstream transport of subglacially-exported sediments, in the actual context of rapid deglaciation. However, the research has limitations that are discussed here.

The quantifications of bedload flux (Chapter 2), used in Chapters 4 and 5, used a geophysical inversion model to convert continuous seismic records into transport rates. However, to date, there has been no systematic study addressing the lower limit of bedload grain size detection by out-of-stream geophones, as has been done for other measurement sensors. For example, in-stream Swiss plate geophones have an approximate lower detection threshold of ca. 20 mm (Rickenmann et al., 2013). This questions the extent to which the partitioning between suspended and bedload is clear; it is possible that the total transport rates are under-estimated if there is a sediment size missing from either method; or over-estimated if there is a sediment size included both. Whether it is a gap or an overlap likely depends on turbulence intensity, as a control on both suspension and the noise associated with particle interactions, and hence on discharge. In a system with such strong diurnal discharge fluctuations (Chapter 2), this is likely a serious question for further research. Additionally, the Fluvial Model Inversion (FMI) of Dietze et al. (2019a) is built around 15 variables describing the topographical, sedimentological and seismic ground proprieties of the study area. These parameters use fixed values, but it is possible that these can vary over time in long surveys, such as entire melt seasons. As explained in the supplementary information of Chapter 2, the stream width, the $D_{50}$ of the transported sediments and the parameter values for parameters describing the seismic ground proprieties have been measured only once in the field. However, it is known that both the stream width and the transported grain sizes depend on the instantaneous discharge rates (e.g. Leopold and Maddock, 1953; Turowski et al., 2011), while atmospheric conditions can change soil proprieties modifying, in turn, the interactions (i.e. propagation speed and magnitude attenuation) between the medium and the seismic waves (e.g. Whang and Hao, 2002). Whilst some of these challenges were addressed by choosing stable cross-sections, under- and over-underestimations may propagate into bedload flux quantifications.

Consequently, to improve the reliability of the inversion method it would be necessary to conduct further studies on the effective sensitivity of geophones to bedload particle sizes. This could be achieved through controlled laboratory experiments, as already been done for acoustic methods such as Japanese pipes (e.g. Mizuyama et al., 2010) and Swiss plate geophones (e.g. Wyss et al., 2016), and include the temporal variability of the above-mentioned parameter values. However, this may be difficult to implement for two technical reasons. On the one hand, the continuous sampling of the data needed to quantify these parameter values can be challenging, demanding of post-processing techniques and independent validation datasets. On the other hand, including temporal variable values in the geophysical inversion models would add further complexity to already complex physical models. That said, it should be emphasized that uncertainties in bedload transport rates in predictive models extend across 5 or more orders of magnitude (Antoniazza et al., 2020, 2022), but differences between geophones and seismic methods extend across only 1 order of magnitude. Further, here, we were able to reconcile two different approaches to bedload transport estimation, morphological based on DEMs of difference, and seismically estimates (see below). This suggests that at least at present, the seisimic approach is very valuable.

To improve the overall quality of the study and to better reveal the dynamics of bedload transport in proglacial environments, two interesting methods could be deployed: the distributed acoustic sensing and particle tracking. Unlike more traditional systems such as geophones, that rely on spatially discrete measuring at specific sites, DAS uses optical fibre cables composed so providing multiple seismometers for detecting acoustic signals over long distances (Daley et al., 2016; Lindsey et al., 2017). This method has already been used for detecting micro-seismicity events in glacial environments (e.g. Walter et al., 2020), groundwater hydrology dynamics (e.g. Tribaldos and Ajo-Franklin, 2021), permafrost thaw

(e.g. Dou et al., 2017), subsurface geologic proprieties in terrestrial (e.g. Piana Agostinetti et al., 2022) and underwater environments (e.g. Lior et al., 2021), and earthquake monitoring and localization (e.g. Lentas et al., 2023). The cable could be installed along the length of an entire proglacial forefield to produce continuous bedload transport rates in both space and time, and then combined with discharge data to investigate transport dynamics as the water wave propagates downstream. Particle tracking consists in passive integrated transponders (PIT tags), active radio frequency identificator (RFID), and GPS systems, installed in gravel or pebble sediments, sometimes also embedded with motion and accelerometer sensors, to follow sediment paths in fluvial systems (McNamara and Borden, 2004; Olinde and Johnson, 2015; Liébault et al., 2023). This technique was traditionally used in fisheries and ornithology studies for understanding animal behaviors, habitats and migrations (e.g. Bonter and Bridge, 2011; Richer et al., 2017; Liébault et al., 2023). In fluvial geomorphology, this technique has been already applied for the investigation of bedload particle transport distance in relation to particle size (e.g. Dell'Agnese et al., 2015; Mao et al., 2020; Rainato et al., 2018, 2020) and discharge (e.g. Arnaud et al., 2017; Gilet et al., 2020), for the effects of morphological conditions on particle mobility (e.g. Lamarre and Roy, 2008; Mao et al., 2020; McQueen et al., 2021) and for determining the incipient motion for bedload transport (e.g. Petit et al., 2015). Currently, survey methods are normally ground-based using mobile or fixed antennas, but their installation on new airborne technologies such as UAV (Cassel et al., 2020) opened the way to the way to large scale and high-frequency detections (Liébault et al., 2023). The adoption of this tool, combined with UAV surveys for detection and quantification of surficial erosion and deposition patterns, in proglacial forefield studies can drastically enhance the comprehension of the relationship between morphodynamic processes and downstream sediment transport. It may also be possible to conduct coupled glacier-proglacial margin transfers. Jenkin et al. (2023) recently injected tagged particles into the subglacial channels via drilled boreholes and were able to track them under the ice. A very interesting experiment would be then to track them through the proglacial margin.

In Chapter 4, the influence of morphodynamics process in filtering the subglacial sediment export signal was investigated by combining continuous sediment transport monitoring with spatial information on the proglacial stream configuration at low flow conditions collected at discrete time periods. To better investigate this relationship, it would be interesting to increase the frequency of quantification to include high flow conditions. However, this would require a drastic change in the strategy for collecting topographical information because, as already highlighted in Chapter 4, the use of the quadcopter DJI Phantom 4 Pro for covering extended areas as proglacial forefield is extremely time consuming. The use of satellite imagery is not suitable as the spatial resolution is too coarse, but fixed-wing UAV platforms (for example SenseFly eBee, Wingtra and BirdsEyeView Firefly6) could provide a good alternative to obtain both high resolution and large spatial scale data with lower survey times (Garg et al., 2022). The reduction of survey time should also help to avoid the effects of changes in discharge and light conditions during data acquisition. Such data acquisition platforms have already been used in disciplines for ecological (e.g. Anderson and Gaston, 2013), glaciological (e.g. Huss et al., 2018) and fluvial geomorphological studies in Alpine (e.g. Seier et al., 2017; Hemmelder et al., 2018), Arctic (e.g. Dømgaard et al., 2023) and coastal (e.g. Brunier et al., 2016) environments. The only weakness of these instruments, unlike the quadcopter rotor-wing ones, is the higher sensitivity to wind-induced turbulence which may reduce image quality (Beard et al., 2014). Additionally, depending on the UAV platform, there is the need for a flat, clear-of-obstacle landing strip, which can be hard to find in high mountain regions.

The differences in volumetric changes from continuous seismically-estimated sediment budget data and discrete surficial geomorphic changes from DEMs showed a similar temporal evolution, and the differences in magnitude were encouragingly small as compared, for example, with errors in predictive models of bedload transport (Antoniazza et al., 2022). However, quantifications obtained using seismometry were generally higher than those issued with the second one. This discrepancy may arise from two source of errors in the bathymetric method: the difficulty of estimating erosion and deposition with the limits of detection associated with inundated areas and the small proportion of water depth spatial variability (50-60% of the total variance) explained by the bathymetric model. In this latter case, as explained in Chapter 3, the reason may be related to the insufficient total number of water depth measurements used to calibrate the model, or to the need of adding more planimetric information as explanatory variables. This work cannot conclusively say whether there is an over-estimation of seismically-measured transport rates or an under-estimate of morphologically-estimated channel changes, or some combination of the two.

Despite these weaknesses, water depth maps obtained through the application of the bathymetric model developed in Chapter 3 are not only limited to topographic change quantification over time. Future studies could use model outputs for investigating the spatially proprieties of hydraulic parameters in natural stream channels. For example, by knowing the spatial distribution of both riverbed slope and water depth it is possible to apply resistance equation to reveal the spatial distribution of shear stress magnitude, or even use DEM of dry and wet regions as initial boundary condition in hydromorphodynamic models.

The last limitations of the thesis concern the numerical model used in Chapter 5 to generalize the results to forefields constraint by different boundary conditions. The *eRiDynaS* model has been proven to reliably reproduce the behavior of both braiding and meandering mega river systems in tropical and sub-tropical environments (Nicholas, 2013a,b; Nicholas et al., 2013). For the purpose of the thesis, it was deployed for the first time in high-altitude settings where other non-fluvial variables not considered in the model can influence both stream morphodynamics and sediment transport. This is especially the case for buried ice patches in the proglacial margin, which may significantly impact the development of the braided stream network limiting lateral erosion and promoting vertical incision (e.g. Hambrey, 1984; Hauer and Pulg, 2021). Consequently, the ground-ice effects on stream patterns are also not reproduced in the numerical simulations. The reason why it has not been included in the model is the limited knowledge of the conditions needed for its presence and its interactions with the hydraulic proprieties. Future studies could focus on the evolution of proglacial morphodynamic filtering over longer temporal scales (i.e. decades). In this case, the numerical model must be revised to take into account four temporal variations in boundary conditions.

First, the dimension of the model domain, especially in the longitudinal x-axis, has to increase over time to take into account glacier retreat. Rates of available space increase have to be based on long term datasets, such as historical aerial images and field records (e.g. Gardent et al., 2014; Diolaiuti et al., 2011; Lane et al., 2017; Freudiger et al., 2018; Mancini and Lane, 2020), or predictions to different climatic scenarios (e.g. Jouvet and Huss, 2019).

Second, as it is now well established, decreasing glacier size influence the balance between subglacial meltwater and sediment export rates (Huss and Hock, 2018; Zhang et al., 2022, 2023). To have a valuable temporal representation of the influence of morphodynamics processes on the longitudinal sediment connectivity during forefield development, it is important that the inlet conditions are able to reproduce the variability of these two variables. The same apply to the lateral supply of sediment coming from valley-sidewalls after

deglaciation which decrease over time (Church and Ryder, 1972; Warburton, 1990). These two aspects are relatively easy to implement in a numerical model, but their calibration may be very challenging because of the lack of long-term quantitative datasets (Lane et al., 2017).

Third, depending on the temporal scale of interest, vegetation colonization is another important variable to consider as roots may increase soil resistance to fluvial erosion slowing down morphodynamic activity (Gurnell et al., 1999; Collins et al., 2004; Miller and Lane, 2019).

Finally, with ongoing deglaciation, glacier-bed overdeepenings may play an important role in filtering the longitudinal connectivity between glacial and proglacial fluvial environments, significantly affecting the geomorphic response of proglacial forefields in regards of the sediment budget (Swift et al., 2021).

The implementation of all the above mentioned features into a single glacio-hydro-morpho-eco numerical model to accurately represent the complexity of degrading glacierized catchments is challenging, and highly dependent on the tradeoff between computational resources (i.e. processing time, infrastructures,…) and associated costs.

# Chapter 7: Conclusions

This thesis aimed to determine the influence of proglacial forefield morphodynamics on the longitudinal flux of sediments exported subglacially from Alpine glaciers. The studies presented in the thesis were based on a specific study area (Chapters 2 to 4), which permitted the generation of spatially-extensive and temporally-continuous datasets on both sediment transport flux and proglacial forefield morphodynamics over two glacier melt seasons. The findings were generalized using a numerical model (Chapter 5) calibrated and validated on the basis of field-collected data. A number of key conclusions emerged.

The retreat of Alpine glaciers promotes the extension of proglacial margins. These are generally characterized by the development of active braided streams. This work showed that these can act as sediment sinks but also which, through their morphodynamics, buffer and delay the downstream transport of subglacially-evacuated bedload sediment. This happens at a sub-daily timescale, whilst finer material is less impeded by the forefield. The main mechanism responsible for this effect is the combination of a high braiding intensity, where zones of flow divergence reduce the efficiency of longitudinal transfer by the proglacial stream, and the high daily discharge variation. These two processes interact to reduce the advection length of coarser particles. Consequently, bedload-sized particles need multiple reworking events before in order to be evacuated from the proglacial margin system.

This generic process was shown to be strongly impacted by the subglacial discharge, as a control on sediment transport capacity, and sediment supply conditions due to their influence on proglacial stream morphology and notably braiding intensity. Changes in their ratio have repercussion for the sediment flux dynamics through the proglacial forefield. Periods where subglacial sediment supply is higher than transport capacity are associated with increasing braiding intensity and higher rates of aggradation; when supply is lower than capacity, river flow becomes confined into fewer channels with enhanced erosion rates and net export of reworked material out of the proglacial margin system. These observations specifically showed the central role of forefield bar construction processes and flow divergence regions for the buffering of the longitudinal connectivity between glacier snouts and downstream regions; and that this is autogenically-influenced, that is the conditions that lead to aggradation further encourage aggradation.

The generalization of these findings was investigated by using numerical simulation to assess how proglacial filtering effects might vary between Alpine catchments according to their hydrological and geomorphological settings. Simulations confirmed the importance of the subglacial boundary conditions (discharge, sediment supply rate) in determining both geomorphic and morphodynamic response of the proglacial margin, and consequently on its longitudinal sediment connectivity. However, the magnitude of the proglacial filtering was shown to be influenced by the topography of the newly-deglaciated terrain in proglacial margins, with stronger buffering in systems with wider and flatter valley bottoms.

This research contributed to a broader understanding of proglacial margin responses to deglaciation in terms of both geomorphic evolution and sediment transport dynamics. At the same time, it opened up new research questions that have to be addressed to better predict the future sediment transport dynamics in Alpine regions following glacier retreat. These include the effects of retreating glacier size and water availability, the expected increase of both extreme precipitation events and the changing importance non-glacial source of sediments such as permafrost thaw due to climate warming, as well as feedbacks of

progressive vegetation colonization, on the proglacial morphodynamic filtering magnitude of downstream transported sediments. The consideration of these aspects will help improve the prediction of sediment flux dynamics in proglacial margins, a knowledge necessary to prepare measures for mitigating hydrological hazards in high mountain regions and to ensure profitable hydropower production in the actual context of rapid deglaciation.

# References

Abbott, J. E., Francis, J. R. D., & Owen, P. R. (1997). Saltation and suspension trajectories of solid grains in a water stream. *Philosophical Transactions of the Royal Society of London. Series A, Mathematical and Physical Sciences*, *284*(1321), 225–254. https://doi.org/10.1098/rsta.1977.0009.

Adams, J. (1979). Gravel size analysis from photographs. *Journal of the Hydraulics Division*, 105(10), 1247-1255.

Aki, K., & Richards, P. G. (2002). *Quantitative Seismology*. University Science Book.

Alley, R. B., Cuffey, K. M., Evenson, E. B., Strasser, J. C., Lawson, D. E., & Larson, G. J. (1997). How glaciers entrain and transport basal sediment: Physical constraints. *Quaternary Science Reviews*, *16*(9), 1017–1038. https://doi.org/10.1016/S0277-3791(97)00034-6.

Almeida, T. G., Walker, D. T., & Warnock, A. M. (2017). Estimating River Bathymetry from Surface Velocity Observations Using Variational Inverse Modeling. *Journal of Atmospheric and Oceanic Technology*, *35*(1), 21–34. https://doi.org/10.1175/JTECH-D-17-0075.1.

Amundson, J. M., & Iverson, N. R. (2006). Testing a glacial erosion rule using hang heights of hanging valleys, Jasper National Park, Alberta, Canada. *Journal of Geophysical Research: Earth Surface*, *111*(F1). https://doi.org/10.1029/2005JF000359.

Anderson, K., & Gaston, K. J. (2013). Lightweight unmanned aerial vehicles will revolutionize spatial ecology. *Frontiers in Ecology and the Environment*, *11*(3), 138–146. https://doi.org/10.1890/120150.

Anderson, S.W. (2019). Uncertainty in quantitative analyses of topographic change: error propagation and the role of thresholding. *Earth Surface Processes and Landforms*, 44(5), 1015-1033. https://doi.org/10.1002/esp.4551.

Antoniazza, G., Bakker, M., & Lane, S. N. (2019). Revisiting the morphological method in two-dimensions to quantify bed-material transport in braided rivers. *Earth Surface Processes and Landforms*, *44*(11), 2251–2267. https://doi.org/10.1002/esp.4633.

Antoniazza, G., Nicollier, T., Wyss, C. R., Boss, S., & Rickenmann, D. (2020). Bedload Transport Monitoring in Alpine Rivers: Variability in Swiss Plate Geophone Response. *Sensors*, *20*(15), Article 15. https://doi.org/10.3390/s20154089.

Antoniazza, G., Nicollier, T., Boss, S., Mettra, F., Badoux, A., Schaefli, B., Rickenmann, D., & Lane, S. N. (2022). Hydrological Drivers of Bedload Transport in an Alpine Watershed. *Water Resources Research*, *58*(3), e2021WR030663. https://doi.org/10.1029/2021WR030663.

Antoniazza, G., Mancini, D., Rieckmann, D., Nicollier, T., Boss, S., Turowski, J.M., Dietze, M. & Lane, S.N. (2023). Anatomy of a bedload transport event: an Alpine watershed-scale seismic-array monitoring. *Journal of Geophysical Research: Earth Surface*, 128, 22022JF007000. https://doi.org/10.1029/2022JF007000.

Arnaud, F., Piégay, H., Béal, D., Collery, P., Vaudor, L., & Rollet, A.-J. (2017). Monitoring gravel augmentation in a large regulated river and implications for process-based restoration. *Earth Surface Processes and Landforms*, *42*(13), 2147–2166. https://doi.org/10.1002/esp.4161.

Ashmore, P. E. (1982). Laboratory modelling of gravel braided stream morphology. Earth Surface Processes and Landforms, 7(3), 201–225. https://doi.org/10.1002/esp.3290070301.

Ashmore, P., & Parker, G. (1983). Confluence scour in coarse braided streams. *Water Resources Research*, *19*(2), 392–402. https://doi.org/10.1029/WR019i002p00392.

Ashmore, P. E. (1988). Bed load transport in braided gravel-bed stream models. *Earth Surface Processes and Landforms*, *13*(8), 677–695. https://doi.org/10.1002/esp.3290130803.

Ashmore, P. (1991a). Channel Morphology and Bed Load Pulses in Braided, Gravel-Bed Streams. *Geografiska Annaler. Series A, Physical Geography*, *73*(1), 37–52. https://doi.org/10.2307/521212.

Ashmore, P. (1991b). How do gravel-bed rivers braid? *Canadian Journal of Earth Sciences*, *28*(3), 326–341. https://doi.org/10.1139/e91-030.

Ashmore, P.E., Ferguson, R.I., Prestergaad, K.L., Ashworth, P.J. & Paola, C. (1992). Secondary flow in anabranch confluences of a braided, gravel-bed stream. *Earth Surface Processes and Landforms*, 17, 299-311. https://doi.org/10.1002/esp.3290170308.

Ashmore, P., Bertoldi, W. & Gardner, J.T. (2011). Active width of gravel-bed braided rivers. *Earth Surface Processes and Landforms*, 36(1), 1510-1521. https://doi.org/10.1002/esp.2182.

Ashmore, P. (2013). 9.17 Morphology and Dynamics of Braided Rivers. In J. F. Shroder (Ed.), *Treatise on Geomorphology* (pp. 289–312). Academic Press. https://doi.org/10.1016/B978-0-12-374739-6.00242-6.

Ashworth, P. J., & Ferguson, R. (1989). Size-selective entrainment of bed load in gravel bed streams. *Water Resources Research*, *25*, 627–634. https://doi.org/10.1029/WR025I004P00627.

Ashworth, P. J. (1996). Mid-Channel Bar Growth and Its Relationship to Local Flow Strength and Direction. *Earth Surface Processes and Landforms*, *21*(2), 103–123. https://doi.org/10.1002/(SICI)1096-9837(199602)21:2<103::AID-ESP569>3.0.CO;2-O.

Asselman, N. E. M., & Middelkoop, H. (1995). Floodplain sedimentation: Quantities, patterns and processes. *Earth Surface Processes and Landforms*, 20(6), 481-499. https://doi.org/10.1002/esp.3290200602.

Auer, I., Böhm, R., Jurkovic, A., Lipa, W., Orlik, A., Potzmann, R., Schöner, W., Ungersböck, M., Matulla, C., Briffa, K., Jones, P., Efthymiadis, D., Brunetti, M., Nanni, T., Maugeri, M., Mercalli, L., Mestre, O., Moisselin, J.-M., Begert, M., … Nieplova, E. (2007). HISTALP—historical instrumental climatological surface time series of the Greater Alpine Region. *International Journal of Climatology*, *27*(1), 17–46. https://doi.org/10.1002/joc.1377.

Aureli, F., Maranzoni, A., Mignosa, P. & Ziveri, C. (2008). A weighted surface-depth gradient method for the numerical integration of the 2D shallow water equations with topography, *Advances in Water Resources*, Vol 31, 962–974.

Baewert, H., & Morche, D. (2014). Coarse sediment dynamics in a proglacial fluvial system (Fagge River, Tyrol). *Geomorphology*, *218*, 88–97. https://doi.org/10.1016/j.geomorph.2013.10.021.

Bagnold, R. A. (1997). The nature of saltation and of 'bed-load' transport in water. *Proceedings of the Royal Society of London. A. Mathematical and Physical Sciences*, *332*(1591), 473–504. https://doi.org/10.1098/rspa.1973.0038.

Bakker, M., & Lane, S. N. (2017). Archival photogrammetric analysis of river–floodplain systems using Structure from Motion (SfM) methods. *Earth Surface Processes and Landforms*, *42*(8), 1274–1286. https://doi.org/10.1002/esp.4085.

Bakker, M., Antoniazza, G., Odermatt, E., & Lane, S. N. (2019). Morphological Response of an Alpine Braided Reach to Sediment-Laden Flow Events. *Journal of Geophysical Research: Earth Surface*, *124*(5), 1310–1328. https://doi.org/10.1029/2018JF004811.

Bakker, M., Gimbert, F., Geay, T., Misset, C., Zanker, S., & Recking, A. (2020). Field Application and Validation of a Seismic Bedload Transport Model. *Journal of Geophysical Research: Earth Surface*, *125*(5), e2019JF005416. https://doi.org/10.1029/2019JF005416.

Ballantyne, C. K. (2002). A general model of paraglacial landscape response. *The Holocene*, *12*(3), 371–376. https://doi.org/10.1191/0959683602hl553fa.

Bangen, S. G., Wheaton, J. M., Bouwes, N., Bouwes, B., & Jordan, C. (2014). A methodological intercomparison of topographic survey techniques for characterizing wadeable streams and rivers. *Geomorphology*, 206, 343–361. https://doi.org/10.1016/j.geomorph.2013.10.10.

Bangen, S., Hensleigh, J., McHugh, P., & Wheaton, J. (2016). Error modeling of DEMs from topographic surveys of rivers using fuzzy inference systems. *Water Resources Research*, 52(2), 1176–1193. https://doi.org/10.1002/2015WR018299.

Baptist, M.J., Babovic, V., Rodriguez Uthubrubu, J., Keijzer, M., Uittenbogaadr, R.E., Mynett, A. & Verwey, A. (2007). On inducing equations for vegetation resistance, *Journal of Hydraulic Research*,Vol 45, pp. 435-450.

Bates, P.D., Horritt, M.S. & Fewtrell, T.J. (2010). A simple inertial formulation of the shallow water equations for efficient two dimensional flood inundation modelling, *Journal of Hydrology*, Vol 387. https://doi.org/10.1016/j.jhydrol.2010.03.027.

Beard, R. W., Ferrin, J., & Humpherys, J. (2014). Fixed Wing UAV Path Following in Wind With Input Constraints. *IEEE Transactions on Control Systems Technology*, 22(6), 2103–2117. https://doi.org/10.1109/TCST.2014.2303787.

Beaton, A. E., & Tukey, J. W. (1974). The Fitting of Power Series, Meaning Polynomials, Illustrated on Band-Spectroscopic Data. *Technometrics*, *16*(2), 147–185. https://doi.org/10.2307/1267936.

Beaud, F., Flowers, G. E., & Venditti, J. G. (2016). Efficacy of bedrock erosion by subglacial water flow. *Earth Surface Dynamics*, *4*(1), 125–145. https://doi.org/10.5194/esurf-4-125-2016.

Beaud, F., Flowers, G. E., & Venditti, J. G. (2018a). Modeling Sediment Transport in Ice-Walled Subglacial Channels and Its Implications for Esker Formation and Proglacial Sediment Yields. *Journal of Geophysical Research: Earth Surface*, *123*(12), 3206–3227. https://doi.org/10.1029/2018JF004779.

Beaud, F., Venditti, J. G., Flowers, G. E., & Koppes, M. (2018b). Excavation of subglacial bedrock channels by seasonal meltwater flow. *Earth Surface Processes and Landforms*, *43*(9), 1960–1972. https://doi.org/10.1002/esp.4367.

Beven, K. & Binley, A. (1992). The future of distributed models: Model calibration and uncertainty prediction. *Hydrological Processes*, 6(3), 279–298. https://doi.org/10.1002/hyp.3360060305.

Beven, K. & Binley, A. (2014). GLUE: 20 years on. Hydrological Processes, 28(24), 5897-5918. https://doi.org/10.1002/hyp.10082.

Beawert, H. & Morche, D. (2014). Coarse sediment dynamics in a proglacial fluvial system (Fagge River, Tyrol). *Geomorphology*, 218, 88.97. https://doi.org/10.1016/j.geomorph.2013.10.021.

Beerbower, J. R. (1964). Cyclothems and Cyclic Depositional Mechanisms in Alluvial Plain Sedimentation. *Kansas Geological Survey Bulletin*, *169*, 31–32.

Begin, Z.B. (1981). Stream Curvature and Bank Erosion: A Model Based on the Momentum Equation. *The Journal of Geology*, 89(4), 497-504.

Benn, D. I., & Evans, D. J. A. (2010). *Glaciers and Glaciation*. Hodder Education.

Bertoldi, W., Ashmore, P., & Tubino, M. (2009). A method for estimating the mean bed load flux in braided rivers. *Geomorphology*, 103(3), 330-340. https://doi.org/10.1016/j.geomorph.2008.06.014.

Best, J. L., & Reid, I. (1984). Separation Zone at Open-Channel Junctions. *Journal of Hydraulic Engineering*, 110(11), 1588-1594. https://doi.org/10.1061/(ASCE)0733-9429(1984)110:11(1588).

Best, J. L. (1988). Sediment transport and bed morphology at river channel confluences. *Sedimentology*, 35(3), 481–498. https://doi.org/10.1111/j.1365-3091.1988.tb00999.x.

Beven, K., & Binley, A. (1992). The future of distributed models: Model calibration and uncertainty prediction. *Hydrological Processes*, *6*(3), 279–298. https://doi.org/10.1002/hyp.3360060305.

Beven, K., & Binley, A. (2014). GLUE: 20 years on. *Hydrological Processes*, *28*(24), 5897–5918. https://doi.org/10.1002/hyp.10082.

Beylich, A. A., Laute, K., Liermann, S., Hansen, L., Burki, V., Vatne, G., Fredin, O., Gintz, D., & Berthling, I. (2009). Subrecent sediment dynamics and sediment budget of the braided sandur system at Sandane, Erdalen (Nordfjord, Western Norway). *Norsk*

*Geografisk Tidsskrift - Norwegian Journal of Geography*, *63*(2), 123–131. https://doi.org/10.1080/00291950902907934.

Bezinge, A., Clark, M.J., Gurnell, A.M. & Warburton, J. (1989). The management of sediment transported by glacial melt-water streams and its significance for the estimation of sediment yield. *Annals of Glaciology*, 13.

Bluck, B. J. (1982). Texture of gravel bars in braided streams. In Hey, R.D., Bathurst, J.C. & Thorne, C.R. (Eds.), *Gravel bed rivers: Fluvial processes, engineering and management* (pp. 339–355). Wiley.

Bogen, J., Xu, M., & Kennie, P. (2015). The impact of pro-glacial lakes on downstream sediment delivery in Norway. *Earth Surface Processes and Landforms*, *40*(7), 942–952. https://doi.org/10.1002/esp.3669.

Bonter, D. N., & Bridge, E. S. (2011). Applications of radio frequency identification (RFID) in ornithological research: A review. *Journal of Field Ornithology*, *82*(1), 1–10. https://doi.org/10.1111/j.1557-9263.2010.00302.x.

Boothroyd, J. C., & Ashley, J. M. (1975). Process, bar morphology and sedimentary structure on braided outwash fans, northwestern Gulf of Alaska. In Jopling, V.A & MacDonald, B. (Eds.), *Glaciofluvial and glaciolacustrine sedimentation*, 193–222. SEPM Publication.

Bosson, J.-B., Deline, P., Bodin, X., Schoeneich, P., Baron, L., Gardent, M., & Lambiel, C. (2015). The influence of ground ice distribution on geomorphic dynamics since the Little Ice Age in proglacial areas of two cirque glacier systems. *Earth Surface Processes and Landforms*, *40*(5), 666–680. https://doi.org/10.1002/esp.3666.

Brasington, J., Rumsby, B. T., & McVey, R. A. (2000). Monitoring and modelling morphological change in a braided gravel-bed river using high resolution GPS-based survey. *Earth Surface Processes and Landforms*, *25*(9), 973–990. https://doi.org/10.1002/1096-9837(200008)25:9<973::AID-ESP111>3.0.CO;2-Y.

Brasington, J., Langham, J., & Rumsby, B. (2003). Methodological sensitivity of morphometric estimates of coarse fluvial sediment transport. *Geomorphology*, *53*(3), 299–316. https://doi.org/10.1016/S0169-555X(02)00320-3.

Brasington, J., Vericat, D. & Rychkov, I. (2012). Modeling river bed morphology, roughness, and surface sedimentology using high resolution terrestrial laser scanning. *Water Resources Research*, 48, W11519. https://doi.org/10.1029/2012WR012223.

Breaux, H. J. (1967). *On stepwise multiple linear regression (Report No. 1369)*. U.S. Army Material Command, Ballistic Research Laboratories.

Brice, J. C. (1975). *Airphoto interpretation of the form and behavior of alluvial rivers* (ADA008108). U.S. Army Research Office, Washington University, St. Louis.

Bridge, J. S., & Gabel, S. L. (1992). Flow and sediment dynamics in a low sinuosity, braided river: Calamus River, Nebraska Sandhills. *Sedimentology*, *39*(1), 125–142. https://doi.org/10.1111/j.1365-3091.1992.tb01026.x.

Bristow, C. S., & Best, J. L. (1993). Braided rivers: Perspectives and problems. *Geological Society, London, Special Publications*, 75(1), 1–11. https://doi.org/10.1144/GSL.SP.1993.075.01.01.

Brunier, G., Fleury, J., Anthony, E. J., Pothin, V., Vella, C., Dussouillez, P., Gardel, A., & Michaud, E. (2016). Structure-from-Motion photogrammetry for high-resolution coastal and fluvial geomorphic surveys. *Géomorphologie : Relief, Processus, Environnement*, *22*(2), Article 2. https://doi.org/10.4000/geomorphologie.11358.

Bunte, K., Abt, S. R., Potyondy, J. P., & Swingle, K. W. (2008). A Comparison of Coarse Bedload Transport Measured with Bedload Traps and Helley-Smith Samplers. *Geodinamica Acta*, *21*(1–2), 53–66. https://doi.org/10.3166/ga.21.53-66.

Burri, M., Allimann, M., Chessex, R., Dal Piaz, G. V., Delle Valle, G., Du Bois, L., Gouffon, Y., Guermani, A., Hagen, T., Krummenacher, D., & Looser, M.-O. (1998). *Feuille 101, Chanrion-Mt-Vélan (CN 1346/1366), Atlas Géologique de la Suisse 1:25 000* [Map].

Bures, L., Sychova, P., Maca, P., Roub, R., & Marval, S. (2019). River Bathymetry Model Based on Floodplain Topography. *Water*, 11(6), 1287. https://doi.org/10.3390/w11061287.

Burtin, A., Bollinger, L., Vergne, J., Cattin, R., & Nábělek, J. L. (2008). Spectral analysis of seismic noise induced by rivers: A new tool to monitor spatiotemporal changes in stream hydrodynamics. *Journal of Geophysical Research: Solid Earth*, *113*(B5). https://doi.org/10.1029/2007JB005034.

Burtin, A., Cattin, R., Bollinger, L., Vergne, J., Steer, P., Robert, A., Findling, N., & Tiberi, C. (2011). Towards the hydrologic and bed load monitoring from high-frequency seismic noise in a braided river: The "torrent de St Pierre", French Alps. *Journal of Hydrology*, *408*(1), 43–53. https://doi.org/10.1016/j.jhydrol.2011.07.014.

Burtin, A., Hovius, N., & Turowski, J. M. (2016). Seismic monitoring of torrential and fluvial processes. *Earth Surface Dynamics*, *4*(2), 285–307. https://doi.org/10.5194/esurf-4-285-2016.

Butler, J. B., Lane, S. N., & Chandler, J. H. (2001). Automated extraction of grain-size data from gravel surfaces using digital image processing. *Journal of Hydraulic Research*, 39(5), 519-529. https://doi.org/10.1080/00221686.2001.9628276.

Carbonneau, P. E., Lane, S. N., & Bergeron, N. E. (2004). Catchment-scale mapping of surface grain size in gravel bed rivers using airborne digital imagery. *Water Resources Research*, *40*(7). https://doi.org/10.1029/2003WR002759.

Carbonneau, P. E., Bergeron, N., & Lane, S. N. (2005). Automated grain size measurements from airborne remote sensing for long profile measurements of fluvial grain sizes. *Water Resources Research*, *41*(11). https://doi.org/10.1029/2005WR003994.

Carbonneau, P. E., & Dietrich, J. T. (2017). Cost-effective non-metric photogrammetry from consumer-grade sUAS: Implications for direct georeferencing of structure from motion photogrammetry. *Earth Surface Processes and Landforms*, 42(3), 473–486. https://doi.org/10.1002/esp.4012.

Carling, P. A., & Reader, N. A. (1982). Structure, composition and bulk properties of upland stream gravels. *Earth Surface Processes and Landforms*, 7(4), 349-365. https://doi.org/10.1002/esp.3290070407.

Carling, P.A. (1999). Subaqueous gravel dunes. *Journal of Sedimentary Research*, 69, 534-545.

Carling, P.A., Richardson, K. & Ikeda, H. (2005). A flume experiment on the development of subaqueous fine gravel dunes from a lower stage plane bed. *Journal of Geophysical Research: Earth Surface*, 110, F04S05. https://doi.org/10.1029/2004JF000205.

Carling, P. A., Gupta, N., Atkinson, P. M., & He, H. Q. (2016). Criticality in the planform behavior of the Ganges River meanders. *Geology*, *44*(10), 859–862. https://doi.org/10.1130/G38382.1.

Carrillo, R., & Mao, L. (2020). Coupling Sediment Transport Dynamics with Sediment and Discharge Sources in a Glacial Andean Basin. *Water*, *12*(12), Article 12. https://doi.org/10.3390/w12123452.

Carrivick, J. L., & Rushmer, E. L. (2009). Inter- and Intra-Catchment Variations in Proglacial Geomorphology: An Example From Franz Josef Glacier and Fox Glacier, New Zealand. *Arctic, Antarctic, and Alpine Research*, *41*(1), 18–36. https://doi.org/10.1657/1523-0430-41.1.18.

Carrivick, J. L., Geilhausen, M., Warburton, J., Dickson, N. E., Carver, S. J., Evans, A. J., & Brown, L. E. (2013). Contemporary geomorphological activity throughout the proglacial area of an alpine catchment. *Geomorphology*, *188*, 83–95. https://doi.org/10.1016/j.geomorph.2012.03.029.

Carrivick, J., & Heckmann, T. (2017). Short-term geomorphological evolution of proglacial systems. *Geomorphology*, *287*, 3–28. https://doi.org/10.1016/j.geomorph.2017.01.37.

Carrivick, J. L., Heckmann, T., Turner, A., & Fischer, M. (2018). An assessment of landform composition and functioning with the first proglacial systems dataset of the central European Alps. *Geomorphology*, *321*, 117–128. https://doi.org/10.1016/j.geomorph.2018.08.030.

Carrivick, J., Heckmann, T., Fischer, M., & Davies, B. (2019). An Inventory of Proglacial Systems in Austria, Switzerland and Across Patagonia. In Heckmann, T. & Morche, D. (Eds.), *Geomorphology of Proglacial Systems: Landform and Sediment Dynamics in*

*Recently Deglaciated Alpine Landscapes*, 43–57. Springer International Publishing. https://doi.org/10.1007/978-3-319-94184-4_3.

Carrivick, J. L., & Tweed, F. S. (2021). Deglaciation controls on sediment yield: Towards capturing spatio-temporal variability. *Earth-Science Reviews*, *221*, 103809. https://doi.org/10.1016/j.earscirev.2021.103809.

Cartigny, M.J.B., Ventra, D., Postma, G. & van Den Berg, J. (2013). Morphodynamics and sedimentary structure of bedforms under supercticial-flow conditions: New insights from flume experiments. *Sedimentology*, 61(3), 712-748. https://doi.org/10.1111/sed.12076.

Cassel, M., Piégay, H., Fantino, G., Lejot, J., Bultingaire, L., Michel, K., & Perret, F. (2020). Comparison of ground-based and UAV a-UHF artificial tracer mobility monitoring methods on a braided river. *Earth Surface Processes and Landforms*, *45*(5), 1123–1140. https://doi.org/10.1002/esp.4777.

Chandler, J., Ashmore, P., Paola, C., Gooch, M., & Varkaris, F. (2002). Monitoring River-Channel Change Using Terrestrial Oblique Digital Imagery and Automated Digital Photogrammetry. *Annals of the Association of American Geographers*, *92*(4), 631–644. https://doi.org/10.1111/1467-8306.00308.

Chew, L. C., & Ashmore, P. E. (2001). Channel adjustment and a test of rational regime theory in a proglacial braided stream. *Geomorphology*, 37(1), 43-63. https://doi.org/10.1016/S0169-555X(00)00062-3.

Church, M. (1972). Baffin Island sandurs: A study of Arctic fluvial processes. *Bulletin of Geological Survey Canada*, *216*, 1–208.

Church, M., & Ryder, J. (1972). Paraglacial Sedimentation: A Consideration of Fluvial Processes Conditioned by Glaciation. *GSA Bulletin*, *83*(10), 3059–3072. https://doi.org/10.1130/0016-7606(1972)83[3059:PSACOF]2.0.CO;2.

Church, M. (2006). Bed Material Transport and the Morphology of Alluvial River Channels. *Annual Review of Earth and Planetary Sciences*, *34*(1), 325–354. https://doi.org/10.1146/annurev.earth.33.092203.122721.

Church, M., & Ferguson, R. I. (2015). Morphodynamics: Rivers beyond steady state. *Water Resources Research*, *51*(4), 1883–1897. https://doi.org/10.1002/2014WR016862.

Clifford, N. J., Richards, K. S., Brown, R. A., & Lane, S. N. (1995). Scales of Variation of Suspended Sediment Concentration and Turbidity in a Glacial Meltwater Stream. *Geografiska Annaler. Series A, Physical Geography*, *77*(1/2), 45–65. https://doi.org/10.2307/521277.

Collins, D. B. G., Bras, R. L., & Tucker, G. E. (2004). Modeling the effects of vegetation-erosion coupling on landscape evolution. *Journal of Geophysical Research: Earth Surface*, *109*(F3). https://doi.org/10.1029/2003JF000028.

Collins, D. N. (2008). Climatic warming, glacier recession and runoff from Alpine basins after the Little Ice Age maximum. *Annals of Glaciology*, *48*, 119–124. https://doi.org/10.3189/172756408784700761.

Comiti, F., Mao, L., Penna, D., Dell'Agnese, A., Engel, M., Rathburn, S., & Cavalli, M. (2019). Glacier melt runoff controls bedload transport in Alpine catchments. *Earth and Planetary Science Letters*, *520*, 77–86. https://doi.org/10.1016/j.epsl.2019.05.031.

Cook, S. J., Swift, D. A., Kirkbride, M. P., Knight, P. G., & Waller, R. I. (2020). The empirical basis for modelling glacial erosion rates. *Nature Communications*, *11*(1), Article 1. https://doi.org/10.1038/s41467-020-14583-8.

Copland, L., Harbor, J., Gordon, S., & Sharp, M. (1997). The Use of Borehole Video in Investigating the Hydrology of a Temperate Glacier. *Hydrological Processes*, *11*(2), 211–224. https://doi.org/10.1002/(SICI)1099-1085(199702)11:2<211::AID-HYP496>3.0.CO;2-7.

Cossart, E., Braucher, R., Fort, M., Bourlès, D.L. & Carcaillet, J. (2008). Slope instabilty in relation to glacial debuttressing in alpine areas (Upper Durance catchment, southeastern France): Evidence from field data and [10]Be cosmic ray exposure age. *Geomorphology*, 95, 3-26. https://doi.org/10.1016/j.geomorph.2006.12.022.

Coulthard, T. J., Lewin, J., & Macklin, M. G. (2005). Modelling differential catchment response to environmental change. *Geomorphology*, *69*(1), 222–241. https://doi.org/10.1016/j.geomorph.2005.01.008.

Coulthard, T. J., & Van De Wiel, M. J. (2007). Quantifying fluvial non linearity and finding self organized criticality? Insights from simulations of river basin evolution. *Geomorphology*, *91*(3–4), 216–235. https://doi.org/10.1016/j.geomorph.2007.04.011.

Cowton, T., Nienow, P., Sole, A., Wadham, J., Lis, G., Bartholomew, I., Mair, D., & Chandler, D. (2013). Evolution of drainage system morphology at a land-terminating Greenlandic outlet glacier. *Journal of Geophysical Research: Earth Surface*, *118*(1), 29–41. https://doi.org/10.1029/2012JF002540.

Cudden, J. R., & Hoey, T. B. (2003). The causes of bedload pulses in a gravel channel: The implications of bedload grain-size distributions. *Earth Surface Processes and Landforms*, *28*(13), 1411–1428. https://doi.org/10.1002/esp.521.

Curran, J. H., Loso, M. G., & Williams, H. B. (2017). Glacial conditioning of stream position and flooding in the braid plain of the Exit Glacier foreland, Alaska. *Geomorphology*, *293*, 272–288. https://doi.org/10.1016/j.geomorph.2017.06.004.

Curry, A. M., Cleasby, V., & Zurkowskyi, P. (2006). Paraglacial response of steep, sediment-mantled slopes to post-'Little Ice Age' glacier recession in the central Swiss Alps -. *Journal of Quaternary Science*, *21*, 221–225. https://doi.org/10.1002/jqs.954.

Daley, T.M., Miller, D.E., Dodds, K., Cook, P. & Freideld, B.M. (2016). Field testing of modular borehole monitoring with simultaneous distributed acoustic sensing and geophone vertical seismic profiles at Citronelle, Alabama. Geophysical Prospecting, 64(5), 1318-1334. https://doi.org/10.1111/1365-2478.12324.

Davies, T.R.H. (1987). Problems of bed load transport in braided gravel-bed rivers. In Thorne, C.R., Bathurst, J.C. & Hey, R.D. (Eds.), *Sediment Transport in Gravel Bed Rivers*, 793-811. Chichester: John Wiley & Sons.

de Almeida, G. A. M., Bates, P., Freer, J.E. & Souvignet, M. (2012). Improving the stability of a simple formulation of the shallow water equations for 2-D flood modeling, *Water Resources Research*, Vol 48. https://doi.org/10.1029/2011WR011570.

de Winter, I. L., Storms, J. E. A., & Overeem, I. (2012). Numerical modeling of glacial sediment production and transport during deglaciation. *Geomorphology*, *167–168*, 102–114. https://doi.org/10.1016/j.geomorph.2012.05.023.

Delaney, I., Bauder, A., Werder, M. A., & Farinotti, D. (2018). Regional and Annual Variability in Subglacial Sediment Transport by Water for Two Glaciers in the Swiss Alps. *Frontiers in Earth Science*, *6*. https://www.frontiersin.org/articles/10.3389/feart.2018.00175.

Delaney, I., & Adhikari, S. (2020). Increased Subglacial Sediment Discharge in a Warming Climate: Consideration of Ice Dynamics, Glacial Erosion, and Fluvial Sediment Transport. *Geophysical Research Letters*, *47*(7), e2019GL085672. https://doi.org/10.1029/2019GL085672.

Dell'Agnese, A., Mao, L., & Comiti, F. (2014). Calibration of an acoustic pipe sensor through bedload traps in a glacierized basin. *CATENA*, *121*, 222–231. https://doi.org/10.1016/j.catena.2014.05.021.

Dell'Agnese, A., Brardinoni, F., Toro, M., Mao, L., Engel, M., & Comiti, F. (2015). Bedload transport in a formerly glaciated mountain catchment constrained by particle tracking. *Earth Surface Dynamics*, *3*(4), 527–542. https://doi.org/10.5194/esurf-3-527-2015.

Deluigi, N., Lambiel, C., & Kanevski, M. (2017). Data-driven mapping of the potential mountain permafrost distribution. *Science of The Total Environment*, *590–591*, 370–380. https://doi.org/10.1016/j.scitotenv.2017.02.041.

Deltares (2018). D-FLOW Flexible mesh user manual, version 1.2.1, Deltares.

Dey, S. (2014). Bedforms. In Dey, S. (Ed.), *Fluvial Hydrodynamics: Hydrodynamics and Sediment Transport Phenomena*. Springer.

Dhont, B. & Ancey, C. (2018). Are bedload transport processes pulses in gravel bed rivers created by bar migration or sediment waves?. *Geophysical Research Letters*, 45(11), 5501-5508. https://doi.org/10.1029/2018GL077792.

Dietrich, J. T. (2017). Bathymetric Structure-from-Motion: Extracting shallow stream bathymetry from multi-view stereo photogrammetry. *Earth Surface Processes and Landforms*, *42*(2), 355–364. https://doi.org/10.1002/esp.4060.

Dietze, M. (2018). The R package "eseis" – a software toolbox for environmental seismology. *Earth Surface Dynamics*, *6*(3), 669–686. https://doi.org/10.5194/esurf-6-669-2018.

Dietze, M., Lagarde, S., Halfi, E., Laronne, J. B., & Turowski, J. M. (2019a). Joint Sensing of Bedload Flux and Water Depth by Seismic Data Inversion. *Water Resources Research*, *55*(11), 9892–9904. https://doi.org/10.1029/2019WR026072.

Dietze, M., Gimbert, F., Turowski, J. M., Stark, K. A., Cadol, D. & Laronne, J. B. (2019b). *The seismic view on sediment laden ephemeral flows—Modelling of ground motion data for fluid and bedload dynamics in the Arroyo de los Pinos* [Computer software manual]. Retrieved from http://micha-dietze.de/pages/publications/other/Dietze_et_al_2019b.pdf (Paper to SEDHYD conference)

Diolaiuti, G. A., Maragno, D., D'Agata, C., Smiraglia, C., & Bocchiola, D. (2011). Glacier retreat and climate change: Documenting the last 50 years of Alpine glacier history from area and geometry changes of Dosdè Piazzi glaciers (Lombardy Alps, Italy). *Progress in Physical Geography: Earth and Environment*, *35*(2), 161–182. https://doi.org/10.1177/0309133311399494.

Dømgaard, M., Kjeldsen, K. K., Huiban, F., Carrivick, J. L., Khan, S. A., & Bjørk, A. A. (2023). Recent changes in drainage route and outburst magnitude of the Russell Glacier ice-dammed lake, West Greenland. *The Cryosphere*, *17*(3), 1373–1387. https://doi.org/10.5194/tc-17-1373-2023.

Dou, S., Lindsey, N., Wagner, A. M., Daley, T. M., Freifeld, B., Robertson, M., Peterson, J., Ulrich, C., Martin, E. R., & Ajo-Franklin, J. B. (2017). Distributed Acoustic Sensing for Seismic Monitoring of The Near Surface: A Traffic-Noise Interferometry Case Study. *Scientific Reports*, *7*(1), Article 1. https://doi.org/10.1038/s41598-017-11986-4.

Draper, N. R., & Smith, H. (1998). *Applied Regression Analysis* (3th Edition). Wiley.

Egholm, D. L., Pedersen, V. K., Knudsen, M. F., & Larsen, N. K. (2012). Coupling the flow of ice, water, and sediment in a glacial landscape evolution model. *Geomorphology*, *141–142*, 47–66. https://doi.org/10.1016/j.geomorph.2011.12.019.

Egli, P. E., Irving, J., & Lane, S. N. (2021a). Characterization of subglacial marginal channels using 3-D analysis of high-density ground-penetrating radar data. *Journal of Glaciology*, *67*(264), 759–772. https://doi.org/10.1017/jog.2021.26.

Egli, P. E., Belotti, B., Ouvry, B., Irving, J., & Lane, S. N. (2021b). Subglacial Channels, Climate Warming, and Increasing Frequency of Alpine Glacier Snout Collapse. *Geophysical Research Letters*, *48*(21), e2021GL096031. https://doi.org/10.1029/2021GL096031.

Egozi, R., & Ashmore, P. (2008). Defining and measuring braiding intensity. *Earth Surface Processes and Landforms*, 33(14), 2121-2138. https://doi.org/10.1002/esp.1658.

Egozi, R., & Ashmore, P. (2009). Experimental analysis of braided channel pattern response to increased discharge. *Journal of Geophysical Research: Earth Surface*, *114*(F2). https://doi.org/10.1029/2008JF001099.

Ehrbar, D., Schmocker, L., Vetsch, D. F., & Boes, R. M. (2018). Hydropower Potential in the Periglacial Environment of Switzerland under Climate Change. *Sustainability*, *10*(8), Article 8. https://doi.org/10.3390/su10082794.

Einstein, H. A. (1950). *The Bed-Load Function for Sediment Transportation in Open Channel Flows* (Technical Bulletin 1026). United States Department of Agriculture, Soil Conservation Service.

Eltner, A., Baumgart, P., Maas, H.G. & Faust, D. (2015). Multi-temporal UAV data for automatic measurement of rill and interrill erosion on loess soil. *Earth Surface Processes and Landforms*, 40, 741-255. https://doi.org/10.1002/esp.3673.

Engelund, F. & Hansen, E. (1967). *A monograph on sediment transport in alluvial streams*, TEKNISKFORLAG Skelbrekgade 4 Copenhagen V, Denmark, 64p.

Farina, G., Alvisi, S., Franchini, M., Corato, G. & Moramarco (2015). Estimation of bathymetry (and discharge) in natural river cross-sections by using an entropy approach. *Journal of Hydrology*, 527, 20-29. https://doi.org/10.1016/j.jhydrol.2015.04.037.

Farinotti, D., Round, V., Huss, M., Compagno, L., & Zekollari, H. (2019). Large hydropower and water-storage potential in future glacier-free basins. *Nature*, *575*(7782), Article 7782. https://doi.org/10.1038/s41586-019-1740-z.

Fenn, C. R., Gurnell, A. M., & Beecroft, I. R. (1985). An Evaluation of the Use of Suspended Sediment Rating Curves for the Prediction of Suspended Sediment Concentration in a Proglacial Stream. *Geografiska Annaler. Series A, Physical Geography*, *67*(1/2), 71–82. https://doi.org/10.2307/520467.

Ferguson, R. I., & Werritty, A. (1983). Bar development and channel changes in the gravelly River Fehsie, Scotland. *International Assoication of Sedimentologists Special Publications*, *6*, 181–193.

Ferguson, R.I. (1987). Hydraulic and sedimentary controls of channel pattern. In Richards, K. (Ed.), *River Channels: Environment and Processes*, 129-158. The Institute of British Geographers, Blackwell: Oxford.

Ferguson, R. I., & Ashworth, P. (1992). Spatial patterns of bedload transport and channel change in braided and near braided rivers. In P. Billi, R.D. Hey, C.R. Thorne, P. Taconni (Eds.), *Dynamics of gravel-bed rivers,* 477–492. John Wiley and Sons.

Ferguson, R. I. (1993). Understanding braiding processes in gravel-bed rivers: Progress add unsolved problems. In Best, J.L. & Bristow, C.S. (Eds.), *Braided Rivers*, 73–87. Geological Society Special Publication.

Ferguson, R.I. (1994). Critical discharge for entrainment of poorly sorted gravel. Earth Surface Processes and Landforms, 19, 179-186. https://doi.org/10.1002/esp.3290190208.

Fernandez Luque, R., & Van Beek, R. (1976). Erosion And Transport Of Bed-Load Sediment. *Journal of Hydraulic Research*, *14*(2), 127–144. https://doi.org/10.1080/00221687609499677.

Fickert, T. (2017). Glacier Forelands – Unique Field Laboratories for the Study of Primary Succession of Plants. In Godone, D. (Ed.), *Glacier Evolution in a Changing World*. IntechOpen. https://doi.org/10.5772/intechopen.69479.

Fischer, A., Fickert, T., Schwaizer, G., Patzelt, G., & Groß, G. (2019). Vegetation dynamics in Alpine glacier forelands tackled from space. *Scientific Reports*, 9(1), Article 1. https://doi.org/10.1038/s41598-019-50273-2.

Flener, C. (2013). Estimating deep water radiance in shallow water: Adapting optical bathymetry modelling to shallow river environments. *Boreal environment research*, *18*, 488-502.

Flener, C., Vaaja, M., Jaakkola, A., Krooks, A., Kaartinen, H., Kukko, A., Kasvi, E., Hyyppä, H., Hyyppä, J., & Alho, P. (2013). Seamless Mapping of River Channels at High Resolution Using Mobile LiDAR and UAV-Photography. *Remote Sensing*, *5*(12), 6382–6407. https://doi.org/10.3390/rs5126382.

Fonstad, M. A., & Marcus, W. A. (2005). Remote sensing of stream depths with hydraulically assisted bathymetry (HAB) models. *Geomorphology*, 72, 320–339. https://doi.org/10.1016/j.geomorph.2005.06.005.

Fonstad, M. A., Dietrich, J. T., Courville, B. C., Jensen, J. L., & Carbonneau, P. E. (2013). Topographic structure from motion: A new development in photogrammetric measurement. *Earth Surface Processes and Landforms*, *38*(4), 421–430. https://doi.org/10.1002/esp.3366.

Fountain, A. G., & Walder, J. S. (1998). Water flow through temperate glaciers. *Reviews of Geophysics*, *36*(3), 299–328. https://doi.org/10.1029/97RG03579.

Frascati, A. & Lanzoni, S. (2009). Morphodyamic regime and long-term evolution of meandering rivers. *Journal of Geophysical Research: Earth Surface*, 144. https://doi.org/10.1029/2008JF001101.

Frascati, A. & Lanzoni, S. (2013). A mathematical model for meandering rivers with varying width. Journal of Geophysical Research: Earth Surface, 118, 1641-1657. https://doi.org/10.1002/jgrf.20084.

Freudiger, D., Mennekes, D., Seibert, J., & Weiler, M. (2018). Historical glacier outlines from digitized topographic maps of the Swiss Alps. *Earth System Science Data*, *10*(2), 805–814. https://doi.org/10.5194/essd-10-805-2018.

Frings, R.M., Schütterumpf, H. & Vollmer, S. (2011). Verification of porosity predictors for fluvial sand-gravel deposits. *Water Resources Research*, 47, W07525. https://doi.org/10.1029/2010WR009690.

Fryirs, K. (2013). (Dis)Connectivity in catchment sediment cascades: A fresh look at the sediment delivery problem. *Earth Surface Processes and Landforms*, *38*(1), 30–46. https://doi.org/10.1002/esp.3242.

Fryirs, K., & Brierley, G. J. (1999). Slope–channel decoupling in Wolumla catchment, New South Wales, Australia: The changing nature of sediment sources following European settlement. *CATENA*, *35*(1), 41–63. https://doi.org/10.1016/S0341-8162(98)00119-2.

Gabbud, C., Bakker, M., Clémençon, M. & Lane, S.N. (2019a). Hydropower Flushing Events Causes Severe Loss of Macrozoobenthos in Alpine Streams. *Water Resources Research*, 55, 10056-10081. https://doi.org/10.1029/2019WR024758.

Gabbud, C., Robinson, C. T., & Lane, S. N. (2019b). Summer is in winter: Disturbance-driven shifts in macroinvertebrate communities following hydroelectric power exploitation. *Science of The Total Environment*, *650*, 2164–2180. https://doi.org/10.1016/j.scitotenv.2018.09.180.

Gao, M., Tian, J., Ai, L., & Zhang, F. (2008). Sewage Image Feature Extraction and Turbidity Degree Detection Based on Embedded System. *2008 International Conference on MultiMedia and Information Technology*, 357–360. https://doi.org/10.1109/MMIT.2008.196.

Ganti, V., Lamb, M. P., & McElroy, B. (2014). Quantitative bounds on morphodynamics and implications for reading the sedimentary record. *Nature Communications*, *5*(1), Article 1. https://doi.org/10.1038/ncomms4298.

Gardent, M., Rabatel, A., Dedieu, J.-P., & Deline, P. (2014). Multitemporal glacier inventory of the French Alps from the late 1960s to the late 2000s. *Global and Planetary Change*, *120*, 24–37. https://doi.org/10.1016/j.gloplacha.2014.05.004

Garg, P. K. (2022). Characterisation of Fixed-Wing Versus Multirotors UAVs/Drones. *Journal of Geomatics*, *16*(2), Article 2. https://doi.org/10.58825/jog.2022.16.2.44.

Gaudard, L., Romerio, F., Dalla Valle, F., Gorret, R., Maran, S., Ravazzani, G., Stoffel, M., & Volonterio, M. (2014). Climate change impacts on hydropower in the Swiss and Italian Alps. *Science of The Total Environment*, *493*, 1211–1221. https://doi.org/10.1016/j.scitotenv.2013.10.012.

Geilhausen, M., Morche, D., Otto, J.-C., & Schrott, L. (2013). Sediment discharge from the proglacial zone of a retreating Alpine glacier. *Zeitschrift Für Geomorphologie, Supplementary Issues*, 29–53. https://doi.org/10.1127/0372-8854/2012/S-00122.

Germanoski, D., & Schumm, S. A. (1993). Changes in Braided River Morphology Resulting from Aggradation and Degradation. *The Journal of Geology*, *101*(4), 451–466. https://doi.org/10.1086/648239.

Gilet, L., Gob, F., Gautier, E., Houbrechts, G., Virmoux, C., & Thommeret, N. (2020). Hydro-morphometric parameters controlling travel distance of pebbles and cobbles in three gravel bed streams. *Geomorphology*, *358*, 107117. https://doi.org/10.1016/j.geomorph.2020.107117.

Gilvear, D. J., Waters, T. M., & Milner, A. M. (1995). Image analysis of aerial photography to quantify changes in channel morphology and instream habitat following placer mining in interior Alaska. *Freshwater Biology*, *34*(2), 389–398. https://doi.org/10.1111/j.1365-2427.1995.tb00897.x.

Gilvear, D. J., Waters, T. M., & Milner, A. M. (1998). Image analysis of aerial photography to quantify the effect of gold placer mining on channel morphology, interior Alaska. In Lane, S.N., Richards, K.S. & Chandler, J.H. (Eds.), *Landform Monitoring, Modelling and Analysis,* 195–216. Wiley.

Gimbert, F., Tsai, V. C., & Lamb, M. P. (2014). A physical model for seismic noise generation by turbulent flow in rivers. *Journal of Geophysical Research: Earth Surface*, *119*(10), 2209–2238. https://doi.org/10.1002/2014JF003201.

Gimbert, F., Tsai, V. C., Amundson, J. M., Bartholomaus, T. C., & Walter, J. I. (2016). Subseasonal changes observed in subglacial channel pressure, size, and sediment transport. *Geophysical Research Letters*, *43*(8), 3786–3794. https://doi.org/10.1002/2016GL068337.

Goff, J. R., & Ashmore, P. (1994). Gravel transport and morphological change in braided sunwapta river, Alberta, Canada. *Earth Surface Processes and Landforms*, *19*(3), 195–212. https://doi.org/10.1002/esp.3290190302.

Gomez, B., Naff, R.L. & Hubbell, D.W. (1989). Temporal variation in bedload transport rates associated with the migration of bedforms. *Earth Surface Processes and Landforms*, 14(2), 135-156. https://doi.org/10.1002/esp.329014025.

Guillon, H., Mugnier, J.-L., & Buoncristiani, J.-F. (2018). Proglacial sediment dynamics from daily to seasonal scales in a glaciated Alpine catchment (Bossons glacier, Mont Blanc massif, France). *Earth Surface Processes and Landforms*, *43*(7), 1478–1495. https://doi.org/10.1002/esp.4333.

Gurnell, A. M. (1982). The dynamics of suspended sediment concentration in a proglacial stream system. In Glen, J.W. (Ed.), *Hydrological Aspects of Alpine and High-Mountain Areas*, 59–89. Wiley.

Gurnell, A. M., Edwards, P. J., Petts, G. E., & Ward, J. V. (1999). A conceptual model for alpine proglacial river channel evolution under changing climatic conditions. *CATENA*, *38*(3), 223–242. https://doi.org/10.1016/S0341-8162(99)00069-7.

Hallet, B., Hunter, L., & Bogen, J. (1996). Rates of erosion and sediment evacuation by glaciers: A review of field data and their implications. *Global and Planetary Change*, *12*(1), 213–235. https://doi.org/10.1016/0921-8181(95)00021-6.

Hamberey, M. J., & Glasser, N. F. (2005). Sedimentary processes. In Salley R. C., Cocks, R. M. & Plomer I. R. (Eds.), *Encyclopedia of Geology*. Elsevier Inc.

Hambrey, M. J. (1984). Sedimentary Processes and Buried Ice Phenomena in the Pro-Glacial Areas of Spitsbergen Glaciers. *Journal of Glaciology*, *30*(104), 116–119. https://doi.org/10.3189/S002214300000856X.

Harper, J. T., Humphrey, N. F., & Greenwood, M. C. (2002). Basal conditions and glacier motion during the winter/spring transition, Worthington Glacier, Alaska, U.S.A. *Journal of Glaciology*, *48*(160), 42–50. https://doi.org/10.3189/172756502781831629.

Harten, A., Lax, P.D. & van Leer, B. (1984). On Upstream Differencing and Godunov-Type Schemes for Hyperbolic Conservation Laws. *SIAM Review*, 25(1). https://doi.org/10.1137/1025002.

Hasbargen, L. E., & Paola, C. (2000). Landscape instability in an experimental drainage basin. *Geology*, *28*(12), 1067–1070. https://doi.org/10.1130/0091-7613(2000)28<1067:LIIAED>2.0.CO;2.

Hasolt, B., Krüger, J. & Skjernaa, L. (2008). Landscape and sediment processes in a proglacial valley, the Mittivakkat Glacier area, Southeast Greenland. *Geografisk Tidsskrift – Danish Journal of Geography*, *108*(1), 97-110. https://doi.org/10.1080/00167223.2008.10649576.

Hassan, M. A., Church, M., & Schick, A. P. (1991). Distance of movement of coarse particles in gravel bed streams. *Water Resources Research*, *27*(4), 503–511. https://doi.org/10.1029/90WR02762.

Hauer, C., & Pulg, U. (2021). Buried and forgotten—The non-fluvial characteristics of postglacial rivers. *River Research and Applications*, *37*(2), 123–127. https://doi.org/10.1002/rra.3596.

Heckmann, T., Hilger, L., Vehling, L., & Becht, M. (2016). Integrating field measurements, a geomorphological map and stochastic modelling to estimate the spatially distributed rockfall sediment budget of the Upper Kaunertal, Austrian Central Alps. *Geomorphology*, *260*, 16–31. https://doi.org/10.1016/j.geomorph.2015.07.003.

Helley, E. J., & Smith, W. (1971). *Development and calibration of a pressure-difference bedload sampler* (73–108). United States Department of the Interior, Geological Survey, Water Resources Division. https://doi.org/10.3133/ofr73108.

Hemmelder, S., Marra, W., Markies, H., & De Jong, S. M. (2018). Monitoring river morphology & bank erosion using UAV imagery – A case study of the river Buëch, Hautes-Alpes, France. *International Journal of Applied Earth Observation and Geoinformation*, *73*, 428–437. https://doi.org/10.1016/j.jag.2018.07.016.

Herman, F., Beyssac, O., Brughelli, M., Lane, S. N., Leprince, S., Adatte, T., Lin, J. Y. Y., Avouac, J.-P., & Cox, S. C. (2015). Erosion by an Alpine glacier. *Science*, *350*(6257), 193–195. https://doi.org/10.1126/science.aab2386.

Herman, F., & King, G. E. (2018). Luminescence Thermochronometry: Investigating the Link between Mountain Erosion, Tectonics and Climate. *Elements*, *14*(1), 33–38. https://doi.org/10.2138/gselements.14.1.33.

Hiatt, M., Sonke, W., Addink, E.A., van Dijk, W.M., van Kreveld, M., Ophelders, T., Verbeek, K., Vlaming, J., Speckmann, B. & Kleinhans, M.G. (2019). Geometry and Topology of Estuary and Braided River Channel Networks Automatically Extracted From Topographic Data. *Journal of Geophysical Research: Earth Surface*, 125, e2019JF005206. https://doi.org/10.1029/2019JF005206.

Hicks, D.M. (2012). Remotely sensed topographic change in gravel riverbeds with flowing channels. In Church, M., Biron, P., & Roy, A. (Eds.), *Gravel-bed Rivers: Processes, Tools*, Environments. Wiley.

Hilger, L., & Beylich, A. A. (2019). Sediment Budgets in High-Mountain Areas: Review and Challenges. In Heckmann, T. & Morche, D. (Eds.), *Geomorphology of Proglacial Systems: Landform and Sediment Dynamics in Recently Deglaciated Alpine Landscapes*, 251–269. Springer International Publishing. https://doi.org/10.1007/978-3-319-94184-4_15.

Hodgkins, R., Cooper, R., Wadham, J., & Tranter, M. (2003). Suspended sediment fluxes in a high-Arctic glacierised catchment: Implications for fluvial sediment storage. *Sedimentary Geology*, *162*(1), 105–117. https://doi.org/10.1016/S0037-0738(03)00218-5.

Hodson, A., Gurnell, A., Tranter, M., Bogen, J., Hagen, J. O., & Clark, M. (1998). Suspended sediment yield and transfer processes in a small High-Arctic glacier basin, Svalbard. *Hydrological Processes*, *12*(1), 73–86. https://doi.org/10.1002/(SICI)1099-1085(199801)12:1<73::AID-HYP564>3.0.CO;2-S.

Hodson, A. J., & Ferguson, R. I. (1999). Fluvial suspended sediment transport from cold and warm-based glaciers in Svalbard. *Earth Surface Processes and Landforms*, *24*(11), 957–974. https://doi.org/10.1002/(SICI)1096-9837(199910)24:11<957::AID-ESP19>3.0.CO;2-J.

Hoey, T. B., & Sutherland, A. J. (1991). Channel morphology and bedload pulses in braided rivers: A laboratory study. *Earth Surface Processes and Landforms*, *16*(5), 447–462. https://doi.org/10.1002/esp.3290160506.

Hong, L. B., & Davies, T. R. H. (1979). A study of stream braiding. *GSA Bulletin*, 90, 1839-1859. https://doi.org/10.1130/GSAB-P2-90-1839.

Howard, A.D., Keetch, M.E. & Vincent, C.L. (1970). Topographical and geomorphic proprieties of braided streams. *Water Resources Research*, 6(6), 1647-1688. https://doi.org/10.1029/WR006i006p01674.

Hugenholtz, C. H., Moorman, B. J., Barlow, J., & Wainstein, P. A. (2008). Large-scale moraine deformation at the Athabasca Glacier, Jasper National Park, Alberta, Canada. *Landslides*, *5*(3), 251–260. https://doi.org/10.1007/s10346-008-0116-5.

Hugenholtz, C.H., Whitehead, K., Brown, O.W., Barchyn, T.E., Moorman, B.J., Le Clair, A-. Riddell, K. & Hamilton, T. (2013). Geomorphological mapping with a small unmanned aircraft system (sUAS): Feature detection and accuracy assessment of a photogrammetrically-derived digital terrain model. *Geomorphology*, 194, 16-24. https://doi.org/10.1016/j.geomorph.2013.03.023.

Humphrey, N. F., & Raymond, C. F. (1994). Hydrology, erosion and sediment production in a surging glacier: Variegated Glacier, Alaska, 1982–83. *Journal of Glaciology*, *40*(136), 539–552. https://doi.org/10.3189/S0022143000012429.

Hundey, E. J., & Ashmore, P. E. (2009). Length scale of braided river morphology. *Water Resources Research*, *45*(8). https://doi.org/10.1029/2008WR007521.

Huss, M., Bookhagen, B., Huggel, C., Jacobsen, D., Bradley, R.S., Clague, J.J., Vuille, M., Buytaert, W., Cayan, D.R., Greenwood, G., Mark, B.G., Milner, A.M., Weingartner, R. & Winder, M. (2017). Toward mountains without permanent snow and ice. *Earth's Future*, 5(5), 418-435. https://doi.org/10.1002/2016EF000514.

Huss, M., & Hock, R. (2018). Global-scale hydrological response to future glacier mass loss. *Nature Climate Change*, *8*(2), Article 2. https://doi.org/10.1038/s41558-017-0049-x.

Ikeda, S. (1982). Lateral Bed Load Transport on Side Slopes. *Journal of the Hydraulics Division*, 108(11), 1369–1373. https://doi.org/10.1061/JYCEAJ.0005937.

Intergovernmental Panel on Climate Change. (2007). *Climate change 2007: The physical science basis: Contribution of Working Group I to the Fourth Assessment Report of the Intergovernmental Panel on Climate Change*. Cambridge University Press.

Iwasaki, T., Shimizu, Y. & Kimura, I. (2016). Numerical simulation of bar and bank erosion in a vegetated floodplain: A case study in the Otofuke River. *Advances in Water Resources*, 93, 118-134. https://doi.org/10.1016/j.advwatres.2015.02.001.

Jagers, H.R.A (2003). *Modelling planform changes of braided rivers*. Ph.D. thesis, University of Twente.

James, G., Witten, D., Hastie, T., & Tibshirani, R. (2013). Linear Regression. In G. James, D. Witten, T. Hastie, & R. Tibshirani (Eds.), *An Introduction to Statistical Learning: With Applications in R*, 59–126. Springer. https://doi.org/10.1007/978-1-4614-7138-7_3.

James, M. R., Robson, S., d'Oleire-Oltmanns, S., & Niethammer, U. (2017a). Optimising UAV topographic surveys processed with structure-from-motion: Ground control quality, quantity and bundle adjustment. *Geomorphology*, *280*, 51–66. https://doi.org/10.1016/j.geomorph.2016.11.021.

James, M. R., Robson, S., & Smith, M. W. (2017b). 3-D uncertainty-based topographic change detection with structure-from-motion photogrammetry: Precision maps for ground control and directly georeferenced surveys. *Earth Surface Processes and Landforms*, 42(12), 1769–1788. https://doi.org/10.1002/esp.4125.

James, M. R., Antoniazza, G., Robson, S., & Lane, S. N. (2020). Mitigating systematic error in topographic models for geomorphic change detection: Accuracy, precision and considerations beyond off-nadir imagery. *Earth Surface Processes and Landforms*, *45*(10), 2251–2271. https://doi.org/10.1002/esp.4878.

Javernick, L., Brasington, J., & Caruso, B. (2014). Modeling the topography of shallow braided rivers using Structure-from-Motion photogrammetry. *Geomorphology*, *213*, 166–182. https://doi.org/10.1016/j.geomorph.2014.01.006.

Jenkin, M., Hofmann, M., Hubbard, B., Mancini, D., Miesen, F. M., Herman, F., & Lane, S. N. (2023). Tracking coarse sediment in an Alpine subglacial channel using radio-tagged particles. *Journal of Glaciology*, 1–15. https://doi.org/10.1017/jog.2023.77.

Jenkin, M., Mancini, D., Miesen, F.M., Müller, T., Fischer, M., Dietze, M. & Lane, S.N. (submitted to Journal of Geophysical Research: Earth Surface). Subglacial sediment Export from an Alpine Glacier.

Jerolmack, D. J., & Paola, C. (2010). Shredding of environmental signals by sediment transport. *Geophysical Research Letters*, *37*(19). https://doi.org/10.1029/2010GL044638.

Jouvet, G., & Huss, M. (2019). Future retreat of Great Aletsch Glacier. *Journal of Glaciology*, *65*(253), 869–872. https://doi.org/10.1017/jog.2019.52.

Kaser, G., Großhauser, M., & Marzeion, B. (2010). Contribution potential of glaciers to water availability in different climate regimes. *Proceedings of the National Academy of Sciences*, *107*(47), 20223–20227. https://doi.org/10.1073/pnas.1008162107.

Kasprak, A., Wheaton, J. M., Ashmore, P. E., Hensleigh, J. W., & Peirce, S. (2015). The relationship between particle travel distance and channel morphology: Results from

physical models of braided rivers. *Journal of Geophysical Research: Earth Surface*, *120*(1), 55–74. https://doi.org/10.1002/2014JF003310.

Kasprak, A., Brasington, J., Hafen, K., Williams, R.D. & Wheaton, J.M. (2019). Modelling braided river morphodynamics using a particle travel length framework. *Earth Surface Dynamics*, 7, 247-274. https://doi.org/10.5194/esurf-7-247-2019.

Kasvi, E., Salmela, J., Lotsari, E., Kumpula, T., & Lane, S. N. (2019). Comparison of remote sensing based approaches for mapping bathymetry of shallow, clear water rivers. *Geomorphology*, *333*, 180–197. https://doi.org/10.1016/j.geomorph.2019.02.017.

Kim, W., Paola, C., Swenson, J. B., & Voller, V. R. (2006). Shoreline response to autogenic processes of sediment storage and release in the fluvial system. *Journal of Geophysical Research: Earth Surface*, *111*(F4). https://doi.org/10.1029/2006JF000470.

Koppes, M. N., & Montgomery, D. R. (2009). The relative efficacy of fluvial and glacial erosion over modern to orogenic timescales. *Nature Geoscience*, *2*(9), Article 9. https://doi.org/10.1038/ngeo616.

Lagarde, S., Dietze, M., Gimbert, F., Laronne, J. B., Turowski, J. M., & Halfi, E. (2021). Grain-Size Distribution and Propagation Effects on Seismic Signals Generated by Bedload Transport. *Water Resources Research*, *57*(4), e2020WR028700. https://doi.org/10.1029/2020WR028700.

Lague, D. (2020). Chapter 8—Terrestrial laser scanner applied to fluvial geomorphology. In P. Tarolli & S. M. Mudd (eds.), *Developments in Earth Surface Processes* (pp. 231–254). Elsevier. https://doi.org/10.1016/B978-0-444-64177-9.00008-4.

Lamarre, H., & Roy, A. G. (2008). The role of morphology on the displacement of particles in a step–pool river system. *Geomorphology*, *99*(1), 270–279. https://doi.org/10.1016/j.geomorph.2007.11.005.

Lambiel, C., & Reynard, E. (2001). Regional modelling of present, past and future potential distribution of discontinuous permafrost based on a rock glacier inventory in the Bagnes-Hérémence area (Western Swiss Alps). *Norsk Geografisk Tidsskrift - Norwegian Journal of Geography*, *54*(4), 219–223. https://doi.org/10.1080/00291950152746559.

Lancaster, S. T., & Casebeer, N. E. (2007). Sediment storage and evacuation in headwater valleys at the transition between debris-flow and fluvial processes. *Geology*, *35*(11), 1027–1030. https://doi.org/10.1130/G239365A.1.

Lane, S. N., Richards, K. S., & Chandler, J. H. (1994). Developments in monitoring and modelling small-scale river bed topography. *Earth Surface Processes and Landforms*, *19*(4), 349–368. https://doi.org/10.1002/esp.3290190406.

Lane, S. N., Richards, K. S., & Chandler, J. H. (1996). Discharge and sediment supply controls on erosion and deposition in a dynamic alluvial channel. *Geomorphology*, *15*(1), 1–15. https://doi.org/10.1016/0169-555X(95)00113-J.

Lane, S. N. (1998). The use of digital terrain modelling in the understanding of dynamic river channel systems. In Lane S. N., Richards, K. S. & Chandler J. H. (Eds.), *Landform Monitoring, Modelling and Analysis*, 311–342. Wiley.

Lane, S. N., Westaway, R. M., & Murray Hicks, D. (2003). Estimation of erosion and deposition volumes in a large, gravel-bed, braided river using synoptic remote sensing. *Earth Surface Processes and Landforms*, *28*(3), 249–271. https://doi.org/10.1002/esp.483.

Lane, S. N., Widdison, P.E., Thomas, R.E., Ashworth, P.J., Best, J.L., Lunt, I.A., Sambrook Smith, G.H. & Simpson, C.J. (2010). Quantification of braided river channel change using archival digital image analysis. *Earth Surface Processes and Landforms*, 35, 971-985. https://doi.org/10.102/esp.2015.

Lane, S. N., Bakker, M., Gabbud, C., Micheletti, N., & Saugy, J.-N. (2017). Sediment export, transient landscape response and catchment-scale connectivity following rapid climate warming and Alpine glacier recession. *Geomorphology*, *277*, 210–227. https://doi.org/10.1016/j.geomorph.2016.02.015.

Lane, S. N., & Nienow, P. W. (2019). Decadal-Scale Climate Forcing of Alpine Glacial Hydrological Systems. *Water Resources Research*, *55*(3), 2478–2492. https://doi.org/10.1029/2018WR024206.

Lane, S. N., Gentile, A., & Goldenschue, L. (2020). Combining UAV-Based SfM-MVS Photogrammetry with Conventional Monitoring to Set Environmental Flows: Modifying Dam Flushing Flows to Improve Alpine Stream Habitat. *Remote Sensing*, *12*(23), Article 23. https://doi.org/10.3390/rs12233868.

Larose, E., Carrière, S., Voisin, C., Bottelin, P., Baillet, L., Guéguen, P., Walter, F., Jongmans, D., Guillier, B., Garambois, S., Gimbert, F., & Massey, C. (2015). Environmental seismology: What can we learn on earth surface processes with ambient noise? *Journal of Applied Geophysics*, *116*, 62–74. https://doi.org/10.1016/j.jappgeo.2015.02.001.

Leggat, M. S., Owens, P. N., Stott, T. A., Forrester, B. J., Déry, S. J., & Menounos, B. (2015). Hydro-meteorological drivers and sources of suspended sediment flux in the pro-glacial zone of the retreating Castle Creek Glacier, Cariboo Mountains, British Columbia, Canada. *Earth Surface Processes and Landforms*, *40*(11), 1542–1559. https://doi.org/10.1002/esp.3755.

Legleiter, C. J., Roberts, D. A., Marcus, W. A., & Fonstad, M. A. (2004). Passive optical remote sensing of river channel morphology and in-stream habitat: Physical basis and feasibility. *Remote Sensing of Environment*, *93*(4), 493–510. https://doi.org/10.1016/j.rse.2004.07.019.

Legleiter, C. J., & Roberts, D. A. (2005). Effects of channel morphology and sensor spatial resolution on image-derived depth estimates. *Remote Sensing of Environment*, *95*(2), 231–247. https://doi.org/10.1016/j.rse.2004/12.013.

Lentas, K., Bowden, D., Melis, N. S., Fichtner, A., Koroni, M., Smolinski, K., Bogris, A., Nikas, T., Simos, C., & Simos, I. (2023). Earthquake location based on Distributed Acoustic Sensing (DAS) as a seismic array. *Physics of the Earth and Planetary Interiors*, *344*, 107109. https://doi.org/10.1016/j.pepi.2023.107109.

Leopold, L. B., & Maddock Jr., T. (1953). *The hydraulic geometry of stream channels and some physiographic implications* (USGS Numbered Series 252; Professional Paper, p. 64). U.S. Government Printing Office. http://pubs.er.usgs.gov/publication/pp252.

Leopold, L. B. (1992). Sediment size that determines channel geometry. In Billi, P., Hey, R.D., Thorne C.R. & Tacconi, P. (Eds.), *Dynamics of gravel-bed rivers*. Wiley.

Li, D., Overeem, I., Kettner, A. J., Zhou, Y., & Lu, X. (2021). Air Temperature Regulates Erodible Landscape, Water, and Sediment Fluxes in the Permafrost-Dominated Catchment on the Tibetan Plateau. *Water Resources Research*, *57*(2), e2020WR028193. https://doi.org/10.1029/2020WR028193.

Liang, Q., Du, G., Hall, J.W. & Borthwick, A. (2008). Flood inundation modelling with an adaptive quadtree grid shallow water equation solver, *Journal of Hydraulic Engineering*, Vol 134, 1603-1610.

Liébault, F., Piégay, H., Cassel, M., & Arnaud, F. (2024). Bedload tracing with RFID tags in gravel-bed rivers: Review and meta-analysis after 20 years of field and laboratory experiments. *Earth Surface Processes and Landforms*, *49*(1), 147–169. https://doi.org/10.1002/esp.5704.

Lindsey, N. J., Martin, E. R., Dreger, D. S., Freifeld, B., Cole, S., James, S. R., Biondi, B. L., & Ajo-Franklin, J. B. (2017). Fiber-Optic Network Observations of Earthquake Wavefields. *Geophysical Research Letters*, *44*(23), 11,792-11,799. https://doi.org/10.1002/2017GL075722.

Lior, I., Sladen, A., Rivet, D., Ampuero, J.-P., Hello, Y., Becerril, C., Martins, H. F., Lamare, P., Jestin, C., Tsagkli, S., & Markou, C. (2021). On the Detection Capabilities of Underwater Distributed Acoustic Sensing. *Journal of Geophysical Research: Solid Earth*, *126*(3), e2020JB020925. https://doi.org/10.1029/2020JB020925.

Lisle, T. E., Ikeda, H., & Iseya, F. (1991). Formation of stationary alternate bars in a steep channel with mixed-size sediment: A flume experiment. *Earth Surface Processes and Landforms*, 16(5), 463–469. https://doi.org/10.1002/esp.3290160507.

Lisle, T.E., Iseya, F. & Hikeda, H. (1993). Response of a channel with alternate bars to a decrease in supply of mixed-size bed load: A flume experiment. *Water Resources Research*, 29(11), 3623-3629. https://doi.org/10.1029/93WR01673.

Liu, Y., Chen, Y., & Fang, X. (2018). A Review of Turbidity Detection Based on Computer Vision. *IEEE Access*, 6, 60586–60604. https://doi.org/10.1109/ACCESS.2018.2875071.

Mackin, J. (1948). Concept of the graded river. *Geological Society of America Bulletin*, 59, 463-511.

Maddock, I. (1999). The importance of physical habitat assessment for evaluating river health. *Freshwater Biology*, 41, 373-391.

Mair, D., Nienow, P., Sharp, M., Wohlleben, T., & Willis, I. (2002). Influence of subglacial drainage system evolution on glacier surface motion: Haut Glacier d'Arolla, Switzerland. *Journal of Geophysical Research: Solid Earth*, *107*(B8), EPM 8-1-EPM 8-13. https://doi.org/10.1029/2001JB000514.

Maizels, J. (2002). *Sediments and landforms of modern proglacial terrestrial environments* (pp. 279–316). https://doi.org/10.1016/B978-075064226-2/50012-X.

Mancini, D., & Lane, S. N. (2020). Changes in sediment connectivity following glacial debuttressing in an Alpine valley system. *Geomorphology*, *352*, 106987. https://doi.org/10.1016/j.geomorph.2019.106987.

Mancini, D., Dietze, M., Müller, T., Jenkin, M., Miesen, F., Roncoroni, M., Nicholas, A. P., & Lane, S. N. (2023a). Filtering of the Signal of Sediment Export From a Glacier by Its Proglacial Forefield. *Geophysical Research Letters*, 50(21), e2023GL106082. https://doi.org/10.1029/2023GL106082.

Mancini, D., Dietze, M., Jenkin, M., Miesen, F., & Lane, S. N. (2023b). *Suspended sediment load and bedload flux from the Glacier d'Otemma proglacial forefield (summers 2020 and 2021)* [dataset]. Zenodo. https://doi.org/10.5281/zenodo.8380815.

Mancini, D., Antoniazza, G., Roncoroni, M., Mettra, F. & Lane, S.N. (2024a). Heuristic estimation of river bathymetry in braided streams using digital image processing. *Earth Surface Processes and Landforms*. https://doi.org/10.1002/esp.5944.

Mancini, D., Antoniazza, G., Roncoroni, M., Mettra, F. & Lane, S.N. (2024b). Heuristic estimation of river bathymetry in braided streams using digital image processing: model workflow (Version 1). Zenodo. https://doi.org/10.5281/zenodo.12720137.

Mancini, D., Roncoroni, M., Miesen, F., Pythoud, Q. & Lane, S.N. (2024c). *Temporal morphodynamic evolution of the Glacier d'Otemma proglacial forefield for melt seasons 2020 and 2021: data collection and post-processing* [Data set]. Zenodo. https://doi.org/10.5281/zenodo.11347458.

Mancini, D., Roncoroni, M., Dietze, M., Jenkin, M., Müller, T., Ouvry, B., Miesen, F., Pythoud, Q., Hofmann, M., Lardet, F., Nicholas, A. & Lane, S.N. (2024d). Rates of evacuation of bedload sediment from an Alpine glacier control proglacial stream morphodynamics. *Journal of Geophysical Research: Earth Surface*. https://doi.org/10.1029/2024JF007727.

Mandlburger, G., Hauer, C., Wieser, M., & Pfeifer, N. (2015). Topo-Bathymetric LiDAR for Monitoring River Morphodynamics and Instream Habitats—A Case Study at the Pielach River. *Remote Sensing*, *7*(5), Article 5. https://doi.org/10.3390/rs70506160.

Manger, E.G. (1963). *Porosity and Bulk Density of Sedimentary Rocks (Geological Survey Bulletin 1144-E)*. U.S. Atomic Energy Commission, United States Government Printing Office.

Marcus, W. A., Legleiter, C. J., Aspinall, R. J., Boardman, J. W., & Crabtree, R. L. (2003). High spatial resolution hyperspectral mapping of in-stream habitats, depths, and woody debris in mountain streams. *Geomorphology*, 55(1), 363–380. https://doi.org/10.1016/S0169-555X(03)00150-8.

Marcus, W. A., & Fonstad, M. A. (2008). Optical remote mapping of rivers at sub-meter resolutions and watershed extents. *Earth Surface Processes and Landforms*, 33(1), 4–24. https://doi.org/10.1002/esp.1637.

Marcus, W.A., Fonstad, M.A. & Legleiter, C.J. (2012). Management applications of optical remote sensing in the active river channel. In Carbonneau, P.E & Piegay, H. (Eds.), *Fluvial Remote Sensing for Science and Management*. Wiley-Blackwell.

Mao, L., Dell'Agnese, A., Huincache, C., Penna, D., Engel, M., Niedrist, G., & Comiti, F. (2014). Bedload hysteresis in a glacier-fed mountain river. *Earth Surface Processes and Landforms*, *39*(7), 964–976. https://doi.org/10.1002/esp.3563.

Mao, L., & Carrillo, R. (2017). Temporal dynamics of suspended sediment transport in a glacierized Andean basin. *Geomorphology*, *287*, 116–125. https://doi.org/10.1016/j.geomorph.2016.02.003.

Mao, L., Comiti, F., Carrillo, R., & Penna, D. (2019). Sediment Transport in Proglacial Rivers. In Heckmann, T. & Morche, D. (Eds.), *Geomorphology of Proglacial Systems: Landform and Sediment Dynamics in Recently Deglaciated Alpine Landscapes*, 199–217. Springer International Publishing. https://doi.org/10.1007/978-3-319-94184-4_12.

Mao, L., Toro, M., Carrillo, R., Brardinoni, F., & Fraccarollo, L. (2020). Controls Over Particle Motion and Resting Times of Coarse Bed Load Transport in a Glacier-Fed Mountain Stream. *Journal of Geophysical Research: Earth Surface*, *125*(4), e2019JF005253. https://doi.org/10.1029/2019JF005253.

Marren, P. M. (2002). Glacier margin fluctuations, Skaftafellsjökull, Iceland: Implications for sandur evolution. *Boreas*, *31*(1), 75–81. https://doi.org/10.1111/j.1502-3885.2002.tb01057.x.

Marren, P. M. (2005). Magnitude and frequency in proglacial rivers: a geomorphological and sedimentological perspective. *Earth-Science Reviews*, *70*(3), 203-251. https://doi.org/10.1016/j.earscirew.2004.12.002.

Marren, P. M., & Toomath, S. C. (2013). Fluvial adjustments in response to glacier retreat: Skaftafellsjökull, Iceland. *Boreas*, *42*(1), 57–70. https://doi.org/10.1111/j.1502-3885.2012.00275.x.

Marren, P. M., & Toomath, S. C. (2014). Channel pattern of proglacial rivers: Topographic forcing due to glacier retreat. *Earth Surface Processes and Landforms*, *39*(7), 943–951. https://doi.org/10.1002/esp.3545.

Martínez-Jaramillo, J. E., van Ackere, A., & Larsen, E. (2023). Long term impacts of climate change on the transition towards renewables in Switzerland. *Energy*, *263*, 126089. https://doi.org/10.1016/j.energy.2022.126089.

Maxwell, A. E. (1975). Limitations on the Use of the Multiple Linear Regression Model. *British Journal of Mathematical and Statistical Psychology*, 28(1), 51–62. https://doi.org/10.1111/j.2044-8317.1975.tb00547.x.

McKay, M. D. (1992). Latin hypercube sampling as a tool in uncertainty analysis of computer models. *Proceedings of the 24th Conference on Winter Simulation*, 557–564. https://doi.org/ 10.1145/167293.167637.

McNamara, J. P., & Borden, C. (2004). Observations on the movement of coarse gravel using implanted motion-sensing radio transmitters. *Hydrological Processes*, *18*(10), 1871–1884. https://doi.org/10.1002/hyp.1453.

McQueen, R., Ashmore, P., Millard, T., & Goeller, N. (2021). Bed Particle Displacements and Morphological Development in a Wandering Gravel-Bed River. *Water Resources Research*, *57*(2), e2020WR027850. https://doi.org/10.1029/2020WR027850.

Mersel, M. K., Smith, L. C., Andreadis, K. M., & Durand, M. T. (2013). Estimation of river depth from remotely sensed hydraulic relationships. *Water Resources Research*, *49*(6), 3165–3179. https://doi.org/10.1002/wrcr.20176.

Métivier, F. (1999). Diffusivelike buffering and saturation of large rivers. *Physical Review E*, *60*(5), 5827–5832. https://doi.org/10.1103/PhysRevE.60.5827.

Meyer-Peter, E., & Muller, R. (1948). Formulas for Bed Load Transport. *Proceedings of 2nd Meeting of the International Association for Hydraulic Structures Research, Delft*, 39–64.

Micheletti, N., Lane, S. N., & Chandler, J. H. (2015a). Application of archival aerial photogrammetry to quantify climate forcing of alpine landscapes. *The Photogrammetric Record*, *30*(150), 143–165. https://doi.org/10.1111/phor.12099.

Micheletti, N., Lambiel, C., & Lane, S. N. (2015b). Investigating decadal-scale geomorphic dynamics in an alpine mountain setting. *Journal of Geophysical Research: Earth Surface*, *120*(10), 2155–2175. https://doi.org/10.1002/2015JF003656.

Milan, D.J., Heritage, G.L. & Hetherington, D. (2007). Application of a 3D laser scanner in the assessment of erosion and deposition volumes and channel change in a proglacial river. *Earth Surface Processes and Landforms*, 31(11), 1657-1474. https://doi.org/10.1002/esp.1592.

Miller, H. R., & Lane, S. N. (2019). Biogeomorphic feedbacks and the ecosystem engineering of recently deglaciated terrain. *Progress in Physical Geography: Earth and Environment*, *43*(1), 24–45. https://doi.org/10.1177/0309133318816536.

Milner, A. M., Khamis, K., Battin, T. J., Brittain, J. E., Barrand, N. E., Füreder, L., Cauvy-Fraunié, S., Gíslason, G. M., Jacobsen, D., Hannah, D. M., Hodson, A. J., Hood, E., Lencioni, V., Ólafsson, J. S., Robinson, C. T., Tranter, M., & Brown, L. E. (2017). Glacier shrinkage driving global changes in downstream systems. *Proceedings of the National Academy of Sciences*, *114*(37), 9770–9778. https://doi.org/10.1073/pnas.1619807114.

Misset, C., Recking, A., Legout, C., Bakker, M., Bodereau, N., Borgniet, L., Cassel, M., Geay, T., Gimbert, F., Navratil, O., Piegay, H., Valsangkar, N., Cazilhac, M., Poirel, A., & Zanker, S. (2020). Combining multi-physical measurements to quantify bedload transport and morphodynamics interactions in an Alpine braiding river reach. *Geomorphology*, *351*, 106877. https://doi.org/10.1016/j.geomorph.2019.106877.

Mizuyama, T., Oda, A., Laronne, J. B., Nonaka, M., & Matsuoka, M. (2010). *Laboratory Tests of a Japanese Pipe Geophone for Continuous Acoustic Monitoring of Coarse Bedload* (2010–5091; pp. 319–335). US Geological Survey Scientific Investigations Report.

Mjaavatten, A. (2023). Curvature of a 1D curve in a 2D or 3D space (https://www.mathworks.com/matlabcentral/fileexchange/69452-curvature-of-a-1d-curve-in-a-2d-or-3d-space), MATLAB Central File Exchange. Retrieved September 4, 2023.

Moon, T. (2017). Saying goodbye to glaciers. *Science*, *356*(6338), 580–581. https://doi.org/10.1126/science.aam9625.

Morgan, J.A., Kumar, N., Horner-Devine, A.R., Ahrendt, S., Istanbullouglu, E. & Bandaragoda, C. (2020). The use of a morphological acceleration factor in the simulation of large-scale fluvial morphodynamics, *Geomorphology*, Vol 356. https://doi.org/10.1016/j.geomorph.2020.107088.

Mosley, M. P. (1982). Analysis of the effect of changing discharge on channel morphology and instream uses in a Braided River, Ohau River, New Zealand. *Water Resources Research*, 18(4), 800-812. https://doi.org/10.1029/WR018i004p00800.

Mosley, M.P. (1983). Response of braided rivers to changing discharge. *Journal of Hydrology (New Zealand)*, 22(1), 18-67.

Müller, T., & Miesen, F. (2022). *Stream discharge, stage, electrical conductivity & temperature dataset from Otemma glacier forefield, Switzerland (from July 2019 to October 2021)* [dataset]. Zenodo. https://doi.org/10.5281/zenodo.6202732.

Müller, T., Lane, S. N., & Schaefli, B. (2022). Towards a hydrogeomorphological understanding of proglacial catchments: An assessment of groundwater storage and release in an Alpine catchment. *Hydrology and Earth System Sciences*, *26*(23), 6029–6054. https://doi.org/10.5194/hess-26-6029-2022.

Müller, T., Roncoroni, M., Mancini, D., Lane, S. N., & Schaefli, B. (2024). Current and future roles of meltwater–groundwater dynamics in a proglacial Alpine outwash plain. *Hydrology and Earth System Sciences*, *28*(4), 735–759. https://doi.org/10.5194/hess-28-735-2024.

Murray, A. B., & Paola, C. (1994). A cellular model of braided rivers. *Nature*, 371(6492), Article 6492. https://doi.org/10.1038/371054a0.

Neter, J., Kutner, M. H., & Wasserman, W. (1983). *Applied linear regression models*. McGraw-Hill Higher Education.

Nezu, I., Nakagawa, H., & Tominaga, A. (1985). Secondary Currents in a Straight Channel Flow and the Relation to Its Aspect Ratio. In Bradbury, L. J. S, Durst, F., Launder, B.E., Schmidt, F. W. & Whitelaw J. H. (Eds.), *Turbulent Shear Flows 4*, 246–260, Springer. https://doi.org/10.1007/978-3-642-69996-2_20.

Nicholas, A. P., Ashworth, P. J., Kirkby, M. J., Macklin, M. G., & Murray, T. (1995). Sediment slugs: Large-scale fluctuations in fluvial sediment transport rates and storage volumes. *Progress in Physical Geography: Earth and Environment*, *19*(4), 500–519. https://doi.org/10.1177/030913339501900404.

Nicholas, A. (2013a). Morphodynamic diversity of the world's largest rivers. *Geology*, *41*(4), 475–478. https://doi.org/10.1130/G34016.1.

Nicholas, A. P. (2013b). Modelling the continuum of river channel patterns. *Earth Surface Processes and Landforms*, *38*(10), 1187–1196. https://doi.org/10.1002/esp.3431.

Nicholas, A. P., Ashworth, P. J., Sambrook Smith, G. H., & Sandbach, S. D. (2013). Numerical simulation of bar and island morphodynamics in anabranching megarivers. *Journal of Geophysical Research: Earth Surface*, *118*(4), 2019–2044. https://doi.org/10.1002/jgrf.20132.

Nicholas, A.P. (submitted). Modelling river and floodplain evolution using physics-based and reduced-complexity approaches. *Earth Surface Processes and Landforms*.

Nienow, P., Sharp, M., & Willis, I. (1998). Seasonal changes in the morphology of the subglacial drainage system, Haut Glacier d'Arolla, Switzerland. *Earth Surface Processes and Landforms*, *23*(9), 825–843. https://doi.org/10.1002/(SICI)1096-9837(199809)23:9<825::AID-ESP893>3.0.CO;2-2.

Niethammer, U., Rothmund, S., James, M.R., Travelletti, J. & Joswig, M. (2010). UAV-based remote sensing of landslides. *International Archives of Photogrammetry, Remote Sensing, and Spatial Information Sciences*, 38, 496-501.

Olinde, L., & Johnson, J. P. L. (2015). Using RFID and accelerometer-embedded tracers to measure probabilities of bed load transport, step lengths, and rest times in a mountain stream. *Water Resources Research*, *51*(9), 7572–7589. https://doi.org/10.1002/2014WR016120.

Olsen, A. A., McLaughlin, J. E., & Harpe, S. E. (2020). Using multiple linear regression in pharmacy education scholarship. *Currents in Pharmacy Teaching and Learning*, 12(10), 1258–1268. https://doi.org/10.1016/j.cptl.2020.05.017.

Orwin, J. F., & Smart, C. C. (2004). Short-term spatial and temporal patterns of suspended sediment transfer in proglacial channels, small River Glacier, Canada. *Hydrological Processes*, *18*(9), 1521–1542. https://doi.org/10.1002/hyp.1402.

Ouedraogo, M.M., Degre, A., Debouche, C. & Lisein J. (2014). The evaluation of unmanned aerial system-based photogrammetry and terrestrial laser scanning to generate DEMs of agricultural watersheds. *Geomorphology*, 214, 339-355. https://doi.org/10.1016/j.geomorph.2014.02.016.

Paola, C. (2001). Modelling stream braiding over a range of scales. In Mosley, M.P. (Ed.), *Gravel-bed rivers*. New Zealand Hydrological Society.

Parker, G. (1979). Hydraulic geometry of active gravel-bed rivers. *Journal of Hydraulic Division*, 105, 1185-1201.

Parker, G., Shimizu, Y., Wilkerson, G. V., Eke, E. C., Abad, J. D., Lauer, J. W., Paola, C., Dietrich, W. E., & Voller, V. R. (2011). A new framework for modeling the migration of meandering rivers. *Earth Surface Processes and Landforms*, 36(1), 70–86. https://doi.org/10.1002/esp.2113.

Parsons, A. J., Cooper, J., Wainwright, J., & Sekiguchi, T. (2018). Virtual velocity of sand transport in water. *Earth Surface Processes and Landforms*, *43*(3), 755–761. https://doi.org/10.1002/esp.4262.

Paster, M., Flödl, P., Neureiter, A., Weyss, G., Hynek, B., Pulg, U., Skoglund, R. Ø., Habersack, H., & Hauer, C. (2022). Channel evolution processes in a diamictic glacier foreland. Implications on downstream sediment supply: Case study Pasterze/Austria. *Hydrology and Earth System Sciences Discussions*, 1–20. https://doi.org/10.5194/hess-2022-347.

Pelosi, A., & Parker, G. (2014). Morphodynamics of river bed variation with variable bedload step length. *Earth Surface Dynamics*, *2*(1), 243–253. https://doi.org/10.5194/esurf-2-243-2014.

Pelto, M. S. (2011). Hydropower: Hydroelectric Power Generation from Alpine Glacier Melt. In Singh, V.P., Singh, P. & Haritashya, U.K. (Eds.), *Encyclopedia of Snow, Ice and Glaciers*, 546–551). Springer Netherlands. https://doi.org/10.1007/978-90-481-2642-2_624.

Perolo, P., Bakker, M., Gabbud, C., Moradi, G., Rennie, C., & Lane, S. n. (2019). Subglacial sediment production and snout marginal ice uplift during the late ablation season of a temperate valley glacier. *Earth Surface Processes and Landforms*, *44*(5), 1117–1136. https://doi.org/10.1002/esp.4562.

Petit, F., Houbrechts, G., Peeters, A., Hallot, E., Van Campenhout, J., & Denis, A.-C. (2015). Dimensionless critical shear stress in gravel-bed rivers. *Geomorphology*, *250*, 308–320. https://doi.org/10.1016/j.geomorph.2015.09.008.

Phillips, J. D. (2003). Sources of nonlinearity and complexity in geomorphic systems. *Progress in Physical Geography: Earth and Environment*, *27*(1), 1–23. https://doi.org/10.1191/0309133303pp340ra.

Piana Agostinetti, N., Villa, A., & Saccorotti, G. (2022). Distributed acoustic sensing as a tool for subsurface mapping and seismic event monitoring: A proof of concept. *Solid Earth*, *13*(2), 449–468. https://doi.org/10.5194/se-13-449-2022.

Powell, D. M. (1998). *Patterns and processes of sediment sorting in gravel-bed rivers*.

Pratomo, D. G., Khomsin, & Putranto, B. F. E. (2019). Analysis of the green light penetration from Airborne LiDAR Bathymetry in Shallow Water Area. *IOP Conference Series: Earth and Environmental Science*, *389*(1), 012003. https://doi.org/10.1088/1755-1315/389/1/012003.

Rainato, R., Mao, L., & Picco, L. (2018). Near-bankfull floods in an Alpine stream: Effects on the sediment mobility and bedload magnitude. *International Journal of Sediment Research*, *33*(1), 27–34. https://doi.org/10.1016/j.ijsrc.2017.03.006.

Rainato, R., Mao, L., & Picco, L. (2020). The effects of low-magnitude flow conditions on bedload mobility in a steep mountain stream. *Geomorphology*, *367*, 107345. https://doi.org/10.1016/j.geomorph.2020.107345.

Ranasinghe, R., Swinkels, C., Luijendijk, A., Bosboom, J., Roelvink, D., Stive, M. & Walstra, D. (2011). Morphodynamic upscaling with the MORFAC approach, *Coastal Engineering*, Vol 32. https://doi.org/10.9753/icce.v32.sediment.59.

Raymond, C. F., Benedict, R. J., Harrison, W. D., Echelmeyer, K. A., & Sturm, M. (1995). Hydrological discharges and motion of Fels and Black Rapids Glaciers, Alaska, U.S.A.: Implications for the structure of their drainage systems. *Journal of Glaciology*, *41*(138), 290–304. https://doi.org/10.3189/S002214300001618X.

Reid, H.E., Williams, R.D., Brierley, G.J., Coleman, S.E., Lamb, R., Rennie, C.D. & Tancock, M.J. (2019). *Earth Surface Processes and Landforms*, *44*, 596-613. https://doi.org/10.1002/esp.4521.

Richards, K. (1984). Some observations on suspended sediment dynamics in Storbregrova, Jotunheimen. *Earth Surface Processes and Landforms*, *9*(2), 101–112. https://doi.org/10.1002/esp.3290090202.

Richardson, W. R., & Thorne, C. R. (1988). Secondary Currents around Braid Bar in Brahmaputra River, Bangladesh. *Journal of Hydraulic Engeneering*, 124, 325–328.

Richer, E. E., Fetherman, E. R., Kondratieff, M. C., & Barnes, T. A. (2017). Incorporating GPS and Mobile Radio Frequency Identification to Detect PIT-Tagged Fish and Evaluate Habitat Utilization in Streams. *North American Journal of Fisheries Management*, *37*(6), 1249–1264. https://doi.org/10.1080/02755947.2017.1374312.

Rickenmann, D. (1991). Hyperconcentrated Flow and Sediment Transport at Steep Slopes. *Journal of Hydraulic Engineering*, *117*(11), 1419–1439. https://doi.org/10.1061/(ASCE)0733-9429(1991)117:11(1419).

Rickenmann, D. (2001). Comparison of bed load transport in torrents and gravel bed streams. *Water Resources Research*, *37*(12), 3295–3305. https://doi.org/10.1029/2001WR000319.

Rickenmann, D., Turowski, J. M., Fritschi, B., Wyss, C., Laronne, J., Barzilai, R., Reid, I., Kreisler, A., Aigner, J., Seitz, H., & Habersack, H. (2013). Bedload transport measurements with impact plate geophones: Comparison of sensor calibration in different gravel-bed streams. *Earth Surface Processes and Landforms*, *39*(7), 928–942. https://doi.org/10.1002/esp.3499.

Rickenmann, D. (2020). Effect of Sediment Supply on Cyclic Fluctuations of the Disequilibrium Ratio and Threshold Transport Discharge, Inferred From Bedload Transport Measurements Over 27 Years at the Swiss Erlenbach Stream. *Water Resources Research*, *56*(11), e2020WR027741. https://doi.org/10.1029/2020WR027741.

Riihimaki, C. A., MacGregor, K. R., Anderson, R. S., Anderson, S. P., & Loso, M. G. (2005). Sediment evacuation and glacial erosion rates at a small alpine glacier. *Journal of Geophysical Research (Earth Surface)*, *110*, F03003. https://doi.org/10.1029/2004JF000189.

Roncoroni, M., Mancini, D., Kohler, T. J., Miesen, F., Gianini, M., Battin, T. J., & N. Lane, S. (2022). Centimeter-scale mapping of phototrophic biofilms in glacial forefields using visible band ratios and UAV imagery. *International Journal of Remote Sensing*, *43*(13), 4723–4757. https://doi.org/10.1080/01431161.2022.2079963.

Roncoroni, M., Mancini, D., Miesen, F., Müller, T., Gianini, M., Ouvry, B., Clémençon, M., Lardet, F., Battin, T. J., & Lane, S. N. (2023a). Decrypting the stream periphyton physical habitat of recently deglaciated floodplains. *Science of The Total Environment*, *867*, 161374. https://doi.org/10.1016/j.scitotenv.2022.161374.

Roncoroni, M., Mancini, D., & Miesen, F. (2023b). *SfM-MVS derived orthomosaics of the Otemma glacier forefield (2020)* [dataset]. Zenodo. https://doi.org/10.5281/zenodo.7514935.

Roncoroni, M., Ballu, A., Selitaj, A., Mancini, D., Miesen, F., Aguet, M., Battin, T. I., & Lane, S. N. (2024). Ecosystem engineering by periphyton in Alpine proglacial streams. *Earth Surface Processes and Landforms*, *49*(1), 417–431. https://doi.org/10.1002/esp.5712.

Rose, K. C., Hamilton, D. P., Williamson, C. E., McBride, C. G., Fischer, J. M., Olson, M. H., Saros, J. E., Allan, M. G., & Cabrol, N. (2014). Light attenuation characteristics of glacially-fed lakes. *Journal of Geophysical Research: Biogeosciences*, 119(7), 1446–1457. https://doi.org/10.1002/2014JG002674.

Roussel, E., Marren, P. M., Cossart, E., Toumazet, J.-P., Chenet, M., Grancher, D., & Jomelli, V. (2018). Incision and aggradation in proglacial rivers: Post-Little Ice Age long-profile adjustments of Southern Iceland outwash plains. *Land Degradation & Development*, *29*(10), 3753–3771. https://doi.org/10.1002/ldr.3127.

Roy, D. P., Huang, H., Houborg, R., & Martins, V. S. (2021). A global analysis of the temporal availability of PlanetScope high spatial resolution multi-spectral imagery. *Remote Sensing of Environment*, *264*, 112586. https://doi.org/10.1016/j.rse.2021.112586.

Sanchez-Sesma, F. J., Weaver, R. L., Kawase, H., Matsushima, S., Luzon, F., & Campillo, M. (2011). Energy partition among elastic waves for dynamic surface loads in a semi-infinite solid. *Bulletin of the Seismological Society of America*, *101*, 1704–1709. https://doi.org/10.1785/0120100196.

Schaefli, B., Manso, P., Fischer, M., Huss, M., & Farinotti, D. (2019). The role of glacier retreat for Swiss hydropower production. *Renewable Energy*, *132*, 615–627. https://doi.org/10.1016/j.renene.2018.07.104.

Schaperow, J. R., Li, D., Margulis, S. A., & Lettenmaier, D. P. (2019). A Curve-Fitting Method for Estimating Bathymetry From Water Surface Height and Width. *Water Resources Research*, *55*(5), 4288–4303. https://doi.org/10.1029/2019WR024938.

Schiefer, E., & Gilbert, R. (2007). Reconstructing morphometric changes in a proglacial landscape using historical aerial photography and automated DEM generation. *Geomorphology*, *88*(1), 167–178. https://doi.org/10.1016/j.geomorph.2006.11.003.

Schmandt, B., Gaeuman, D., Stewart, R., Hansen, S. M., Tsai, V. C., & Smith, J. (2017). Seismic array constraints on reach-scale bedload transport. *Geology*, *45*(4), 299–302. https://doi.org/10.1130/G38639.1.

Schneider, J. M., Rickenmann, D., Turowski, J. M., Bunte, K., & Kirchner, J. W. (2015). Applicability of bed load transport models for mixed-size sediments in steep streams considering macro-roughness. *Water Resources Research*, *51*(7), 5260–5283. https://doi.org/10.1002/2014WR016417.

Schuum, S. A. (1977). *The Fluvial System*. Wiley.

Schumm, S. A. (1981). Evolution and Response of the Fluvial System, Sedimentologic Implications. In F. G. Ethridge & R. M. Flores (Eds.), *Recent and Ancient Nonmarine Depositional Environments: Models for Exploration* (Vol. 31, p. 0). SEPM Society for Sedimentary Geology. https://doi.org/10.2110/pec.81.31.0019.

Schuum, S. A. (1985). Patterns of alluvial rivers. *Annual Review of Earth and Planetary Sciences*, *13*, 5–7.

Schuurman, F., Marra, W.A. & Kleinhans, M.G. (2013). Physical-based modeling of large braided sand-bed rivers: bar pattern formation, dynamics and sensitivity. *Journal of Geophysical Research: Earth Surface*, 118, 2509-2527. https://doi.org/10.1002/2013JF002896.

Schuurman, F., & Kleinhans, M. G. (2015). Bar dynamics and bifurcation evolution in a modelled braided sand-bed river. *Earth Surface Processes and Landforms*, *40*(10), 1318–1333. https://doi.org/10.1002/esp.3722.

Seier, G., Stangl, J., Schöttl, S., Sulzer, W., & Sass, O. (2017). UAV and TLS for monitoring a creek in an alpine environment, Styria, Austria. *International Journal of Remote Sensing*, *38*(8–10), 2903–2920. https://doi.org/10.1080/01431161.2016.1277045.

Sharp, M. J., Richards, K. S., & Tranter, M. (1998). *Glacier hydrology and hydrochemistry*. John Wiley & Sons.

Shreve, R. L. (1972). Mouvement of water in glaciers. *Journal of Glaciology*, *11*, 205–214.

Siegfried, L., Vittoz, P., & Lane, S. N. (2023). Hydrological heterogeneity and the plant colonization of recently deglaciated terrain. *Arctic, Antarctic, and Alpine Research*, *55*(1), 2259677. https://doi.org/10.1080/15230430.2023.2259677.

Smith, N. D. (1985). Proglacial fluvial environment. In Ashley, G.M., Shaw, J. & Smith, N.D. (Eds.), *Glacial Sedmentary Environments*, 85–134. SEPM Society for Sedimentary Geology.

Smith, M. w., & Vericat, D. (2014). Evaluating Shallow-Water Bathymetry from Through-Water Terrestrial Laser Scanning Under a Range of Hydraulic and Physical Water Quality Conditions. *River Research and Applications*, 30(7), 905–924. https://doi.org/10.1002/rra.2687.

Staines, K. E. H., Carrivick, J. L., Tweed, F. S., Evans, A. J., Russell, A. J., Jóhannesson, T., & Roberts, M. (2015). A multi-dimensional analysis of pro-glacial landscape change at Sólheimajökull, southern Iceland. *Earth Surface Processes and Landforms*, *40*(6), 809–822. https://doi.org/10.1002/esp.3662.

Stecca, G., Federizzi, D., Measures, R., Hicks, D.M., Hoyle, J. & Zolezzi, G. (2022). Development of a numerical model for braided river morphology and vegetation development with application to the Lower Waitaki River (Aotearoa – New Zealand). *Advances in Water Resources*, 166, 104236. https://doi.org/10.1016/j.advwatres.2022.104236.

Stoffel, M., & Huggel, C. (2012). Effects of climate change on mass movements in mountain environments. *Progress in Physical Geography: Earth and Environment*, *36*(3), 421–439. https://doi.org/10.1177/0309133312441010.

Stott, T., & Mount, N. (2007). Alpine proglacial suspended sediment dynamics in warm and cool ablation seasons: Implications for global warming. *Journal of Hydrology*, *332*(3), 259–270. https://doi.org/10.1016/j.jhydrol.2006.07.001.

Stott, T., Nuttall, A.-M., Eden, N., Smith, K., & Maxwell, D. (2008). Suspended Sediment Dynamics in the Morteratsch Pro-Glacial Zone, Bernina Alps, Switzerland. *Geografiska*

*Annaler: Series A, Physical Geography, 90*(4), 299–313. https://doi.org/10.1111/j.1468-0459.2008.00347.x.

Straub, K. M., Duller, R. A., Foreman, B. Z., & Hajek, E. A. (2020). Buffered, Incomplete, and Shredded: The Challenges of Reading an Imperfect Stratigraphic Record. *Journal of Geophysical Research: Earth Surface*, *125*(3), e2019JF005079. https://doi.org/10.1029/2019JF005079.

Struiksma, N., Olesen, K. W., Flokstra, C., & De Vriend, H. J. (1985). Bed deformation in curved alluvial channels. *Journal of Hydraulic Research*, 23(1), 57–79. https://doi.org/10.1080/00221688509499377.

Swift, D. A., Nienow, P. W., & Hoey, T. B. (2005). Basal sediment evacuation by subglacial meltwater: Suspended sediment transport from Haut Glacier d'Arolla, Switzerland. *Earth Surface Processes and Landforms*, *30*(7), 867–883. https://doi.org/10.1002/esp.1197.

Swift, D. A., Tallentire, G. D., Farinotti, D., Cook, S. J., Higson, W. J., & Bryant, R. G. (2021). The hydrology of glacier-bed overdeepenings: Sediment transport mechanics, drainage system morphology, and geomorphological implications. *Earth Surface Processes and Landforms*, *46*(11), 2264–2278. https://doi.org/10.1002/esp.5173.

Swiss Competence Center for Energy Research - Supply of Electricity (SSCER-SoE). (2019). *Climate change impact of Swiss hydropower productio: Synthesis report.* http://static.seismo.ethz.ch/sccer-soe/Reports/Synth_Rep_Climate_change_impact_on_Swiss_hydropower_production_lowres.pdf.

Szafarczyk, A., & Toś, C. (2023). The Use of Green Laser in LiDAR Bathymetry: State of the Art and Recent Advancements. *Sensors*, *23*(1), Article 1. https://doi.org/10.3390/s23010292.

Tabesh, M., Vollmer, S., Schüttrumpf, H. & Frings, R.M. (2022). Spatial variability in river bed porosity determined by nuclear density gauging: A case study from a French gravel-bed river. *Sedimentology*, 62(2), 823-844. https://doi.org/10.1111/sed.12928.

Tamminga, A., Hugenholtz, C., Eaton, B., & Lapointe, M. (2015). Hyperspatial Remote Sensing of Channel Reach Morphology and Hydraulic Fish Habitat Using an Unmanned Aerial Vehicle (UAV): A First Assessment in the Context of River Research and Management. *River Research and Applications*, *31*(3), 379–391. https://doi.org/10.1002/rra.2743.

Tate, N.J., Brundson, C., Charlton, M., Fotheringham, A.S. & Jarvis, C.H. (2005). Smoothing/filtering LiDAR digital surface models. Experiments with lows regression and discrete wavelets. *Journal of Geographical Systems*, 7, 279-290. https://doi.org/10.1007/s10109-005-0007-4.

Taylor, J. R. (1997). *An Introduction to Error Analysis: The Study of Uncertainties in Physical Measurements*. University Science Books.

Thompson, C. G., Kim, R. S., Aloe, A. M., & Becker, B. J. (2017). Extracting the Variance Inflation Factor and Other Multicollinearity Diagnostics from Typical Regression Results. *Basic and Applied Social Psychology*, 39(2), 81–90. https://doi.org/10.1080/01973533.2016.1277529.

Tribaldos, V. R., & Ajo-Franklin, J. B. (2021). Aquifer Monitoring Using Ambient Seismic Noise Recorded With Distributed Acoustic Sensing (DAS) Deployed on Dark Fiber. *Journal of Geophysical Research: Solid Earth*, *126*(4), e2020JB021004. https://doi.org/10.1029/2020JB021004.

Tsai, V. C., Minchew, B., Lamb, M. P., & Ampuero, J.-P. (2012). A physical model for seismic noise generation from sediment transport in rivers. *Geophysical Research Letters*, *39*(2). https://doi.org/10.1029/2011GL050255.

Turowski, J. M., Rickenmann, D., & Dadson, S. J. (2010). The partitioning of the total sediment load of a river into suspended load and bedload: A review of empirical data. *Sedimentology*, *57*(4), 1126–1146. https://doi.org/10.1111/j.1365-3091.2009.01140.x.

Turowski, J. M., Badoux, A., & Rickenmann, D. (2011). Start and end of bedload transport in gravel-bed streams. *Geophysical Research Letters*, *38*(4). https://doi.org/10.1029/2010GL046558.

Van De Wiel, M. J., & Coulthard, T. J. (2010). Self-organized criticality in river basins: Challenging sedimentary records of environmental change. *Geology*, *38*(1), 87–90. https://doi.org/10.1130/G30490.1.

Van Dijk, M., Postma, G., & Kleinhans, M. G. (2009). Autocyclic behaviour of fan deltas: An analogue experimental study. *Sedimentology*, *56*(5), 1569–1589. https://doi.org/10.1111/j.1365-3091.2008.01047.x.

van Leer, B. (1979). Towards the ultimate conservation difference scheme. V. A second-order sequel to Godunov's method, *Journal of Computational Physics*, Vol 32, 101-136.

van Rijn, L. C. (1984). Sediment Transport, Part II: Suspended Load Transport. *Journal of Hydraulic Engineering*, *110*(11), 1613–1641. https://doi.org/10.1061/(ASCE)0733-9429(1984)110:11(1613).

van Rijn, L. C. (1993). *Principles of Sediment Transport in Rivers, Estuaries and Coastal Seas*. Aqua Publications.

Vázquez-Tarrío, D., Recking, A., Liébault, F., Tal, M., & Menéndez-Duarte, R. (2019). Particle transport in gravel-bed rivers: Revisiting passive tracer data. *Earth Surface Processes and Landforms*, *44*(1), 112–128. https://doi.org/10.1002/esp.4484.

Vehling, L., Baewert, H., Glira, P., Moser, M., Rohn, J., & Morche, D. (2017). Quantification of sediment transport by rockfall and rockslide processes on a proglacial rock slope (Kaunertal, Austria). *Geomorphology*, *287*, 46–57. https://doi.org/10.1016/j.geomorph.2016.10.032.

Venditti, J.G., Nelson, P.A., Bradley, R.W., Haught, D. & Gitto, A.B. (2017). Bedforms, Structures, Patches and Sediment Supply in Gravel-Bed Rivers. In Tsutsumi, D. & Laronne, B. (Eds.), *Gravel-Bed Rivers: Processes and Disasters*. Wiley

Vericat, D., Church, M., & Batalla, R. J. (2006). Bed load bias: Comparison of measurements obtained using two (76 and 152 mm) Helley-Smith samplers in a gravel bed river. *Water Resources Research*, *42*(1). https://doi.org/10.1029/2005WR004025.

Walter, F., Gräff, D., Lindner, F., Paitz, P., Köpfli, M., Chmiel, M., & Fichtner, A. (2020). Distributed acoustic sensing of microseismic sources and wave propagation in glaciated terrain. *Nature Communications*, *11*(1), Article 1. https://doi.org/10.1038/s41467-020-15824-6.

Wang, S., & Hao, H. (2002). Effects of random variations of soil properties on site amplification of seismic ground motions. *Soil Dynamics and Earthquake Engineering*, *22*(7), 551–564. https://doi.org/10.1016/S0267-7261(02)00038-6.

Warburton, J. (1990). An Alpine Proglacial Fluvial Sediment Budget. *Geografiska Annaler. Series A, Physical Geography*, *72*(3/4), 261–272. https://doi.org/10.2307/521154.

Warburton, J. (1996). Active braidplain width, bed load transport and channel morphology in a model braided river. *Journal of Hydrology New Zealand*, 35, 259-285.

Ward, J.V., Tockner, K., Arscott, D.B. & Claret, C. (2002). Riverine landscape diversity. *Freshwater Biology*, 47, 517-39. https://doi.org/10.1046/j.1365-2427.2002.00893.x.

Weber, M. D., & Pasternack, G. B. (2017). Valley-scale morphology drives differences in fluvial sediment budgets and incision rates during contrasting flow regimes. *Geomorphology*, 288, 39–51. https://doi.org/10.1016/j.geomorph.2017.03.018.

Westaway, R. M., Lane, S. N., & Hicks, D. M. (2000). The Development of an automated correction procedure for digital photogrammetry for the study of wide, shallow, gravel-bed rivers. *Earth Surface Processes and Landforms*, 25, 209–226. https://doi.org/10.1002/(SICI)1096-9837(200002)25:2<209::AID-ESP84>3.0.CO;2-Z.

Westaway, R. M., Lane, S. N., & Hicks, D. M. (2001). Remote sensing of clear-water, shallow, gravel-bed rivers using digital photogrammetry. *Photogrammetric Engineering & Remote Sensing*, 67(11), 1271–1281.

Westaway, R. M., Lane, S. N., & Hicks, D. M. (2003). Remote survey of large-scale braided, gravel-bed rivers using digital photogrammetry and image analysis. *International Journal of Remote Sensing*, *24*(4), 795–815. https://doi.org/10.1080/01431160110113070.

Westoby, M. J., Brasington, J., Glasser, N. F., Hambrey, M. J., & Reynolds, J. M. (2012). 'Structure-from-Motion' photogrammetry: A low-cost, effective tool for geoscience

applications. *Geomorphology*, *179*, 300–314. https://doi.org/10.1016/j.geomorph.2012.08.021.

Wetterauer, K., Scherler, D., Anderson, L. S., & Wittmann, H. (2022). Temporal evolution of headwall erosion rates derived from cosmogenic nuclide concentrations in the medial moraines of Glacier d'Otemma, Switzerland. *Earth Surface Processes and Landforms*, *47*(10), 2437–2454. https://doi.org/10.1002/esp.5386.

Wheaton, J. M., Brasington, J., Darby, S. E., Kasprak, A., Sear, D., & Vericat, D. (2013). Morphodynamic signatures of braiding mechanisms as expressed through change in sediment storage in a gravel-bed river. *Journal of Geophysical Research: Earth Surface*, *118*(2), 759–779. https://doi.org/10.1002/jgrf.20060.

Wilcock, P.R. & Crowe, J.C. (2003). Surface-based Transport Model for Mixed-Size Sediment. *Journal of Hydraulic Engineering*, 129, 120-128. https://doi.org/10.1061/(asce)0733-9429(2003)129:2(120).

Wilcock, P. R., Pitlick, J., & Cui, Y. (2009). *Sediment transport primer: Estimating bed-material transport in gravel-bed rivers* (General Technical Report RMRS-GTR-226). U.S. Department of Agriculture, Forest Service.

Williams, R., Brasington, J., Vericat, D., Hicks, M., Labrosse, F., & Neal, M. (2011). Monitoring Braided River Change Using Terrestrial Laser Scanning and Optical Bathymetric Mapping. In Smith, M. J., Paron, P. & Griffiths, J.S. (Eds.), *Developments in Earth Surface Processes*, 15, 507-532. Elsevier. https://doi.org/10.1016/B978-0-444-53446-0.00020-3.

Williams, R. D., Measures, R., Hicks, D. M., & Brasington, J. (2016a). Assessment of a numerical model to reproduce event-scale erosion and deposition distributions in a braided river. *Water Resources Research*, *52*(8), 6621–6642. https://doi.org/10.1002/2015WR018491.

Williams. R.D., Brasington, J. & Hicks, D.M. (2016b). Numerical Modelling of Braided River Morphodynamics: Review and Challenges. *Geography Compass*, 10, 102-127. https://doi.org/10.1111/gec3.12260.

Winterbottom, S. J., & Gilvear, D. J. (1997). Quantification of channel bed morphology in gravel-bed rivers using airborne multispectral imagery and aerial photography. *Regulated Rivers: Research & Management*, 13(6), 489–499. https://doi.org/10.1002/(SICI)1099-1646(199711/12)13:6<489::AID-RRR471>3.0.CO;2-X.

Wolman, M. G. (1954). A method of sampling coarse river-bed material. *Eos, Transactions American Geophysical Union*, 35(6), 951-956. https://doi.org/10.1029/TR035i006p00951.

Woodget, A., Carbonneau, P., Visser, F., & Maddock, I. (2015). Quantifying submerged fluvial topography using hyperspatial resolution UAS imagery and structure from motion photogrammetry. *Earth Surface Processes and Landforms*, 40(1), 47–64. https://doi.org/10.1002/esp.3613.

Wyss, C. R., Rickenmann, D., Fritschi, B., Turowski, J. M., Weitbrecht, V., & Boes, R. M. (2016). Laboratory flume experiments with the Swiss plate geophone bed load monitoring system: 1. Impulse counts and particle size identification. *Water Resources Research*, *52*(10), 7744–7759. https://doi.org/10.1002/2015WR018555.

Zemp, M., Haeberli, W., Hoelzle, M., & Paul, F. (2006). Alpine glaciers to disappear within decades? *Geophysical Research Letters*, *33*(13). https://doi.org/10.1029/2006GL026319.

Zhang, T., Li, D., East, A. E., Walling, D. E., Lane, S., Overeem, I., Beylich, A. A., Koppes, M., & Lu, X. (2022). Warming-driven erosion and sediment transport in cold regions. *Nature Reviews Earth & Environment*, *3*(12), Article 12. https://doi.org/10.1038/s43017-022-00362-0.

Zhang, T., Li, D., East, A. E., Kettner, A. J., Best, J., Ni, J., & Lu, X. (2023). Shifted sediment-transport regimes by climate change and amplified hydrological variability in cryosphere-fed rivers. *Science Advances*, *9*(45), eadi5019. https://doi.org/10.1126/sciadv.adi5019.

Zhou, J.G., Causon, D.M., Mingham, C.G. & Ingram, D.M. (2001). The surface gradient method for the treatment of source terms in the shallow water equations. *Journal of Computational Physics*, Vol 168, 1-25.